



DOCTORAL THESIS

**TOWARDS TESTING THE TIDAL
DOWNSIZING HYPOTHESIS FOR
PLANET FORMATION**

Author:
Mark FLETCHER

Supervisor:
Prof. Sergei NAYAKSHIN

*A thesis submitted for the degree of Doctor of Philosophy
in the*

**Theoretical Astrophysics group
Department of Physics & Astronomy
University of Leicester**

March 11, 2019

“Thanks to my solid academic training, today I can write hundreds of words on virtually any topic without possessing a shred of information, which is how I got a good job in journalism.”

Dave Barry

UNIVERSITY OF LEICESTER

Abstract

TOWARDS TESTING THE TIDAL DOWNSIZING HYPOTHESIS FOR PLANET FORMATION

by Mark FLETCHER

Formation theories for planets are facing significant challenges in the light of observed planets and system architecture that greatly differs from our own solar system. The discovery of extrasolar planets is now an almost daily occurrence, with each confirmed detection adding more constraints to the planet forming process.

In this thesis I study several topics relevant to the Tidal Downsizing scenario of planet formation. In this scenario massive gas clumps are born in cold discs beyond tens of AU. As they migrate in, they accrete pebbles and assemble massive solid cores and planetesimals by grain growth and sedimentation to the centre of the clump. Some of the clumps are disrupted, releasing both cores and planetesimals, others survive as gas giant planets.

Dust modelling is a recent addition to full 3D simulations for planet formation. I have worked on implementing an implicit dust scheme for PHANTOM's two-fluid dust scheme. I show the current state of my implementation as well as a suite of tests at the end of Chapter 2 after a summary of current SPH methods. While the implicit dust time step scheme is working for the basic tests there are still problems with the integration over long time periods.

Chapter 3 presents population synthesis study of how this scenario can explain observed trends in the frequency of occurrence of planetesimal debris discs, massive cores and gas giants with their host star metallicity. In particular, classical theory predicted that debris, cores and giants should be all more abundant in high metallicity systems. However observations showed that the first two correlate with metallicity only very weakly. I find that in Tidal Downsizing these observations are natural as both debris and cores are produced when giants are destroyed.

Chapter 4 investigates the robustness of numerical modelling of clump migration and accretion with 6 particle based and one grid based codes. There is a general qualitative agreement between the codes, but the quantitative agreement is only good to within a factor of two. I find that the artificial viscosity treatment may account for much of the differences between the codes. Code performance is nevertheless encouraging given very different numerical algorithms and the fact that physical uncertainties of the problem are far greater than numerical disagreements. We also compare prescriptions from three previous population synthesis studies to try and reproduce our numerical results. None of the three are very accurate over the wide parameter space of the problem, with some over-predicting and others under-predicting the number of objects surviving disc dissipation on wide orbits. Our results should help build better population synthesis to extract from observations of present day wide separation objects their primordial numbers and properties.

Acknowledgements

I acknowledge encouragement, help and guidance from my supervisor Sergei Nayakshin. Other members of Theoretical Astrophysics group in Leicester have also contributed to my professional growth through discussions and advice at group meetings and astro-ph presentations in particular. My fellow PhD students Hossam Ali, Martin Bourne, Tom Hands, Charlie Field, Lilian Garratt-Smithson, Christian Faber, Hasaniuddin, Amery Gration, Rob Sanders, Jack Humphries, Miriam Hogg, Anagha Raj, Elen Golightly, Guila Ball, Emma Longstaff, Sarah Gibson and Skye Rosetti. I would like to thank Jack Boughton for taking the time to read my thesis I would like to thank my parents and my family for continually supporting me through my entire education and on into the future.

Contents

Abstract	ii
Acknowledgements	iv
0.1 Declaration of additional work	1
0.1.1 First author published papers	1
1 Introduction	2
1.1 Exoplanet observational methods	2
1.1.1 Transit detection method	3
1.1.2 Radial velocity method	5
1.1.3 Direct imaging	6
1.1.4 Microlensing	8
1.2 Brief summary of observational constraints on planet formation . .	11
1.2.1 Environmental constraints on planet formation process . . .	13
1.2.2 Other components of stellar systems	14
1.2.3 Observed metallicity correlations	17
Gas giants and brown dwarfs	17
Sub-giants	18
Debris discs	18
1.3 Circumstellar discs	18
1.3.1 Disc structure and evolution	19

1.3.2	Heating and cooling of the disc	23
1.3.3	Photo-evaporation	24
	EUV, FUV and X-rays	24
1.3.4	Debris discs	26
1.4	Fragmentation of discs	26
1.5	Planet migration	28
1.5.1	The impulse approximation	29
1.5.2	Resonant torques on the planet	31
1.5.3	Type I migration	32
1.5.4	Type II migration	34
1.5.5	Type III, runaway migration	37
1.6	Planet formation theories	38
1.6.1	Core accretion	38
1.6.2	Gravitational instability	39
1.6.3	Tidal downsizing	40
1.6.4	Motivation	43
1.7	Thesis structure	44
2	An overview of SPH	46
2.1	Smoothed particle hydrodynamics	46
2.1.1	Kernel functions	48
2.1.2	Hydrodynamics	48
2.1.3	Shocks and artificial viscosity	50
2.1.4	Cooling	52
2.1.5	Time integration	53
2.1.6	Sink particles and accretion	53
2.2	Dust-gas mixture	56

2.2.1	The one-fluid dust model	56
2.2.2	The two-fluid dust model	57
	Continuity equations	58
	Evolution equations	58
2.2.3	Drag regimes	60
	Epstein regime	60
	Stokes regime	61
2.2.4	Explicit timestepping	62
2.3	Implicit integration scheme for dust in PHANTOM	63
2.3.1	Implicit dust particle integration	64
2.4	The dust particle drift analytic solution	66
2.5	Results	69
2.5.1	DUSTYBOX	69
2.5.2	Radial drift in a disc, the Weidenschiling test	70
	Prescribed velocity field test	70
	A live SPH velocity field	72
2.6	Discussion	76
2.7	Conclusion	77
3	Planets, debris and their host metallicities	78
3.1	Chapter abstract	78
3.2	Introduction	80
3.2.1	Planet debris and the classical scenario	80
3.2.2	Metallicity correlation challenges	81
	Planets	81
	Debris discs	82
3.2.3	Tidal downsizing alternative	84

	Planet correlations	84
	Origin of debris discs in TD	85
3.3	Numerical method	87
3.3.1	Population synthesis	87
3.3.2	Debris model	90
3.4	Results: planets	93
3.5	Results: debris discs	98
3.5.1	Debris disc masses	98
3.5.2	Debris discs metallicity correlations	100
3.5.3	Planet - debris disc relations	107
	Gas giants	107
	Sub-giant planets	108
3.5.4	Preliminary comparison to observations	109
3.6	Discussion	111
3.6.1	Planetesimal hypothesis	111
3.6.2	Main findings	113
3.6.3	Comparison to observations	114
3.6.4	Predictions for future observations	115
3.7	Conclusions	116
3.8	Additional information	117
4	Migration code comparison	123
4.1	Chapter abstract	123
4.2	Introduction	125
4.3	Problem and numerical detail	128
4.3.1	Contributing codes	128
4.3.2	Problem choice	128

4.3.3	Initial conditions	130
4.3.4	Approach to code algorithm differences	133
	GADGET	134
	PHANTOM	135
	SPHINX	136
	SPHNG	137
	GIZMO	138
	SEREN	138
	FARGO	139
4.3.5	The comparison runs	140
4.3.6	Analytical expectations	141
4.4	Results	143
4.4.1	At a glance	143
4.4.2	Analysis of runs 1-3	147
	Migration rates	147
	Hill mass versus sink mass	150
4.4.3	Run 3 and Run 4	154
	Gap opening	154
	Gas accretion time scales	158
4.4.4	Importance of artificial viscosity prescription	160
4.5	Comparison to population synthesis	168
4.6	Discussion	174
4.6.1	Numerics	174
4.6.2	Observational implications	177
4.6.3	Some further exploration of parameter space	179
4.7	Auxiliary information	183

4.7.1 Artificial viscosity implementation in PHANTOM	183
4.8 Conclusions	187
5 Conclusion	188
5.1 Future Work	190
Bibliography	192

List of Figures

1.1	Schematic of transit detection	4
1.2	Schematic of Radial velocity method	7
1.3	HR8799 Image	9
1.4	Schematic of microlensing detection	10
1.5	Planet mass vs. star-planet separation of exoplanet population . . .	12
1.6	disc life time	15
2.1	Weidenschilling Solution for Dust drift	68
2.2	DUSTYBOX velocity test	71
2.3	Dust radial velocity test with prescribed velocity field	72
2.4	Dust radial velocity with SPH velocity field	74
2.5	Dust radial velocity dispersion in stopping time bins	75
3.1	Planet Mass vs Separation from population synthesis model	94
3.2	Giant planet survival probability against metallicity	97
3.3	Sub-Giant planet survival probability against Metallicity	99
3.4	Debris disc masses for model 1	101
3.5	Debris disc masses for model 2	102
3.6	Debris disc metallicity distributions for model 1	103
3.7	Debris disc metallicity distributions for model 2	104
3.8	Detection Probability for a debris disc of given metallicity	106
3.9	Porbability of star hosting, DDs and/or sub-giant planet	110

3.10 Cumulative frequency distributions for observed and population synthesis systems	112
3.11 Histogram of observed planet separation binned by planet mass	118
3.12 Histogram of observed planet mass binned by separation	118
3.13 Histogram of simulated planet population separation binned by planet mass	119
3.14 Histogram of simulated planet mass binned by separation	120
3.15 Histogram of observed planet metallicity	121
4.1 Relaxed initial conditions for all of the SPH runs	132
4.2 Planet separation versus time for Run 1. These do not allow the planet to gain mass from the disc, so the sink mass is fixed at $M_{p0} = 2 M_J$	143
4.3 Planet separation versus time for Run 2. These do not allow the planet to gain mass from the disc, so the sink mass is fixed at $M_{p0} = 2 M_J$	144
4.4 Planet separation (top panel) and sink particle mass (lower panel) versus time for Runs 3.	145
4.5 Planet separation (top panel) and sink particle mass (lower panel) versus time for Runs 4.	146
4.6 Migration timescales over 4000 and 7000 yrs	149
4.7 Hill masses for Runs 1-3	153
4.8 Planet mass vs separation with analytic gap opening curves	157
4.9 Accretion rates for run 3 and 4	161
4.10 Run 3 viscosity test	163
4.11 Migration rates for viscosity test	166
4.12 Accretion timescales for viscosity test	167

4.13 Population synthesis comparison to run 3	175
4.14 Population synthesis comparison to run 4	176
4.15 Mass, Separation vs time for β_{cool} and separation	180
4.16 Migration timescales for β_{cool} and separation	181
4.17 Accretion timescales for β_{cool} and separation	182
4.18 $\langle h \rangle / H$ of initial disc conditions	184
4.19 Surface density profiles for all four runs at three times	185

List of Tables

- 3.1 Parameters of the population synthesis model and their values. See text for detail. 91
- 4.1 The parameters distinguishing the Runs presented in this work. R_a , h_s , and M_{p0} are the sink accretion radius, the gravitational softening parameter, and the mass of the planet, respectively. All the other parameters and initial conditions are the same for all four Runs. 141

List of Abbreviations

GI	Gravitational Instability
TD	Tidal Downsizing
CA	Core Accretion
DD	Debris Discs
SPH	Smoothed Particle Hydrodynamics
mfm	meshless finite mass
AU	Astronomical Unit

Physical Constants

Speed of Light	$c_0 = 2.997\,924\,58 \times 10^8 \text{ m s}^{-1}$
pi	$\pi = 3.1415926536$
Gravitational constant	$G = 6.672\,041 \times 10^{-8} \text{ cm}^2 \text{ g}^{-2}$
Gas Constant	$R_g = 8.314 \times 10^7 \text{ ergsmole}^{-1} \text{ K}^{-1}$
Electron mass	$M_e = 9.109\,382\,91 \times 10^{-28} \text{ g}$
Mass Proton	$M_p = 1.672\,621\,58 \times 10^{-24} \text{ g}$
Atomic Mass Unit	$\text{AMU} = 1.660\,538\,921 \times 10^{-24} \text{ g}$
Boltzmann constant	$\sigma_k = 1.380\,66 \times 10^{-16} \text{ erg/K}$
Electron Volt	$\text{eV} = 1.602\,19 \times 10^{-12} \text{ erg}$
Charge on electron	$Q_e = 4.803\,206\,8 \times 10^{-10} \text{ esu}$
Solar Mass	$M_\odot = 1.9891 \times 10^{33} \text{ g}$
Solar Radius	$R_\odot = 6.959\,500 \times 10^{10} \text{ cm}$
Earth Mass	$M_\oplus = 5.979 \times 10^{27} \text{ g}$
Earth Radius	$R_\oplus = 6.371\,315 \times 10^8 \text{ cm}$
Jupiter Mass	$M_J = 1.898\,13 \times 10^{30} \text{ g}$
Astronomical Unit	$\text{Au} = 1.496 \times 10^{13} \text{ cm}$

List of Symbols

a	distance	cm
P	power	W (J s^{-1})
M_p	Mass of planet	
M_\odot	Mass of the Sun	
M_\oplus	Mass of the Earth	
M_J	Mass of Jupiter	
ω	angular frequency	rad

Dedicated to my late grandfather Philip Percy Parker

0.1 Declaration of additional work

I have also worked on the population synthesis model that was the basis of my work in Chapter 3. The results of the population synthesis model were published in Nayakshin and Fletcher, 2015. The main results of the study are a set of observational predictions that differ from CA predictions. These predictions are: (i) composition of the massive cores is always dominated by rocks not ices; (ii) the core mass function is smooth with no minimum at $\sim 3M_{\oplus}$ and has no ice-dominated cores; (iii) gas giants beyond 10 au are insensitive to the host-star metallicity; (iv) objects more massive than $\sim 10M_J$ do not correlate or even anti-correlate with metallicity.

My main contribution to the population synthesis model was to investigate the addition of mass accretion onto the planet as well as mass crossing the planet gap, so as to transfer mass from the outer disc to the inner disc which is seen in full 3D simulations but must be parametrised for 1D models. I started with a disc model from Alexander and Armitage, 2009 for planet accretion and gap crossing mass flow rate. Since this paper was led by my supervisor and was completed in the first half a year of my PhD, I decided not to include it in this thesis.

0.1.1 First author published papers

Planets, debris and their host metallicity correlations, Fletcher and Nayakshin, 2016

Chapter 1

Introduction

Planet formation theory faces several major challenges, first of which is to reproduce the solar system with its 3 types of planets; terrestrial, gas giant and ice giant planets. Secondly to explain the new planets being found around other stars in extreme conditions, such as hot Jupiter's and planets in binary systems. Thirdly the span in dynamical range that planet formation operates on, from dust in the micrometer size range to objects the size of Jupiter and above, is immense. Fourthly, planet formation must separate mass and angular momentum as the central star contains an overwhelming fraction of the systems mass while contributing very little to the solar systems angular momentum. This thesis aims to explore just some of the currently outstanding issues in the framework of the Tidal Downsizing (TD) hypothesis for planet formation.

1.1 Exoplanet observational methods

We wish to compare theories, including population synthesis models, against observations of planets. Unfortunately, observations remain difficult and are biased towards systems that are easier to observe. Extensive work has been required to understand these biases, completeness functions and other limitations. The two

most effective methods of planet hunting to date are the radial velocity and the transit methods. While these two methods have different biases, they tend to be most effective for large planets orbiting their host stars at separations smaller than the Earth-Sun separation. Below we overview these and other major observational techniques for planet detection before discussing major observational results and how they compare to planet formation theories.

1.1.1 Transit detection method

Planet detection through the transit method utilises the dip in flux from the star as the planet transits in between the observer and the host star. A simple schematic of this process can be seen in fig. 1.1. As the planet progresses from left to right in the diagram, it starts to block light from the star. This corresponds to a gradual decrease in the detected flux from the star until the planet is completely in front of the stellar disc. This results in a plateau in the observed flux. As the planet begins its egress from the star, less light is blocked, and the light curve returns to the pre-transit levels. This produces the classic U-shaped transit that is seen for planets. A secondary transit can occur when the planet passes behind the star, in which case it is the star that blocks the light from the planet. However, as the planet is much less luminous than the star, such a transit is much harder to detect.

Planets usually block as little as one part in a million of the stellar light as seen from the Earth. To make routine planet detection with the transit method, large telescope surveys, both ground and space based, such as CoRoT, Kepler and NGTS (Auvergne et al., 2009; Borucki et al., 2010; Wheatley et al., 2018) were therefore required. Transit detections now contribute most of the planets observed so far. However, the method produces a high false detection rate due to star spots, binary star systems and stellar variability, and also gives us the radius

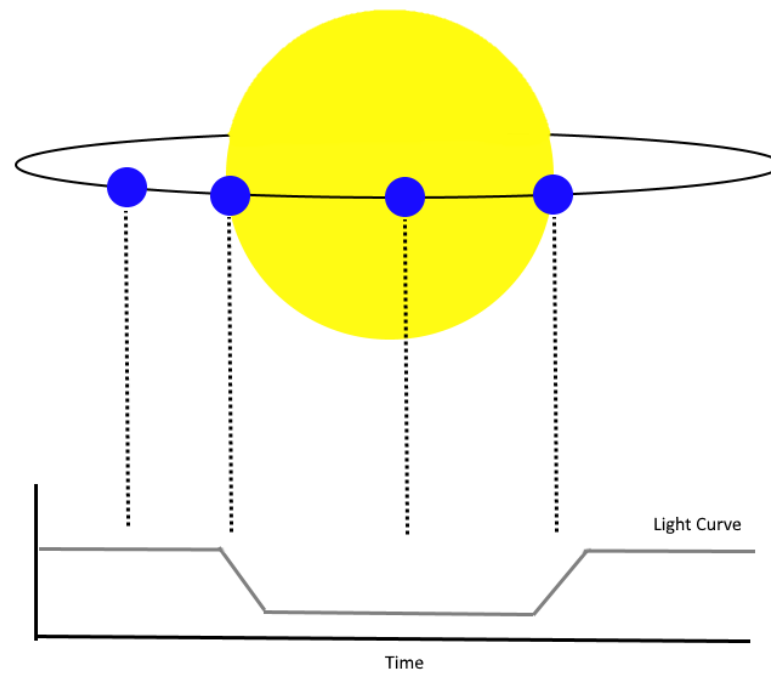


FIGURE 1.1: A schematic view of an idealised transit detection seen edge on. As the planet passes between the star and the observer the observed light will decrease as the planet blocks some of the stars light.

but not the planet mass. To counter these problems, multiple planetary transits are required to rule out false positives and to increase the signal-to-noise ratio of the detected flux. Radial velocity follow-ups are also needed to establish the planet mass.

Since transit detection surveys became operational only in the last decade or so, there is a planet detection bias to finding planets on short period orbits. Efforts have been made to map both detection and geometric biases in studies such as Vanderburg et al. (2016) and Kipping and Sandford (2016). These studies aimed to finding biases in the properties of planets as well as the detection rate. It was found a nonuniform distribution in the impact parameters of detected transiting exoplanets can be explained by observational bias.

1.1.2 Radial velocity method

Struve (1952) was the first to propose the use of stellar spectra to find planet-like objects in orbit around stars. When including the effect of the planet on the star, we find that the star and the planet orbit the common centre of mass of the system; this is usually within the star for the case of a single star systems. Fig. 1.2 (Top) is a schematic view of a simple case of a single star and a planet orbiting the barycentre of the system. As the star recedes away from the observer (left of figure) the stellar spectrum seen by the observer is red-shifted. As the star approaches the observer, (right of figure) the spectrum is now blue-shifted. Fig. 1.2 (Bottom) is an idealised radial velocity curve – the Doppler shift in the observed spectrum versus time – produced by a planet in a circular orbit. The orbital period of the planet in this case is simply the period of the sine function and the planet mass can be calculated from the amplitude of the Doppler shift.

The Radial velocity (RV) method of planet detection detects the relative motion of the planet and its host star by carefully monitoring selected emission lines of the star. As the star and the planet orbit one another, the gravitational force of the planet will move the star away from the barycentre of the system, albeit a very small amount, and this motion can be detected via red or blue shifts in the emission lines of the star. This technique has now been successfully employed for over twenty years, and thus RV detections are pushing the upper limits on planet separation of observed exoplanets (e.g., Sousa et al., 2008; Mayor et al., 2011; Buchhave et al., 2012). The resultant movement of a star can be calculated by,

$$K = \left(\frac{2\pi G}{P} \right)^{\frac{1}{3}} \frac{M_p \sin i}{(M_* + M_p)^{\frac{2}{3}} \sqrt{1 - e^2}} \quad (1.1)$$

The Earth's effect on the Sun, measured via the maximum orbital velocity that the Sun acquires due to this interaction, is 0.09ms^{-1} , whereas Jupiter produces a radial velocity of 12.5ms^{-1} , despite being five times further away from the Sun. This shows the strong bias towards higher mass planets in this method. Therefore, radial velocity measurements of stars are sensitive primarily to massive objects orbiting at relatively small separations.

The radial velocity method successfully detected the first ever exoplanet, 51 Peg b of mass $0.5M_J$ circling the star at separation of just 0.05 AU, famously called a hot Jupiter (Mayor and Queloz, 1995). In the original discovery an upper limit of $2M_J$ was put on the planet mass with a minimum of $0.5M_J$. In later follow up observations with better spectral resolution this mass estimate has been constrained to $0.476^{+0.032}_{-0.031} M_J$ by Birkby et al. (2017).

1.1.3 Direct imaging

The Direct or high contrast imaging method uses observations primarily at near-infrared wavelengths where giant planets are expected to be relatively bright compared to their host stars that emit most of their radiation in the optical. Several images are taken at different exposure times; short exposures are taken of the central star so that the image is not saturated. This allows for characterisation and accurate positioning of the star. These observations are followed by longer exposure ones which are saturated around the star but crucially are more sensitive to faint companions of the star (Marois et al., 2008). A technique called angular differential imaging (Marois et al., 2006) can be used to reduce noise or speckling from atmospheric turbulence. This process allows the field of view of the image to rotate around the observed star. Over the period of the exposure the speckling effect of the atmosphere will be smeared out.

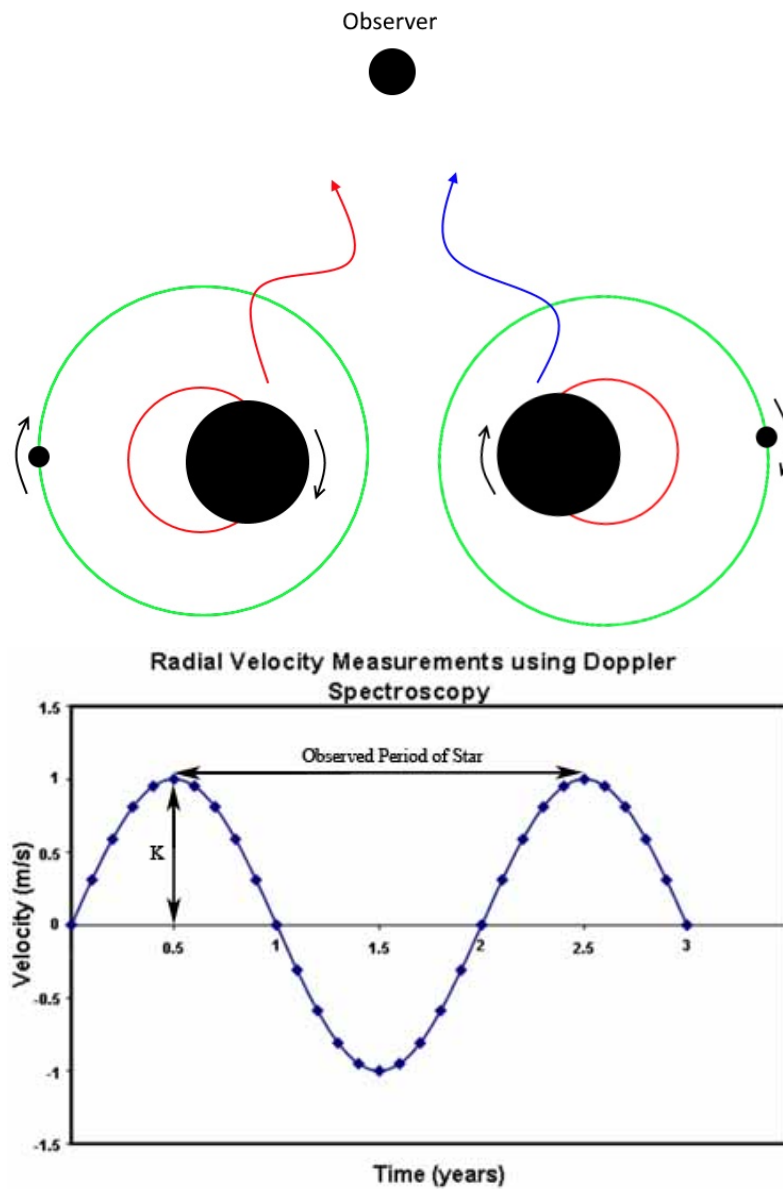


FIGURE 1.2: **Top.** A schematic view of a star and planet system as they orbit around the barycenter. **Bottom.** The resultant radial velocity sine wave produced by the orbiting planet.

By directly detecting planets around their host stars in multiple epochs, planetary orbits could in principle be reconstructed. Clearly, this technique is best for relatively wide separation, e.g., tens of AU, objects. These methods lead to the breakthrough discovery of the HR8799 system hosting four giant planets each of a $\sim 5 - 7$ Jupiter masses and orbiting the star at separation from 14.5 (HR8799 e) to 68 (HR 8799 b) AU (Marois et al., 2008; Marois et al., 2010).

A significant challenge to this method is the fact that theoretical models of planetary evolution needs to be employed to interpret the observations, as planet luminosity does not tell us anything directly about its mass. Stellar wobble in these systems is too small to be detectable via RV methods. There are theoretical uncertainties in planet luminosity versus age track depending on how exactly the planet was assembled (Burrows et al., 2000; Burrows et al., 2001; Marley et al., 2007).

1.1.4 Microlensing

The Microlensing detection method uses the variations in a stellar mass gravitational lens caused by the presence of a planet. In the normal case the light from a background star is magnified by the lensing star that lies on the observer's line of sight. This is detected as an increase in the luminosity of the source object. The duration of the event is the primary observable feature, and depends upon mass of the lens, distance to both lens and source and velocity. The size of the Einstein ring created by the lens can be calculated by,

$$\theta = \sqrt{\frac{4GM_L}{c^2} \frac{d_{LS}}{d_L d_S}} \quad (1.2)$$

where M_L is the mass of the lens, d_{LS} is the distance between the source and the lens, d_L is the distance to the lens from the observer and d_S is the distance from

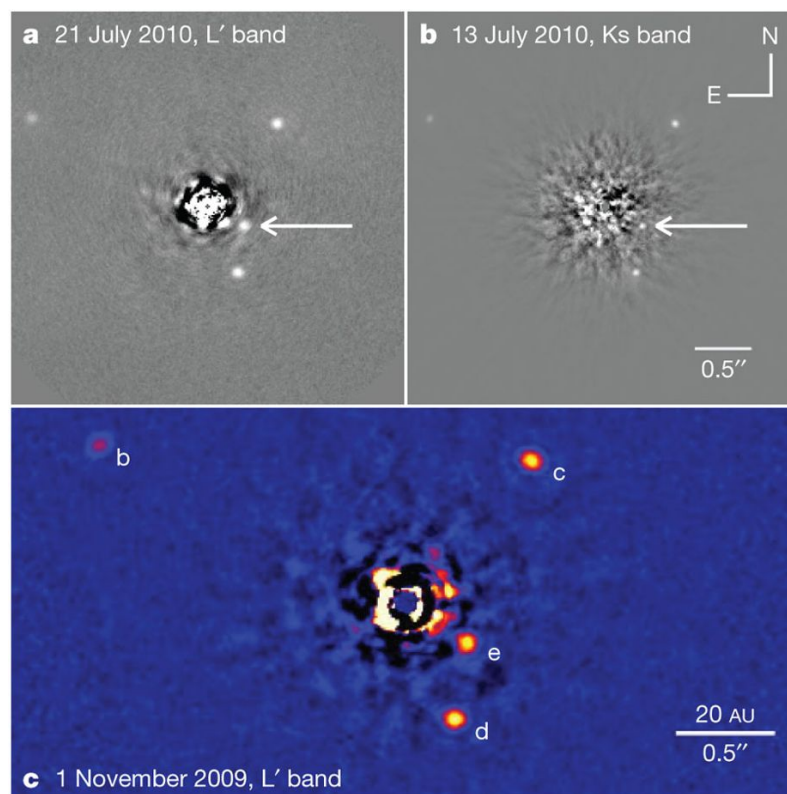


FIGURE 1.3: Image of the four planets in the HR8799 system, image from Marois et al. (2010).

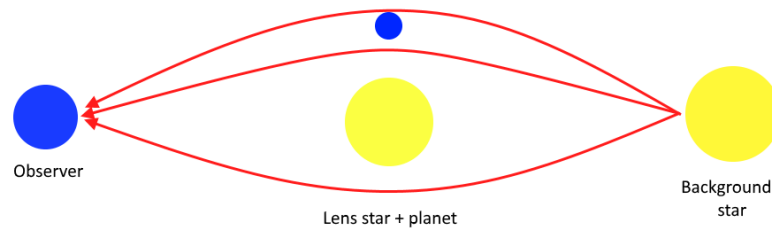


FIGURE 1.4: A schematic view side on of a microlensing detection. Light from the background star is gravitationally bent by the lensing star and planet.

source to observer. A planet in the lensing system will produce an asymmetry in the gravitational potential and its own lensing effect on the light curve. Using eq. 1.2 for a main sequence solar mass star gives an unresolvable angle for current telescopes. As such the lensing effect from the planet only adds to the magnitude amplification of the source star. It is then possible to infer the mass of the planet as well as its separation, or at least put constraints on these quantities.

Planets are, of course, much less massive than stars, therefore, create only a small addition to the lensing effect. For this reason, although microlensing for planets was first seriously discussed by Liebes (1964) and later by Mao and Paczynski (1991), the technology and the high sensitivity large survey data have only recently become available. Gould et al. (2010) looks at 3 years of microlensing data from large surveys and specific planet hunting microlensing campaigns. However, to date most microlensing planets come from an initial microlensing survey detection and then rapid follow up by other teams.

1.2 Brief summary of observational constraints on planet formation

The population of known planets is best displayed in terms of planets mass and separation from their host star. In the bottom left panel of fig. 1.5, the current observed planet population is shown with planet mass in Jupiter masses against star-planet separation in units of AU. The planets have been colour-coded by their detection method. As discussed in section 1.1 both the transit method and radial velocity method have yielded many more planets than the other methods so far. The top panel of fig. 1.5 is a histogram for all planets in the star-planet separation plane. The right panel is a histogram of all planet masses. Fig 1.5 does not include the many planet candidates that are missing constraints on either planet mass or separation. The data for the figure is provided by the exoplanet.eu data base (Schneider et al., 2011).

The observational data from the radial velocity surveys can be used to create a completeness function for planet mass and star-planet separation. These functions can then be applied to the data set which will allow for a better comparison to the simulated data set. The reverse is also possible; the sensitivity of the instruments is known, at least to an approximate level that will suffice for our needs. The sensitivity is basically a cut on the sample; by looking at the observational data the same cut can be applied to simulated data. With both samples limited by the same restrictions comparisons can now be made.

The distribution of exoplanets is heavily influenced by the observational bias; this can be seen on fig. 1.5 as the low mass high separation region of the figure is empty. Fig. 1.5 shows the data split into several populations; the main three populations of planets seen in this figure are the cold gas giants, the “Hot

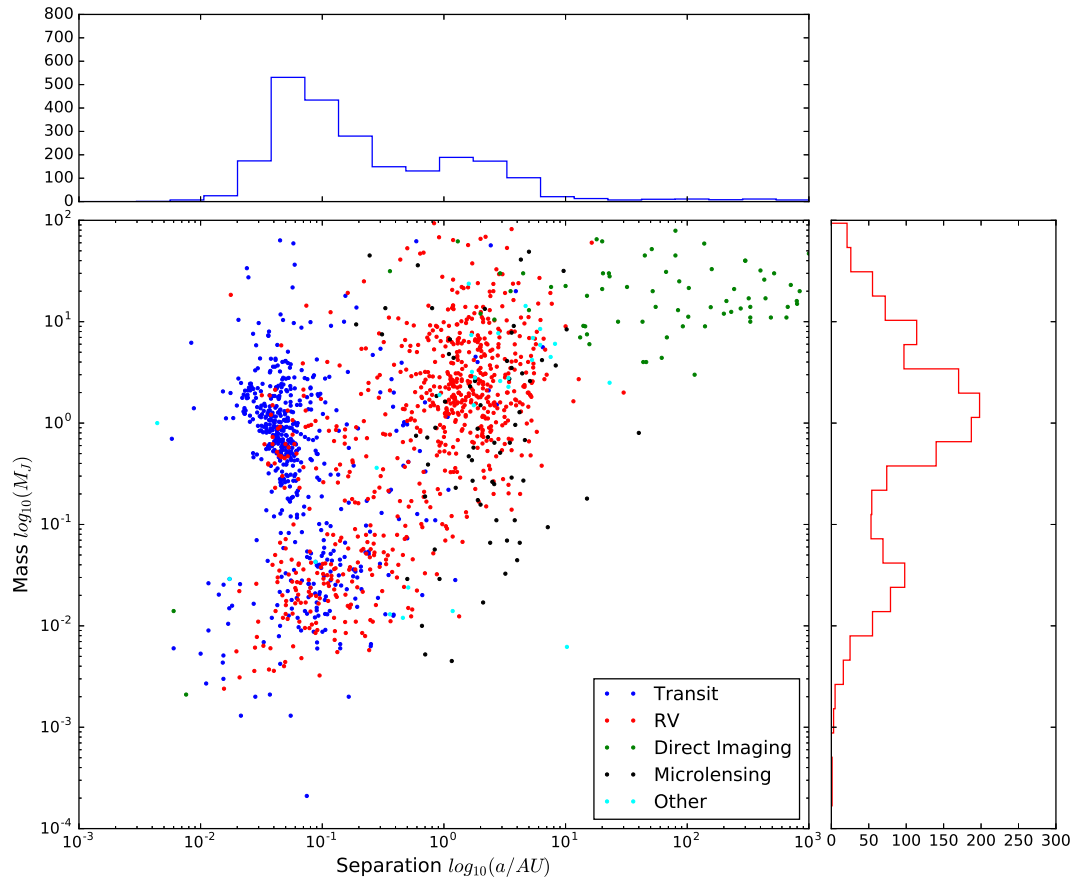


FIGURE 1.5: Mass vs separation plot of current confirmed exoplanets, with masses. Colours represent detection method: (blue) Transit detection, (red) Radial velocity, (green) direct imaging, (black) microlensing and (cyan) transit timing, pulsars and astrometric detections. histograms for total planet populations in mass and separation are shown on their respective axes.

Jupiters” and the super-Earth population. These groups are clearly resolved into two populations with a separation “valley” in each, focused on $\sim 8 \times 10^{-2} AU$ and $10^{-1} M_J$. These separation “valleys” are well within the observational limits, so are considered to be real rather than an artefact of the observational methods.

1.2.1 Environmental constraints on planet formation process

Observations of circumstellar discs provide constraints on the timescale for planet formation since by observing young stellar clusters we can obtain a better handle on the age of a star-planet forming system than we could if we observed just one isolated system (eg. Haisch, Lada, and Lada, 2001; Damjanov et al., 2007). Several conclusions were drawn from such studies.

1. Planet formation needs to be very rapid. Discs have been observed to be dispersed on time scales from between 1 to at most 10 Myr (Haisch, Lada, and Lada, 2001). This means that at least gas giant planet formation must be complete on these timescales. The discovery of hot Jupiters constrains planet formation to even earlier than the disc life time as the planet needs to form and then migrate inwards (Mayor and Queloz, 1995; Lin, Bodenheimer, and Richardson, 1996). In further support of rapid formation are the recent HL Tau observations which show signs of planet presence at an age as small as $\sim 0.5 - 1$ Myr (ALMA Partnership et al., 2015; Dipierro et al., 2015; Dipierro et al., 2016).

2. Planet formation should occur around stars in a broad range of masses, from very low mass stars to at a few Solar masses (eg. Proxima B and Trappist systems). Results from the Kepler mission have shown a high occurrence rate of sub-Neptune mass planets around low mass M stars, these range in masses from $0.075 - 0.5 M_{\odot}$. This rate could be as high as 2.5 ± 0.2 planets, sized $1 - 4 R_{\oplus}$ per M dwarf (Dressing and Charbonneau, 2015). Multi-planet systems have also

been detected around low mass M dwarfs. To appreciate the challenge, note that the circumstellar disc mass should scale with stellar mass, so that low mass stars should have low mass planet-forming discs (Pascucci et al., 2016). This provides more challenges for planet formation as there is less material to form planets. For example, observations of Trappist-1 (Gillon et al., 2017), indicate 7 planets around a very low mass star, $M_* \sim 0.1M_\odot$.

3. Planet formation around binaries (Fabrycky et al., 2014) indicates that the process is not only fast but very robust, operating in very dynamic environments that occur due to the presence of a secondary high mass object. Calculations show that the binaries, many of which are eccentric, should give significant velocity kicks to the populations of planetesimals orbiting the binary and that these planetesimals should then collide at very large velocities, leading to fragmentation rather than growth (e.g., Paardekooper, Rein, and Kley, 2013).

1.2.2 Other components of stellar systems

We know that planets are not the only objects orbiting their host stars. It is possible that understanding formation of these other bodies will yield valuable constraints on planet formation.

1. We know that both in the Solar System and around other stars, there are discs or rings composed of large solids bodies known as debris discs (Wyatt et al., 2007; Wyatt, 2008). These discs are detectable through the thermal emission as they can be seen as an infra-red excess in the stellar spectra, (Oudmaijer et al., 1992; Mannings and Barlow, 1998). The star light is absorbed by the nearby dust, the dust acts as a black body and re-emits in the infra-red wavelength. Modern observations with better angular resolution are able to resolve parts of the disc. For example, Ricci et al. (2015)

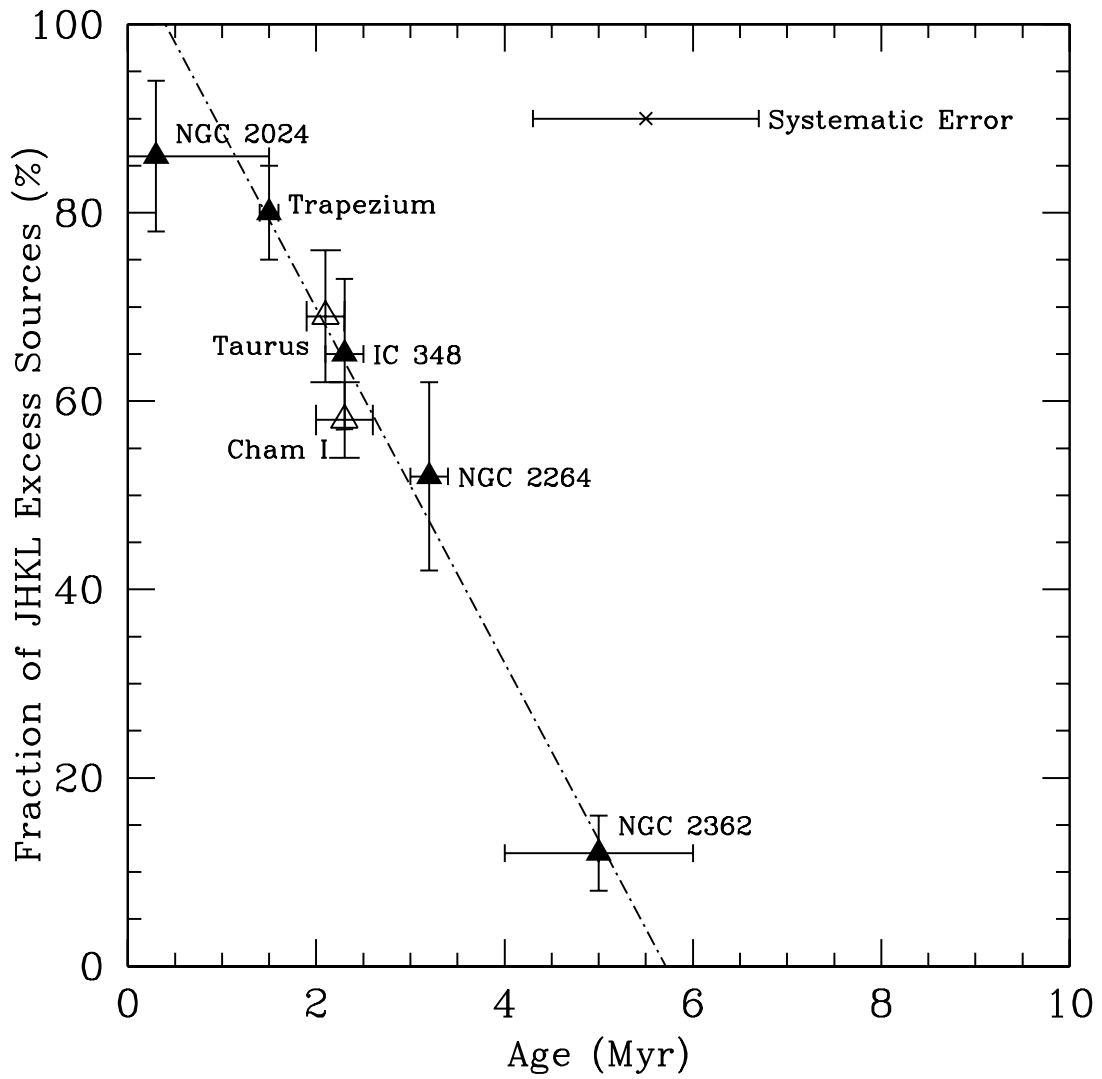


FIGURE 1.6: disc life times for nearby young star clusters as a fraction of stars with discs. Figure from Haisch, Lada, and Lada (2001)

present results for a debris disc observed with ALMA at the millimetre wavelengths. The irradiation for the central star is of great importance as is the reflectivity of the debris to detecting the system and DD, although, this is highly dependent upon the material. Through collisions between objects in the disc the larger material will be ground down; this process releases the dust that emits in the infra-red.

2. Brown dwarfs (BD). The well established paradigm of star formation (Larson, 1969) posits that formation of brown dwarfs and stars start with the birth of a few Jupiter mass gas clump called the "first core" which then grows through gas accretion. Therefore, the first cores could be the common starting point for the origins of planets and more massive objects via Gravitational Instability scenario (e.g., Rice, Lodato, and Armitage, 2005; Stamatellos and Whitworth, 2008; Stamatellos and Whitworth, 2009; Stamatellos, 2015). Furthermore, Core Accretion scenario for planet formation may also produce brown dwarfs by accretion of gas onto planets in high mass discs (Mordasini et al., 2012). There is, therefore, good physical motivation to include brown dwarf observational data (e.g., Raghavan et al., 2010; Troup et al., 2016) as a source of constraints on our planet formation scenarios.
3. Stellar secondaries in binary systems are also assembled by gas accretion onto first cores, and therefore should also be considered in our quest to understand planet formation. In fact, one of the first detailed investigations on the origin of the Solar System proposed that the planet and stellar binary formation share many similarities, e.g., start from a gas clump of a few Jupiter masses (Kuiper, 1951a).

1.2.3 Observed metallicity correlations

With the fundamental building blocks of planets being dust grains a stellar systems metallicity is an important factor to consider. A higher metallicity would mean more metals, in the form of dust, to build planets. A star's metallicity can be measured through observations of spectral lines; Fe is a commonly used tracer due to its easy to identify spectral features (Matteucci, 2012; Fischer and Valenti, 2005). However, a distinction needs to be drawn between the Iron fraction [Fe/H] that is observed and the total metal fraction [M/H] that is usually discussed in theory.

Gas giants and brown dwarfs

The existence of Hot Jupiters, Jupiter mass planets with very small separations from their host stars, correlate strongly with the host star having relatively high metallicity (Miller and Fortney, 2011; Thorngren et al., 2016). This correlation holds out to a separation of a few AU as the radial velocity surveys now have large sample size at these separations (Gonzalez, 1999; Fischer and Valenti, 2005; Mayor et al., 2011; Wang and Fischer, 2015). These early observational results provided a strong support for the Core Accretion model of planet formation (Pollack et al., 1996) which predicted such a correlation (Ida and Lin, 2004b).

Interestingly, however, planets more massive than ~ 5 Jupiter masses, and brown dwarfs, were recently shown to not correlate with the host stars metallicity (Raghavan et al., 2010; Troup et al., 2016; Santos et al., 2017), in direct contradiction to the predictions of Core Accretion (Mordasini et al., 2012).

Sub-giants

For sub-giant planets, those smaller in mass than Saturn, occurrence rates do not correlate with host star metallicity (Mayor et al., 2011; Buchhave et al., 2014; Buchhave and Latham, 2015). In a more recent study sub-Neptune mass planets are only twice as likely to form around stars of $[M/H] > 0$ compared to stars $[M/H] < 0$. This is seen as a very weak or no correlation as Gas-giants are 9 times more likely to occur around $[M/H] > 0$.

Debris discs

A thermal excess in an observed star's spectrum can indicate the presence of a debris disc. This infra-red excess is caused by dust grains reprocessing stellar light into the thermal part of the spectrum (Oudmaijer et al., 1992; Mannings and Barlow, 1998). There is an ongoing debate but most studies find that debris discs do not correlate with host star metallicity (Wyatt, 2008; Moro-Martín et al., 2015). These relations will become more defined over time as our sample of debris discs increases. However it can already be seen that debris disc presence does not correlate with the presence of gas giant planets in the system (Moro-Martín et al., 2007; Bryden et al., 2009; Kóspál et al., 2009).

1.3 Circumstellar discs

The process of planet formation either through gravitational instability, GI, or core accretion, CA, occurs within the circumstellar discs that form around many young stars. As the planets form, features in the disc as well as its composition, mass and radial extent will all impact planet formation.

The circumstellar disc can be characterised by several parameters. The main disc parameters include mass, radial extent, disc geometric aspect ratio H/r , surface density $\Sigma(r)$, the temperature profile and age. These can (in principle) be inferred directly from observations of the disc spectral energy distribution, SED, and observation in the radio (which tends to provide best resolved information), infrared and visible. Observations of disc mass have recorded *gas masses* of up to $0.4M_{\odot}$ (Kawabe et al., 1993), although observations primarily trace the dust component of the disc and not the neutral hydrogen which makes up most of the mass (Williams and Cieza, 2011). A large range of radii have also been observed; for example, a range of radii from 14 to 198 AU was found by (Andrews and Williams, 2005) for a sample of protoplanetary discs. However, both disc radius and disc mass are time dependant quantities, creating a large spread in observed characteristics of the systems. Additionally, we have the best chance of observing old (few Myr old) systems whereas Gravitational Instability may operate in very young systems. Further to this, as a planet forms it will influence the disc surface density profile around the planet. The strength of the effect will be proportional to the planet's mass. This in turn will affect the temperature profile and disc geometric aspect ratio.

1.3.1 Disc structure and evolution

Disc evolution is extremely important to planet formation; the lifetime of the disc sets an upper limit on the time-scale for planet formation. The disc will evolve through viscosity in the disc driving accretion onto the central star and, in later stages photo-evaporation will dominate and evaporate what is left of the disc material. The continuity and angular momentum equations can be described for

an azimuthally averaged, viscous, one dimensional disc in the form,

$$R \frac{\partial \Sigma}{\partial t} + \frac{\partial}{\partial R} (R \Sigma(R) v_R) = 0, \quad (1.3)$$

$$R \frac{\partial}{\partial t} (R^2 \Omega \Sigma(R)) + \frac{\partial}{\partial t} (R^2 \Omega \cdot R \Sigma(R) v_R) = \frac{1}{2\pi} \frac{\partial G_\tau}{\partial R}, \quad (1.4)$$

where $\Sigma(R)$ is the surface density of the disc, R , is the radial position in the disc, v_R , is the velocity in the radial direction, where $\Omega = \sqrt{GM_*/R^3}$ is the Keplerian angular frequency at radius R and G_τ is the torque. G_τ can be given as,

$$G_\tau = 2\pi R \cdot v_R \Sigma R \frac{\partial \Omega}{\partial R} \cdot R. \quad (1.5)$$

where, viscosity, v_R , is given by,

$$v_R = \alpha_{SS} c_s H, \quad (1.6)$$

where α_{SS} is the Shakura and Sunyaev disc viscosity parameter, c_s and H are the midplane sound speed and the disc scale height.

Equation 1.3 is the continuity equation or mass conservation equation for the disc, while equation 1.4 is the conservation of angular momentum equation. These two along with the associated equation 1.5 are used to evolve the disc over time (Shakura and Sunyaev, 1973; Pringle, 1981).

We define the vertical scale-height of a stable disc as,

$$H \equiv \frac{c_s}{\Omega} \quad (1.7)$$

$$c_s^2 = \frac{k_B T_c}{\mu m_p}, \quad (1.8)$$

where, k_B is the Boltzmann constant, T_c is the midplane temperature of the disc, μ is the mean molecular weight of the gas and m_p is the mass of a proton.

Eq. 1.7 can be recast for a stable disc in vertical hydrostatic equilibrium into the useful the more useful parameter, H/R ,

$$\frac{H}{R} = \frac{c_s}{v_k} \quad (1.9)$$

where v_k is the keplerian velocity at position R Eq. 1.3 only considers disc viscous torques. We must now extend that equation to include the presence of a planet. The planet will exert an extra torque onto the disc. $\Sigma(R)$ is now evolved using the the equation

$$\frac{\partial \Sigma}{\partial t} = \frac{3}{R} \frac{\partial}{\partial R} \left[R^{1/2} \frac{\partial}{\partial R} (R^{1/2} \nu \Sigma) \right] - \frac{1}{R} \frac{\partial}{\partial R} (2\Omega R^2 \lambda \Sigma) \quad (1.10)$$

where $\lambda = \Lambda / (\Omega R)^2$, and Λ is the specific tidal torque from the planet (e.g., Lin and Papaloizou, 1986). These depend on whether the planet is embedded into the surrounded disc (type I migration) or it was able to clear its immediate vicinity of gas (type II migration). For population synthesis studies below we must model both type I and type II migration. The respective specific torques are then expressed as λ_I, λ_{II} , and are combined in the weighted sum, λ :

$$\lambda = \lambda_I (1 - f_{II}) + \lambda_{II} f_{II}, \quad (1.11)$$

where λ_I is given by (Nayakshin, 2015c),

$$\lambda_I = \lambda' \exp \left[-\frac{|\Delta R|}{\Delta R_I} \right], \quad (1.12)$$

where $\Delta R = R - a$ and $\Delta R_I = H + R_H$, a is the position of the planet in the disc and R_H is the hill radius, $R_H = a(M_p/3M_*)^{1/3}$. λ' is calculated by the sum of the type I torque from the planet on the disc to be equal to the negative of the disc torque on the planet, given by $M_p (GM_*a)^{1/2} / 2t_I$ t_I is the timescale for migration type I. f_{II} is a switch controlling planet migration regime. This switch can vary between 0 and 1. In type II $f_{II} = 1$, whereas in type I $f_{II} = 0$. The basis of this switch comes from two-dimensional simulations by Crida, Morbidelli, and Masset (2006) that show a deep gap in the disc is opened when the parameter,

$$c_p = \frac{3H}{4R_H} + 50\alpha_{ss} \left(\frac{H}{a} \right)^2 \frac{M_*}{M_p} \lesssim 1, \quad (1.13)$$

where H is the disc vertical scale-height at planet location, a , and $\alpha_{ss} < 1$ is the Shakura-Sunyaev viscosity parameter. We therefore set,

$$f_{II} = \min \{1, \exp [-(c_p - 1)]\}. \quad (1.14)$$

(Nayakshin, 2015c; Nayakshin and Fletcher, 2015) The type II migration normalised specific torque is given by the expression,

$$\begin{aligned} \lambda_{II} &= \frac{q^2}{2} \left(\frac{a}{\Delta R} \right)^4 & R > a \\ \lambda_{II} &= -\frac{q^2}{2} \left(\frac{R}{\Delta R} \right)^4 & R < a. \end{aligned} \quad (1.15)$$

q is the mass ratio of planet to star, M_p/M_* (Armitage and Bonnell, 2002; Lodato and Clarke, 2004; Alexander, Clarke, and Pringle, 2006).

1.3.2 Heating and cooling of the disc

Accretion and turbulence within the disc provide a source of heating for the gas and dust. This is countered by radiative cooling and – if these two processes can balance one another – the disc will be in a thermal equilibrium state. Radiative cooling is mostly controlled by the opacity of the disc. The opacity is affected by the dust grain size distribution, grain composition, grain growth size and settling into the mid plane. The cooling time-scale can also be greatly affected by convection currents set up in regions. We start by looking at the optical depth at the mid-plane of the disc, τ ,

$$\tau = \frac{1}{2}\kappa_R\Sigma(R), \quad (1.16)$$

where κ_R is the Rosseland mean opacity and $\Sigma(R)$ is the disc surface density. The Rosseland mean opacity uses the temperature derivative of the Planck function averaged over all wavelengths or The vertical energy flux, $F(z)$, is given by,

$$F_z(z) = \frac{16\sigma T^3}{3\kappa_R\rho} \frac{dT}{dz}, \quad (1.17)$$

where ρ is the vertical density profile in the disc, σ is the Stefan-Boltzmann constant. Assuming all energy dissipation occurs at $z = 0$ then $F(z) = \sigma T_{disc}^4$ is a constant with height above the mid-plane. To continue we must assume that opacity is constant and $\tau \gg 1$. This simplifies the final result, which can be combined with stellar irradiation, T_{irr} to give,

$$T_c^4 \simeq \frac{3}{4}\tau T_{disc}^4 + T_{irr}^4. \quad (1.18)$$

where

$$T_{disc}^4 = \frac{3GM_*\dot{M}}{8\pi\sigma r^3} \left(1 - \sqrt{\frac{R_*}{r}}\right) \quad (1.19)$$

and

$$T_{irr} = \left(\frac{L_*}{4\pi\sigma}\right)^{1/4} r^{-1/2} \quad (1.20)$$

where, L_* is stellar luminosity and σ is the Stephan-Boltzmann constant. The central temperature, T_c , can then be used in 1.8 to calculate c_s . This implies that the central temperature is usually several times higher than the disc surface temperature (Armitage, 2010).

1.3.3 Photo-evaporation

The time over which a gaseous disc is completely removed from the system provides a very important timescale for the end of the first stage of planet formation during which the creation of gas giant planets must be completed. Photo-evaporation, is a mechanism for removing mass from the disc through heating of gas due to radiation from both the host star (Bally and Scoville, 1982; Hollenbach et al., 1994; Shu, Johnstone, and Hollenbach, 1993) and external sources such as massive O type stars (Johnstone, Hollenbach, and Bally, 1998). Observations of massive externally photo-evaporating discs were first reported by O'dell, Wen, and Hu (1993) where a strong ionised gaseous outflow from the disc can be seen.

EUV, FUV and X-rays

Extreme ultraviolet (EUV) photons can ionise the surface layer of the disc. Photons with energy, $E > 13.6$ eV, can raise the temperature of the surface layer to $T \approx 10^4$ K. At this temperature the sound speed of the gas is $c_s \approx 10$ km s⁻¹.

A critical radius, r_g , can be defined such that gas outside of this is unbound due to the sound speed being higher than local Keplerian speed. This radius can be simply calculated as,

$$r_g = \frac{GM_*}{c_s^2}. \quad (1.21)$$

from Hollenbach et al. (1994). In most star forming regions the flux of external EUV radiation is too low to provide the required photo-evaporation to clear the disc as rapidly as observations demand (Adams et al., 2006). Therefore, an internal source of photo-ionising radiation must provide the required flux to clear the disc. Further studies of numerical simulations Begelman, McKee, and Shields (1983), Owen et al. (2010), Owen, Ercolano, and Clarke (2011), and Owen, Clarke, and Ercolano (2012) show that X-ray and EUV photoevaporation can reproduce mass loss rates similar to those observed $\sim 10^{-10} - 10^{-7} M_\odot \text{ yr}^{-1}$. Analytic fits to the mass loss rates from the wind are were calculated by Alexander and Armitage (2007),

$$\dot{M}_{\text{wind}} \approx 1.6 \times 10^{-10} \left(\frac{\Phi}{10^{41} \text{ s}^{-1}} \right)^{1/2} \left(\frac{M_*}{1 M_\odot} \right)^{1/2} M_\odot \text{ yr}^{-1} \quad (1.22)$$

EUV and FUV radiation from the central star is also very quickly absorbed by the inner regions of the disc and its photo-sphere. X-ray photons, on the other hand, have a higher penetration depth due to their much higher energies and may dominate the mass loss rate for certain stellar types (Ercolano, Clarke, and Drake, 2009). The X-rays can also come in high fluxes from close by massive stars that we expect to find in star forming regions.

Photoevaporation driving disc winds produces a viscosity that can drive disc

evolution this essentially adds an additional term to the surface density evolution equations discussed earlier (Clarke, Gendrin, and Sotomayor, 2001; Alexander, Clarke, and Pringle, 2006).

1.3.4 Debris discs

From the point of view of planet formation, a Debris Disc (DD) is material left over after the majority of the gas disc has been dispersed, leaving behind larger solid material that cannot easily be swept from the system by stellar winds or radiation pressure from the star. This leaves large dust grains and bigger objects in the system. Dust particles in a debris disc are formed through the collision of planetesimals and when these large objects break down into much smaller bodies they can form a dust disc.

In Core Accretion, planetesimals are predecessors of planets. In contrast, in Tidal Downsizing planetesimals could be formed inside gas clump and then released back into the disc by disruption of the gas clump (Nayakshin and Cha, 2012). We shall consider later observational differences in predictions of these theories concerning debris discs.

1.4 Fragmentation of discs

Giant planet formation through gravitational instability was considered as long ago as Kuiper (1951a), who argued that planet formation is an extension of stellar binary formation down to planetary scales. However, to form a planet from a disc we must first show that discs can become gravitationally unstable. The Toomre Q parameter (Toomre, 1964) is an indicator of the stability of a region against gravitational collapse, under self-gravity. The Q parameter is defined as

$$Q = \frac{c_s \kappa}{\pi G \Sigma} \quad (1.23)$$

where c_s is the sound speed within the gas, κ is the epicyclic frequency and Σ is the surface density of the disc. For a nearly Keplerian disc the epicyclic frequency at which the gas oscillates is very similar to the angular rotation frequency of the disc, $\Omega(R) = \sqrt{GM_*/R^3}$. The top part of eq. 1.23 is the stability term from gas pressure and rotation while the bottom is the instability caused by gravity. Thus, as the mass increases or the temperature decreases, Q is reduced. Toomre (1964) showed that instability growth at short wavelengths is stabilised by the gas pressure gradient, whereas long wavelengths are stabilised by the rotation of the disc. For sufficiently low values of Q , $Q \lesssim 1$, there is a range in wavelengths for which the disc is susceptible to a rapid instability growth. In particular, the most unstable wavelength for an axisymmetric perturbation is given by

$$\lambda_m = \frac{2\pi^2 G \Sigma}{\kappa^2}. \quad (1.24)$$

and the disc collapses at the critical value of $Q_{\text{cr}} = 1$. For a non-axisymmetric disturbance, the critical value for gravitational collapse is slightly higher, $Q_{\text{cr}} = 1.5$ (Toomre, 1964).

The $Q_{\text{cr}} \approx 1$ disc collapse condition may be recast into an approximate global form using the vertical hydrostatic balance equation, $H = c_s/\Omega$, and the disc mass estimate of $M_{\text{disc}} = \pi r^2 \Sigma$. Applying these to equation 1.23 and assuming the instability sets in at $Q_{\text{cr}} = 1$, we get

$$\frac{M_{\text{disc}}}{M_*} \gtrsim \frac{H}{R} \quad (1.25)$$

As the gas sound speed decreases with temperature, the disc needs to be cool and massive for the gravitational instability to develop.

If the $Q < Q_{\text{cr}}$ condition is satisfied, small perturbations grow initially exponentially on the time scale of the orbital period (Durisen et al., 2007). However, the non-linear outcome of gravitational instability depends on the disc thermodynamics. Analytical arguments and 2D simulations by Gammie (2001) showed that the cooling time scale should be less than a few dynamical times, $t_{\text{cool}} < 3\Omega^{-1}$ to allow the disc to collapse to arbitrarily large gas densities. For larger cooling times, the non-axisymmetric disturbances in the disc produced by the instability avert the disc collapse. Instead, transient spiral density arms appear in the disc and help to transfer disc angular momentum (Rice, Lodato, and Armitage, 2005; Forgan and Rice, 2011; Forgan and Rice, 2012).

1.5 Planet migration

The migration of planets was introduced to solve the issue of the discovered Hot Jupiters (Lin, Bodenheimer, and Richardson, 1996) as existing planet formation theories could not explain the formation of gas giants at such small separations. This led to the proposal that planets migrate within their host proto-planetary disc whilst the planet was still forming, as predicted by (Lin and Papaloizou, 1979; Goldreich and Tremaine, 1980). Torques from the disc acting on the planet can reduce the planet's semi-major axis, in effect pushing the planet inwards. There are several requirements for this to happen, firstly, the disc must be non-axisymmetric. It is now commonly accepted that all planets will migrate during their time within the disc. The most common forms of migration in a gas disc are generally known as Type I, (Goldreich and Tremaine, 1980; Tanaka, Takeuchi, and Ward, 2002) and Type II (Lin and Papaloizou, 1986). Type III migration, (Masset

and Papaloizou, 2003) has been a more recent addition to the theory. All three will be discussed later in the chapter, but we start with a simplified model for migration that looks at a planets interaction with a gas particle. This is known as the impulse approximation from Lin and Papaloizou (1979).

1.5.1 The impulse approximation

The impulse approximation was originally laid out in Lin and Papaloizou (1979). Gas flowing past a planet of mass, M_p , will have a velocity difference of Δv and some point of closest approach, b . In the frame of the planet the change in perpendicular velocity, to the direction of travel, will be,

$$|\delta v_{\perp}| = \frac{2GM_p}{b\Delta v} \quad (1.26)$$

for a circular orbit this velocity is directed radially. By equating gas kinetic energies per unit mass for before and after the interaction in terms of perpendicular and parallel velocities we have,

$$\Delta v^2 = |\delta v_{\perp}|^2 + (\Delta v - \delta v_{\parallel})^2 \quad (1.27)$$

therefore, δv_{\parallel} is,

$$\delta v_{\parallel} = \frac{1}{2\Delta v} \left(\frac{2GM_p}{b\Delta v} \right)^2 \quad (1.28)$$

this solution can now be used to express the change in angular momentum of the planet, $\Delta J = \delta(amv)$, in the unit mass regime $\Delta j = a\delta v$ for fixed star-planet separation a . This gives,

$$\Delta j = \frac{2G^2 M_p^2 a}{b^2 \Delta v^3} \quad (1.29)$$

To convert Δj to the total angular momentum change dJ/dt we must consider the gas mass that interacts gravitationally with the planet. We adopt an annulus from b to $b + db$, meaning the change in mass becomes,

$$dm \approx 2\pi a \Sigma db \quad (1.30)$$

However, all the mass in the annulus is not interacting with the planet at one time. Using the difference in angular velocity between the gas and the planet, $\Omega_g - \Omega_p$ we can define a time over which all the mass in the annulus will interact with the planet. Assuming $b \ll a$ we can make the approximation,

$$|\Omega_g - \Omega_p| \approx \frac{3\Omega_p}{2a} b, \quad (1.31)$$

then

$$\Delta t = \frac{4\pi a}{3\Omega_p b}. \quad (1.32)$$

We can now combine these equations and integrate to find the total change in angular momentum. To keep the integral from becoming divergent we set an artificial inner boundary, b_{\min} otherwise as $b \rightarrow 0$, $\Delta J \rightarrow \infty$ which is unphysical,

$$\frac{dJ}{dt} = \int_{b_{\min}}^{\infty} \frac{8G^2 M_p^2 a \Sigma}{9\Omega_p^2 b^4} db = \frac{8G^2 M_p^2 a \Sigma}{27\Omega_p^2 b_{\min}^3} \quad (1.33)$$

In Lin and Papaloizou (1979) b_{\min} can be taken as the Roche radius, $r_L = a(q/3)^{1/3}$ for the planet. The impulse approximation provides two informative results, the first is that gas exterior to the planet will gain angular momentum from the planet, thus causing inwards migration. The gas interior to the planet

will lose angular momentum to the planet and therefore, the planet migrates outwards. The second result is that migration timescales, $\tau = J / |dJ/dt|$ scale inversely with planet mass as $J \propto M_p$ where as $|dJ/dt| \propto M_p^2$.

1.5.2 Resonant torques on the planet

The resonant torques from the planet on the disc can be derived by considering perturbations of the gravitational potential due to the planet gravity and the response of the disc to this perturbation (Goldreich and Tremaine, 1979; Tanaka, Takeuchi, and Ward, 2002). The disc's response to the perturbation can be used to calculate the torques upon the planet. There are many resonances within the disc but not all will be relevant here. The first important resonance is the co-rotation resonance; this is where the angular frequency of the planet, Ω_p , on a circular orbit equals the orbital frequency of the gas disc, $\Omega(r)$. Neglecting the variation from Keplerian velocity of the gas disc, the co-orbital resonance will occur at the planet's orbital location. We now consider the Lindblad resonance, which was originally noted in galactic dynamics. This is where gas in the disc is excited at its natural frequency for radial and epicyclic oscillations $\kappa(r)$,

$$m [\Omega(r) - \Omega_p] = \pm \kappa(r), \quad (1.34)$$

where m is an integer. For a Keplerian disc the location for the orbital and epicyclic frequencies is given by,

$$r_L = \left(1 \pm \frac{1}{m}\right)^{2/3} a, \quad (1.35)$$

where a is the semi major axis of the planet. This produces a range of resonances that become more densely packed around the planet for larger m . These

are set around the co-orbital co-rotation resonance. To allow for the changing potential of a non-circular orbit, the potential experienced by the planet can be broken into several sets of rigidly rotating components. These components are represented by,

$$\Omega_p^{l,m} = \Omega_p + \frac{(l-m)}{m} \Omega_p, \quad (1.36)$$

where l is another integer. The condition for resonance is only satisfied when $\Omega_p^{l,m}$ is equal to a natural resonance of the disc. Only a few of these resonances will be relevant due to the amplitude of the perturbation scaling with $|l-m|$ th power (Goldreich and Tremaine, 1980).

Once the location of the resonances has been found, the torque on the planet can be calculated by summing the torques from the individual resonances. The magnitude of the contribution depends upon two factors: the strength of the resonance itself and the mass of gas at the resonance location. The strength of the resonance is not as affected by the planet as the amount of gas is. This leads to two cases: Type I where the planet's gravitational torques are not strong enough to push away the gas which leads to the planet remaining embedded within the disc as the planet cannot strongly disrupt or perturb the disc. The second case, Type II is where the planet is massive enough to strongly disrupt the disc in the local region. This reduces the gas density around the planet, leading to the starvation of gas at the resonance locations.

1.5.3 Type I migration

As discussed in section 1.5.2, Type I migration occurs when the planet is unable to strongly perturb the disc. This leaves the planet embedded within the disc. Due to the large number of resonances being able to exert a torque upon the planet,

migration can take place over a very short time scale. The total torque can be calculated as the sum of the torques; for a planet in a circular orbit with a given surface density and temperature profile the torque can be written as,

$$\Gamma = \sum_{m=1}^{\infty} \Gamma_{OLR}(m) + \sum_{m=2}^{\infty} \Gamma_{ILR}(m) + \Gamma_{CR}, \quad (1.37)$$

where Γ_{OLR} and Γ_{ILR} are the outer and inner Lindblad resonance torque contributions and Γ_{CR} is the torque from the co-rotating resonance. The sums to infinity mean that the resonances become more densely packed approaching the planet, however, at large m the effective location of the resonances are moved by pressure from the gas disc (Lin and Papaloizou, 1986). This creates an annulus around the planet without resonances,

$$r = a \pm \left(\frac{2}{3}\right) h. \quad (1.38)$$

The most important resonances prove to be,

$$m \sim \left(\frac{h}{r}\right)^{-1}, \quad (1.39)$$

where h is the scale-height of the disc and r is the radial position in the disc and a is the planets semi-major axis. With this being the case, the higher m terms become less important, allowing the torque to converge. Type I migration scales with the square of the planet mass, M_{pl}^2 .

The migration rate depends upon the momentum change of the planet; to migrate inwards angular momentum must be lost. This can be achieved through the outer Lindblad resonance, Γ_{OLR} , however, angular momentum is also gained from the disc at the inner Lindblad resonance, Γ_{ILR} . Therefore, the migration will depend upon the difference between these torques. This can be represented as,

$$f = \frac{\Gamma_{ILR} + \Gamma_{OLR}}{|\Gamma_{ILR}| + |\Gamma_{OLR}|}, \quad (1.40)$$

if this f parameter is less than 0 angular momentum loss to the outer disc is greater than the gain from the inner disc. Thus the planet migrates inwards. The opposite is also possible, if $f > 0$ then the planet will migrate outwards. At the $f = 0$ condition the planet does not migrate and the angular momentum transport is from inner to outer disc via the planet. Inward migration will occur under almost all physical disc conditions and to produce outward migration an unrealistically steep surface density would be required. However, it is not quite this simple; due to the gradient of the surface density being so high there is now a greater radial pressure gradient; this has the effect of moving the outer Lindblad resonances closer to the planet increasing their effect. Tanaka, Takeuchi, and Ward (2002) performed a three-dimensional simulation of a planet with an isothermal gas disc. They find the total torques from both the Lindblad and co-rotation torques to be,

$$\Gamma_{total} = -(1.36 + 0.54\alpha) \left(\frac{M_p}{M_*}\right)^2 \left(\frac{h}{r}\right)^{-2} \Sigma a^4 \Omega_K^2, \quad (1.41)$$

where M_* is the star's mass, Ω_K is the orbital angular frequency. Although, the simulations in Tanaka, Takeuchi, and Ward (2002) are limited due to the isothermal assumption; this work provides a good estimate.

1.5.4 Type II migration

The torques exerted by the planet in Type I scale with, M_{pl}^2 , meaning that they strengthen unrestrained as a planet grows unless they become strong enough to alter the disc structure rather than just perturb it. When this happens the process

continues in the same fashion as Type I; angular momentum is added to the outer disc and removed from the inner disc. The consequence of this transport is to move gas away from the planet's orbit, reducing the surface density of the disc in the local vicinity of the planet, eventually opening a gap (Takeuchi, Miyama, and Lin, 1996). This opening is naturally a function of the planet's mass; higher planet mass will lead to a deeper gap. Once the gap is open, a new model is required as the assumption for Type I, an undisrupted disc, is no longer applicable and the theory breaks down. Early models predicted that the planet approximately migrates with the disc's viscous time scale (Ward, 1982; Lin and Papaloizou, 1986). Though recent work has shown that even in type II the migration rate may not be fixed to the disc's accretion rate (Dürmann and Kley, 2015)

The gap is maintained by the balancing of processes both from the planet and the disc. The torques from the planet will drive material away opening the gap while the viscosity in the disc, which is the internal angular momentum transport, attempts to close the gap through viscous spreading of material in the disc. These two competing processes determine the size and depth of the gap. A simple approximation for opening a gap can be achieved through several arguments. A gap of width of the order of $a \pm \frac{h}{2}$ is expected to be the smallest possible as this is where the Lindblad resonances are at their strongest. Further to this a smaller gap is expected to be unstable as the width is much smaller than the thickness of the disc. Assuming a gap of width h the critical mass ratio, $q_{crit} = M_p / M_*$, where a planet can open a gap is given by,

$$q_{crit} = \left(\frac{27\pi}{8} \right)^{1/2} \left(\frac{h}{r} \right)^{5/2} \alpha^{1/2}, \quad (1.42)$$

where (h/r) is taken as the thickness of the unperturbed disc, α is the Shakura-Sunyaev- α prescription (Shakura and Sunyaev, 1973) given by,

$$\nu = \alpha c_s h \quad (1.43)$$

Eq. 1.43 relates the speed of sound, the scale height and the viscosity to one another. A disc with parameters of $\alpha = 10^{-2}$ and $h/r = 0.05$ produces a $q_{crit} \simeq 2 \times 10^{-4}$ which is roughly a Saturn mass planet around a stellar mass star to produce a gap. It should be noted that α could be much smaller than this, in work by Duffell and MacFadyen (2013) a much lower viscosity $\sim 10^{-4}$ allows a few Earth mass planet to open a gap. A lower disc viscosity is supported by recent ALMA observations (Flaherty et al., 2015) that find a $\nu = 0.0031 c_s$ which corresponds to an $\alpha = 9.6 \times 10^{-4}$. The turbulent velocities are derived from observations of CO transition lines from the disc around HD 163296.

A second method to determine gap opening is the thermal gap opening criteria (Ward, 1997) where $r_h \gtrsim h$,

$$q_{crit} \geq 3 \left(\frac{h}{r} \right)^3. \quad (1.44)$$

Both methods yield similar values of approximately a Saturn mass planet. This introduces a boundary between Type I and Type II migration, although, analytically this boundary is sharp where as in reality a planet of mass $\sim q_{crit}$ will only partially clear the disc around the planet's orbit; this looked at in more detail in §1.5.5. The effects of both pressure and viscosity was investigated by Crida, Morbidelli, and Masset (2006) who used numerical simulations to determine the gap opening criteria, Showing a planet at this boundary in a transitional state with the effects of both types of migration contributing strongly to the migration rate. Therefore, a planet is solely in the type II regime when $q \gg q_{crit}$; once this is satisfied the planet will migrate with the viscous time of the disc. This is given

by,

$$v_{\text{mig}} = -\frac{3\nu}{2r} \quad (1.45)$$

the viscosity, ν can be expressed using the Shakura-Sunyaev disc viscosity eq. 1.43, giving,

$$v_{\text{mig}} = -\frac{3}{2}\alpha \left(\frac{h}{r}\right)^2 v_K \quad (1.46)$$

1.5.5 Type III, runaway migration

Type III migration is a more recent addition (Masset and Papaloizou, 2003; Artymowicz, 2004) to the field of planet migration. This applies in the discussed above transitional state where $q \sim q_{\text{crit}}$ and the planet only partially opens a gap. From investigations into fast migration Masset and Papaloizou (2003) were able to numerically find the critical drift rate for fast migrating planets,

$$|\dot{a}_c| = \frac{|A_p| x^2}{2\pi a} \quad (1.47)$$

where $A_p = \frac{1}{2}r\partial\Omega/\partial r$ and x is the impact parameter of an approaching fluid element in the horseshoe region of the planet. The horseshoe region is the region close to the planets orbit within its gravitation effect. When a planets drift rate exceeds this critical threshold runaway migration starts to take over. Due to the speed of migration the fluid elements in the horseshoe region will miss the planet thus no longer contributing to the co-rotation torque. The numerical tests in Masset and Papaloizou (2003) were conducted using a planet in a fixed orbit then measuring the torques imposed onto the disc from the planet.

1.6 Planet formation theories

1.6.1 Core accretion

Core accretion is currently the most widely accepted scenario for planet formation. Its roots can be traced to a seminal book written by Safronov (1972). In brief, planets grow in this scenario from microscopic grains into massive solid cores such as the Earth, which can optionally accrete a massive gaseous atmosphere if the correct conditions are met.

In this model, microscopic dust particles within the protoplanetary disc are allowed to grow through sticking collisions due to molecular forces. The process however is believed to terminate when particles grow to no more than $\sim 1\text{m}$ in diameter when they start to drift rapidly radially into the star and also collide with relative velocities of the order of tens of m/s (Weidenschilling, 1977b; Windmark et al., 2012). The next stage of growth remains contentious. One idea is gravitational collapse of a thin layer of solids that sedimented down to the mid-plane of the protoplanetary disc (Goldreich and Ward, 1973). This however is difficult due to turbulence driven by instabilities on the gas-dust layer boundary (Weidenschilling, 1988). More recently, it has been shown that dust clumping can occur from turbulence within the disc, with the dust migrating toward or away from turbulent areas depending upon grain size (Johansen et al., 2007; Cuzzi, Hogan, and Shariff, 2008). Streaming instabilities (Youdin and Goodman, 2005) were shown to result in dust particle accumulation in non-turbulent or low turbulence discs. These processes are suggested to lead to the eventual formation of km-sized or larger solid bodies called planetesimals (Johansen et al., 2015).

Pebble accretion can also emphasise the growth of planetesimals, (Lambrechts and Johansen, 2012; Lambrechts and Johansen, 2014). Small grains in the disc can

continue to accrete onto a gravitational bound object. Once a planetesimal or core is formed pebble accretion can rapidly increase the mass of the object.

Growth from planetesimals to larger bodies can be facilitated by collisions that can now be sticking due to gravity of the colliding bodies. The main problem of this phase is the long duration of this growth. A bouncing barrier at $\sim 1\text{mm}$ also means collisions of particles of this size preferentially bounce off one another rather than sticking (Windmark et al., 2012). Planetesimal collisions must be very gentle to avoid their shattering (Leinhardt and Stewart, 2009), which then mean that the time scale for assembly of a solid core ranges from $\sim 1\text{ Myr}$ at 1 AU to as long as $\sim 100\text{ Myr}$ at 50 AU (Kenyon and Luu, 1999).

Another time scale problem for Core Accretion is the gas envelope contraction phase (Pollack et al., 1996; Helled and Bodenheimer, 2014). The core must form fast enough to reach the runaway mass limit which is around $\sim 10M_{\oplus}$ before the gas disc is depleted. A fraction of the gas flowing through the Hill volume of the planet will become bound to the planet, as this mass increases the Hill volume will grow thus allowing for more gas accretion (Greenberg et al., 1978).

1.6.2 Gravitational instability

Gravitational instability (GI; e.g., Kuiper, 1951b; Cameron, Decamp, and Bodenheimer, 1982; Boss, 1997) requires the presence of a very massive primordial disc that can become self-gravitating; this becomes one of the primary assumptions for the theory that the disc in the initial stages is massive enough. Once the assumption is made we can move forward with creating the instabilities within the disc. The instability can form at any part of the disc which has become cool enough or has reached a high enough surface density (Durisen et al., 2007). This is normally seen at large orbital radii as the disc receives a lower influx of radiation as well

as the surface density being lower and therefore less dense, allowing more radiation to escape. If the self-gravity of the local gas disc can become large enough as discussed in section 1.4, compared to pressure forces within the disc, then the gas can begin to alter the structure of the disc thereby creating an instability.

1.6.3 Tidal downsizing

Tidal downsizing is a possible alternative theory of planet formation that can naturally explain the population of exoplanets that has recently been discovered. This new theory is a continuation of existing work on Gravitational Instability. GI has been seen as a way of forming planets at large separations, such as those planets observed in HR8799. As an extension to this work (Nayakshin, 2010a; Nayakshin, 2015d) GI can be used to create the whole range of planet masses at a range of separations.

The suggestion of Boley et al. (2010) that the combined disruption and migration of clumps allowed massive fragments of the disc formed at several tens of AU from the parent star to form all planet types that have been observed; which was before considered non-physical (e.g., Rice, Lodato, and Armitage, 2005; Rafikov, 2005). This contributed towards this theory of planet formation being discounted in favour of CA (Donnison and Williams, 1975). Before this GI was only able to form Jupiter mass planets and brown dwarfs. With the addition of planet and fragment migration the possibility to form planets at all separations has been opened up (e.g., Lin and Papaloizou, 1979; Goldreich and Tremaine, 1980). The paper by Boley et al. (2010) found that a Jupiter mass gas fragment formed in the outer 100 AU of a circumstellar disc can migrate inwards (in as little as $\sim 10^4$ yrs; see also Baruteau, Meru, and Paardekooper, 2011; Cha and Nayakshin, 2011; Zhu et al., 2012a). The fragments formed are extended objects

and only slightly bound, therefore, take up to a few Myrs (e.g., Bodenheimer, 1974; Bodenheimer et al., 1980; Vazan and Helled, 2012) to contract and collapse into a gas giant planet. This is considered to be the “hot start” of gas giants (Marley et al., 2007). The migration time-scale can be much shorter than the collapse time of the fragment; this allows the planet to reach in the inner few AU of the disc without collapsing which then exposes the fragment to tidal stresses and possible tidal stripping and disruption. Nayakshin (2010b), Nayakshin (2011), and Nayakshin (2010a) used analytical estimates and simulations of core formation using only isolated disc gas fragments to reach similar conclusions .

As the local gas begins to collapse under its own gravity, this contraction converts the potential energy into thermal energy and the gas begins to heat up. The contraction also causes the gas to become denser; over time, as the density increases the gas will dislocate from the rest of gas in the disc. This is due to the object acting in a more Keplerian manner because it is no longer supported by the gas pressure within the disc. If the fragment can cool rapidly enough the contraction will continue. However, this is not a simple process as the opacity rises as the density of the fragment increases. This can reduce or even halt the speed of the collapse. For most situations the fragment can collapse slowly as it cools in the outer disc. While the contraction continues, the fragment can migrate through the disc; the migration of extended objects through the disc is not as well understood as for fully formed planets. The migration is treated as it would be for a normal planet under the same disc conditions meaning that the fragment will initially migrate through Type I migration because it is embedded in the thick outer disc. As the fragment contracts further and moves closer in, it can perturb the disc further and open a gap. The fragment has transitioned from Type I to Type II migration slowing the migration rate and allowing more time

for the planet to collapse. In the simplest case there are two outcomes: the planet cools and collapses or the planet stays extended and is disrupted.

The first case to consider is when the planet can contract fast enough that it can collapse to form a stable gas giant planet. The collapsing gas fragment will be heated by its own collapse; there may also be a component of stellar irradiation if the fragment has opened a gap in the disc or is extended enough to reach the disc surface. For the fragment to collapse into a gas giant type planet, the central temperature must reach $T_c \geq 2500\text{K}$ through gravitational contraction. Once this temperature is exceeded then the molecular Hydrogen is disassociated and a rapid collapse can occur (Nayakshin, 2015a). The radiative cooling time-scale, t_{rad} for fragments is given by,

$$t_{\text{rad}} = -\frac{E_{\text{tot}}}{2L}, \quad (1.48)$$

where L is the luminosity of the fragment and E_{tot} is the total energy of the fragment. This time-scale must be shorter than the migration time-scale for the planet to collapse into a stable gas giant configuration. The radiation time-scale can be reduced by pebble-accretion; the accretion of metals onto the fragment accelerates its collapse (Nayakshin, 2015a).

If the planet can collapse it moves into a more stable configuration where it can no longer be disrupted due to the radius of the planet being much smaller than the planet's Hill sphere. A gas giant has been formed and can continue to migrate through the disc as well as undergo internal evolution. The condition for disruption is when the planets' radius is bigger than the Hill sphere R_{H} , which is given by,

$$R_{\text{H}} \approx a \sqrt[3]{\frac{M_{\text{p}}}{3M_{*}}}, \quad (1.49)$$

where M_p is the mass of the planet, M_* is the mass of the central star and a is the semi-major axis of the planet. As the planet migrates inwards the Hill radius of the planet will decrease but if the contraction of the planet does not keep pace the planet will be disrupted by tidal forces from the star. This is the second outcome for the fragment.

The previously discussed disruption condition is not the only possibility. With the addition of pebble accretion the fragment can accrete large amounts of mass; this accretion combined with the contraction of the metal core will cause the core to become luminous. The higher mass cores will produce significant luminosity to heat the surrounding envelope and cause an expansion of the outer envelope of the core. If the accretion rate is maintained onto the core through grain settling the fragment can self-disrupt. This can occur at large separations and early times within the disc, leaving behind the rocky core still surrounded by gas. The core can accrete gases to make a Neptune sized planet with substantial atmosphere, but sub-giant mass. This method of self-disruption becomes more important when looking at the formation of debris discs that will be discussed later in section §4.

1.6.4 Motivation

The current models for planet formation have several issues and were originally based on only reproducing the solar system. Since the discovery of exoplanets these theories have been forced to be revised. This has also led to the possibility of other formation methods. The large differences in structure between extrasolar systems and our own indicates that the planet formation process is very versatile with a vast range of outcomes. The new theory and models provide predictions for further observations.

The aim of this project is to match theory to the observational trends that already exist as well as being able to make new predictions about planet population relations and patterns. As well as extending these relations to other structures that are observed such as debris discs.

1.7 Thesis structure

In chapter 3 I outline my work in the formation of debris discs in the tidal downsizing hypothesis. Using the results of a population synthesis model from Nayakshin and Fletcher (2015) I take the disruption data and apply two models for calculating the mass in solids released back into the disc after the disruption. This released mass can then be used to create a debris disc. The first model takes a fraction of the total mass of metals within the fragment just before disruption as a trace for the mass available to form a debris disc. The second model utilises the core mass of the fragment at the time of disruption as a tracer of how efficient the fragment is at making large bodies.

In chapter 4 I investigate massive planet migration using multiple different SPH codes and a grid code. The migration of massive clumps in the outer regions of discs is an important part of determining the frequency of giant planet formation through GI. I look at 4 standardised scenarios to test all of the codes against. For runs 1-3 we inject a $2M_J$ planet and for run 4 a $12M_J$ is injected into a $0.2M_\odot$ disc. The first two focus solely at planet migration with no accretion onto the planet. Only the gravitational softening of the sink particle changes between cases, this is to test the effect of gravitational softening on planet migration. The third case includes accretion onto the planet. For the last run we look at a higher mass planet to test how the codes handle the transition between type I and type II migration.

In chapter 2 I cover the implementation of an implicit dust scheme into PHANTOM. The stokes number of a particle will change greatly as much as 3 orders of magnitude, as the grain transitions from the unperturbed disc into a self-gravitating fragment. However, there is not a single numerical method for modelling dust over such a large dynamical range. To achieve this we use the implicit approximation for the two-fluid dust model.

Chapter 2

An overview of SPH

2.1 Smoothed particle hydrodynamics

Smoothed particle hydrodynamics (SPH) is the basis for much the modelling in astrophysics. In SPH particles are used to trace the flow of mass (Monaghan, 1992; Price, 2012). The foundation of SPH is calculating density using these particles, to do this the weighted summation over nearby particles is taken. The weighting is scaled by distance from the particle with more distant particles contributing less to the summation. The accuracy of the density estimate is then dependant on the weighting and the fall off of the weighting function.

On a primitive level the most important quantities to know for SPH are particle positions, \mathbf{r} , velocities, \mathbf{v} and density, ρ . These can be simply related to one either as such,

$$\frac{d\mathbf{r}}{dt} = \mathbf{v} \quad (2.1)$$

and

$$\frac{d\rho}{dt} = -\rho (\nabla \cdot \mathbf{v}) \quad (2.2)$$

The density is a fundamental property required for SPH but is a continuous

parameter and therefore must be computed from the discrete distribution of particles. The density at particle, a is given by summing over nearby particles, b .

$$\rho_a = \sum_b m_b W(|\mathbf{r}_a - \mathbf{r}_b|, h_a) \quad (2.3)$$

where, W is the kernel function and, h_a is the smoothing length for particle a . Taking the time derivative of eq. 2.3, by using $d/dt = \partial/\partial t + \mathbf{v} \cdot \nabla$, we find a discretised version eq. 2.2

$$\frac{d\rho}{dt} = \frac{1}{\Omega_a} \sum_b m_b (\mathbf{v}_a - \mathbf{v}_b) \cdot \nabla_a W(|\mathbf{r}_a - \mathbf{r}_b|, h_a) \quad (2.4)$$

Ω relates the gradient of the smoothing length (Springel and Hernquist, 2002; Monaghan, 2002)

The density iterates over the particles neighbours, these are give as particles within a distance of $\mathbf{R}_{\text{kern}} \mathbf{h}_a$ of particle a . \mathbf{R}_{kern} is a radius at which the kernel cuts off, this prevents the kernel from covering all particles and becoming prohibitive slow.

The smoothing length must first be set so the size of the kernel and thus the number of neighbours can be determined. The smoothing length is set using the number density of particles, n_a .

$$h_a = h_{\text{fact}} n_a^{1/3} \quad (2.5)$$

assuming equal mass particles, h_a can be rewritten as

$$h_a = h_{\text{fact}} \left(\frac{m_a}{\rho_a} \right)^{1/3} \quad (2.6)$$

h_{fact} relates the smoothing length to the local properties and can be varied from one simulation to another but kept constant for all SPH particles.

2.1.1 Kernel functions

The choice and form of Kernels vary widely each with either own benefits and drawbacks. The Kernel, $W_{a,b}$

$$W_{a,b}(r, h) \equiv \frac{C_{\text{norm}}}{h^3} f(q) \quad (2.7)$$

where $f(q)$ is a dimensionless function of q given by,

$$q \equiv \frac{|\mathbf{r}_a - \mathbf{r}_b|}{h} \quad (2.8)$$

The B-spline family of kernels has been the default for SPH since Monaghan and Lattanzio (1985). In this family of kernels $f(q)$ takes the form,

$$f(q) = \begin{cases} 1 - \frac{3}{2}q^2 + \frac{3}{4}q^3, & 0 \leq q < 1 \\ \frac{1}{4}(2 - q)^3, & 1 \leq q < 2 \\ 0, & q \geq 2 \end{cases} \quad (2.9)$$

For this example of the quintic kernel, M_4 , $C_{\text{norm}} = 1/\pi$ when used in 3D calculations.

2.1.2 Hydrodynamics

The evolution of a particle is based on a summation of the forces acting on it thus giving a change in velocity,

$$\frac{d\mathbf{v}}{dt} = -\frac{\nabla P}{\rho} + \Pi_{\text{shock}} + \mathbf{a}_{\text{ext}}(\mathbf{r}, \mathbf{t}) + \mathbf{a}_{\text{sink-gas}} + \mathbf{a}_{\text{selfgrav}} \quad (2.10)$$

This is simply the pressure support of the gas with the accelerations from all sources. Π_{shock} is the dissipation caused by shocks in the gas, this is required to accurately model entropy increase caused by shocks.

The specific internal energy, u evolves as,

$$\frac{du}{dt} = -\frac{P}{\rho} (\nabla \cdot \mathbf{v}) + \Lambda_{\text{shock}} - \frac{\Lambda_{\text{cool}}}{\rho} \quad (2.11)$$

Λ_{shock} is again a dissipative term to caused by shocks. Λ_{cool} is the change in internal energy from the cooling of the gas.

Equations 2.10 and 2.11 must now be adapted to function in the form of SPH, essentially discretised due to the population of particles and not a continuous fluid. By applying the principles of SPH and the kernel weighting we discussed above to eq. 2.10 and 2.11 we gain the equation of motion and internal energy evolution for a particle.

$$\begin{aligned} \frac{d\mathbf{v}_a}{dt} = & - \sum_b m_b \left[\frac{P_a + q_{a,b}^a}{\rho_a^2 \Omega_a} \nabla_a W_{a,b}(h_a) + \frac{P_b + q_{a,b}^b}{\rho_b^2 \Omega_b} \nabla_a W_{a,b}(h_b) + \right] \\ & + \mathbf{a}_{\text{ext}}(\mathbf{r}, \mathbf{t}) + \mathbf{a}_{\text{sink-gas}} + \mathbf{a}_{\text{selfgrav}} \end{aligned} \quad (2.12)$$

$$\frac{du}{dt} = \frac{P_a}{\rho_a^2 \Omega_a} \sum_b m_b \mathbf{v}_{ab} \cdot \nabla_a W_{a,b}(h_a) + \Lambda_{\text{shock}} - \frac{\Lambda_{\text{cool}}}{\rho} \quad (2.13)$$

We can now turn to the equation of state (EOS), to close the set of equations and relate pressure to density and internal energy.

$$P = (\gamma - 1) \rho u \quad (2.14)$$

where γ is the adiabatic gas constant. The sound speed of the gas is given by,

$$c_s = \sqrt{\frac{\gamma P}{\rho}}, \quad (2.15)$$

and finally temperature can be related to internal energy through the pressure,

$$P = \frac{\rho k_B T}{\mu m_H} \quad (2.16)$$

setting this equal to eq. 2.14 and rearranging for T we get,

$$T = \frac{\mu m_H}{k_B} (\gamma - 1) u. \quad (2.17)$$

A simplistic example is where we assume heating from shocks is radiated away as well as no cooling then u evolves as,

$$\frac{du}{dt} = \frac{P}{\rho^2} \frac{d\rho}{dt} \quad (2.18)$$

This can be integrated to give,

$$P = K\rho^\gamma \quad (2.19)$$

where K is the polytropic constant, which is just the ratio of energy transfer in heat to energy transfer in work done.

2.1.3 Shocks and artificial viscosity

Dissipation of momentum and internal energy caused by shocks in the fluid are accounted for by, Π_{shock} and Λ_{shock} respectively. These originate from work by Monaghan (1992) and has been expanded upon by many authors some examples are, Morris and Monaghan (1997), Price and Federrath (2010), Laibe and Price

(2014), and Lodato and Price (2010). Π_{shock}^a is the shock capturing momentum term and given by,

$$\Pi_{\text{shock}}^a = - \sum_b m_b \left[\frac{q_{ab}^a}{\rho_a^2 \Omega_a} \nabla_a W_{ab}(h_a) + \frac{q_{ab}^b}{\rho_b^2 \Omega_b} \nabla_a W_{ab}(h_b) \right], \quad (2.20)$$

where q is given by,

$$q_{ab}^a = \begin{cases} -\frac{1}{2} \rho_a v_{\text{sig},a} \mathbf{v}_{ab} \cdot \hat{\mathbf{r}}_{ab}, & \mathbf{v}_{ab} \cdot \hat{\mathbf{r}}_{ab} < 0 \\ 0, & \text{otherwise} \end{cases} \quad (2.21)$$

and

$$\mathbf{v}_{ab} = \mathbf{v}_a - \mathbf{v}_b, \quad (2.22)$$

$$\hat{\mathbf{r}}_{ab} = \frac{\mathbf{r}_a - \mathbf{r}_b}{|\mathbf{r}_a - \mathbf{r}_b|} \quad (2.23)$$

v_{sig} is the signal speed between two particles and is controlled by the physics implemented. For just the hydrodynamics v_{sig} is given by,

$$v_{\text{sig}} = \alpha_a^{\text{AV}} c_{s,a} + \beta^{\text{AV}} (\mathbf{v}_{ab} \cdot \hat{\mathbf{r}}_{ab}) \quad (2.24)$$

The shock term for internal energy, Λ_{shock} ,

$$\begin{aligned} \Lambda_{\text{shock}} = & -\frac{1}{\rho_a \Omega_a} \sum_b m_b v_{\text{sig},a} \frac{1}{2} (\mathbf{v}_{ab} \cdot \hat{\mathbf{r}}_{ab})^2 F_{ab}(h_a) \\ & + \sum_b m_b \alpha^u v_{\text{sig}}^u (u_a - u_b) \frac{1}{2} \left[\frac{F_{ab}(h_a)}{\rho_a \Omega_a} + \frac{F_{ab}(h_b)}{\rho_b \Omega_b} \right] \\ & + \Lambda_{\text{artes}} \end{aligned} \quad (2.25)$$

where

$$F_{ab} = \frac{C_{\text{norm}}}{h^4} f'(q), \quad (2.26)$$

and Λ_{artes} is the heating term from the artificial resistivity. When using self-gravity, v_{sig}^u is simply

$$v_{\text{sig}}^u = (\mathbf{v}_{ab} \cdot \hat{\mathbf{r}}_{ab}) \quad (2.27)$$

from Wadsley, Veeravalli, and Couchman (2008).

Shocks are now included in our evolution equations but no way of detecting shocks. We will now discuss this.

Since Morris and Monaghan (1997) the standard way to reduce dissipation from shocks was to use a dimensionless viscosity parameter, α that can be evolved for each SPH particle.

$$\frac{d\alpha}{dt} = \max(-\nabla \cdot \mathbf{v}_d, 0) - \frac{\alpha_a - \alpha_{\text{min}}}{\tau_a} \quad (2.28)$$

where τ_a is the decay time set by,

$$\tau_a = \frac{h}{\omega_{\text{decay}} v_{\text{sig}}} \quad (2.29)$$

ω_{decay} is a constant that controls the rate of decay.

2.1.4 Cooling

We can define a simple cooling timescale as,

$$t_{\text{cool}} = \frac{\Omega(R)}{\beta_{\text{cool}}} \quad (2.30)$$

where, β_{cool} is a global parameter fixed at the start of the simulation. This cooling timescale can then be related to a cooling term for use in the internal energy evolution equations.

$$\Lambda_{\text{cool}} = \frac{\rho u}{t_{\text{cool}}}. \quad (2.31)$$

2.1.5 Time integration

A common time integrator used in several astrophysical SPH codes is the Leapfrog method (Price et al., 2017; Springel, 2005; Wadsley, Stadel, and Quinn, 2004). Here the particles are updated from time, t^n to t^{n+1} with a timestep of $\Delta t = t^{n+1} - t^n$.

$$\mathbf{v}^{n+\frac{1}{2}} = \mathbf{v}^n + \frac{1}{2}\Delta t\mathbf{a}^n \quad (2.32)$$

$$\mathbf{r}^{n+1} = \mathbf{r}^n + \Delta t\mathbf{v}^{n+\frac{1}{2}} \quad (2.33)$$

$$\mathbf{a}^{n+1} = \mathbf{a}(\mathbf{r}^{n+1}) \quad (2.34)$$

$$\mathbf{v}^{n+1} = \mathbf{v}^{n+\frac{1}{2}} + \frac{1}{2}\Delta t\mathbf{a}^{n+1} \quad (2.35)$$

2.1.6 Sink particles and accretion

High density regions naturally have many particles in a small volume. To prevent interpenetration of particles and accurately track these particles the timesteps on which they are evolved must be short, As density increases and timestep decreases, a point is reached where simulation time becomes too long and the

timestep prohibitively short. Sink particles were first introduced in Bate, Bonnell, and Price (1995a).

Sink particles are treated separately than the SPH particles as they do not have the fluid pressure support of the gas and are treated more closely to N-body particles which are only affected by gravitational interactions (Price et al., 2017).

The equations of motion for the sink particles have contributions from both the SPH and other sink particles.

$$\frac{d\mathbf{v}_i}{dt} = \sum_{j=1}^{N_{\text{sink}}} GM_j \phi'_{ij}(\epsilon) \hat{\mathbf{r}}_{ij} - \sum_{b=1}^{N_{\text{part}}} Gm_b \phi'_{ib}(\epsilon_{ib}) \hat{\mathbf{r}}_{ib} \quad (2.36)$$

where ϕ'_{ab} is the softening kernel used for the SPH, N_{sink} and N_{part} are the total number of sink and SPH particles respectively. ϵ is the fixed softening length for the sink particles, while ϵ_{ib} is the sink-gas softening length and is maximum between the SPH softening length ϵ_b and ϵ . The SPH particles received a corresponding acceleration due to the presence of the sink particle.

$$\mathbf{a}_{\text{sink-gas}}^a = - \sum_{j=1}^{N_{\text{sink}}} GM_j \phi'_{aj}(\epsilon_{aj}) \hat{\mathbf{r}}_{aj} \quad (2.37)$$

similarly additional sink particles also receive an additional acceleration from the sink-sink interaction,

$$\mathbf{a}_{\text{sink-sink}}^i = - \sum_{j=1}^{N_{\text{sink}}} GM_j \phi'_{ij}(\epsilon) \hat{\mathbf{r}}_{ij} \quad (2.38)$$

To reduce the issue of reducing timesteps SPH particles must be accreted onto the sink particle and removed from the simulation. However, there is a risk of over accreting particles, therefore, several accretion checks are used to see if a SPH particle should be accreted. The most simple of these is a simple distance argument. The accretion radius, r_{acc} of the sink particle is given at the beginning

of the simulation. Whenever a particle moves inside this region it is accreted onto the sink particle. The particles mass, velocity and angular momentum are then added to the sink particles. Newer versions of SPH codes track the spin up or down of the sink particle.

Using PHANTOM (Price et al., 2017) as an example here are some additional checks that can be made in an SPH particle before it is accreted.

1. Specific angular momentum of the particle must be lower than that of the specific angular momentum of a Keplerian orbit at r_{acc} .
2. The particle is gravitationally bound to the sink particle.
3. The particle is most bound to the sink particle in question.

As mentioned above if all the checks are passed the particle is accreted and the sink particle properties are updated according to,

$$\mathbf{r}_i = \frac{\mathbf{r}_a m_a + \mathbf{r}_i M_i}{m_a + M_i} \quad (2.39)$$

$$\mathbf{v}_i = \frac{\mathbf{v}_a m_a + \mathbf{v}_i M_i}{m_a + M_i} \quad (2.40)$$

$$\mathbf{a}_i = \frac{\mathbf{a}_a m_a + \mathbf{a}_i M_i}{m_a + M_i} \quad (2.41)$$

$$S_i = S_i + \frac{m_a M_i}{m_a + M_i} [(\mathbf{r}_a - \mathbf{r}_i) \times (\mathbf{v}_a - \mathbf{v}_i)] \quad (2.42)$$

$$M_i = M_i + m_a \quad (2.43)$$

2.2 Dust-gas mixture

Two main methods have arisen to simulate dust using SPH: the two-fluid and the one-fluid approach. As the names suggest these either treat the gas and dust separately or as a single mixture. The reason why both methods are currently needed is the vast range of parameter space that dust can inhabit. This is easily seen through the stopping time, t_s , induced by the drag on the dust by the velocity differential with the gas.

$$t_s = \frac{\rho_g \rho_d}{K (\rho_g + \rho_d)} \quad (2.44)$$

where, ρ_g and ρ_d are the local gas and dust densities respectively and K is the drag coefficient, the different drag regimes will be discussed in more depth later in section 2.2.3. Dust in the limit of $t_s \rightarrow 0$ is considered well coupled to the gas and can therefore be modelled using one-fluid. However, when $t_s \rightarrow \infty$ the dust can move completely independently from the gas and, as such, a single fluid approximation is no longer reasonable. With gas and dust densities ranging in $\sim 3 - 6$ orders of magnitude in a circumstellar disc versus dense gas clumps, the stopping times vary by a similar amount. Therefore, dust particles of same size may be in the well coupled and the poorly coupled regimes in different regions of a self-gravitating disc.

2.2.1 The one-fluid dust model

Modelling dust as well as gas presents new challenges for SPH, first of which is how to include the dust into the already existing framework of SPH. The one-fluid approach is where the SPH particles now carry information about the surrounding dust as well, e.g., the local dust density and velocity (Price and Laibe,

2015). The latter is, in general, different from the local gas velocity, permitting dust particle drift through gas. This drift velocity cannot be too large in practice, however, so for the dust and gas to be represented by a single particle/tracer, the mixture of gas and dust must be relatively well coupled. This equates to a small stokes number, $s \leq 1$ (Laibe and Price, 2014).

A single fluid implementation has several advantages over the two-fluid methods discussed below. Firstly, the one-fluid dust model is a simple expansion of the standard SPH model, where now the SPH particles also trace out a population of dust particles as well as the gas. This has the advantage of being simpler than adding in a second set of particles of different mass with their own governing equations. Secondly, when the $t_s \rightarrow 0$, dust particles simply move exactly in step with the gas flow, requiring no additional time-integration constraints. This is in contrast to the two-fluid methods, which may become very expensive in the limit of very short stopping time, as we shall see below.

The primary disadvantage of the single fluid approach is that in the long stopping time regime, dust particles move through the gas at high relative velocity which also depends on particle size and even which direction the particle came from. This situation cannot be reduced to a single velocity difference between the gas and the dust flow because this is non-physical.

2.2.2 The two-fluid dust model

The two-fluid dust model utilises a second particle population that traces dust particles in the simulation. These particles follow their own equations of motion and have a separate smoothing length from the SPH particles. The benefits of using the two-fluid model is in allowing the dust and gas to cross one another,

which is impossible for the one-fluid approach (Laibe and Price, 2012a; Laibe and Price, 2012b).

Continuity equations

The continuity equations are as follows,

$$\frac{\partial \hat{\rho}_g}{\partial t} + \nabla \cdot (\rho_g \mathbf{v}_g) = 0. \quad (2.45)$$

$$\frac{\partial \hat{\rho}_d}{\partial t} + \nabla \cdot (\rho_d \mathbf{v}_d) = 0. \quad (2.46)$$

Where v_d and v_g are dust and gas fluid velocities respectively. $\hat{\rho}_d = (1 - \theta)\rho_d$ and $\hat{\rho}_g = \theta\rho_g$, where ρ_g and ρ_d are the gas and dust densities respectively (Laibe and Price, 2012a; Laibe and Price, 2012b). Lastly, θ is the volume fraction available to the gas.

Evolution equations

The gas density and velocity, ρ_g, \mathbf{v}_g , evolve as usual with the addition of the volume drag force between the gas and dust, F_{drag} ,

$$\frac{\partial \rho_g}{\partial t} + (\mathbf{v}_g \dot{\nabla}) \rho_g = -\rho_g (\nabla \cdot \mathbf{v}_g), \quad (2.47)$$

$$\frac{\partial \rho_d}{\partial t} + (\mathbf{v}_d \dot{\nabla}) \rho_d = -\rho_d (\nabla \cdot \mathbf{v}_d), \quad (2.48)$$

$$\frac{\partial \mathbf{v}_g}{\partial t} + (\mathbf{v}_g \dot{\nabla}) \mathbf{v}_g = -\frac{\nabla P}{\rho_g} + \frac{F_{\text{drag}}}{\rho_g}, \quad (2.49)$$

$$\frac{\partial \mathbf{v}_d}{\partial t} + (\mathbf{v}_d \cdot \nabla) \mathbf{v}_d = -\frac{F_{drag}}{\rho_d}, \quad (2.50)$$

where,

$$F_{drag} = K (\mathbf{v}_g - \mathbf{v}_d) \quad (2.51)$$

K , is the drag coefficient which is set based on the physical conditions the dust particle is in, this will be discussed in more detail in §2.2.3. Evolution in the internal energy of the gas, u_g , caused by interactions between dust and gas particles is given by,

$$\hat{\rho}_g \frac{d\mathbf{u}_g}{dt} = P_g (\theta \nabla \cdot \mathbf{v}_g + (1-\theta) \nabla \cdot \mathbf{v}_d + \Lambda_{drag} + \Lambda_{therm}). \quad (2.52)$$

The first term is simply the compressive work done, the second term is work done by the gas causing buoyancy (Laibe and Price, 2012a). Λ_{drag} is given by,

$$\Lambda_{drag} = \hat{\rho}_g K (\mathbf{v}_g - \mathbf{v}_d)^2. \quad (2.53)$$

Both the heating term Λ_{drag} and the drag force F_{drag}^V scale with the coefficient K . This coefficient has dimensions of mass per unit volume per unit time and is related to the difference in velocities between the the two fluids; in this case the dust and gas (Laibe and Price, 2012b). Λ_{therm} is the coupling of the dust temperature to the gas temperature. If the two species have different temperatures this term can become large. It is governed by the conduction, Λ_{cond} and radiation Λ_{rad} . Λ_{therm} can thus be calculated using the temperature of the dust, T_d , and gas, T_g .

$$\Lambda_{cond} = \Lambda_{rad} + \Lambda_{therm} = Q(T_g - T_d) + R(aT_g^4 - aT_d^4), \quad (2.54)$$

Q and R are coefficients derived from the dust and gas properties and a is a radiative constant (Laibe and Price, 2012a). Furthermore, we express the dust thermal energy as,

$$\hat{\rho}_d \frac{d\mathbf{u}_d}{dt} = -\Lambda_{therm}. \quad (2.55)$$

2.2.3 Drag regimes

We now consider two regimes the dust may experience in an astrophysical context. The first case is where the dust size, s , is much smaller than the mean free path of the gas, λ_g (eg. $s \ll \lambda_g$). The second is the inverse so $s \gg \lambda_g$. These are both extreme cases which bound the domain the dust would exist in.

The generalised expression for the stopping time, t_s is given by,

$$t_s = \frac{\rho_g \rho_d}{K(\rho_g + \rho_d)}, \quad (2.56)$$

this equation can be recast into a SPH applicable form to give the stopping time between a dust particle, a , and SPH particle, j , t_s^{aj} (Price et al., 2017),

$$t_s^{aj} = \frac{\rho_a \rho_j}{K_{aj}(\rho_a + \rho_j)}, \quad (2.57)$$

Epstein regime

The Epstein regime covers dilute media where the dust grains are small enough to not significantly alter the gas velocity distribution from its expected Maxwellian distribution. This gives us the condition of $\lambda_g > 4s/9$ to be in the Epstein regime. We make the assumption of spherical dust particles and the gas molecule weight is negligible (Laibe and Price, 2012a).

There are several expressions for the Epstein regime, however, the one currently used is (Laibe and Price, 2012b; Paardekooper and Mellema, 2006),

$$\mathbf{F}_{drag} = -\frac{4\pi}{3}\rho_g s^2 \sqrt{\frac{8}{\pi\gamma}c_s} \sqrt{1 + \frac{9\pi}{128} \frac{\Delta v^2}{c_s^2}} \Delta \mathbf{v} \quad (2.58)$$

\mathbf{F}_{drag} is for single grains. The other two expressions for the Epstein regime are discussed and compared in section 5 of Laibe and Price (2012b). The general conclusion is that the difference between them is negligible so the simpler implementation that deals with both high and low Mach numbers can be used. For the full discussion see Laibe and Price (2012b).

Given this negligible difference the stopping time becomes,

$$t_s = \frac{\rho_{\text{grain}} s_{\text{grain}}}{\rho c_s} \sqrt{\frac{\pi\gamma}{8}} \left(\sqrt{1 + \frac{9\pi}{128} \frac{\Delta v^2}{c_s^2}} \right)^{-1}. \quad (2.59)$$

Stokes regime

The Stokes regime is then the other end of the stopping time spectrum from the Epstein regime discussed in 2.2.3. The Stokes regime is used for dense media where the mean free path of the gas is approximately smaller than the grain size $\lambda_g < 4s/9$

$$\mathbf{F}_{drag} = -\frac{1}{2} C_D \pi s_{\text{grain}}^2 \rho_g \Delta v \Delta \mathbf{v} \quad (2.60)$$

where,

$$C_D \approx \begin{cases} 24Re^{-1} & Re < 1 \\ 24Re^{-0.6} & 1 < Re < 800 \\ 0.44 & Re > 800 \end{cases} \quad (2.61)$$

these relations assume a spherical particle, with uniform density (Whipple, 1972). Re , is the Reynolds number for the particle given by,

$$Re = \frac{2s_{\text{grain}} (|v_d - v_g|)}{\nu} \quad (2.62)$$

where, s_{grain} , is the particle size and ν is the molecular viscosity of the gas, (eg. Whipple, 1972; Lorén-Aguilar and Bate, 2016). The stopping time, t_s , is now redefined to,

$$t_s = \frac{8\rho_{\text{grain}}s_{\text{grain}}}{3\rho|\Delta v|C_D} \quad (2.63)$$

2.2.4 Explicit timestepping

To accurately capture the gas-dust interaction the timestep is now limited by the shortest stopping time of dust particles in question and the gas neighbours. Functionally, this takes the form of,

$$\Delta t_{\text{drag}}^a = \min \left(t_s^{aj} \right) \quad (2.64)$$

This equation shows that the timestep for particle a is calculated as a minimum over all the SPH neighbours, j , of the particle. To maintain the overall block time step the dust particles are then forced onto the closest block timestep.

This timestepping method leads to the primary limitation of the two fluid dust modelling. If $t_s \rightarrow 0$ for a set of particles, then the timestep $\Delta t \rightarrow 0$, becomes numerically prohibitive. In these cases the one-fluid model is faster and designed to deal with short stopping times. However, an alternative to using the one fluid model is to apply an implicit timestep rather than an explicit one.

2.3 Implicit integration scheme for dust in PHANTOM

ALMA observations of protoplanetary discs can now spatially resolve emission of sub-millimetre dust within the disc on scales of \sim ten or less AU for sources located in local star forming regions. This opens up a new set of constraints to test our theories of planet formation, potentially detailing the time and position of planet formation. One of the main surprises of ALMA observations appears to be the fact that massive solid cores are assembled very rapidly, e.g., by $\sim 0.5 - 1$ Myr (ALMA Partnership et al., 2015; Dipierro et al., 2015; Dipierro et al., 2016). This was not predicted by the classical Core Accretion scenario. In fact, the strong positive metallicity correlation of gas giant planets with host star metallicity (Fischer and Valenti, 2005) is best explained by massive core formation taking on average ~ 6 Myr at distances of a few to 10 AU (Mordasini et al., 2009). The cores observed by ALMA in HL Tau at distances of ~ 50 AU require at least an order of magnitude longer assembly.

Tidal Downising, on the other hand, predicts very rapid core assembly in the massive gas clumps migrating in (Nayakshin, 2016), and hence can be a good candidate theory to explain these observations. It is clearly desirable to perform detailed numerical simulations that include dust, so that like for like comparison can be made with the 1D population synthesis calculations of Nayakshin (2016).

2.3.1 Implicit dust particle integration

One idea considered in the literature (Lorén-Aguilar and Bate, 2014; Lorén-Aguilar and Bate, 2015), is to integrate dust particle motion through a time step Δt analytically, assuming that forces on the dust particle do not change during the step. To implement this in PHANTOM, I have attempted to apply a corrective force based on the pairwise treatment for the drag. This correction will hopefully allow for longer time steps in the limit of the stopping time becoming very short.

In the following, we assume the dust density is much lower than the gas density. In this limit the back reaction from the dust onto the gas can be neglected. Define the barycentre velocity, v_{st} , of the gas-dust mixture, as

$$v_{st} = \frac{\rho_g \mathbf{v}_g + \rho_d \mathbf{v}_d}{\rho_g + \rho_d} \quad (2.65)$$

where ρ_g, ρ_d are the gas and dust densities respectively and $\mathbf{v}_g, \mathbf{v}_d$ are the gas and dust velocities. The equation of motion for a dust particle can be expressed as,

$$\frac{d\mathbf{v}_d}{dt} = -\frac{\Delta\mathbf{v}}{t_{st}} + \mathbf{a}_g \quad (2.66)$$

where \mathbf{a}_g is the acceleration from gravity and $\Delta\mathbf{v} = \mathbf{v}_d - \mathbf{v}_g$. We can now use the exponential decay of the dust velocity caused by the gas-dust drag to calculate the dust velocity difference with gas after time step Δt as

$$\Delta\mathbf{v} = \Delta\mathbf{v}_0 e^{-\Delta t/t_s} + \mathbf{a}_g t_s \left(1 - e^{-\Delta t/t_s}\right). \quad (2.67)$$

However, PHANTOM has a pre-existing frame work for the evolution of particles; in the existing method, all forces acting on each particle are summed and

passed as a total to the timestep routine to be applied to the particles. To implement our new dust velocity we now need to recast eq. 2.67 as a force to meet the form of PHANTOM's timestep routine. The dust velocity can be explicitly integrated as,

$$\Delta \mathbf{v} = \Delta \mathbf{v}_0 + \mathbf{a}_{\text{mod}} \Delta t \quad (2.68)$$

where a_{mod} is the modified acceleration on the dust particle. In PHANTOM the acceleration is per unit mass and is therefore, equivalent to a force. By equating eq. 2.67 and eq. 2.68 and rearranging for the acceleration we find,

$$\mathbf{a}_{\text{mod}}^a = \frac{a_g t_s - \Delta v_0}{\Delta t} \left(1 - e^{-\frac{\Delta t}{t_s}} \right), \quad (2.69)$$

where t_s is the stopping time of the dust particle, \mathbf{v}_g is the gas velocity, \mathbf{v}_0 is the velocity of the dust particle at the beginning of the time step and Δt is the timestep, this is due to the force being applied in the code on the predictor step of the leap frog.

In the case where $v_{\text{st}} \neq 0$ the modified acceleration becomes,

$$\mathbf{a}_{\text{mod}}^a = \frac{\mathbf{v}_{\text{st}} - \mathbf{v}_0 + \mathbf{a}_g t_s}{\Delta t} \left(1 - e^{-\frac{\Delta t}{t_s}} \right). \quad (2.70)$$

Complications arise in the implementation as this force correction is applied to the particle, however all the drag calculations are being calculated as a sum of pair interactions between the dust particle and all of its nearest neighbours.

The timestep for the dust particle can now be calculated as the minimum between,

$$\Delta t = \left(\frac{h}{\max(|\Delta v|, c_s)} \right) \quad (2.71)$$

and

$$\Delta t = 0.1 \sqrt{\frac{h}{|\mathbf{a}|}} \quad (2.72)$$

where Δv is the gas to dust velocity and \mathbf{a} is the acceleration on the dust particles. (Lorén-Aguilar and Bate, 2014; Booth, Sijacki, and Clarke, 2015). The dust particles timestep is no longer step by the particles stopping time; allowing for shorter stopping times without the extra computational cost.

2.4 The dust particle drift analytic solution

The Weidenschilling solution for radial velocity motion of dust grains in a gas disc is useful for us to test against. There is also the dust settling tests: These tests are designed to have a well characterised analytic solution that the numerical result can be compared against, Weidenschilling (1977a).

As discussed above the dust particle will feel a head wind from the gas due to the slightly sub-Keplerian velocity of the gas. This velocity difference can be expressed as a function of Keplerian velocity by,

$$v_{\phi, gas} = v_K (1 - \eta)^{1/2}, \quad (2.73)$$

where $v_K = (GM/r)^{1/2}$ is the Keplerian velocity, where $\eta \approx c_s^2/v_K^2 \ll 1$

The velocity differential between dust and gas will lead to aerodynamic drag (Weidenschilling, 1977b) and thus radial migration. We define a timescale over which friction will slow a particle,

$$t_{\text{fric}} = \frac{m\Delta v}{|F_D|}, \quad (2.74)$$

where, m is the mass of a particle and $\Delta v = v_{\text{dust}} - v_{\text{gas}}$ is the difference between gas and dust velocities, and F_D is the aerodynamic friction force on the particle. For simplicity we will assume that gas motion is unperturbed by the dust back reaction force. The radial dust particle velocity evolves according to

$$\frac{dv_r}{dt} = \frac{v_\phi^2}{r} - \Omega_K^2 r - \frac{1}{t_{\text{fric}}} \Delta v_r \quad (2.75)$$

this can be simplified by substituting for Ω_K and assuming a small change in v_r we can calculate the radial velocity motion as,

$$v_r = \frac{\tau_{\text{fric}}^{-1} v_{r,\text{gas}} - \eta v_K}{\tau_{\text{fric}} + \tau_{\text{fric}}^{-1}} \quad (2.76)$$

where,

$$\tau_{\text{fric}} = t_{\text{fric}} \Omega_K \quad (2.77)$$

τ is the dimensionless stopping time. We now have an analytic expectation to test our dust radial migration rate against. The form of the analytic solution can be seen in fig. 2.1, which shows the radial velocity of the dust against the dimensionless stopping time, τ . The maximum dust velocity can be seen as the peak of the curve at stopping time $\tau = 0$. The stopping time is proportional to particle size in the Epstein regime. Very large particles are not effected by the gas head wind and therefore do not have a large radial drift velocity. For very small grains the radial drift is very small for an entirely different reason – the grains are well coupled to the gas.

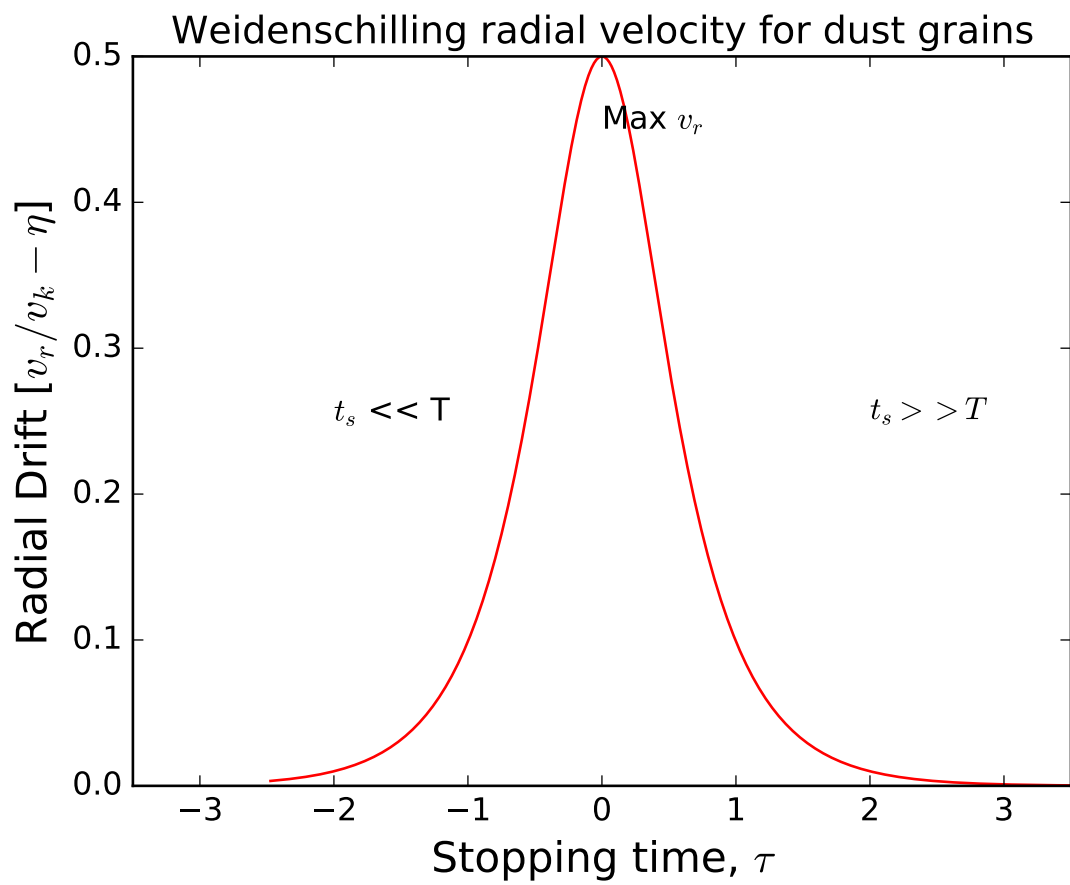


FIGURE 2.1: The radial velocity profile predicted by Weidenschilling (1977). The curve was calculated using a $\Sigma(R) \propto 1/R$ profile.

2.5 Results

I have implemented the implicit timestepping as the modified force as well as adding the new timestep criteria into PHANTOM's Force routine. There are several well defined tests that must be passed before this version of PHANTOM can be merged with the live public copy. I will now show the results of these tests and discuss some of the issues I faced.

2.5.1 DUSTYBOX

The first simple test to perform is a 3D box of SPH and dust particles. A velocity field is imposed on the dust while the SPH particles are stationary. There are no other forces acting on the particles. The drag force calculation on the dust particles can now be tested. There is an expected velocity decay for the dust. The first case has no back reaction from the dust on the gas; this does not conserve momentum as the dust velocity is damped without the gas velocity being affected. The DUSTYBOX test, (Laibe and Price, 2011) is set up with 20^3 particles in both gas and dust and distributed with a uniform density in a cubic lattice; in a box set with periodic boundary conditions. Due to the zero pressure gradient the velocity difference between gas and dust can be exactly known,

$$\Delta v(t) = \Delta v(0)e^{-(t/t_s)} \quad (2.78)$$

where, $\Delta v = v_D - v_G$ and t_s is the stopping time, (Lorén-Aguilar and Bate, 2014).

Fig. 2.2 shows the results of the DUSTYBOX test. The dust is given a $v_x = 1$ while the gas has no velocity field. The gas density is initialised at $\rho_g = 1$ and dust density $\rho_d = 10^{-4}$. These densities have been chosen to place the dust in

the test particle regime as there is no back reaction from the dust onto the gas implemented. For this test the stopping time is fixed at the same value for all dust particles. The dotted green curves show the expected dust velocity at: $t_s = 0.01$, $t_s = 0.1$, $t_s = 1$, $t_s = 10$, $t_s = 10$, $t_s = 100$, from top to bottom on fig. 2.2. The red curve shows dust velocities in the implicit dust scheme against time. As can be seen even when taking long timesteps the approximate shape of the dust velocity curve can be matched.

2.5.2 Radial drift in a disc, the Weidenschilling test

A 3D SPH gas disc is set up and an infinitely thin dust ring is injected into the midplane at a given radius in the disc. The dust would then drift radially with an expected rate given by the Weidenschilling solution as discussed in §2.4.

Firstly, a pure SPH disc is set up using reasonable parameters, $\Sigma(R) = \Sigma_0 R_0/R$, where $10 \leq R(AU) \leq 300$ but with a disc mass of $0.01 M_\odot$ using 10^6 SPH particles. For this test we inject 1000 dust particles at $100AU$ into the disc on circular Keplerian orbits.

Prescribed velocity field test

One of the significant limitation of SPH in general, and not just in its application to the dust dynamics, is an inherent noise in any given quantity, because of this the kernel averaging is employed to reduce random fluctuations. To first avoid this problem we start with tests in which gas particles in the disc have a prescribed velocity field. In particular, we use eq. 2.73 with $\eta = 0.01$, so that the azimuthal gas velocity is equal to $v_{gas} = 0.995\Omega(R)$.

Fig. 2.3 displays individual dust particle radial velocity against log of particle stopping time (the stopping time is in units of dynamical time, Ω^{-1}). Positive

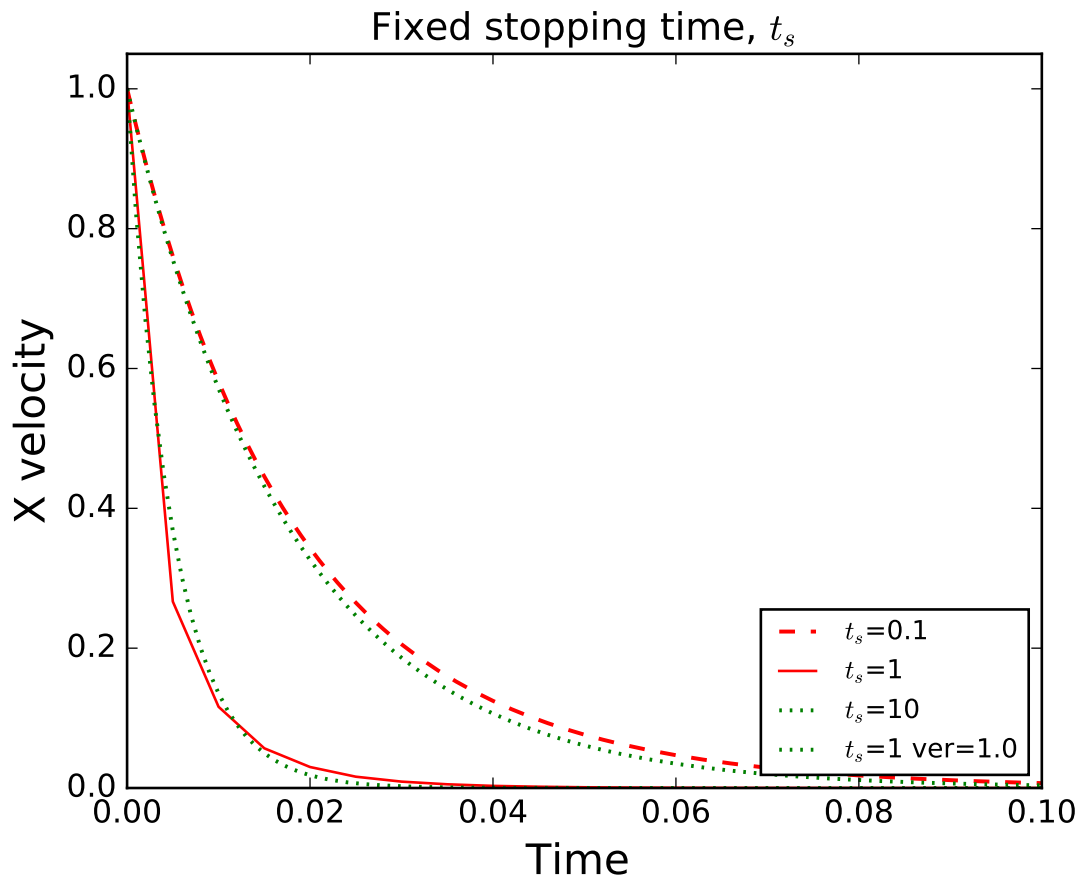


FIGURE 2.2: A simple 3D box of uniform size with dust and gas particles spread out on a uniform cubic lattice. Dust particles are initialised with a uniform velocity in the x direction. The red curve shows the decay of the dust velocities over time. The dust mass is a very small fraction on of the gas mass so that back reaction can be ignored.

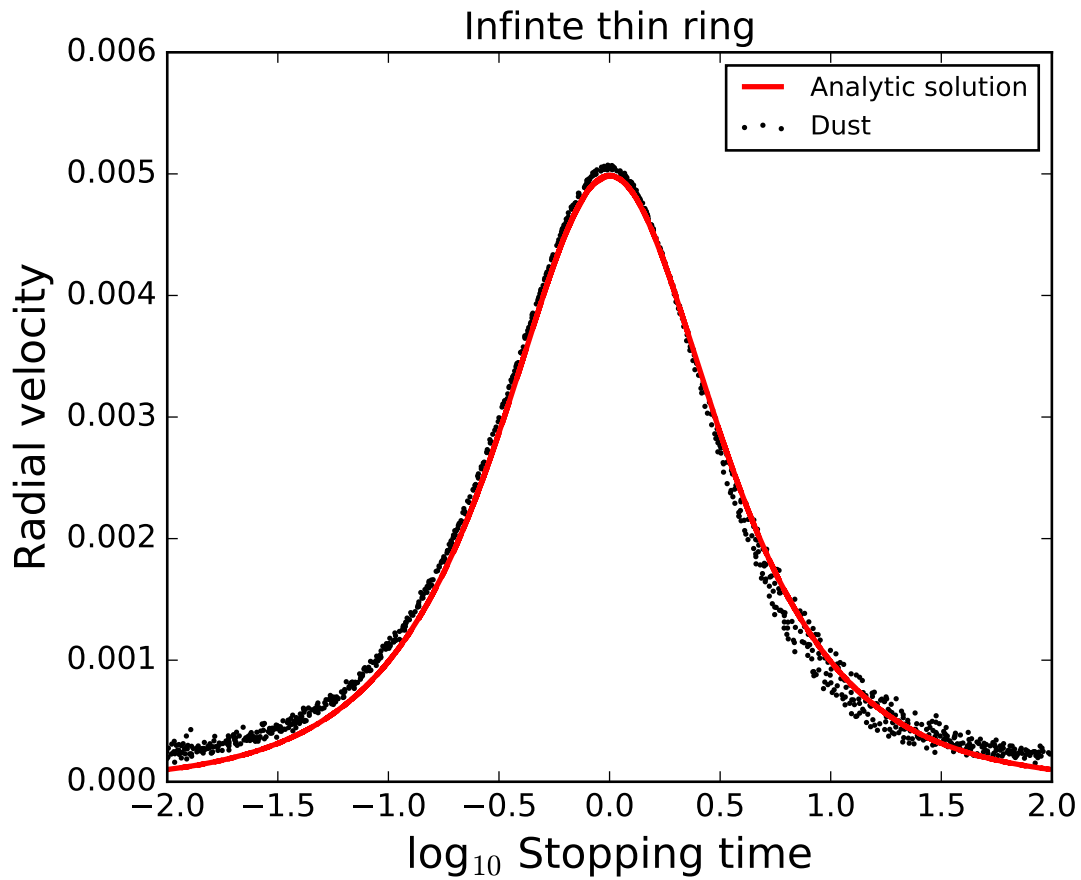


FIGURE 2.3: Radial drift velocity of dust particles (black dots) versus log of particle size in a test with prescribed gas velocity field. The red curve is the analytic solution discussed earlier.

radial velocity is inwards towards the centre of the disc in this figure. The red curve gives the analytic Weidenschilling (1977a) solution. We see that the dust particle velocity field compares well with the expected one.

A live SPH velocity field

In this section we use the live SPH velocity field of the SPH particles. In this case the initial condition for the simulation is obtained by running the SPH disc with a prescribed gas temperature profile and the same initial disc surface density profile, $\Sigma(R) \propto 1/R$, over a long period of time. We then insert dust particles in a

ring and repeat the test as in §2.5.2, but now SPH particles have their individual time-dependent rather than prescribed velocities.

Fig. 2.4 shows a much larger scatter in dust particle velocities compared to fig. 2.3. However, despite this increased scatter, the red curve again shows the expected analytic solution. We see that at any given particle size, the mean of dust particle velocities lies close to the expected analytic result but with a large scatter which is larger for small dust, since that is well coupled to gas.

This correspondence hints that much of the dust velocity scatter is due to the noise in the SPH particle velocity field. We investigate this further in fig. 2.5 where we show the same data as fig. 2.4 but now with dust particles binned in small intervals in the stopping time. The black vertical bars show the standard deviation in dust particle velocity in the bin. For long stopping times these are very small as they are unaffected by the gas. For shorter stopping times the noise in the gas velocity field translates onto the dust.

For comparison, the standard deviation in the gas particle radial velocity at the position of the ring is shown as a blue error bar in both figures. We can see that dust particles have a spread in velocities compared to that of the gas. This indicates that the dust particle velocity spread is indeed driven by random fluctuations in velocities of SPH neighbours of a given dust particle.

Similar results for the dust velocity noise versus particle stopping time were found in GADGET implementation of the implicit scheme in Humphries and Nayakshin (2018). The latter authors found that dust velocity dispersion was a factor of ~ 2 smaller than the SPH particle velocity dispersion. This makes sense as any given dust particle interacts with a number of SPH neighbours, which implies the kernel averaging of the SPH gas velocity field. In fig. 2.5, we see that dust velocity dispersion is approximately a factor of ~ 2 than the SPH velocity

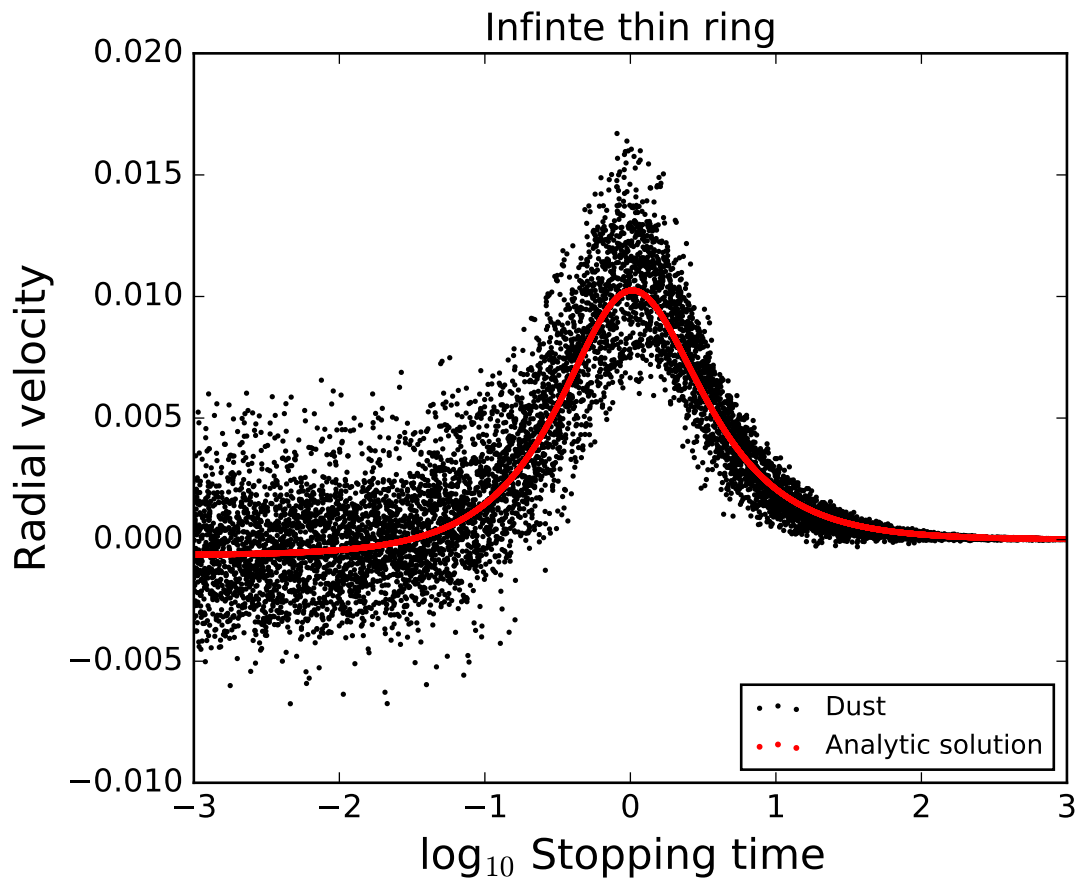


FIGURE 2.4: Radial velocity drift of dust particles using SPH gas velocities. The solid black line shows the averaged gas radial velocity while the blue line is set at 0 radial velocity.

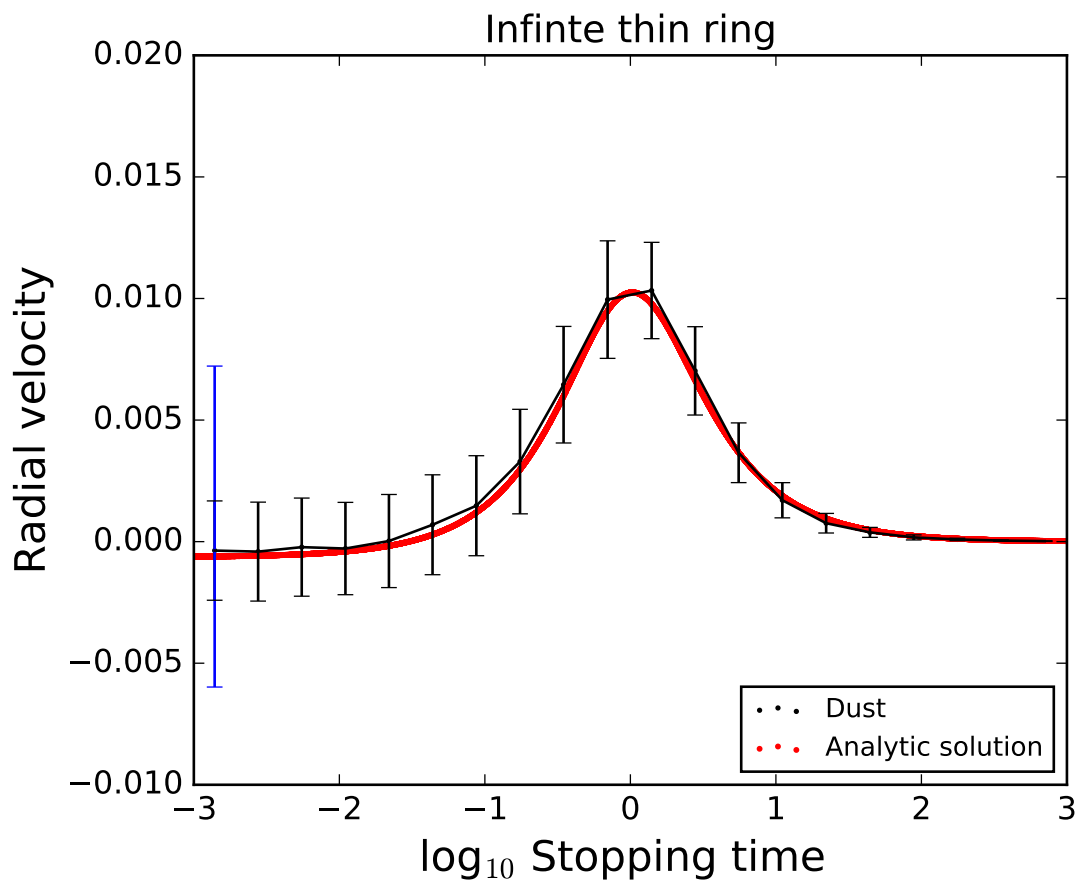


FIGURE 2.5: Same as fig. 2.4 but binned in stopping time, the error bars show the standard deviation of each stopping time bin. The Blue error bar shows the standard deviation of the gas.

dispersion. This is encouraging to see that the two implementations of the same scheme are behaving in a similar manner.

2.6 Discussion

While the modified force can be seen to work in the simple test case of the DUSTY-BOX and when using a prescribed velocity field, there appears to be too much noise in dust particle velocities due to our dust integration scheme implementation in PHANTOM. Over long time scale (many orbits) integrations the dust ring was seen to spread radially and migrate inwards by far more than expected.

We were unable to trace the exact cause of the problems with our dust implementation in the PHANTOM version we used (early 2017). We believe that the root of the problem lies somewhere in how we implemented the dust velocity kick in the code. PHANTOM uses a kick-drift leapfrog integrator with sub-cycles and super-cycles around sink particles such as the central star or an embedded planet. This added level of complexity slowed down our efforts compared with our parallel GADGET work. There were further reasons due to which we decided to stop this work for now. The then public version of PHANTOM did not calculate gravity due to dust particles in the two-fluid implementation, and our long term plans were to implement that. Implementing feedback from dust to gas provided even more challenges with no reasonable solution found, short of moving dust to an independent loop in the timestep routine and potentially over complicating to the existing structure of the code. Additionally, it was clear to us that PHANTOM was very rapidly evolving at the time, building up to the new release reported in Price et al. (2017), and that code edits made by us would have been obsolete in the new code release.

2.7 Conclusion

Here I have laid out the frame work for the implicit timestep scheme to replace the current explicit scheme used in PHANTOM. This new scheme was chosen to reduce cpu time during dust calculations by removing the explicit calculation of the stopping time between dust and gas particles. To resolve this stopping time the timestep for the particles involved had to be reduced resulting in a increase in run time.

The implementation of an implicit timestep into PHANTOM for the two-fluid dust scheme is not completely finished, there are still bugs remaining in the implementation. Specifically surrounding the sub-timestepping and super-timestep aspects of the leapfrog algorithm. In simple tests where these more complex timestepping algorithms are not used the implicit dust scheme does work and the expected analytic drag relation is recovered.

Chapter 3

Planets, debris and their host metallicities

3.1 Chapter abstract

In the classical theory for planet formation, assembly of giant planets requires massive planetesimal discs. Therefore, debris discs (DDs), made up from remnant planetesimals, should correlate with the presence of gas giants and with metallicity of the host star. However, observed DDs do not correlate with $[M/H]$ of the star. Furthermore, giants seem to discourage DD formation: stars with observed gas giant planets are twice less likely to host DDs than stars with smaller planets.

Here we show that these observations are consistent with predictions of Tidal Downsizing (TD) theory for planet formation. In TD, small planets and planetesimal debris is made only when gas fragments, predecessors of giant planets, are tidally disrupted. We show that these disruptions are rare at high metallicity discs but they release more debris per disruption than low $[M/H]$ disruptions. We find that the DD – metallicity correlation pattern predicted by TD depends on survey sensitivity and that there is no obvious correlation between DDs and

[M/H] in general, as observed. A detected gas giant planet implies that its predecessor fragment was not disrupted, thus explaining why DDs are less likely to be found around stars with gas giants. We predict a weak positive correlation between DDs and sub-Saturn planets. In addition, although presently difficult to observe, DDs around M dwarf stars should be more prevalent than around Solar type stars.

3.2 Introduction

3.2.1 Planet debris and the classical scenario

Asteroids, comets and minor bodies in the Solar System are remnants from the planet formation era (see Johansen et al., 2014, for a recent review). Solid debris is also detected around a good fraction of nearby Solar type stars (Wyatt, 2008) through grain thermal emission in infra-red (Oudmaijer et al., 1992; Mannings and Barlow, 1998). These grains should have been blown away rapidly by the stellar radiation pressure, and their continuous presence requires a large reservoir of much bigger solid bodies feeding the fragmentation cascade (e.g., Hellyer, 1970). Naturally, observations of debris discs (DDs) are expected to shed light on planet formation theories.

Core Accretion theory (Safronov, 1972) stipulates that planet formation starts with the formation of minor solid bodies called planetesimals. By sticking together, planetesimals form terrestrial planet mass “embryos”, which grow further by continuing to accrete planetesimals (e.g., Hayashi, Nakazawa, and Nakagawa, 1985; Wetherill, 1990). As solid cores reach the critical mass of $\sim 10M_{\oplus}$, they start to accrete gas, which culminates in the emergence of gas giant planets (e.g., Mizuno, 1980; Pollack et al., 1996; Ida and Lin, 2004a; Hubickyj, Bodenheimer, and Lissauer, 2005). Protoplanetary discs around more metal rich stellar hosts are naturally expected to form more massive planetesimal discs (Ida and Lin, 2004b). This results in a more rapid assembly of massive solid cores, and hence yields more gas giant planets in higher metallicity environments (e.g., Ida and Lin, 2004b; Mordasini et al., 2009). The expected correlation chain in CA is thus “higher [M/H] \rightarrow more planetesimals \rightarrow more solid cores \rightarrow more gas giants” .

3.2.2 Metallicity correlation challenges

Planets

Historically, this correlation chain has been tested by observations in roughly the reverse order since gas giants are the “easiest” to observe. It is now well established that frequency of appearance of gas giant planets correlates strongly with the host star’s metallicity (e.g., Gonzalez, 1999; Fischer and Valenti, 2005). However, sub-Neptune planets are abundant at all metallicities (e.g., Sousa et al., 2008; Mayor et al., 2011; Buchhave et al., 2012). More recent analysis of Wang and Fischer (2015) reveals that planets with radii smaller than $4R_{\oplus}$ (e.g., smaller than Neptune) are correlated with the host stars metallicity albeit weakly: hosts with $[M/H] > 0$ are twice as likely to have a planet in this radius range compared with sub-Solar metallicity hosts (gas giants are nine times as likely for host stars with $[M/H] > 0$).

The weak correlation of massive cores with $[M/H]$ has been interpreted to imply that massive cores in metal-rich systems reach the critical mass for runaway gas accretion before the gas disc dissipates, so they quickly become gas giants (Ida and Lin, 2004b; Mordasini et al., 2009). In metal poor systems, in this picture, massive cores form in gas-free environment and hence do not make gas giants.

However, we note that the observed solid cores outnumber gas giants by approximately ten to one (e.g., Mayor et al., 2011; Howard et al., 2012). If cores do become gas giants very frequently in metal-rich systems, why are gas giants not as numerous as massive cores? Furthermore, recent models of pebble accretion suggest that cores may grow orders of magnitude faster than they do in the planetesimal-based paradigm (e.g., Lambrechts and Johansen, 2012; Lambrechts and Johansen, 2014). If core accretion is to explain rapid formation of massive

cores at separations of $\gtrsim 10$ AU in the Solar System (e.g., Helled and Bodenheimer, 2014), and in the likes of HL Tau (e.g., ALMA Partnership et al., 2015; Dipierro et al., 2015), then observations would also require rapid core formation even at large distances from the star. This casts doubts on the suggestions that cores grow after the gas disc is dissipated in metal-poor discs and leaves the observed planet – [M/H] correlations somewhat puzzling in the context of CA.

Debris discs

Debris disc detection frequency does not correlate with [M/H] of host stars (Maldonado et al., 2012; Marshall et al., 2014; Moro-Martín et al., 2015), directly contradicting a key assumption usually made about formation of planetesimals (that they form in a greater abundance in higher metallicity hosts, e.g., Ida and Lin, 2004b). Furthermore, observed DDs also do not correlate with the presence of gas giant planets (e.g., Moro-Martín et al., 2007; Bryden et al., 2009; Kóspál et al., 2009). In fact, stars orbited by a gas giant are twice half as likely to host a detected DD than stars orbited by planets less massive than $30M_{\oplus}$ (Moro-Martín et al., 2015).

These observational results are paradoxical. All the planets referred to in these surveys are relatively close-in ones, e.g., orbiting the star at separation \lesssim a few AU. Spatial scales of the observed DDs are however much larger, e.g., tens of AU (Wyatt, 2008; Moro-Martín et al., 2015). Thus the *observed* planets and DDs should not interact directly. As both populations should be more abundant at higher [M/H], it would imply that there should be a positive cross-correlation between planets and debris, contrary to what is observed.

Raymond et al. (2011) suggested an explanation for these observational results. They showed that mutual interactions of giant planets initially orbiting the

host star at a few to ~ 10 AU distance are capable of exciting a very large velocity dispersion in the population of planetesimals located further out. This could fuel a strong fragmentation cascade, depleting the debris rings by ~ 1 Gyr age on which DDs are typically observed. These calculations also predicted a strong correlation between DDs and terrestrial-mass planets. Wyatt et al. (2012) report a correlation between debris discs and presence of planets less massive than Saturn, although the more recent study of Moro-Martín et al. (2015) casts doubts on that correlation.

The scenario suggested by Raymond et al. (2011) is physically reasonable but is constricted by the fact that observed gas giants are very rare. The authors invoke three gas giants in a disc. Observations however show that there is less than 0.05 giant planets per star within period of 400 days on average (Santerne et al., 2016). Microlensing surveys (Shvartzvald et al., 2016) constrain the number of gas giants beyond the snow line region to a similarly small regiment. Directly imaged surveys also find that massive gas giants in separations of 10 – 100 AU orbit at most a few % of stars (e.g., Biller et al., 2013; Bowler et al., 2015)¹. In addition to this, the scenario of Raymond et al. (2011) predicts a strong decay in the dust luminosity as a function of stellar age as young massive DDs self-destruct in fragmentation cascades. Fig. 4 of Moro-Martín et al. (2015) does not show any obvious trend in DD detection frequency with time, adding doubt to this theoretical picture.

We therefore conclude that *within observational constraints* CA has not yet provided a reasonable account for the observed relations between planets found at $\lesssim 1$ AU separations and DDs, and the DD-metallicity correlations.

¹We note in passing that the rarity of *observed* gas giants in TD is much less of a problem because the huge majority of Jupiter mass gas fragments born in the outer disc are eventually disrupted and leave behind the much more abundant sub-giant planets. See Nayakshin (2016) for more detail.

3.2.3 Tidal downsizing alternative

Here we propose a solution to all of these observational paradoxes by evoking a different planet formation theory. In the Tidal Downsizing (TD) scenario (Boley et al., 2010; Nayakshin, 2010a), planet formation begins with gravitational instability (GI; e.g., Kuiper, 1951b; Cameron, Decampoli, and Bodenheimer, 1982; Boss, 1997) of a massive young protoplanetary disc, when the latter hatches ~ 1 Jupiter mass gas fragments at distances of tens to hundreds of AU (Rice, Lodato, and Armitage, 2005; Durisen et al., 2007) from the host star. These fragments migrate inward very rapidly (e.g., Vorobyov and Basu, 2006; Baruteau, Meru, and Paardekooper, 2011; Tsukamoto et al., 2015). Since they contract slower than they migrate, most are disrupted by tides from the parent star. Grain sedimentation within fragments is believed to form massive solid cores in the centre of the fragments (Kuiper, 1951b; McCrea and Williams, 1965; Helled, Podolak, and Kovetz, 2008; Boley et al., 2010; Nayakshin, 2011). When the fragments are disrupted, the cores are released back into the protoplanetary disc, potentially yielding rocky planets (Boley et al., 2010; Cha and Nayakshin, 2011). Cores and gas fragments that managed to avoid tidal disruption continue to migrate in. Nayakshin and Fletcher (2015) performs population synthesis of this scenario and finds it promising in explaining many of the observed properties of exoplanets at all separations.

Planet correlations

Nayakshin (2015a) found that gas fragments contract rapidly when pebbles (grains of a few mm in size) are deposited in their outer envelopes by pebble accretion (Ormel and Klahr, 2010; Lambrechts and Johansen, 2012) from the protoplanetary

disc. When the fragments contract sufficiently, e.g., when their central temperature exceeds $\sim 2,000$ K, Hydrogen molecules in the fragment dissociate and the fragment collapses to much higher density (Bodenheimer, 1974). For a rapidly migrating fragment, gravitational collapse is the only way of avoiding an imminent tidal disruption in the inner few AU. Assuming pebbles are more abundant at high metallicities (note that this assumption has nothing to do with abundance of planetesimals, see below), one obtains higher pebble accretion rates, and hence a faster fragment collapse at high $[M/H]$. Unsurprisingly then, one obtains a strong positive metallicity correlation for gas giant planets in the inner few AU (Nayakshin, 2015b; Nayakshin, 2015c) – only the planets that managed to collapse faster than they arrived in the inner few AU disc survive.

On the other hand, Nayakshin and Fletcher (2015) show that sub-giant planets do NOT follow a strong $[M/H]$ correlation because these planets are formed when gas fragments are disrupted. On the other hand, more massive cores are made inside more metal rich fragments. Therefore, while solid cores are most abundant *by numbers* at low $[M/H]$, the most massive of them are found at high $[M/H]$. The combination of these two effects does not produce a clear cut correlation with metallicity of the host star.

TD predictions are therefore qualitatively consistent with the observed metallicity correlations for close-in gas giants and sub-giant planets.

Origin of debris discs in TD

Astrophysical existence of Asteroid and Kuiper belts in the Solar System and DDs around other stars is usually taken as a proof that planetesimal synthesis has taken place *in the main body of the protoplanetary disc* as predicted by the planetesimal hypothesis (Safronov, 1972).

However, Nayakshin and Cha (2012) showed that TD can also naturally yield DD-like structures. In particular, it was suggested that, as the central regions of the fragments become dominated by grains rather than H/He gas, gravitational collapse of the solid component may follow (Nayakshin, 2010b), as in the model of Goldreich and Ward (1973), except for the different geometry. Simulations show that self-gravitating gas fragments formed in proto-planetary discs always rotate rapidly (e.g., Mayer et al., 2004; Boley et al., 2010; Galvagni et al., 2012), so that not all solids are likely to condense into a single central core due to excess angular momentum. Fragments larger than $\sim 1 - 10$ km decouple from the gas aerodynamically, that is, the timescale for in-spiral of these bodies into the core is $\gtrsim 0^5$ years, which is longer than the expected lifetime of the host fragments (see Fig. 1 in Nayakshin and Cha, 2012).

Hydrodynamical simulation of a fragment disruption showed that large solid bodies closest to the core remain bound to it, perhaps contributing to formation of satellites (as needed for Neptune and Uranus). Bodies farther out are however unbound from the core when the gas is removed and form debris rings with kinematic properties (e.g., eccentricity and inclination) resembling the Kuiper and the Asteroid belts in the Solar System.

One can immediately see that TD naturally explains why planets observed at small separations may be connected to DDs observed at tens to hundreds of AU. The close-in planets migrated through these far away regions before arriving at their present day locations. Disruption of a planet at large distances (a) creates a DD there, and (b) changes the type of planet that may be observable at close separations to the star provided the planet migrates there before the gas disc is dissipated. It is also intuitively clear that DD-planet-metallicity relations predicted by TD must differ from that of CA, and it is hence important to clarify

these to aid future observational testing of these two planet formation scenarios.

This chapter is structured as following. In §3.3 we present the numerical methods with which we shall test how the TD scenario for formation of both planets and debris discs changes as a function of the host star's metallicity. In §3.4 we explore the results for planets, and in §3.5 the focus is on the debris discs. §3.6 presents a brief discussion and a comparison of the theory and observations. We conclude in §3.7.

3.3 Numerical method

Our aim is to understand how metallicity of the protoplanetary disc, assumed below to be equal to that of the host star, influences the planet and the debris formation outcomes. Since fragments may form at a range of separations and in discs with varied initial conditions, it is best to approach this question statistically, by performing a population synthesis study (cf. similar approach for CA theory, e.g. Ida and Lin, 2004a). To this end we use the same code and general setup as used by Nayakshin and Fletcher (2015) and Nayakshin (2016). For this reason we only briefly review our numerical methods.

3.3.1 Population synthesis

A 1D viscous time dependent code is used to solve for the disc surface density, temperature and other properties on a logarithmic grid extending from the inner radius, $R_{\text{in}} = 0.08$ AU, to the outer radius, $R_{\text{out}} = 400$ AU. The disc initial surface density is proportional to $1/R$ with an exponential rollover at $R_0 = 100$ AU. The total disc mass is randomly chosen between the limits shown in Table 3.1

(note that when $M_d \approx 0.15M_\odot$ the Toomre parameter Q drops to ~ 1.5 at $R \sim 80 - 90$ AU, so that the disc can fragment there).

The disc viscosity parameter, α , is fixed for each simulation but its value is drawn randomly in the logarithmically uniform fashion between the minimum and the maximum values shown in Table 3.1. The disc is photo-evaporated with the overall normalisation of the photo-evaporation rate also being a Monte-Carlo variable (ζ_{ev}), whose boundaries are selected to fit the roughly exponential decrease in the disc fraction with time, Table 3.1 (see figure B1 in Nayakshin, 2016, for more details). In addition to viscous evolution, our disc is also affected by the gravitational torques that drive planet migration and may open gaps in it (e.g., Goldreich and Tremaine, 1980; Lin and Papaloizou, 1986). The gas disc physics and assumptions are therefore quite similar to those employed by CA population synthesis authors (e.g., Mordasini et al., 2009). Most of the distinctions with CA models is in planet formation physics rather than gas disc physics.

A population synthesis model is started with a fragment with the initial mass, M_0 , in the range between $1/3 M_J$ and $8 M_J$, placed in the disc at distance a_{pl} between 70 and 105 AU (where the disc Toomre's parameter has a broad minimum).

Forgan and Rice (2013b) calculate the mass of the gas fragments, M_0 , based on analytical estimates for Jean's mass (M_{jeans}) in the their self-gravitating disc. While this approach is in principle superior to ours, which decouples M_0 from the conditions in the disc, we feel that any analytical calculation of M_{jeans} cannot be deemed reliable at this point. The fundamental problem here is not how M_{jeans} is derived, but the approximations on which the standard accretion disc theory is built upon. In particular, Shakura and Sunyaev (1973) approach utilises vertically integrated, that is, vertically averaged, equations for the disc. This approach cannot be more accurate than a factor of ~ 2 , as pointed out by Svensson

and Zdziarski (1994), who retained the uncertainty in accretion disc equations (see their parameter ζ). Furthermore, the location of the disc fragmentation and disc properties strongly depend on the irradiation of the disc by the background and stellar fluxes, and these can vary widely at same disc mass (e.g., Stamatellos, Whitworth, and Hubber, 2011). In addition, simulations show that presence of one fragment in the disc may cause the disc to fragment in locations/conditions where it would normally not fragment (Meru, 2015), clearly showing that analytical methods cannot capture the whole variety of outcomes for fragmenting discs.

Since the mass of the fragments depends on the disc scale-height, H , as $M_{\text{jeans}} \propto H^3$ (e.g., eq. 6 in Kratter, Murray-Clay, and Youdin, 2010), an uncertainty in H by a factor of ~ 2 leads to an order of magnitude uncertainty in M_{jeans} . We therefore feel that it is safer to assume that the initial fragment mass varies in a broad range, and explore the resulting outcomes. We do not consider fragments more massive than $8 M_{\text{J}}$ because these are not likely to be tidally disrupted as they contract rapidly and so they do not produce debris discs. As will be shown the main conclusions of this paper are qualitatively independent from the initial fragment mass distribution.

The fragment's separation then decreases due to tidal torques from the disc, and the calculation proceeds until the disc mass reduces to zero due to accretion onto the star and photo-evaporation. The end result of a calculation comprises the final location, mass and composition of the planet.

We use a 1D spherically symmetric approximation for the fragment. Gas fragments are allowed to accrete grains a few mm in size from the disc via pebble accretion in the Hills regime (Lambrechts and Johansen, 2012) unless the planet opens a gap. Gas accretion onto the planet is assumed to be inefficient (see

Nayakshin and Cha, 2013). Pebbles are deposited in the outer layers of the planet. Both incoming pebbles and the grains present in the fragment at its birth grow via sticking collisions as they sediment (e.g., Boss, 1997). Three grain species (water, rocks and CHON) are considered. See sections 4.2, 4.3, and 4.6 of Nayakshin (2015c) for further detail of grain treatment.

The grains that settle all the way to the centre of the fragment are accreted onto the core (see Helled and Schubert, 2008; Helled, Podolak, and Kovetz, 2008; Nayakshin, 2011). The internal structure of the core is not modelled, assuming instead a sphere with a fixed material density, $\rho_0 = 3 \text{ g cm}^{-3}$. As grains accrete onto the core, their accretion luminosity is released back into the gaseous envelope of the fragment, which produces important feedback effects for core masses exceeding a few M_{\oplus} (Nayakshin, 2016).

Table 3.1 summarises the initial conditions used for the population synthesis models. As noted they are almost identical to those from Nayakshin (2016). In the table, f_m is the type I migration multiplier and v_{br} is the breaking velocity of grains within the fragment (grain collisions at velocities higher than that lead to grain fragmentation rather than growth). The metallicity [M/H] distribution of our host stars is a gaussian with a mean of 0 and a standard deviation of 0.22 (Fletcher and Nayakshin, 2016). The exact values of the population synthesis parameters do not influence our main results significantly. 30,000 population synthesis runs are performed in this study.

3.3.2 Debris model

It is not possible to simulate particle instabilities that may form large solids in the central part of the fragment within our 1D spherically symmetric model for the planet. We therefore explore two different assumptions about the mass of

TABLE 3.1: Parameters of the population synthesis model and their values. See text for detail.

Parameter	Value
$M_{\text{disc}} (M_{\odot})$	0.075 - 0.2
$M_{\text{p}} (M_{\text{J}})$	0.333 - 8
a_0 (AU)	70 - 105
α	0.005 - 0.05
f_{m}	1 - 4
$v_{\text{br}} (m\text{s}^{-1})$	5 - 30
ζ_{ev}	0.02 - 10

the debris formed in the fragment which we believe roughly bracket the possible outcomes. We shall later see that these two assumptions lead to same conclusions as far as debris disc – planets – metallicity correlations are concerned.

First of all, one can argue that the total mass of solid debris made by the fragment is a small fraction $0 < \zeta \ll 1$ of the total mass of all of the solids inside the planet (note that we use “planet” and “fragment” inter-exchangeably in this paper), that is,

$$M_{\text{deb}} = \zeta Z M_{\text{p}} , \quad (3.1)$$

where Z is the metallicity of the planet at the moment of its tidal disruption. This assumption is reasonable but ignores the fact that grains sediment differently in fragments of different temperature or age. For example, none of the three (water, rock, CHON) grain species can reach the central part of a fragment with central temperature $T_{\text{c}} \gtrsim 500$ K, since they are vaporised. The grains hence cannot be separated from the gas to make large solids, whereas in a fragment with central temperature of, e.g., 500 K, refractory grains will sediment but organics and water ice will not (e.g., Helled, Podolak, and Kovetz, 2008). Furthermore, even if grains are not vaporised, they sediment at a finite velocity, and this process is opposed by the convective mixing of grains (e.g., Helled and Bodenheimer, 2011), so the fragment’s age at the point of its tidal disruption is important in determining the

fraction of grains that sedimented into the centre.

The second assumption one can make is that the total debris mass released back into the disc is a fraction of the core mass,

$$M_{\text{deb}} = \beta M_{\text{core}}, \quad (3.2)$$

where β is a positive number. This model is more reasonable from the point of view of grain physics since core growth in our model does include grain vapourisation at high temperatures and other grain sedimentation microphysics. However we are still unable to constrain β since we do not know the angular momentum of our fragments, how it is distributed within them, and where exactly large solids form.

While these two models leave normalisation of the debris disc *mass* dependent on either ζ or β , the metallicity trends of our models should be independent of the exact values of these free parameters as long as ζ or β are independent of the host star's metallicity. It is difficult to see, for example, why the distribution of angular momentum within the fragment would be a strong function of metallicity of the disc, and hence why β would be a function of $[M/H]$.

To make our model qualitatively consistent with debris disc observations in terms of the typical DD mass, we set $\beta = 1/10$, and $\zeta = 1/250$. With these choices, our DD masses are typically $M_{\text{deb}} \lesssim 1 M_{\oplus}$ *per disrupted fragment*. Since we expect a dozen or so fragments per a typical DD, the overall mass is expected to be a few to $10 M_{\oplus}$. This is qualitatively consistent with Fig. 3 of Wyatt (2008), which shows the observed *dust* masses. In the protoplanetary disc phase, time $t \lesssim 10$ Million years, the DD mass is likely to be smaller than the mass of the dust in the disc, which are $\sim 10 - 100 M_{\oplus}$ in the figure. Also, we have the minimum mass limit on M_{deb} from the older discs which had their gas-dust disc depleted,

which requires $M_{\text{deb}} \gtrsim 1 M_{\oplus}$ (see fig. 3 in Wyatt, 2008, at $t \gtrsim 10$ Million years). Therefore, typical DD masses are probably in the range of a few to $\sim 10 M_{\oplus}$.

Finally, we assume that more massive debris discs are more likely to be detected, which we model by defining the probability of detecting a debris disc of mass M_{deb} as

$$P(M_{\text{deb}}) = \frac{M_{\text{deb}}^2}{M_{\text{deb}}^2 + M_{\text{det}}^2}, \quad (3.3)$$

where M_{det} is the detection mass limit. For example, if $M_{\text{deb}} = M_{\text{det}}$, only half of debris discs are detectable. Below we chose several values of M_{det} to investigate how our conclusions depend on sensitivity of our synthetic "observation" of population synthesis results.

3.4 Results: planets

As explained in the Introduction, debris is secondary to planets in the context of TD scenario. The debris is only made when a gas fragment is disrupted. Therefore, it makes sense to start the discussion on the relationship between planets and debris in TD by looking at the planet side of the problem first.

Fig. 3.1 shows planet mass versus its separation obtained in the population synthesis calculations. The colours of the symbols indicate the metallicity of the parent star, grouped in four bins as detailed in the legend. Only 1/5 of the actual 30,000 population synthesis runs are plotted for clarity, with systems shown in the figure selected randomly and uniformly from the total set of results. The histogram above the main panel in the figure shows the distribution of the planets over the planet-star separation, whereas the histogram on the right shows the planet mass function integrated over all separations.

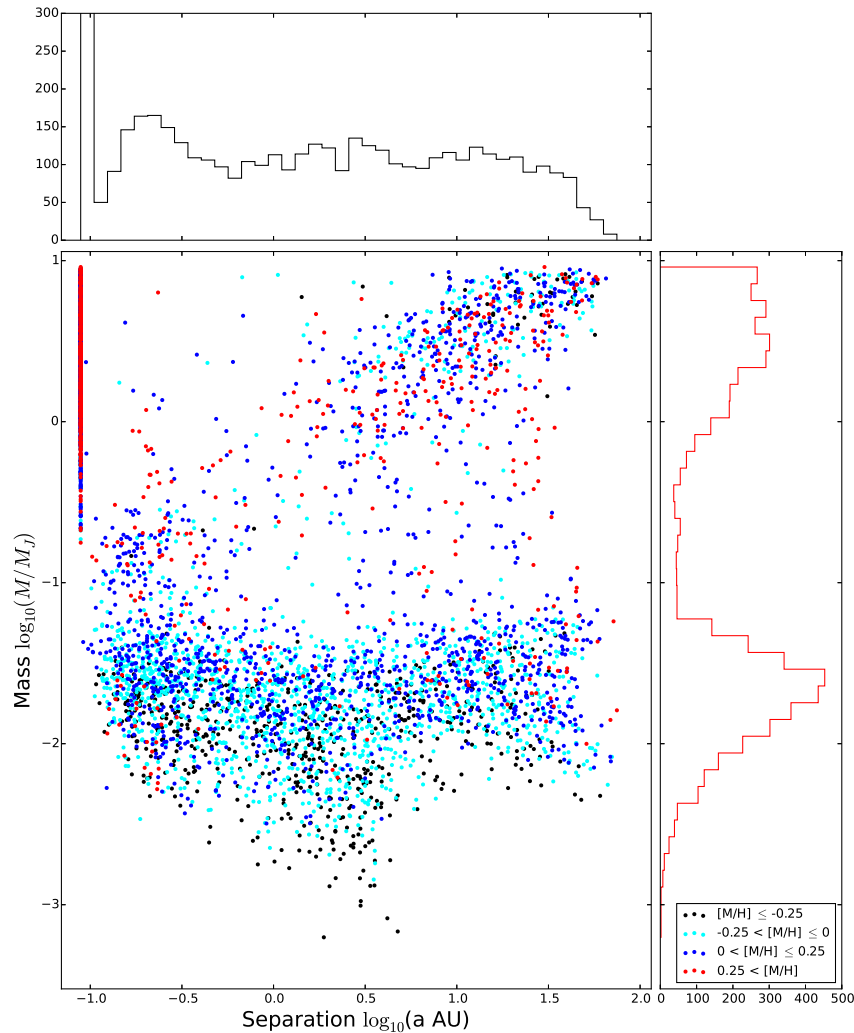


FIGURE 3.1: Planet mass versus planet separation plane from the population synthesis calculations. The colour of the points indicates metallicity of the host star, grouped in four bins as shown in the legend. The histograms above and to the right of the main figure show the distribution of the planets over the planet's separation and mass, respectively. Note a strong role of host star's metallicity in the inner few AU disc for ~ 1 Jupiter mass planets but much less so for Super-Earth mass planets.

These results are very similar to those presented earlier in Nayakshin and Fletcher (2015) and Nayakshin (2016), where it was shown that TD presents a promising alternative to CA in accounting for all of the observed planet-metallicity correlations. Thus here we only focus on issues that are relevant to DDs statistics. It is instructive to look at probabilities, p , of different outcomes as a function of the stellar metallicity, $[M/H]$. To arrive at these, we count the initial number of fragments injected in the outer disc in the beginning of the simulations, N_{init} , for each metallicity bin. We then count the number of planets that satisfy a given condition at the end of the simulations selected, N_{end} , e.g., the planet is a gas giant and is located in a specified separation range. The corresponding probability is then defined as

$$p = \frac{N_{\text{end}}}{N_{\text{init}}}, \quad (3.4)$$

Three outcomes of the simulations are especially relevant to this chapter, and the probabilities of these are shown in Fig. 3.2. The probability of a fragment to be tidally disrupted anywhere in the disc is shown with the black curve (squares). These disruptions leave behind dense planetary cores and also solid debris as described in §3.3.2.

Next, the fragments that manage to collapse and avoid tidal disruption are split into two groups: those that continue to migrate and eventually arrive at the inner disc radius (the green crosses), R_{in} , and those that are left "stranded" in the inner disc, $R_{\text{in}} < a < 5 \text{ AU}$, when the protoplanetary disc is depleted away (red diamonds). The young giant planets from the former group are likely to be disrupted at $R < R_{\text{in}}$ since the disc is very hot there. Alternatively, these fragments may be driven all the way into the star and be assimilated there. Presumably only a small fraction of these planets survive as hot Jupiters, which are very rare

observationally (Santerne et al., 2016). When disrupted, these fragments do not release any solid debris in our model since they are very hot, with their central temperature exceeding $\sim 30,000$ K soon after collapse².

Finally, the planets that are left behind in the inner 5 AU (the red diamonds in the figure) are observable with the transit and radial velocity observations. These show a strong positive correlation with $[M/H]$ of the host star (Nayakshin, 2015b), as observed (e.g., Fischer and Valenti, 2005; Mayor et al., 2011). This result is due to pebble accretion on pre-collapse gas fragments. Pebble accretion increases weight of such fragments and acts as an effective cooling mechanism that replaces the inefficient radiative cooling, accelerating fragment contraction and eventual collapse (see Nayakshin, 2015a, for the physics of this effect). At higher $[M/H]$, pebble abundance in the disc is higher, which increases pebble accretion rate onto fragments. A larger fraction of gas fragments collapse before they are tidally disrupted, and a greater fraction of gas giant planets penetrates inside the “exclusion zone” at a few AU distance from the star (see the red line in fig. 3a in Nayakshin, 2016).

The corollary to the positive gas giant – $[M/H]$ correlation in our model is that tidal disruption events at low $[M/H]$ are more frequent than they are at high metallicities. This is apparent in the behaviour of the black curve in fig. 3.2. This trend shapes one of the key results of our paper, suggesting that, with other things being equal, there should be more debris produced at low $[M/H]$ discs than in high $[M/H]$ discs. This prediction is contrary to CA and hence may be used to differentiate between the two theories observationally, although we shall see that high $[M/H]$ fragments are likely to contain more debris per disruption, so more analysis is needed for a quantitative prediction.

²The fragments that reach the inner boundary are those that went through the H_2 molecule dissociation (see, e.g., Bodenheimer, 1974).

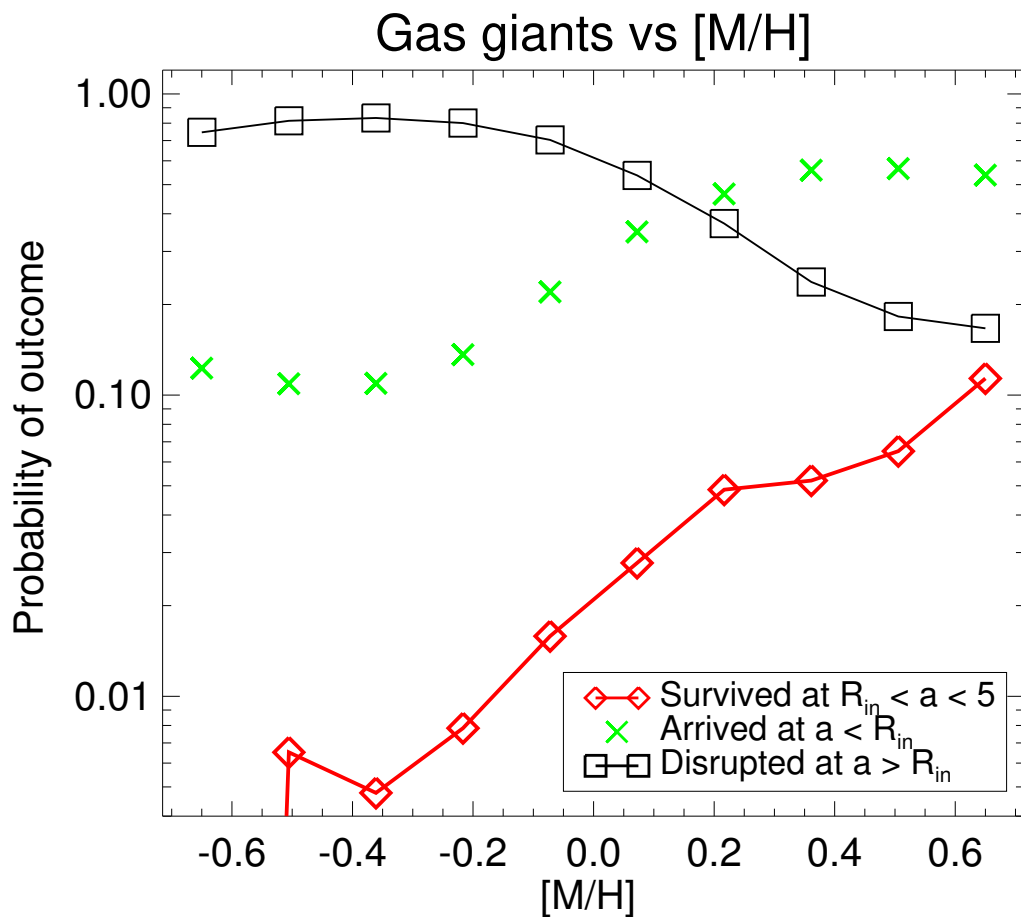


FIGURE 3.2: Probability for a fragment to be tidally disrupted (black squares), reach the inner disc radius, R_{in} (green crosses), or survive in the inner region of the disc (red diamonds), all as a function of the parent star's metallicity $[M/H]$. Note that fragments are tidally disrupted most often at low $[M/H]$, and least frequently at high $[M/H]$. This yields a positive gas giant planet – host metallicity correlation of TD.

To gain further insight, we plot the probability of core-dominated planets being present in the inner 5 AU in the end of the simulations as a function of metallicity in fig. 3.3. The red diamonds show this probability for all core masses. This curve is very similar to the black curve from fig. 3.2. The green crosses and the black square curves show probability of core formation for masses greater than $5M_{\oplus}$ and $12M_{\oplus}$, respectively. These clearly show that most massive cores are made in the most metal rich environments, as could have been expected. We note in passing that this picture – more cores by numbers at low $[M/H]$ but most massive cores appearing at higher $[M/H]$ – may be consistent with the observed weak metallicity correlations for planets with radius smaller than $4R_{\oplus}$ (Wang and Fischer, 2015), although a quantitative comparison utilising synthetic observations of our planets is yet to be made.

3.5 Results: debris discs

We now switch the discussion to planetary debris produced by our model.

3.5.1 Debris disc masses

Fig. 3.4 presents the distribution of the debris mass obtained in the population synthesis via Model 1 (see §3.3.2), with $\zeta = 1/250$. We separated the histogram on the metal rich, $[M/H] > 0$ (blue colour), and the metal-poor populations, $[M/H] < 0$ (red). The peak of the histograms is at $M_c \approx 3M_{\oplus}$ for the former and $M_c \sim 8M_{\oplus}$ for the latter. As expected, debris released by disruptions of metal-rich population is more massive than that of $[M/H] < 0$ discs. As also expected based on figs. 3.2 and 3.3, the low metallicity environments produce more debris disruption events per fragment, so the overall metallicity trend may be a function

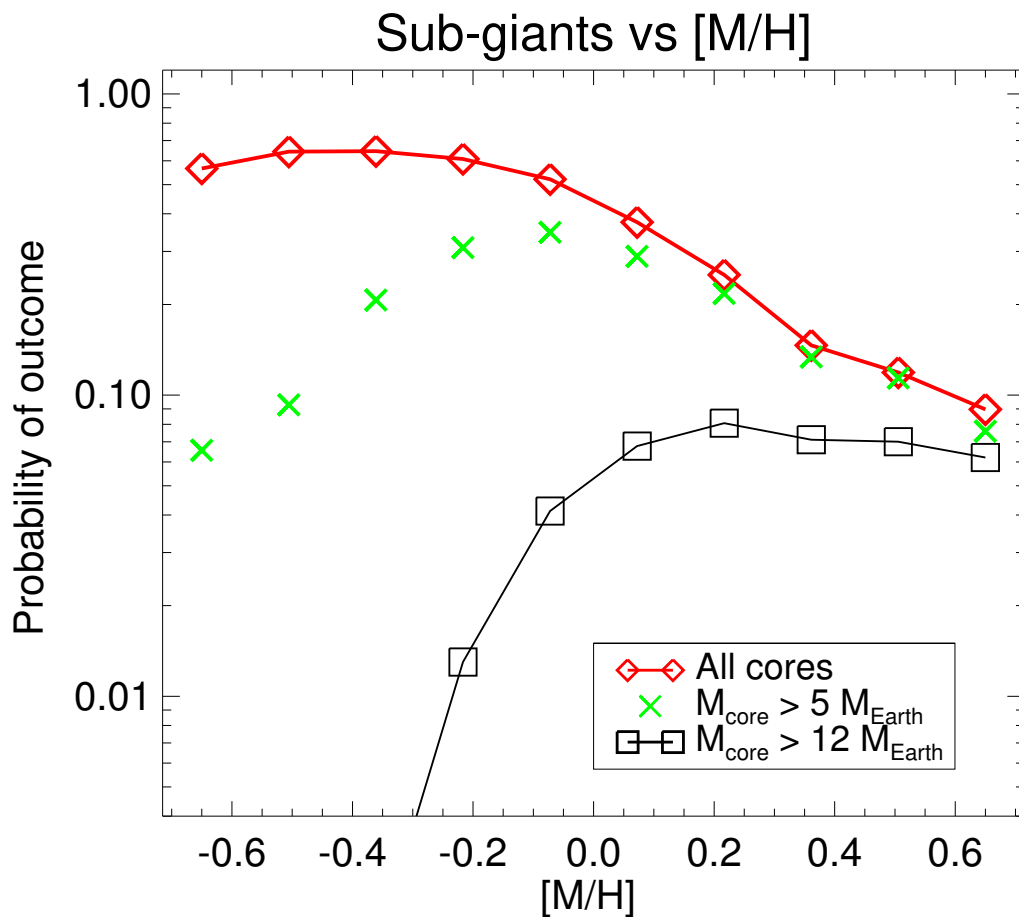


FIGURE 3.3: The probability of core-dominated planet surviving in the inner 5 AU after the gas disc is dispersed in the population synthesis. The red curve shows all the cores while the green and the black are for cores more massive than $5 M_{\oplus}$ and $12 M_{\oplus}$, respectively. Note that low mass cores are formed more readily at low [M/H] whereas high mass cores are formed more frequently at high [M/H] hosts.

of DD survey observational sensitivity. The wide spread for the debris mass in fig. 3.4 is enhanced by the wide range in the fragment's mass in the initial conditions for the simulations (from $M_0 = 1/3 M_J$ to $M_0 = 8 M_J$, see Table 1).

As noted in §3.3.2, Model 1 is an over-simplification which does not take into account grain growth and sedimentation physics. In Model 2, we instead assume that the mass of the debris released is 1/10 of the mass of the core, assembly of which does take into account grain physics. Fig. 3.5 shows the debris mass histograms for Model 2. This shows that, although there are important quantitative differences between Model 1 and Model 2, qualitative trends with metallicity remain similar. The mass of debris per disruption is still larger at higher metallicity. However, the histogram for Model 2 is narrower than that for Model 1, and one also notices a sharp roll-over at the high mass end. The rollover is due to the feedback unleashed by massive cores on their fragments, investigated in Nayakshin (2016). When the core mass exceeds $\sim 10 M_\oplus$, its luminosity output puffs the pre-collapse fragment up, slowing down grain sedimentation and even disrupting the fragment in extreme cases. This leads to a saturation of core masses at around $10 - 20 M_\oplus$. Since our debris discs attain the mass of 1% of M_{core} in Model 2, our DDs peak in masses around $0.2 M_\oplus$.

3.5.2 Debris discs metallicity correlations

Fig. 3.6 shows the metallicity distribution of the detectable debris discs for Model 1, where the debris mass is set to fraction $\zeta = 1/250$ of the total metals' mass inside the disrupted fragment. Three detection limits are considered as indicated in the legend in the figure. The bottom panel shows the normalised distribution for the three cases and also the gaussian distribution for the host star's metallicity distribution.

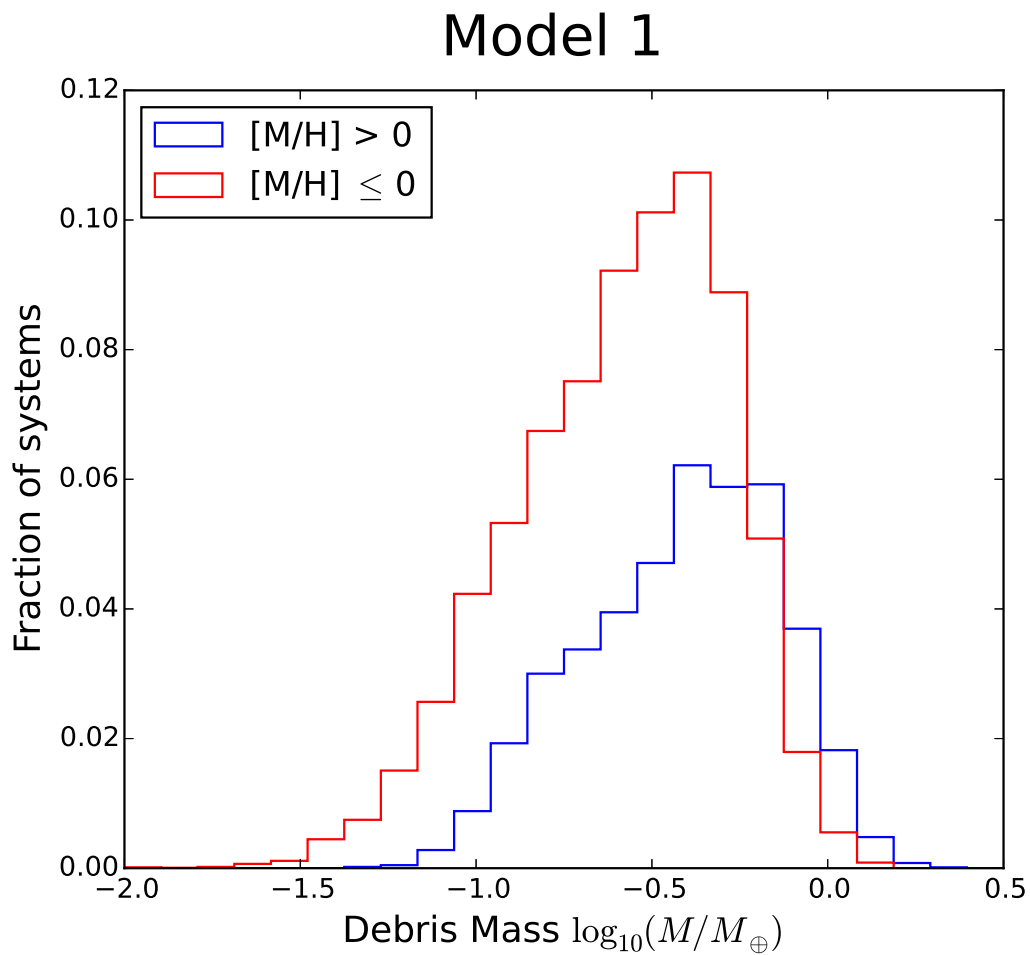


FIGURE 3.4: The histogram of debris discs masses from our population synthesis calculations in Model 1, in which fraction $\zeta = 1/250$ of the fragment's metal content is released back into the disc as large solid debris bodies. As expected from fig. 3.3, metal-rich stars (red histogram) host more DD systems but they are less massive on average compared with DDs around metal-rich stars (blue).

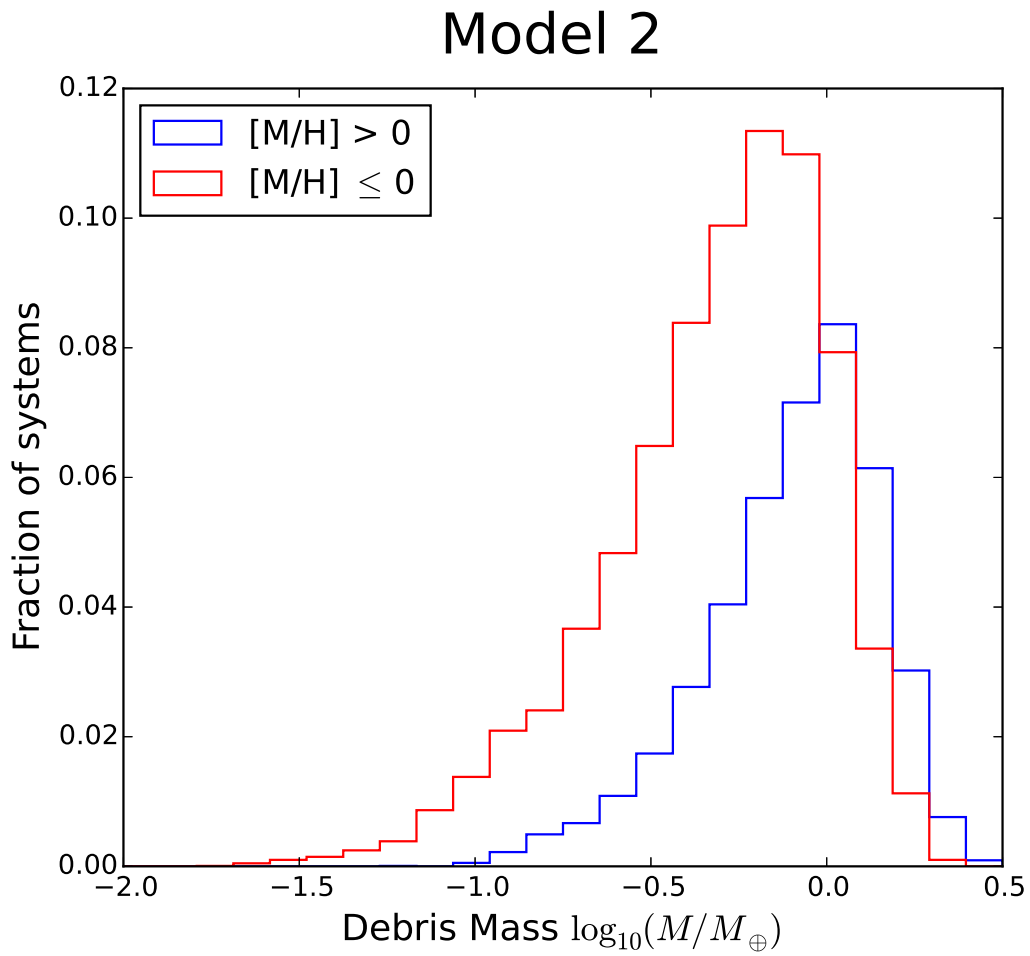


FIGURE 3.5: Same as fig. 3.4 but for Model 2, in which the mass of the debris released is equal to 1/10 of the core. Note that qualitatively the result is the same: metal rich systems produce \sim two to three times more debris mass than their lower metallicity brethren.

Model 1 metallicity distributions

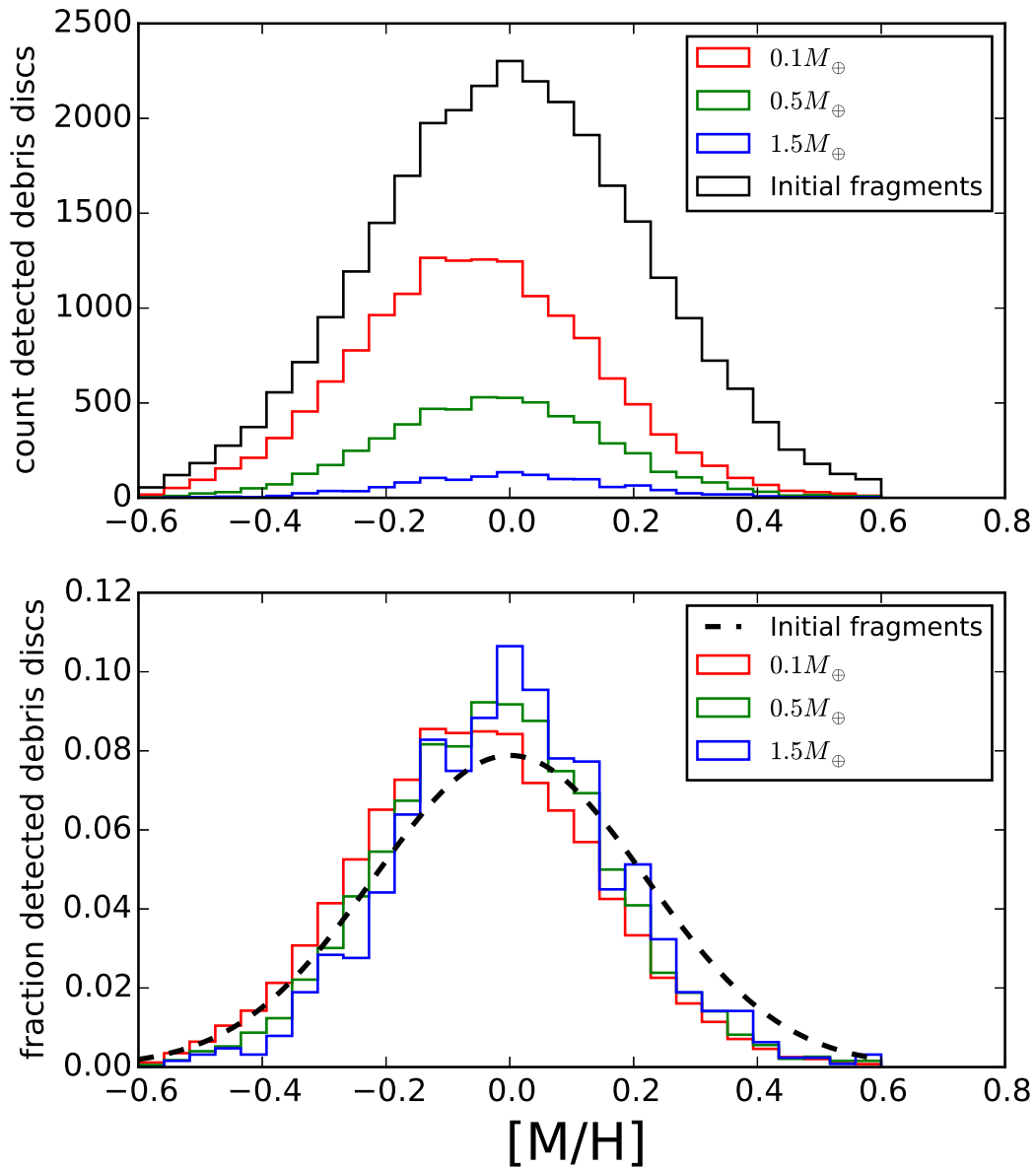


FIGURE 3.6: The distribution of the detectable debris discs over metallicity of the host for Model 1 and three detection values of detection threshold, $M_{\text{det}} = 0.01M_{\oplus}$, $0.05M_{\oplus}$ and $0.15M_{\oplus}$, as indicated in the legend. The green histogram shows the initial fragment distribution over metallicities. The top panel shows the absolute number of systems whereas the bottom panel shows the histograms normalised to the integral of unity.

Model 2 metallicity distributions

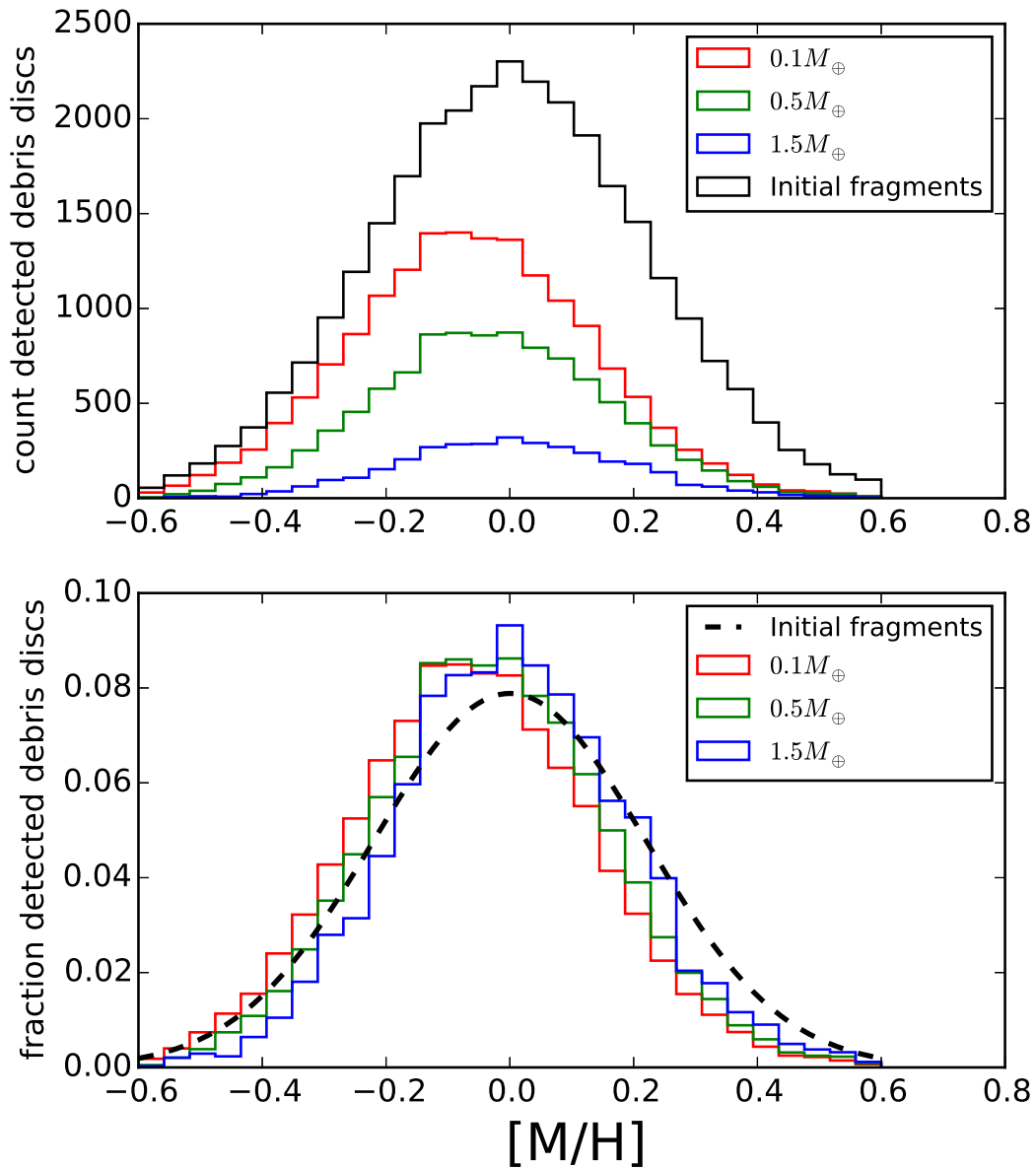


FIGURE 3.7: Same as figure 3.6 but for Model 2, in which the mass of the debris is given by given by 1/100 of the core's mass.

The main conclusions from fig. 3.6 are: (1) the metallicity distribution for the detectable debris discs is similarly broad to that of the host stars, with only mild skewness; (2) the shift in the $[M/H]$ distribution of debris disc hosts is to lower metallicities at low detection threshold and toward higher metallicities for larger values of M_{det} . These results are natural in the context of the discussion in §3.4. At low $[M/H]$, more gas fragments are disrupted, but they have a relatively low metal content. Gas fragments at higher $[M/H]$ are disrupted rarely but they contain more metals. Therefore, if debris detection threshold is low, the debris disc population will be dominated by the metal-poor part of the population. In the opposite case, rare but metal-rich disruptions at higher $[M/H]$ are the main contributors.

Fig. 3.7 shows a similar calculation but now assuming that the mass of the debris is 1/10 of the core (Model 2 in §3.3.2). It is pleasing to see that main results are hardly changed from those obtained with Model 1, suggesting that the insensitivity of the debris mass to the host star metallicity that we find here is robust. Since Model 2 is nevertheless more physically complete as discussed in §3.3.2, we shall continue our analysis based on just this model.

Fig. 3.8 summarises these results in terms of probability that a host star of a given metallicity will have a detectable debris disc for the three detection limits considered. The trends discussed above are clearly visible but depend quite strongly on the sensitivity of our toy synthetic observation model. A sensitive observation would have a low M_{det} , so would detect debris discs mainly around low $[M/H]$ stars, as seen from the red histogram. Brighter debris discs reside around increasingly more metal rich stars. The middle value for M_{det} shows in fig. 3.8 hardly any preference for $[M/H]$ of the host. However, at the highest value for M_{det} considered, one finds debris discs only around high $[M/H]$ stars.

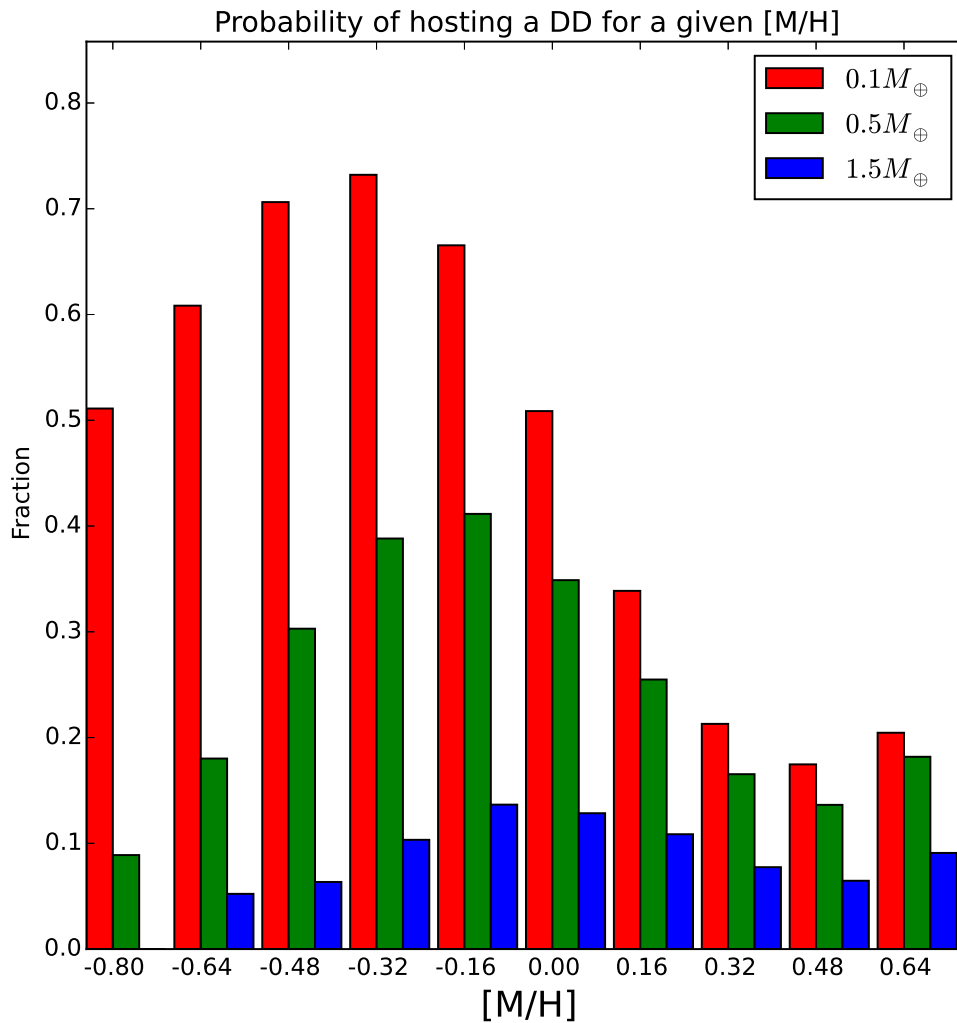


FIGURE 3.8: Probability for a star of given metallicity to host a detectable debris disc for three values of M_{det} (cf. eq. 3.3), as specified in the legend. Note that sensitivity of our toy synthetic observations model (the value of M_{det}) affect the prevalence of DDs as a function of metallicities.

This is qualitatively consistent with the results of Moro-Martín et al. (2015) who found a lack of bright debris discs around low metallicity hosts.

We suggest that one should not read too much into the normalisation of debris disc mass in our plots. Our synthetic observation model can be at best described as a toy model, and the detection limits chosen are arbitrary. Furthermore, here we considered just one fragment migrating per star, but in reality one may expect a dozen to form per lifetime of the disc (e.g., see simulations by Vorobyov and Basu, 2006; Boley et al., 2010; Cha and Nayakshin, 2011). However, we believe that the metallicity trends obtained here will remain qualitatively the same in a more sophisticated analysis with many migrating fragments just because they are based on the simple robust physics explained in section 3.4 – to get the debris one needs to disrupt a gas fragment, and that is more frequent at low $[M/H]$.

3.5.3 Planet - debris disc relations

Gas giants

In our single migrating fragment simulations, just by the nature of the solid debris's origin, there cannot be a correlation between the presence of a debris disc and the presence of a gas giant. In fact, there is an anti-correlation: if a gas giant survives then it implies that no debris was released in a tidal disruption of a fragment. Clearly, in a multi-fragment situation the result is more complicated. For example, fragments born early on may migrate more rapidly and be disrupted, producing solid debris. Fragments appearing closer to the end of the disc's life may be migrating in slower and hence may survive. Hence one may have detectable giant planets and solid debris in this picture, but we see no reason to expect that a positive correlation between gas giants and planetary debris will arise.

The most likely outcome is that debris disc presence will remain anti-correlated with the presence of gas giants.

While multi-fragment simulations will have to be explored in the future for a confirmation of this qualitative assessment, it is encouraging that the anti-correlation trend between gas giants and the debris discs is consistent with the observations. Marshall et al. (2014) finds that stars with observed gas giant planets are twice less likely to host debris discs as opposed to stars with lower mass ($M_p \leq 30 M_\oplus$ planets).

Sub-giant planets

The single migrating fragment scenario also predicts a one-to-one correlation between the presence of debris and lower-mass planets in TD, that is those that were formed by a disruption of a gas fragment. However, finite detectability of the debris discs and the planets themselves will weaken this correlation.

To explore this quantitatively, we consider all the simulations that resulted in formation of a planet with mass $3 M_\oplus < M_p < 30 M_\oplus$ which we call sub-giants, with separation $a < 5$ AU. Now, considering just this population alone, we calculate the fraction of these systems that host a detectable debris disc (setting $M_{\text{det}} = 10 M_\oplus$) in the context of Model 2, as a function of the host's metallicity. The result is plotted in fig. 3.9 with the blue squares.

The blue curve is to be compared with the red asterisks curve which shows probability of a star (without any other additional constraints) to host a detectable DD (calculated with the with same value of M_{det}). It is notable that the population of stars that host sub-giant planets are more likely to host a DD, by about a factor of two, than the "field stars". Thus our model does predict a correlation between sub-giant planets and DDs, although it is far weaker than the one-to-one

relation that is appropriate *if all the debris discs and all the sub-giant planets*, irrespective of their mass and separation, are considered. We may also expect a further reduction in the strength of the correlation in multi-fragment systems and also due to post-evolution of planetary and DD populations, which may see some of these be thrown out from the stellar system or destroyed in collisions (for DDs). Future more sophisticated modelling is needed to address these issues. Nevertheless, predictions of TD appear to be broadly consistent with the weak (if any) *positive* correlation of observed sub-Saturn planets with DDs (e.g., Wyatt et al., 2012; Moro-Martín et al., 2015).

3.5.4 Preliminary comparison to observations

Fig. 3.10 shows how the cumulative fraction of systems with a DD or a planet is distributed over metallicity of the host stars, $[M/H]$. The top panel shows the results of this paper, whereas the bottom panel shows the data from Moro-Martín et al. (2015).

The red histograms show the distribution of gas giants over $[M/H]$. In both the simulations and the observations these distributions are shifted towards higher metallicity. In TD, gas giants prefer high metallicity environments because pebbles (large grains) are more abundant at high $[M/H]$, fuelling a higher pebble accretion rates onto gas fragments. Higher pebble accretion rates allow the fragments to collapse more rapidly (Nayakshin, 2015a), so that a greater fraction of fragments born in the outer cold self-gravitating disc can reach the inner disc avoiding tidal disruption (Nayakshin, 2015b).

The blue histogram in the top panel of fig. 3.10 shows our theoretical debris disc distribution over $[M/H]$, which is broad and has no obvious preference for high metallicity environs. The low panel of the figure shows that observations

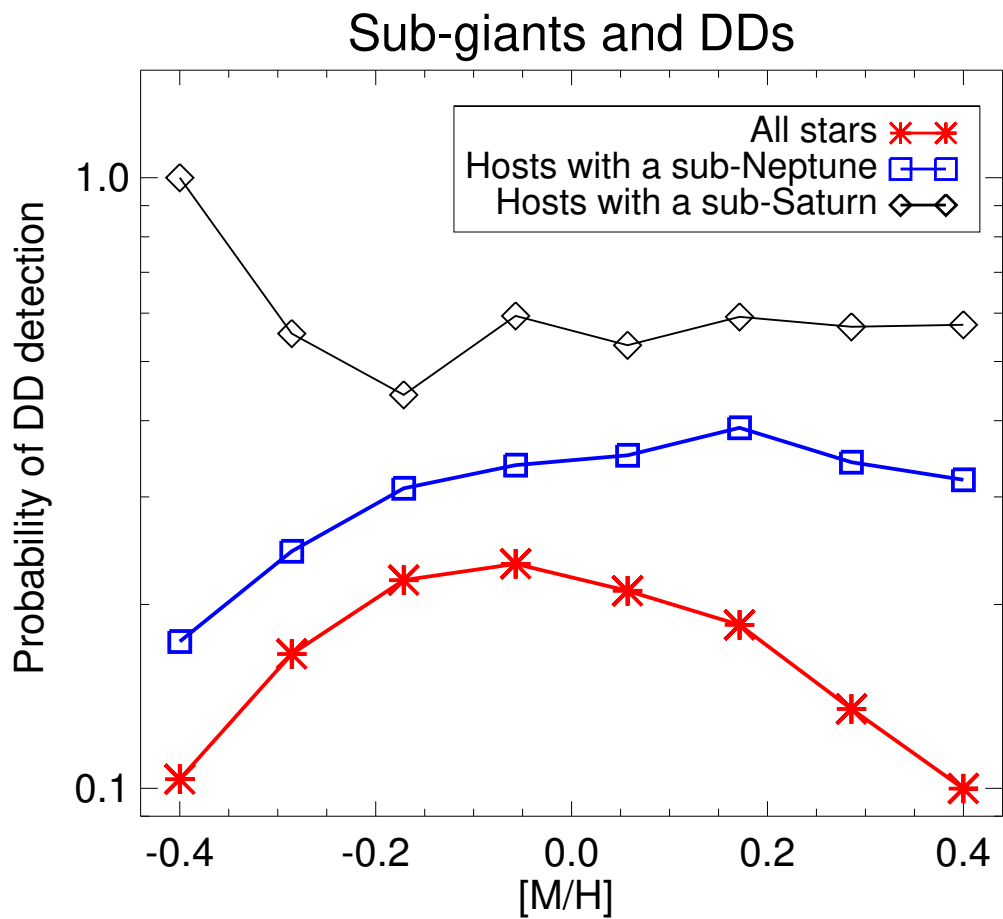


FIGURE 3.9: Probability of a star with a given metallicity $[M/H]$ hosting a detectable debris discs for all stars (red asterisks) and for stars that also host a sub-giant mass planet ($3 M_{\oplus} < M_p < 30 M_{\oplus}$ and $a < 5$ AU, shown with blue squares). Presence of a sub-giant planet in the inner disc increases the chances that a detectable DD will be also present.

show a similar trend for debris discs. Numerous previous observations confirm the insensitivity of DDs to the metallicity of the host star (e.g., Maldonado et al., 2012; Marshall et al., 2014). Our results are hence qualitatively consistent with these observations.

The fact that the frequency of detection of super-Earths is also weakly dependent on $[M/H]$ is well known (Mayor et al., 2011; Howard et al., 2012) and is evident in the bottom panel of fig. 3.10. TD reproduces this result (see the green histogram in the top panel of the figure) with physics already discussed above: at low $[M/H]$, gas fragment disruptions are much more frequent than at high $[M/H]$ but release less massive cores due to the relative scarcity of metals inside the fragments. This has been discussed previously in Nayakshin and Fletcher (2015).

3.6 Discussion

3.6.1 Planetesimal hypothesis

The planetesimal hypothesis (Safronov, 1972) is very deeply rooted in the field of planet formation, underlying the very base of the Core Accretion theory (Hayashi, Nakazawa, and Nakagawa, 1985; Pollack et al., 1996; Alibert et al., 2005). It is usually assumed that debris discs around nearby stars and the asteroid and the Kuiper belts in the Solar System are the evidence that the planetesimal hypothesis is essentially correct.

However, the factual basis for this conclusion is actually *no longer* there. In the absence of TD theory, the only way to make rocky planets, the smaller bodies in the Solar System and the DDs around nearby stars is indeed Core Accretion, and statements of the type “If planetesimals did not form, we would not be here” are

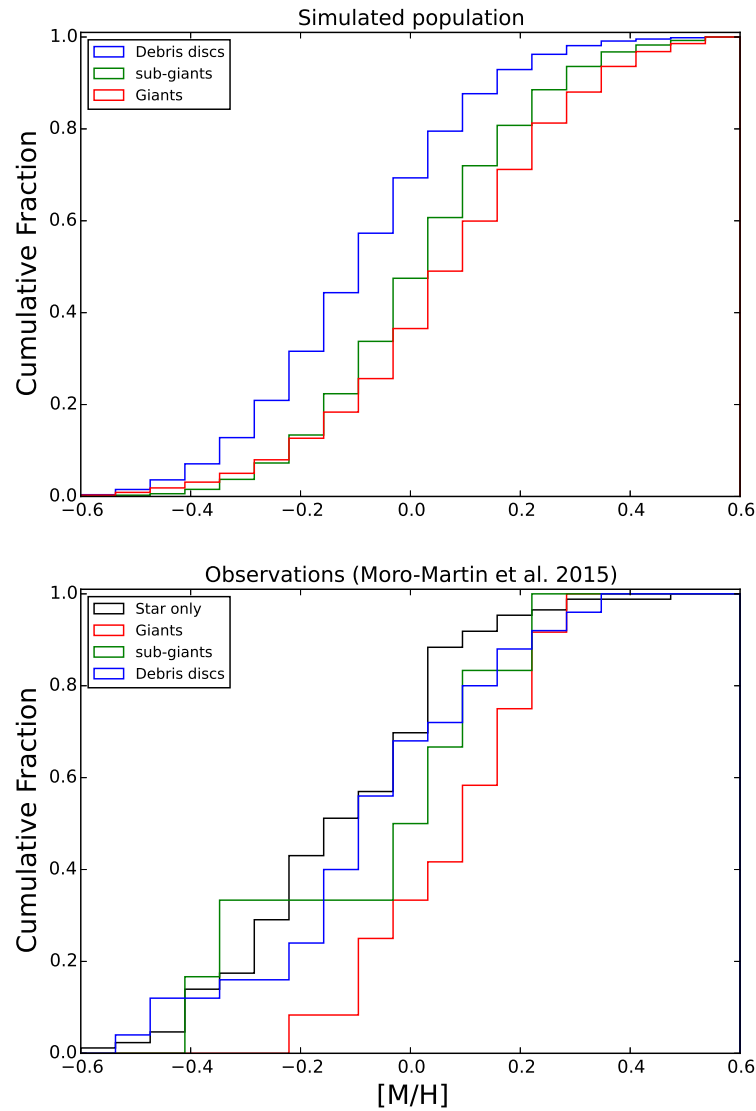


FIGURE 3.10: **Top panel:** the cumulative frequency distributions for DD, sub-giant and giant planets over metallicity of the host star obtained from our population synthesis calculations. See the legend for the meaning of the histograms. **Bottom panel:** data from a survey of nearby stars searching for DDs and planets (Moro-Martín et al., 2015). Gas giant planets are clearly offset towards higher metallicity hosts in both the data and the simulations. Debris discs and sub-giant planets do not correlate with metallicity of the host.

a fair point to make (Wetherill, 1990). However, TD scenario can now account for both giant and rocky planets (e.g., Nayakshin and Fletcher, 2015) in an alternative way not requiring planetesimals to be born before the planets are. Nayakshin and Cha (2012) have also shown that in TD, minor solid bodies can be released from disrupted gas fragments and form debris rings not unlike those making up the asteroid and the Kuiper belts, and the DDs elsewhere.

Observations of DDs may be used to differentiate between the CA and TD scenarios for the origin of the minor solids and their connection to planets. In this paper we have made a first step towards this goal.

3.6.2 Main findings

We found that trends in the debris disc mass with metallicity of the host star and with the likelihood of having a planet of a given type are very different in TD scenario from those of CA model. This implies the debris discs present us with a sensitive diagnostic of planet/debris formation theories.

The overarching result of our calculations is that the same physical effect – pebble accretion – can explain all of the observed metallicity correlations of planets *and* debris discs in the context of TD. In particular,

1. Higher $[M/H]$ hosts provide higher pebble accretion rates onto the fragments, causing them to collapse faster. This results in the larger fraction of gas fragments surviving tidal disruption and yielding a strong positive correlation between gas giants survived in the inner disc and the metallicity of the host (Nayakshin and Fletcher, 2015).

2. The corollary to this is that few gas fragments are tidally disrupted at high $[M/H]$, hence making debris ring formation events relatively rare compared to low $[M/H]$ hosts. This explains why debris discs in TD cannot monotonically correlate with metallicity of the host star. The resulting DD correlation depends on the observational sensitivity of DD survey and can range from an anti- to a weak positive correlation (cf. fig. 3.8).
3. The presence of a detected gas giant planet around a star implies that the fragment from which the planet originated did not go through a tidal disruption. In a single migrating fragment scenario, this would mean that gas giants and debris discs would be mutually exclusive. However, in a more realistic multi-fragment scenario, fragments other than the one that produced the observed giant planet could undergo tidal disruptions and produce debris. Therefore, we expect some anti-correlation between gas giants and DDs rather than a full incompatibility of the two populations.
4. Planets less massive than \sim Saturn mass are also a result of tidal disruptions in the TD theory. Therefore, there should be a correlation between such planets and the DD presence (see fig. 3.9). As explained in §3.5.3, this correlation is one-to-one for a single fragment but may be diluted in a multi-fragment disc.

3.6.3 Comparison to observations

Our results, summarised in the list in §3.6.2, are broadly consistent with the available observations:

1. Gas giant planets are well known to correlate with $[M/H]$ of their host stars (Gonzalez, 1999; Fischer and Valenti, 2005). This is usually attributed to the

larger abundance of planetesimals in high metallicity discs (Ida and Lin, 2004b; Mordasini et al., 2009). However see next point.

2. Debris discs do not correlate with $[M/H]$ of the host star, instead being abundant at all metallicities. Our results are consistent with this prediction for a DD detection threshold of M_{det} above $\sim 0.05 M_{\oplus}$ (see fig. 3.8).
3. It came as a considerable surprise that DDs do not correlate with the presence of gas giant planets (Moro-Martín et al., 2007; Bryden et al., 2009; Kóspál et al., 2009). In CA, these planets require the most metal-rich massive gas discs which are expected to have more massive debris discs left behind. In our scenario, however, DDs are expected to anti-correlate somewhat with gas giant's presence. Moro-Martín et al. (2015) finds that stars with detected gas giants are about twice less likely to host a debris disc than stars with smaller planets, showing that gas giants indeed tend to discourage DD formation.
4. It is currently not clear due to the limited statistics whether DDs correlate with the presence of less massive planets (Moro-Martín et al., 2015). However, some DD samples did show a weak correlation between DDs and low mass planets (Wyatt et al., 2012). This would be consistent with our calculations. More observations are needed to ascertain the correlations of DDs and planets better.

3.6.4 Predictions for future observations

Although our calculations were performed for a fixed mass of the star, $M_{*} = 1M_{\odot}$, we can speculate how these results may depend on the mass of the star. Assuming that initial fragment mass increases with the mass of the host star, we

would expect relatively more disruptions of gas fragments at lower M_* because low mass fragments are more susceptible to those disruptions than higher mass fragments (Nayakshin and Fletcher, 2015). We would therefore expect more debris per star around stars less massive than $1M_{\odot}$ and less debris per star around more passive stars.

This is currently at odds with relative dearth of detected debris discs around low mass stars (e.g., Plavchan et al., 2009), but this may be an artefact of current surveys which are biased towards hotter earlier type stars (see Introduction in Choquet et al., 2015). Future observations should shed more light on the DD frequency trend with host star's mass.

3.7 Conclusions

Given the rarity of gas giant planets, the fact that presence of a giant at ~ 1 AU distance from the star somehow discourages formation of debris discs at distances of tens to hundreds of AU from the star is puzzling in the context of Core Accretion theory for planet formation (§3.2.2). Non-correlation of DD presence with the host metallicity is also mysterious. The most well known success of CA theory, the prediction of the positive gas giant – host star's metallicity correlation, assumes (Ida and Lin, 2004b; Mordasini et al., 2009) that planetesimals are born much more readily at high $[M/H]$.

In contrast, in TD the presence of a gas giant a few AU distance from the star signals that at least this fragment, born at ~ 100 or more AU from the star, was able to migrate inward all this distance without being tidally disrupted. This also means that the fragment did not release any large solids that it could have synthesised inside, thus making the presence of a debris disc less likely. A sub-giant planet observed in the inner disc, however, has been made by a disruption of a

gas fragment further out and then migrated in (Nayakshin and Fletcher, 2015), so that planet may signal that some debris has actually been produced. While multi-fragment discs will weaken these strong predictions (see §3.5.3), we still expect some antipathy between DDs and gas giants, as observed, whereas sub-giant planets should correlate to some degree with DD presence. Furthermore, as tidal disruptions are less likely at high $[M/H]$, our model naturally explains why DDs do not correlate with host star's metallicity.

Future observations of DDs in different environs and their links to planets should help differentiate CA and TD scenarios for planet and debris formation.

3.8 Additional information

Fig. 3.11 and 3.12 show a breakdown of the separation and mass histograms for the exoplanet data.

Fig. 3.11 shows planets separation with the panels showing different mass bins. The top panel of fig. 3.11 shows the highest mass planets; these include Hot Jupiter's. The large number of very low separations is primarily due to observational bias; the peak is emphasised as a result of the Kepler mission easily detecting many high mass low separation planets. The middle panel is the intermediate mass range and the bottom panel shows the low mass range. The bottom panel is poorly populated due to the few planets with low mass that have all the available data; such as mass, separation, metallicity and solar properties. These are all needed to make a comparison with the simulated data. Fig. 3.12 shows the same data set but now displaying the planet mass with separation bins. The top panel shows large separations, but again is under populated due to the data being incomplete for many of the planets in this range. The other two panels are better populated and some trends can be seen. In the middle panel the lack

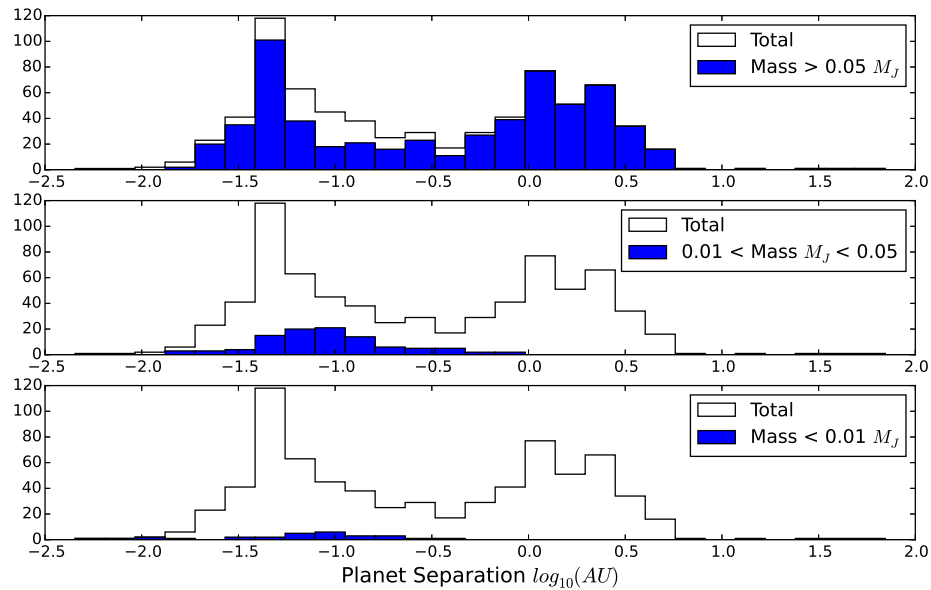


FIGURE 3.11: The figure shows the log of exoplanet separation in AU, the top panel is for high mass planets, mass greater than $0.05 < M_J$, the middle panel shows planets of mass $0.01 \leq M_J \leq 0.05$, the bottom panel shows low mass planets $M_J < 0.01$.

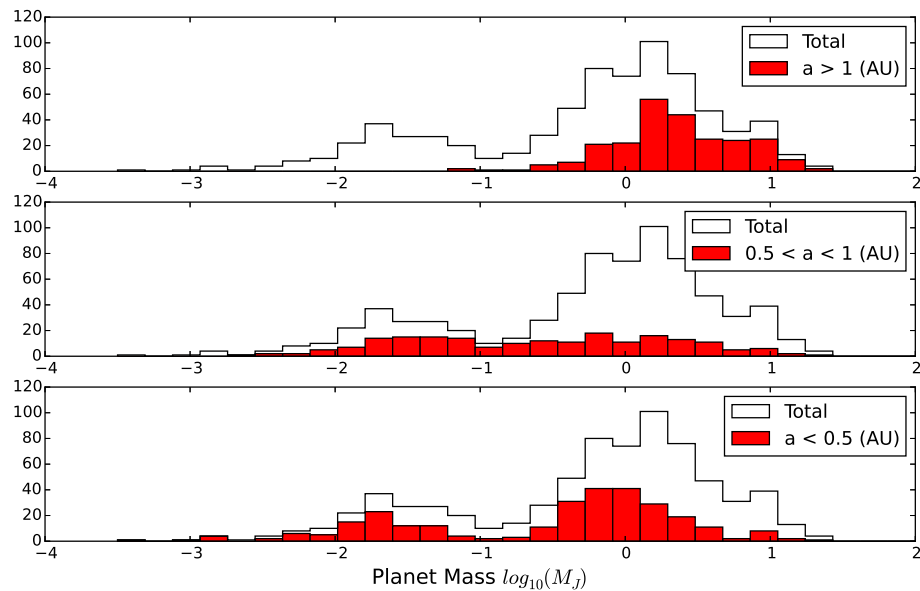


FIGURE 3.12: The figure shows the histogram of log of exoplanet mass in M_J . The mass have been separated into three separation bins. The top panel shows $a > 10(AU)$, the middle panel shows $3.16 \leq a(AU) \leq 10$, and the bottom panel shows $a < 3.16(AU)$

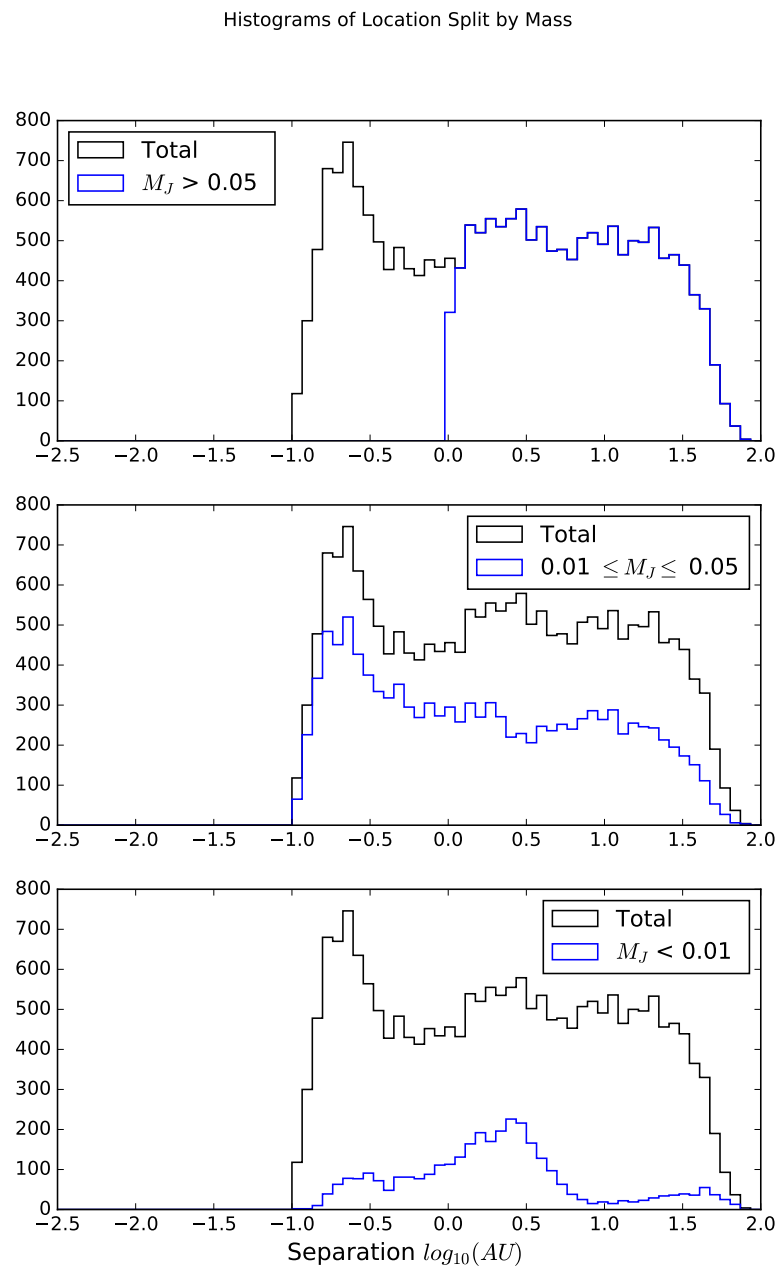


FIGURE 3.13: The figure shows the log of the simulated population of planets separation in AU, the top panel is for high mass planets, mass greater than $0.05 < M_J$, the middle panel shows planets of mass $0.01 \leq M_J \leq 0.05$, the bottom panel shows low mass planets $M_J < 0.01$.

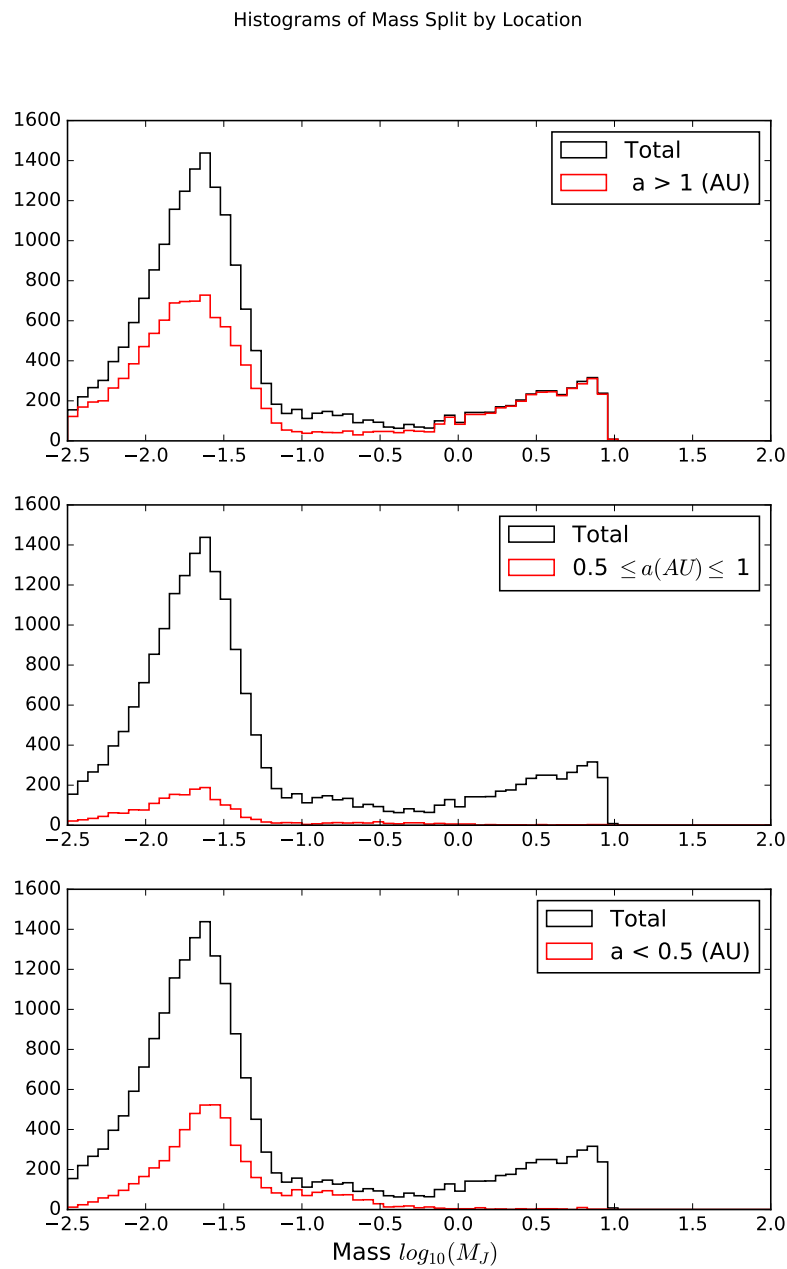


FIGURE 3.14: The figure shows the histogram of log of the simulated population mass in M_J . The mass have been separated into three separation bins. The top panel shows $a > 10(\text{AU})$, the middle panel shows $3.16 \leq a(\text{AU}) \leq 10$, and the bottom panel shows $a < 3.16(\text{AU})$

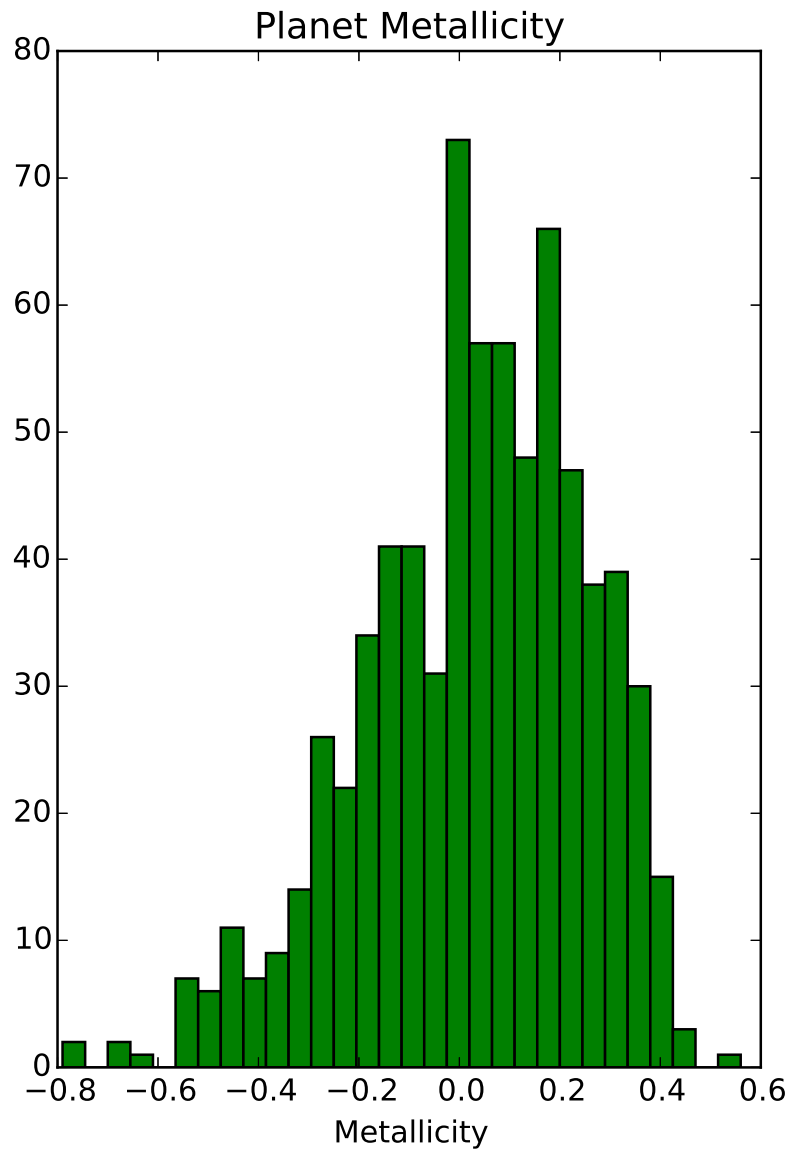


FIGURE 3.15: The figure shows the histogram of metallicity of the planets; this is based on the stellar metallicity which is approximately a Gaussian for the local group.

of high mass planets can be seen; this separation range covers the period valley discussed earlier. For small separations, the bottom panel of fig. 3.12, a bimodal distribution can be seen peaking at approximately a Jupiter mass and in the super Earth mass range.

Fig. 3.13 and 3.14 show the population synthesis data in the same break down as the observed planet population in fig. 3.11, 3.12. Firstly, the absolute numbers are vastly different from one to the other due to the simulated population being far more numerous. In Fig. 3.13 there is a sharp cut off at 0.1 AU partially due to the inner edge of the our computational domain and the rapid migration timescale in that region means planets do not stay in that region for long and therefore less likely to stop there.

Fig. 3.15 shows the metallicity of the observed stars, it reflects an approximate Gaussian function, which is slightly skewed towards the positive metallicities. This allows us to justify the initial conditions for the population synthesis model discussed later. The limited data sample makes analysis more difficult; although many new planets have been found due to the range in observational techniques only a few have all the information required to compare to the simulated data.

Chapter 4

Giant planets and brown dwarfs on wide orbits: a code comparison project

4.1 Chapter abstract

Gas clumps formed within massive gravitationally unstable circumstellar discs are potential seeds of gas giant planets, brown dwarfs and companion stars. Competition between three processes – migration, gas accretion and tidal disruption – establishes what grows from a given seed. Numerical simulations and population synthesis calculations published to date however do not always agree on the outcome. Here we investigate if the codes PHANTOM, GADGET, SPHINX, SEREN, GIZMO-MFM, SPHNG and FARGO give the same answer when faced with the same migrating clump setup. Four tests with varying assumptions about the initial clump mass and gas accretion onto it are performed. We find that the codes disagree in the clump migration rate by between 10% to $\sim 50\%$, depending on the test, but always arrive in the same qualitative picture. Specifically, with

gas accretion turned off, planets migrate through the whole effective computational domain. In contrast, our most massive planets with gas accretion on open deep gaps and stall at separation of order 80 AU. We find that the artificial viscosity treatment and the sink particle prescription may account for much of the differences between the codes. We also attempt to reproduce the planet evolution tracks from our hydrodynamical simulations with prescriptions from three population synthesis studies. We find that the disagreement amongst the population synthesis models is far greater than that between our hydrodynamical simulations.

4.2 Introduction

Secondary star formation via gravitational instability (GI) of massive circumstellar discs has now been observed by ALMA (Tobin et al., 2016) and may be a viable explanation for the high frequency and the host metallicity correlations of stellar binaries with separations less than tens of AU (Moe, Kratter, and Badenes, 2018). Modern star formation simulations (Bate, 2018) and observations of young discs (Tychoniec et al., 2018) also indicate that massive large gas discs could be abundant.

The conditions for disc fragmentation (Gammie, 2001; Rafikov, 2005) are similar to those for forming first hydrostatic cores in star formation (Larson, 1969), implying that the masses of gas clumps born in the discs must be initially similar to those of the opacity-limited fragments, e.g., $\sim 5 - 10 M_J$ (Low and Lynden-Bell, 1976; Rees, 1976; Masunaga, Miyama, and Inutsuka, 1998), although both smaller and larger initial clump masses were considered in the literature (Boley et al., 2010; Kratter, Murray-Clay, and Youdin, 2010; Forgan and Rice, 2013a). Due to these uncertainties and due to strong clump evolution after formation via inward migration (Mayer et al., 2004; Vorobyov and Basu, 2005; Machida, Inutsuka, and Matsumoto, 2011; Baruteau, Meru, and Paardekooper, 2011), gas accretion (Zhu et al., 2012a; Stamatellos, 2015; Mercer and Stamatellos, 2017) and tidal disruption (Boley et al., 2010; Nayakshin, 2010a), it is difficult to predict when and how often disc fragmentation leads to the formation of planets (Kuiper, 1951a), brown dwarfs (Stamatellos and Whitworth, 2008; Stamatellos and Whitworth, 2009) or secondary stellar companions (Kratter, Murray-Clay, and Youdin, 2010).

The scale of uncertainty in this problem is immense and affects our understanding of even the most basic questions, especially in the theory of planet formation. Direct imaging surveys show that the occurrence rate of wide separation

(tens of AU or more) planetary mass companions to FGK stars, and also brown dwarfs, is just a few % (Biller et al., 2013; Chauvin et al., 2015; Reggiani et al., 2016; Vigan et al., 2017). This is much smaller than $\gtrsim 50\%$ observed planet occurrence rate at separations less than a fraction of AU from the star (see chapter 2 in Winn and Fabrycky, 2015). One interpretation of this result is that gravitational disc instability rarely makes planetary-mass objects (Kratter, Murray-Clay, and Youdin, 2010; Forgan and Rice, 2013a; Rice et al., 2015; Vigan et al., 2017). On the other hand, if radial migration and tidal disruption transmogrify planetary mass gas clumps into short period planets, including sub-Neptune mass planets (Boley et al., 2010; Nayakshin and Fletcher, 2015), then the rate at which GI fragmentation forms planetary-mass clumps could be much higher; the resulting planets are simply not where they were born.

Furthermore, there is now observational support that at least some initially widely separated objects end up at sub-AU separations from the star, presumably due to disc migration. The frequency of appearance of planets more massive than ~ 4 Jupiter masses and brown dwarf companions to stars do not correlate with the host star metallicity (Raghavan et al., 2010; Troup et al., 2016; Nayakshin, 2017b; Santos et al., 2017), indicating that these objects probably did not form by Core Accretion (which predicts an opposite correlation, see Mordasini et al., 2012). Additionally, the properties and statistics of very strong episodic flaring of young protostars, known as FU Ori outbursts (Hartmann and Kenyon, 1996), are consistent with stars tidally disrupting and devouring (Vorobyov and Basu, 2006; Takami et al., 2018) up to a dozen gas clumps per lifetime.

There are many physical uncertainties in the physics of the problem, e.g., disc opacity (Meru and Bate, 2010), initial conditions for disc fragmentation (Vorobyov and Basu, 2010; Zhu et al., 2012a), treatment of gas cooling close to and inside the

Hill sphere of the planet (Nayakshin and Cha, 2013; Stamatellos, 2015; Mercer and Stamatellos, 2017), dust growth and dynamics inside the clump, which may strongly affect clump cooling and heating balance (Helled and Bodenheimer, 2011; Nayakshin, 2016), etc.

However, in addition to this, different simulation codes use different numerical algorithms to model the same processes, and it is not clear if applying these codes to the same problem will yield identical results. The goal of this chapter is evaluate how the simulation results differ between some commonly used numerical codes. To focus on this issue alone, we set up a physically simple test problem of a gas giant planet embedded in a massive gas disc at an initial separation of 120 AU. The disc cooling is treated with the widely used idealised β -cooling prescription (Gammie, 2001; Rice, Lodato, and Armitage, 2005).

To disentangle various effects, we perform four comparison runs. The initial planet mass is set to $M_{p0} = 2 M_J$ in three of the runs and to $M_{p0} = 12 M_J$ in the fourth. As explained above, gas accretion onto the gas clumps is an integral part of the problem. Therefore, in two of the $M_{p0} = 2 M_J$ runs we turn off gas accretion onto the planet, setting instead a relatively large gravitational softening length parameter to reduce the amount of gas flowing into the gravitational potential well of the planet (as was also done by Baruteau, Meru, and Paardekooper, 2011). In the other two comparison runs, a sink particle prescription is used to absorb the gas accumulating at the planet location.

The chapter is structured as follows. In §4.3 we describe the physical setup and initial conditions of the problem, and describe the contributing codes. In §4.4 we present main results of this work. A comparison of the results to population synthesis prescriptions is made in §4.5, and in §4.6 we discuss observational implications of this work.

4.3 Problem and numerical detail

4.3.1 Contributing codes

There are five 3D SPH codes that we compare here: PHANTOM (Price et al., 2017), GADGET (Springel, 2005), SPHINX (Dehnen and Aly, 2012), SEREN (Hubber et al., 2011a; Hubber et al., 2011b), and SPHNG (Benz, 1990). The Meshless Finite Mass code GIZMO (Hopkins, 2015) builds on SPH methods and adds a kernel discretization of the volume, coupled to a high-order matrix gradient estimator. The GIZMO-MFM numerical scheme has a higher order consistency and appears to overcome some of the numerical viscosity issues in SPH, and has been recently shown to reproduce the expected convergence of the critical cooling timescale for fragmentation (see Deng, Mayer, and Meru, 2017), which has been hard to achieve with SPH methods previously (e.g., Meru and Bate, 2010). Finally, FARGO is a 2D fixed cylindrical grid finite differencing code (Masset, 2000) which has been widely used for studies of planet migration and has shown consistency with analytical solutions in the linear regime applicable to much lower mass planets (e.g., Baruteau and Masset, 2008) than studied here.

4.3.2 Problem choice

The potential formation of gas giant planets via gravitational instability of protoplanetary discs (e.g., Kratter and Lodato, 2016) motivates our study. To this end, all of our runs use a massive gas disc with initial mass $M_{\text{init}} = 0.2M_{\odot}$ as an initial condition for all of our runs. The disc is in circular rotation around a star with mass $M_{*} = 1M_{\odot}$. At fragmentation, the disc Toomre (1964) Q -parameter is $Q \lesssim$ (e.g., Boley et al., 2010). Such discs generate spiral density arms. Interactions of the planets with the arms give stochastic velocity kicks to the planets

(e.g., Baruteau, Meru, and Paardekooper, 2011). In addition, fragmenting discs usually hatch more than one gas clump. Clump-clump interactions also lead to angular momentum exchange between the clumps (Cha and Nayakshin, 2011) and even mergers (Hall, Forgan, and Rice, 2017). These processes are stochastic and make numerical simulations of planet migration with different codes susceptible to small numerical detail.

To avoid this stochasticity, we simplified the task at hand by choosing the parameters of the problem such that the Toomre parameter of the disc is slightly larger than expected at fragmentation, i.e., $Q \gtrsim 2$ everywhere, which makes the disc gravitationally stable. We then inject a planet into the disc and follow its evolution numerically. It is clearly desirable to extend the code comparison in the future in the regime in which the disc is free to fragment and form more clumps.

An ideal gas equation of state is used in this work with the adiabatic index $\gamma = 7/5$, as appropriate for diatomic gas. The star irradiates the disc and sets the minimum irradiation temperature, which is a function of radius R :

$$T_{\text{irr}} = T_0 \left(\frac{R}{R_0} \right)^{-1/2}, \quad (4.1)$$

where $T_0 = 20$ K and $R_0 = 100$ au. The irradiation temperature corresponds to the specific internal energy,

$$u_{\text{irr}} = \frac{k_B T_{\text{irr}}}{\mu(\gamma - 1)}, \quad (4.2)$$

where $\mu = 2.45m_p$ is the mean molecular weight of the gas.

The radiative cooling of the disc is modelled with the β -cooling prescription widely used in the literature to model marginally stable self-gravitating discs (e.g., Rice, Lodato, and Armitage, 2005). The irradiation from the central star is additionally present as a heating term, so that the specific internal energy of

the gas, u , evolves according to

$$\frac{du}{dt} = -\frac{u - u_{\text{irr}}}{t_{\text{cool}}}, \quad (4.3)$$

where $t_{\text{cool}} = \beta \Omega_{\text{K}}(R)^{-1}$,

$$\Omega_{\text{K}}(R) = \left(\frac{GM_*}{R^3} \right)^{1/2} \quad (4.4)$$

We use $\beta = 10$ for the runs presented below. This value of β is comparable to the critical fragmentation β for $\gamma = 7/5$ as found by Rice, Lodato, and Armitage (2005), although recent simulations with GIZMO-MFM suggest that disc fragmentation may occur at lower β (e.g., Deng, Mayer, and Meru, 2017) for this code. However, the inclusion of external irradiation will also likely lead to fragmentation happening for lower values of β (Rice et al., 2011).

4.3.3 Initial conditions

We first describe the initial conditions for the SPH codes and GIZMO-MFM. The star is treated as a sink particle that accretes any SPH particles that enter inside the sink radius, $R_{\text{sink}} = 3$ au. The gravitational softening of the star is set at $h_g = 0.25$ au. The disc is initially set up with the surface density profile

$$\Sigma_{\text{in}}(R) = \frac{M_{\text{d}}}{2\pi R(R_{\text{out}} - R_{\text{in}})} \quad (4.5)$$

where $R_{\text{in}} = 10$ au and $R_{\text{out}} = 300$ au are the inner and the outer initial disc radii, respectively. The disc is relaxed for about 10 orbits at the outer edge before the planet is inserted. This is done to allow the disc to settle into a vertical hydrostatic

balance and to damp out radial disc oscillations. During the disc relaxation procedure, a small fraction ($\sim 3\%$) of the SPH particles are accreted onto the central star. This is inevitable due to artificial viscosity of the disc increasing in regions of lower particle number, which is usually near the inner disc boundary.

These initial conditions, after the relaxation procedure was applied, are presented in fig. 4.1. The top panel shows the gas column density multiplied by radius, e.g., $\Sigma(R) \times (R/100 \text{ AU})$ and the vertically averaged gas temperature profile $T(R)$. Both of these are compared to the respective column density and temperature profiles before the relaxation (blue dashed curves). We see that both the inner and the outer regions of the disc are depleted by the relaxation process, but that the region between $R \sim 30 \text{ AU}$ and $R \sim 200 \text{ AU}$ has a smooth $\Sigma \propto 1/R$ profile. The gas temperature profile is very close to equation 4.1, except for radii $R \lesssim 20 \text{ AU}$ where the artificial viscosity heating is not negligible. Since our relaxed disc has a strong roll-over at radii smaller than $R \sim 30 \text{ AU}$, we expect that the planet migration process in this numerical setting will be strongly affected at radii of about 40 AU. The bottom panel of Fig. 4.1 presents the disc aspect ratio H/R normalised to 0.1 and the Toomre Q -parameter. As stated in the Introduction, the disc is everywhere stable to self-gravity and does not fragment.

For FARGO, the initial conditions were obtained in the same physical setup but the code was relaxed for 50 orbits at the outer edge.

In the simulations presented below, time is counted from the relaxed initial condition shown in Fig. 1. We inject the planet instantaneously at $t = 0$ on a prograde circular orbit centred on the star at the initial separation of $R = 120 \text{ AU}$. No change is made to the initial velocity of either the gas or the star. Note that for $M_{p0} = 2 M_J$, the planet mass is only 1% of the disc mass and just 0.2% of the total mass of the system, so this approach is justifiable. While for the $M_{p0} = 12 M_J$

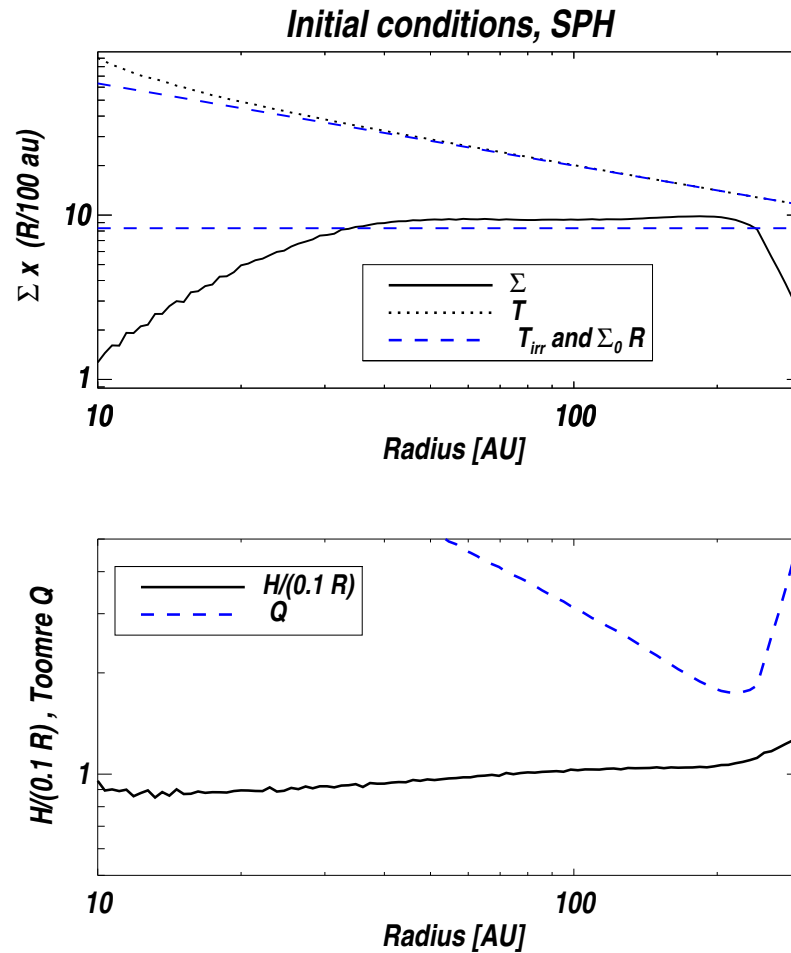


FIGURE 4.1: Initial (relaxed) conditions for all of the SPH runs presented here. **Top:** disc surface density, plotted as $\Sigma \times (R/100 \text{ AU})$, and the temperature profiles. The disc inward of $\sim 30 \text{ AU}$ is strongly affected by the sink (star) particle inner boundary condition. **Bottom:** The ratio of the disc vertical scaleheight H to $0.1R$ (solid) and the Toomre parameter Q .

simulation the error is larger, we prefer this approach because keeping the planet orbit fixed while increasing its mass slowly (a common approach in studies of low mass planet migration) would lead to undesirable modifications of the disc structure for our problem. For example, as found by Malik et al. (2015), the gap opening criterion should include a gap-opening time scale. If the planet migrates across the gap sooner than the gap could be excavated, no gap is opened. However, keeping the planet on a fixed orbit implies an infinite source of angular momentum and therefore may result in the planet opening a gap in the disc where none should be present.

4.3.4 Approach to code algorithm differences

Numerical hydrodynamics codes, whether particle or grid based, employ different numerical algorithms to integrate equations of motions, various time-stepping criteria, and approximate techniques to resolve contact discontinuities such as shocks and singularities arising in the gravitational potential and forces near point masses (Bodenheimer et al., 2007). For example, by default GADGET uses the Monaghan (1997) form of the artificial viscosity with the Balsara-Monaghan switch to reduce artificial viscosity in shear flows (Monaghan, 1992; Balsara, 1995), and the spline kernel for SPH (for details see Springel, 2005). More modern formulations of artificial viscosity exist and different SPH kernels are adopted by some of the other codes (see §4.4.4). It is possible to modify GADGET to use the same approaches. However, it is not possible in practice to modify all of the codes to employ exactly the same numerical algorithms due to significantly different intrinsic code designs. Additionally, such code alterations would defeat the purpose of our code comparison project as the codes actually being compared would then be different from their current community-used versions.

Therefore, we attempted no code modification in this project with only a few exceptions that relate to the most salient physics of the problem. For each test problem presented below, all of the codes use the same gravitational softening parameters and the accretion radii for the two sinks in the problem, as detailed further below. The sections below discuss the implementation of sink particle accretion, gravitational softening and artificial viscosity in the codes used in this chapters work.

GADGET

Our implementation of GADGET is very similar to the code description given in the instrument paper by Springel (2005), with a few changes detailed below. GADGET uses the spline kernel (Monaghan and Lattanzio, 1985) for both the SPH density field and computing the gravitational softening around all particles, including the sink particles. We use 40 particles for the neighbour search. The artificial viscosity of SPH is that given by the Monaghan-Balsara formulation (Gingold and Monaghan, 1982; Balsara, 1995), modified by the viscosity limiter prescription (see eq. 11 in Springel, 2005) to alleviate unwanted angular momentum transport in the presence of shear flows. We follow the default GADGET settings in this work, keeping the artificial viscosity coefficient α_v set to 1 for all times, and $\beta_v = 2\alpha_v$.

The sink particles are implemented in a very simple way. Any SPH particle that is separated from the sink by a distance smaller than the accretion radius R_a is accreted by the sink. The linear momentum and mass of the accreted particle are added to that of the sink. Some authors consider more complicated gas accretion criteria. For example, Bate, Bonnell, and Price (1995b) consider the expected pressure of the gas within the sink region and the binding energy of the

gas with respect to the sink. However, there is much physical uncertainty in picking these additional gas accretion criteria. The sink radius defines the region of space where we have insufficient information (usually, no information at all) about the gas properties. The interactions of that missing gas with the SPH particle in question could change the properties of the latter in ways that cannot be computed. For example, an SPH particle on a hyperbolic trajectory around the sink is formally not bound to the sink and thus would not be accreted if one accretes only particles with negative binding energies (Bate, Bonnell, and Price, 1995b). However, the same particle may be accreted if the particle were to interact with the missing gas within the sink radius, shock due to this interaction, and then lose the excess energy through radiation.

For further discussion of these issues and tests of our GADGET implementation of the sink particle prescription, see Cuadra et al. (2006) and Humphries and Nayakshin (2018). Nayakshin (2017a) found that the sink radius prescription tends to over-estimate the gas accretion rate onto a planet embedded in a massive gas disc for simulation parameters comparable to those used here (see Fig. A1 in Nayakshin, 2017a). Gas accretion rates measured in this chapter should be thus taken as upper limits to the corresponding astrophysical problem.

PHANTOM

Cullen and Dehnen (2010) introduced an artificial viscosity switch which utilizes the derivative of the velocity divergence to detect shocks. Due to the switch, the artificial viscosity coefficient α_v is varied between a minimum value, α_{\min} , far from the shock, and the maximum, $\alpha_{\max} = 1$, reached close to the shock. We use this method for PHANTOM, as described in detail in §§2.2.7-2.2.9 in Price et al. (2017). We fix the artificial viscosity coefficient β_v at 4 for our comparisons

runs (see Price and Federrath, 2010). An exception to this is §4.4.4 where we explore how results depend on the choices of the artificial viscosity prescription for PHANTOM.

Gravitational softening in PHANTOM is different for interactions between sinks and interactions between sinks and SPH particles. The sink-sink softening is set to 0 by default. The sink-gas gravitational softening length is the maximum between the fixed softening length of the sink and the gas particles adaptive softening length. Gravity for SPH particles is softened by the SPH kernel function (see §2.12.2 in Price et al., 2017).

Compared to GADGET, the PHANTOM default sink particle implementation also sets constraints on the binding energy and relative angular momentum of the SPH particle to be accreted. For these tests we disable these additional checks and use the same approach as specified in §4.3.4.

SPHINX

SPHINX is an SPH code based on a conservative formulation (as derived from a variational principle, e.g. Price 2012) with individual artificial dissipation strengths α_v adapted using the Cullen and Dehnen (2010) switch with $\beta_v = 2\alpha_v$. The details of the artificial viscous force differ slightly (by an amount $O(h^2)$) from traditional implementations to accommodate the one-sweep SPH algorithm, which avoids separate sweeps over all particle neighbours for the density and force computations. For the runs here, we use the Wendland (1995) C^2 smoothing kernel, which scales as $w \propto (h-r)^3(h+3r)$ for $r < h$ with smoothing length h , adjusted to obtain $N_h = 4\pi\rho h^3/3m = 80$ at each time step. Gravity is computed using a C^∞ softening kernel with density $\propto (r^2 + h_s^2)^{-7/2}$, which results in a smaller

force bias than traditional Plummer softening (Dehnen, 2001). Individual softening lengths ϵ are scaled to the smoothing lengths h such that the estimates for the gas and gravitating mass densities are mutually consistent (have the same bias). SPHINX uses an oct-tree for neighbour search (and gas-selfgravity which is computed using the fast multipole method Dehnen 2000) and the leap-frog (2nd order symplectic) time integrator. Star and planets are represented by sink particles, whose gravity is computed by direct summation. Any gas particle within one sink radius is accreted by a sink particle, whereby its mass, linear and angular momentum, as well as energy is absorbed by the sink particle (which carries a spin and internal energy for this book keeping).

SPHNG

SPHNG is based on the version developed by (Benz, 1990) and first presented by (Bate, Bonnell, and Price, 1995b). It uses variable individual smoothing lengths h_j and adjusts them so that the number of nearest neighbours for any particle is 50 ± 20 . It also uses individual particle time-steps to simulate dense regions with sufficient precision while avoiding over-simulation of less dense regions, and integrates the particles using a second order Runge-Kutta scheme. The standard artificial viscosity (Monaghan, 1992), with $\alpha_v = 1.0$ and $\beta_v = 2.0$, and standard spline kernel are used. A binary tree is used to calculate neighbour lists and to determine gravitational forces between gas particles, with the gravitational force softened by the SPH kernel function (Price et al., 2017). The gravitational force between the gas particles and the sink particles is, however, done using a direct calculation, which is softened by replacing the $1/r^2$ gravitational force dependence with $1/(r^2 + h_s^2)$. If accretion onto the sink particles is allowed, then particles are only accreted if they are bound and if the specific angular momentum

of the particle is less than that required for them to form a circular orbit at the accretion radius (Bate, Bonnell, and Price, 1995b).

GIZMO

The GIZMO code is a multi-method code which inherits the tree-based gravity algorithm from GADGET3 (see Springel, 2005, for GADGET2 code description) and couples it with different Lagrangian hydrodynamical solvers. We employ the Meshless Finite Mass (MFM) hydro method in GIZMO which solves the inviscid fluid equations by partitioning the computational domain using volume elements associated with a particle distribution, and computing fluxes through the volume ‘overlap’ by means of a Riemann solver as in finite volume Godunov-type methods (Hopkins, 2015). Volume elements are constructed via convolution integrals with kernel functions analogous to those adopted in SPH. Owing to the use of a Riemann solver (here we use the HLLC solver and the minmod slope limiter), GIZMO-MFM employs no explicit artificial viscosity. This numerical method appears significantly less dissipative than SPH for differentially rotating flows, better conserving angular momentum and vorticity (Hopkins, 2015; Deng, Mayer, and Meru, 2017). The kernel for the volume partitioning, the gravitational softening and the sink particle implementation are all identical to those of GADGET (§4.3.4).

SEREN

The SPH code SEREN was developed for star and planet formation simulations by Hubber et al. (2011b) and Hubber et al. (2011a). The code uses an octal tree to compute gravity and find neighbours, multiple particle timesteps, and a 2nd order Runge-Kutta integration scheme. To simulate the effect of physical viscosity

in discs, SEREN uses a time-dependent artificial viscosity (Morris and Monaghan, 1997) with parameters $\alpha_{\min} = 0.1$, $\alpha_{\max} = 1$ and $\beta_v = 2\alpha_v$, so as to reduce artificial shear viscosity away from shocks (this scheme is the predecessor of the Cullen and Dehnen, 2010, method). Sink particles, which interact with the rest of the computational domain only through their gravity, are used to represent the central star and the planet (Bate, Bonnell, and Price, 1995a). Gas particles accrete onto a sink when they are within the sink radius and bound to the sink (see Hubber et al., 2011a). Once gas particles are accreted, their mass and linear angular momentum is added to sink. The gravitational force between gas particles and a sink is found through a direct calculation and softened according to $1/(r^2 + h_s^2)$ to avoid unphysically large gravity forces.

FARGO

FARGO is a 2D grid based, staggered-mesh code (Masset, 2000; Baruteau and Masset, 2008) that has been used extensively to study planet migration (Masset, 2002; Masset and Casoli, 2010; Baruteau, Meru, and Paardekooper, 2011). For the runs presented here, we use a cylindrical grid with 508 and 1536 cells in the radial and azimuthal directions, respectively. The radial grid is logarithmic with the inner and outer boundary conditions set at 10 and 300 AU, respectively. Von Neumann–Richtmyer artificial bulk viscosity is used to treat contact discontinuities (Stone and Norman, 1992).

For these runs, FARGO also uses a fixed gravitational softening parameter h_s as for all the other codes, which is a break with the common practice of scaling h_s with the local disc scaleheight or the star-planet separation (e.g., Baruteau, Meru, and Paardekooper, 2011), but allows for a more uniform comparison between the codes. Specifically, the softening parameter used in grid simulations is typically

set to $h_s = \epsilon H$ where $\epsilon \sim O(0.1)$ (Müller, Kley, and Meru, 2012). In this case the gravitational softening would be a function of position as $H \propto R$ for our simulations (see fig. 4.1). The consequences of this for numerics are not immediately obvious, but we note that for $\epsilon = 0.1$ and $H \sim 0.1R$, the adaptive softening is equivalent to $h_s = 0.4 - 1.2$ AU in the radial range 40-120 AU, which is not too dissimilar from the 1 AU and 2 AU fixed smoothing employed in Runs 1 and 2 (see below). For a relatively large fixed value $\epsilon = 0.7$ we find that the FARGO migration timescales increase by $\approx 50\%$ compared to those presented here.

4.3.5 The comparison runs

It is possible to resolve the pre-collapse gas giant planets (clumps) in modern computer simulations directly (e.g., Boley et al., 2010; Galvagni et al., 2012; Zhu et al., 2012b; Nayakshin, 2017a; Hall, Forgan, and Rice, 2017). However, while the clumps can be resolved and modelled from the point of view of hydrodynamics, other physics, e.g., a proper equation of state including molecular hydrogen internal degrees of freedom, dust dynamics and radiative transfer, are not yet implemented in most of the codes available to us here. Any simplified radiative transfer scheme applied to the clumps would necessarily over-simplify their internal physics (their cooling balance is significantly different from that of the disc; e.g., see Vazan and Helled, 2012) and would thus be riddled with its own uncertainties. A more prudent approach for us to follow here is to model the planet as a sink particle, just as the star, albeit with its own gas accretion (sink) radius.

Table 4.1 shows the parameters that distinguish the four different comparison runs that are presented below. In Runs 1-3, the initial planet mass is set to $M_{p0} = 2 M_J$, whereas Run 4 starts with $M_{p0} = 12 M_J$. In Run 1 and 2, gas accretion onto the sink is completely turned off by setting the accretion radius to zero.

TABLE 4.1: The parameters distinguishing the Runs presented in this work. R_a , h_s , and M_{p0} are the sink accretion radius, the gravitational softening parameter, and the mass of the planet, respectively. All the other parameters and initial conditions are the same for all four Runs.

Run	R_a (AU)	h_s (AU)	M_{p0} (M_J)
Run 1	0.0	1	2
Run 2	0.0	2	2
Run 3	0.5	0.01	2
Run 4	1.0	0.01	12

This is done to try to isolate the effects of planet migration versus gas accretion onto the planet. This is especially important since FARGO is a grid based code in which implementation of gas accretion is drastically different from the sink particle method of SPH codes. Therefore, Runs 1 and 2 can be simulated with SPH codes and FARGO, whereas Runs 3 and 4 are done with SPH only.

Turning off gas accretion onto a planet does not come free of numerical cost. Gas that gets bound to the planet may eventually get very close to the planet. A very high gas density around the planet is numerically challenging as the SPH particle time step becomes too short for the code to execute effectively. Therefore, to avoid that, in Runs 1 and 2 the planet softening radius, h_s is increased to 1 and 2 AU, respectively, from the much smaller value used in Run 3. For a similar reason Run 4 uses a larger accretion radius than Run 3.

The initial SPH particle number is $N = 10^6$ for all of the runs presented here.

4.3.6 Analytical expectations

Tanaka, Takeuchi, and Ward (2002) derived an analytical expression for type I migration of a low mass planet in an isothermal disc. The migration timescale, defined as

$$\tau = \frac{R}{|\dot{R}|}, \quad (4.6)$$

where \dot{R} is the rate of change of planet-star separation due to gravitational torques from the disc, is given by

$$\tau_{\text{iso}} = (2.7 + 1.1\lambda)^{-1} \frac{M_{\star}}{M_p} \frac{M_{\star}}{\Sigma_p r_p^2} \left(\frac{c_s}{r_p \Omega_p} \right)^2 \frac{1}{\Omega_p}. \quad (4.7)$$

Here λ is the exponent of the surface density power law, $\Sigma \propto R^{-\lambda}$, Σ_p is the surface density at the planet location, M_{\star} and M_p are the star and planet masses, respectively, r_p is the planet-star separation, c_s is the gas sound speed at the planet and Ω_p is the planet Keplerian angular velocity. For the initial parameters of our disc and $M_p = 2 M_J$, we obtain a migration time scale of $\tau_{\text{iso}} = 14.6 \times 10^3$ yr. Even though our discs are not isothermal, the results of Tanaka, Takeuchi, and Ward (2002) are widely used, and serve as a useful comparison for us.

Baruteau, Meru, and Paardekooper (2011) used the 2D code FARGO to study planet migration in very massive self-gravitating discs, for which the Toomre parameter Q self-regulates to a value between ~ 1.5 and ~ 3 over a broad range of radii. These authors also offered an analytical expression for the migration time scale:

$$\tau_{\text{sg}} \approx \frac{5.6}{(3.8 - \lambda)} \gamma Q_p \frac{h_p^3}{q} \left(\frac{0.1}{h_p} \right)^2 \frac{2\pi}{\Omega_p}, \quad (4.8)$$

where $q = M_p / M_{\star}$ is the mass ratio; Q_p is the Toomre parameter and $h_p = H/R$ at the planet position. For the initial parameters of our Runs 1-3, eq. 4.8 yields $\tau_{\text{sg}} = 5.0 \times 10^3$ yr at a separation $R = 120$ AU.

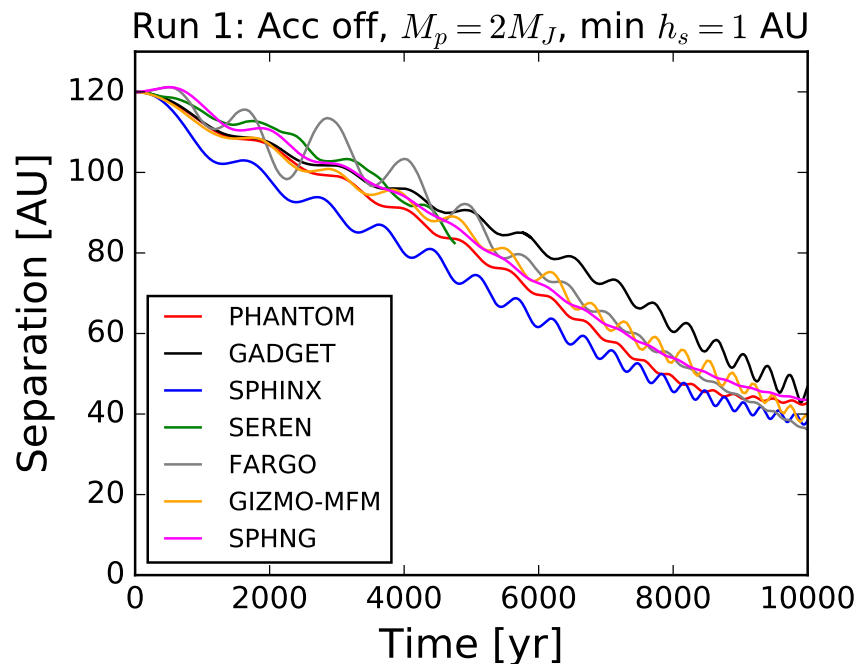


FIGURE 4.2: Planet separation versus time for Run 1. These do not allow the planet to gain mass from the disc, so the sink mass is fixed at $M_{p0} = 2 M_J$.

4.4 Results

4.4.1 At a glance

Fig. 4.2 and 4.3 shows the planet separation against time for Runs 1 & 2. To recap, gas accretion onto the planet is off, and instead a relatively large gravitational softening parameter is used. Despite this, some gas accumulates deep inside the Hill sphere, and differently so for different codes. This appears to be the primary reason why Runs 1 and 2 stalled for SEREN at around 5000 yr. Fig. 4.4 and 4.5 shows the results of Runs 3 & 4 (left and right panels, respectively) in which gas accretion onto the planet (sink particle) is allowed. The sink mass versus time is shown in the lower panels.

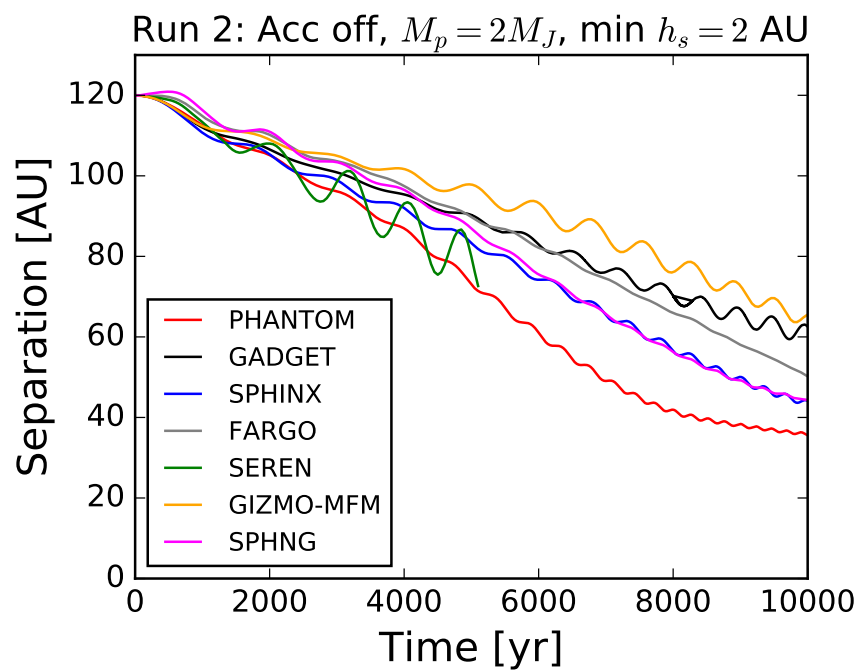


FIGURE 4.3: Planet separation versus time for Run 2. These do not allow the planet to gain mass from the disc, so the sink mass is fixed at $M_{p0} = 2M_J$.

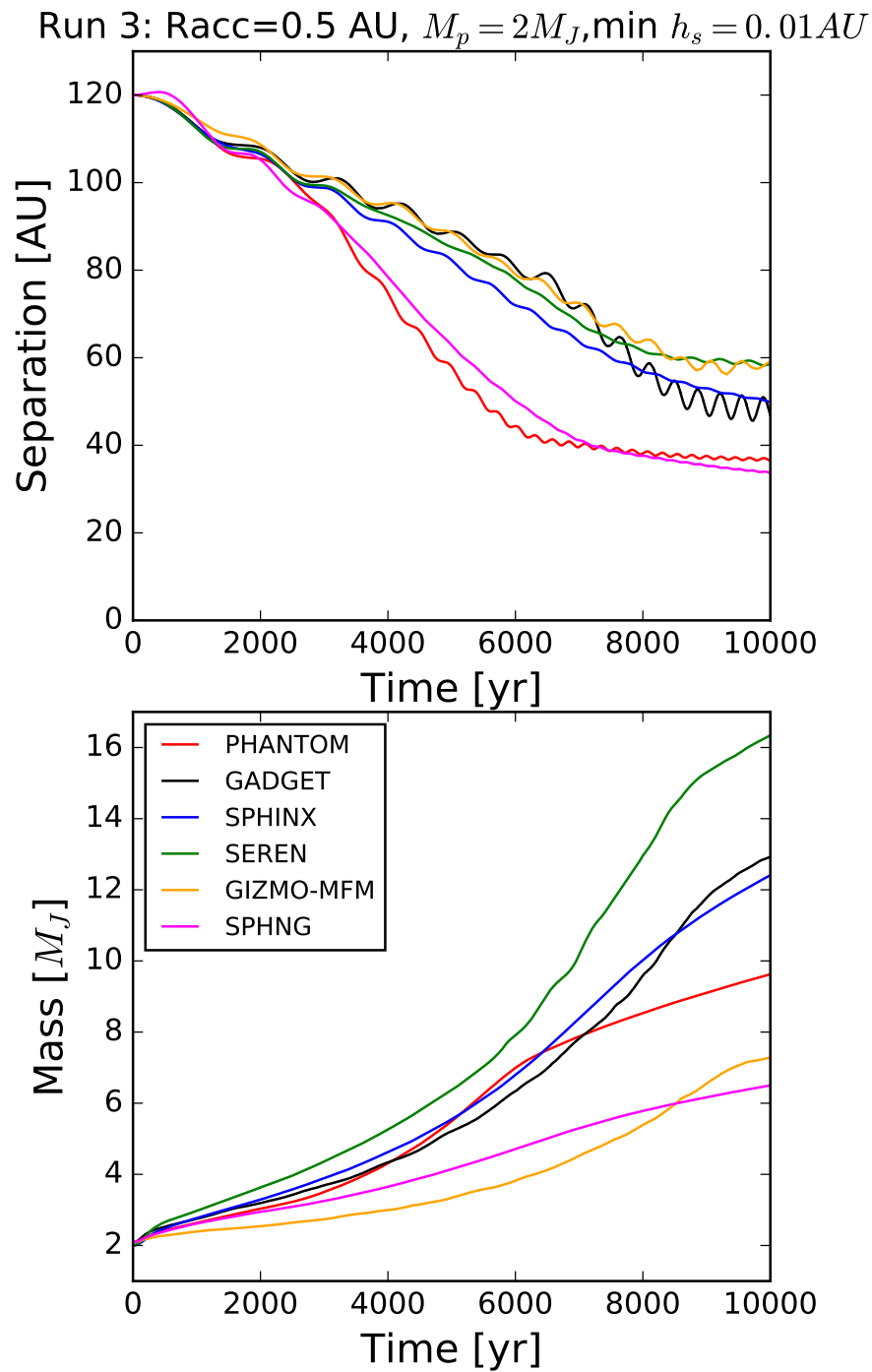


FIGURE 4.4: Planet separation (top panel) and sink particle mass (lower panel) versus time for Runs 3.

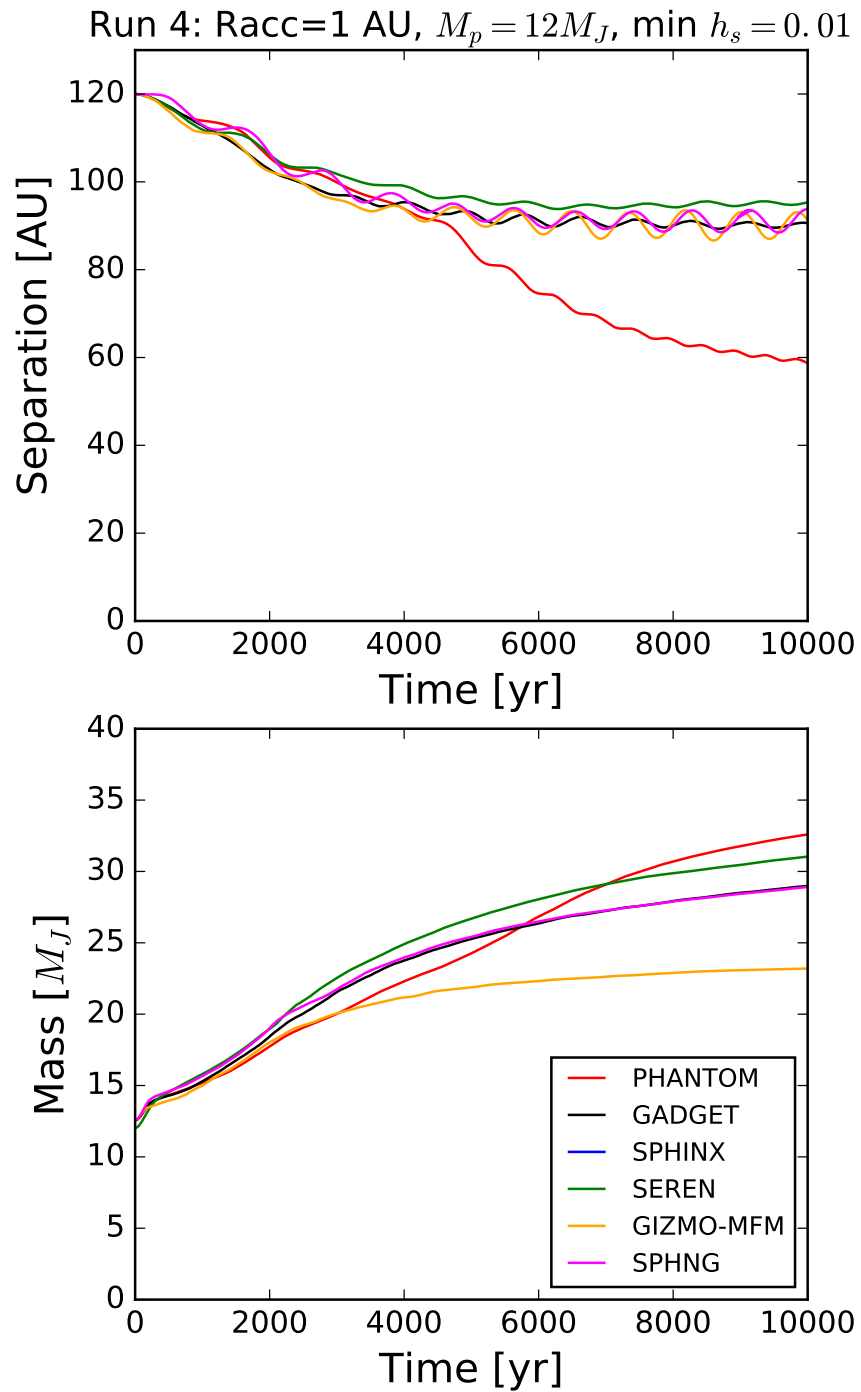


FIGURE 4.5: Planet separation (top panel) and sink particle mass (lower panel) versus time for Runs 4.

A cursory look at figs. 4.2, 4.3, 4.4 & 4.5 shows that there is a general *qualitative* agreement between the different codes. For example, in Runs 1-3 the planet manages to migrate to separations of 40 – 60 AU for most of the codes, whereas in Run 4, in which the planet is much more massive, the planet stalls further out due to it opening a deep gap in the disc. At the same time, there are significant *quantitative* disagreements between the codes. All of the codes show that the planet develops orbital eccentricity, but the actual value of the eccentricity is different, varying between ~ 0.01 to the maximum of ~ 0.1 .

4.4.2 Analysis of runs 1-3

Migration rates

We now analyse Runs 1-3 in which the planet initial mass is $M_{p0} = 2 M_J$. To aid quantitative analysis, we determine migration time scale, τ , from the simulations. A straight-forward use of eq. 4.6 to calculate τ from the simulation data is ill advised due to planets having non-zero eccentricity: the instantaneously defined migration time varies significantly over a fraction of the planet orbital timescale. Some sort of time averaging of τ over times at least as long as an orbital period is thus needed.

To do so, we first define a time-dependent migration rate as the final difference $\Delta R/\Delta t$, where the separation and time differences are counted from the initial values:

$$\dot{R}(t) = \frac{R(t) - R_0}{t}, \quad (4.9)$$

where $R_0 = R(t = 0) = 120$ AU, $t > 0$ is time, and $R(t)$ is the planet-star separation at that time. To remedy the oscillatory behaviour in \dot{R} due to finite

orbital eccentricity, we define an orbit-averaged quantity

$$\dot{\bar{R}}(t) = \frac{1}{T_p} \int_{t-T_p/2}^{t+T_p/2} \dot{R}(t') dt', \quad (4.10)$$

where T_p is the planet orbital period at location $R(t)$. We use this definition to define the planet migration rate after $t = 4,000$ yr for all of the codes, which we label τ_4 . We then also define the migration time scale τ_7 , following the procedure outlined above, but using the data between 4,000 and 7,000 yrs. Comparison of τ_4 and τ_7 tells us how the migration rate varies as the planet gets closer to the star. Due to a non zero planet orbital eccentricity a finer time-resolved analysis of the migration rate does not appear well justified.

Fig. 4.6 compares the migration time scales τ_4 and τ_7 (left and right panels, respectively) for all the codes for Runs 1-3, which are shown with the coloured symbols. The dashed and solid horizontal lines show the migration timescales given by eq. 4.7 and 4.8, respectively. These analytical estimates of τ are computed using the initial disc properties (see fig. 4.1).

Taking the full range of τ_4 and τ_7 values, we see that they vary by a factor of 3 – 4 between the different codes for Runs 1 & 2, and by a smaller factor of ~ 2 for Run 3. For τ_4 , the mean of the migration time scales are closer to the Tanaka, Takeuchi, and Ward (2002) expression, but for τ_7 the mean lies between the analytical estimates of Tanaka, Takeuchi, and Ward (2002) and Baruteau, Meru, and Paardekooper (2011). The range in the migration time scales is similar to the factor of ~ 3 difference between these two analytical results. We also note that τ_4 is longer than τ_7 for most of the runs, implying that migration of the planet accelerates somewhat as the planet gets closer to the star (as long as it remains in the Type I). The same trend is predicted by the formulae shown in equations 4.7 and 4.8. We conclude from fig. 4.6 that there is a qualitative agreement not only

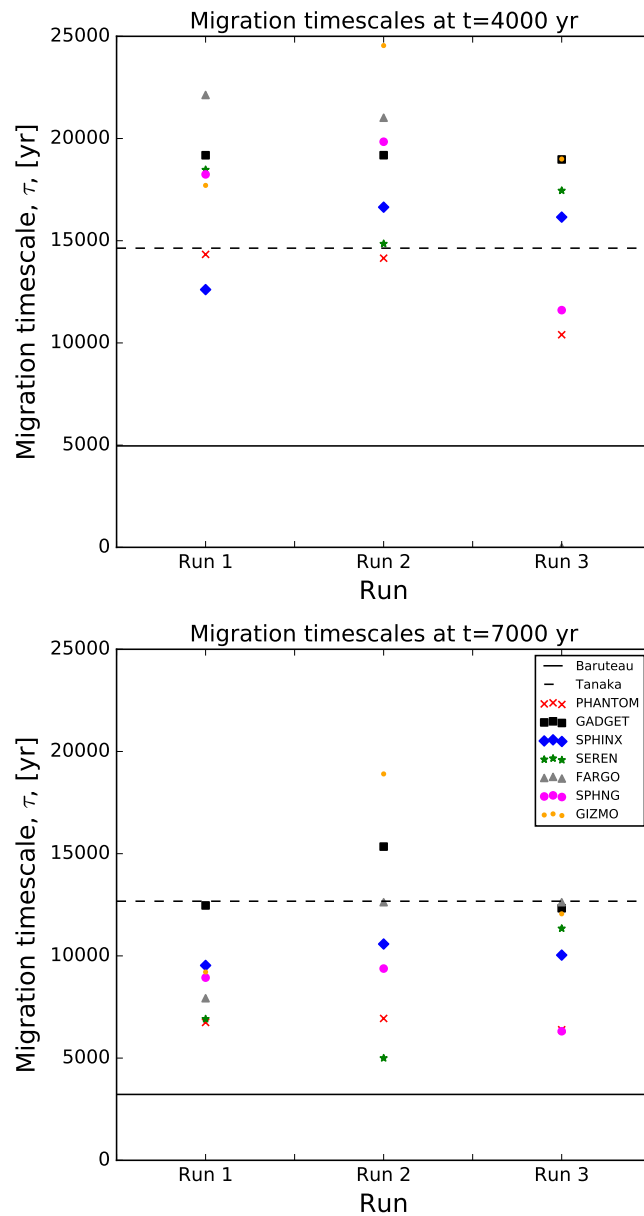


FIGURE 4.6: Migration time scales for all codes for Runs 1-3 are shown with the coloured symbols, calculated for time intervals between 0 and 4,000 years (**Top panel**) and between 4,000 and 7,000 years (**Bottom panel**). The dashed and solid horizontal lines show the analytically computed migration times given by eqs. 4.7 and 4.8, respectively. The SEREN results do not appear for run 2 on the right panel since the code did not progressed to the 7000 year point.

between the different codes but also with the theory.

Comparing Runs 1 and 2, we note that the migration timescales vary by $\sim 10\%$ for most of the codes whereas h_s changes by a factor of two. However, for SEREN the difference the two runs is larger, and is in the opposite sense compared with most of the other codes. This is likely due to a non linear interplay of how gravitational softening affects gravitational torques vs planet accretion. To make further progress we must consider the role of planet accretion in greater detail, as the evolving planet mass certainly affects the migration rate.

Hill mass versus sink mass

The sink particle mass may not always properly reflect the mass of the planet. To quantify this, we define an effective Hill mass of the planet, M_H , as the sink mass plus the mass of the gas within $R_H/2$ of the planet. The choice of $R_H/2$ is motivated by results of Nayakshin (2017a), who finds that gas bound to the planet is usually located within half the Hill radius; material between $R_H/2$ and R_H is much more likely to be lost as the planet migrates inwards.

We should also note that the Hill radius definition needs to include the mass of the gas envelope around the sink itself, that is,

$$R_H = R \left(\frac{M_H}{3M_\star} \right)^{1/3}, \quad (4.11)$$

where we use M_H rather than the sink mass, M_p . When the Hill mass is dominated by the sink mass, M_H can be safely replaced by M_p , and the calculation of M_H from the particle data is trivial. In general, however, the mass of the gas surrounding the sink is not negligible, so we iterate over R_H and M_H to find self-consistent values for these two quantities that obey eq. 4.11.

Fig. 4.7 shows the Hill mass and the sink mass for Runs 1-3 calculated for the different codes. For Run 3, where gas accretion onto the sink is allowed, we see that for all the codes $M_H \approx M_p$. In other words, the gas mass within the Hill sphere is negligible compared with the sink mass. As the sink mass grows rapidly by gas accretion, this also means that once gas enters the Hill sphere it accretes onto the sink rapidly, so there is never a dynamically significant gas envelope around the sink. This is expected since we use a relatively large value of $R_a = 0.5$ AU for Run 3. Nayakshin (2017a) found that the accretion rate onto the sink is roughly proportional to the sink radius (see Appendix in that paper) and that sink radii larger than ~ 0.1 AU over-estimate the rate of gas accretion onto the sink when compared with a simulation in which the clump was directly resolved¹.

Fig. 4.7 shows that in Runs 1 & 2 the mass of gas surrounding the sink particle within $R_H/2$ is comparable to the sink mass by the end of the runs, in stark contrast to Run 3. For PHANTOM in particular, at $t = 10,000$ yr, the Hill mass is dominated by the envelope.

In a qualitative agreement between the codes, M_H is always larger in Run 3 than in Runs 1 and 2. This demonstrates that the gas envelope around the planet particle, which builds up in Runs 1 and 2 but not in Run 3, has a detrimental effect on further gas accretion onto the planet. This is likely due to the extra pressure of the envelope, which makes it more difficult for the gas entering the Hill sphere to remain there. However, the exact trend going from Run 1 to Run 2 in the Hill mass is not the same for the different codes. While for GADGET and GIZMO-MFM a larger gravitational softening results in a lower mass gas envelope, this is not the case for PHANTOM and SPHINX. Therefore, gas accretion onto the

¹However, it is not clear what is the appropriate value of R_a to use in general as it also depends on the numerical resolution, e.g., the number of SPH particles used. Using too low a value of R_a may lead to an under-estimate of the accretion rate as the sink region may become unresolved due to a finite SPH particle resolution.

planet (or the planet envelope) remains a significant source of uncertainty even in the simulations where gas accretion is turned off. An exception to this could be problems where gas accretion onto the planet is physically insignificant, such as when the planet mass is very sub-Jovian or the gas cooling time is very long (as in the $\beta \gg 1$ regime in Nayakshin, 2017a).

Let us now compare the uncertainties in the planet accretion rate versus that in migration. Fig. 4.4 shows that there is more disagreement in the planet mass versus time plot between the different codes for Run 3 than in the planet migration tracks. The mass of gas accreted by the planet varies from a minimum of $\sim 4 M_J$ to a maximum of $\sim 12 M_J$, whereas the planet migration timescales vary by less than a factor of 2. We believe that this smaller disagreement in planet migration rates may be somewhat fortuitous. As the planet mass increases, the analytic formulae in the linear type I regime (e.g., eq. 4.7) predict that the migration rate should increase linearly with planet mass. However, as the planet starts to open a gap, it starts to transition into a slower type II regime. The migration rate therefore depends on the planet mass somewhat less strongly than can be expected based on the theoretical type I predictions.

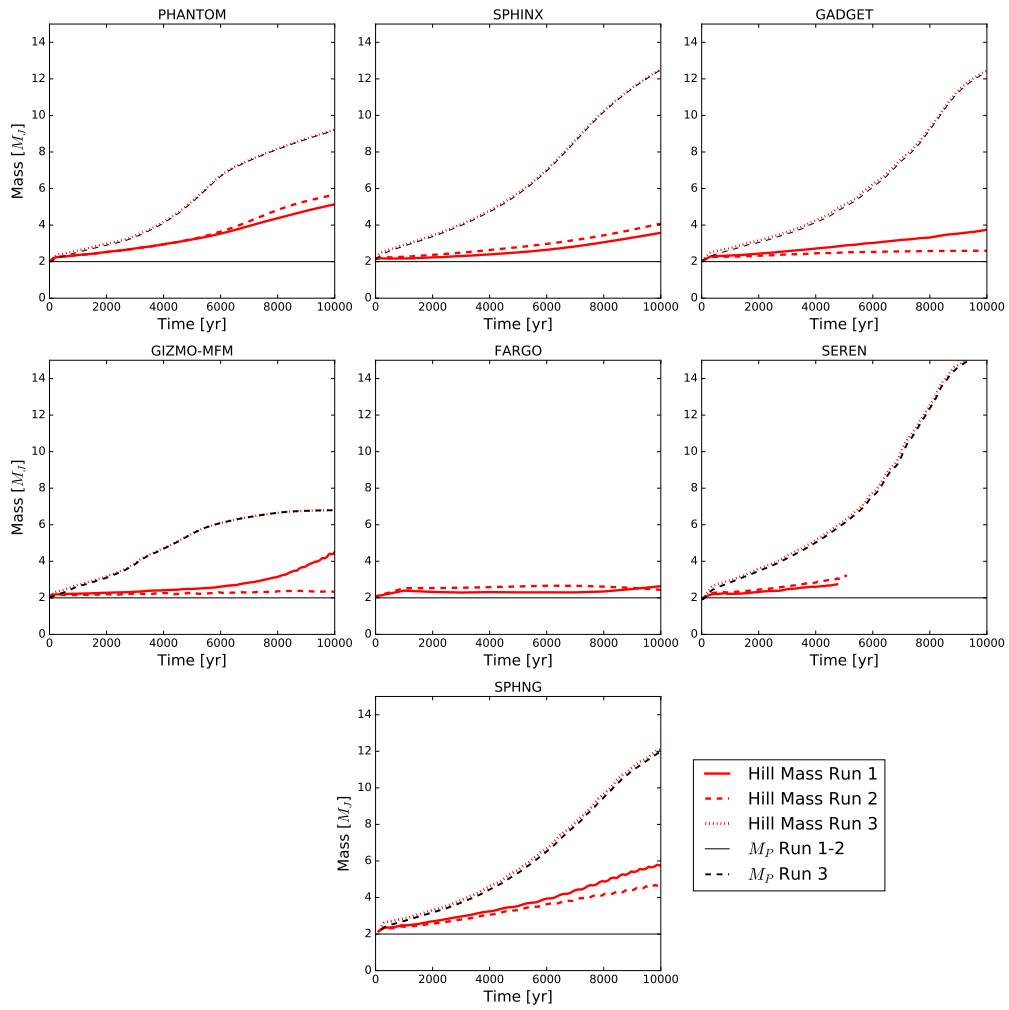


FIGURE 4.7: The Hill mass, M_H (red curves), and the sink mass M_p (black), for Runs 1-3.

4.4.3 Run 3 and Run 4

Gap opening

Runs 3 and 4 both use the sink particle prescription but differ in the initial sink mass, $2 M_J$ and $12 M_J$, respectively. These two simulations cover the parameter space in which a growing planet goes from migrating in type I (no gap in the disc) to type II (a deep gap opened). In the outer massive disc, both planet migration rates and gas accretion rates onto the planet are far larger in the Type I regime than in the Type II regime (e.g., Zhu et al., 2012b; Nayakshin, 2017a). The time and radial location where the switch between migration regimes occurs is thus of a significant importance.

Fig. 4.8 shows with different coloured lines the planet mass versus separation tracks for Runs 3 (left panel) and 4 (right panel) for all the eligible codes. The planets start at the lower right corner and move towards the upper left corner in this diagram.

There are also four black curves in the figure that show theoretical predictions from Crida, Morbidelli, and Masset (2006) for when a deep gap in the disc should be opened. According to these predictions, the planet opens a gap when the parameter C_p is smaller than unity:

$$C_p = \frac{3}{4} \frac{H}{R_H} + \frac{50\alpha H^2}{R^2} \frac{M_*}{M_p} \leq 1. \quad (4.12)$$

Here α is the physical viscosity parameter of the gas disc (Shakura and Sunyaev, 1973). We do not set a physical viscosity parameter in the runs presented here (PHANTOM offers a facility for this but most other SPH codes do not). However, artificial viscosity in numerical schemes can mimic certain effects of a physical

viscosity. Price et al. (2017) show that for the PHANTOM viscosity implementation, artificial viscosity parameter α_v , set to unity for all SPH codes here (but see §4.4.4), results in effective Shakura and Sunyaev (1973) viscosity parameter

$$\alpha = \frac{1}{10} \alpha_v \frac{h_{\text{sml}}}{H}, \quad (4.13)$$

where h_{sml} is the SPH smoothing length and H is the local disc vertical height scale (see Murray, 1996). At the separation where our planets open gaps, we have $h_{\text{sml}}/H \approx 0.4$, and hence the effective disc viscosity of these codes is about $\alpha = 0.03$.

Additionally, self-gravitating protoplanetary discs generate physical viscosity that saturates at a maximum value of $\alpha \sim 0.06$ (Gammie, 2001; Rice, Lodato, and Armitage, 2005) for marginally stable discs. The value of the Q -parameter for our disc is significantly greater than the critical ~ 1.5 and we thus expect that the effective α from the disc self-gravity is much smaller than the maximum value.

Fig. 4.8 show the planet gap-opening mass as a function of separation for our initial discs, defined as the planet mass for which $C_p = 1$. The solid curve sets $\alpha = 0.03$, whereas for the dashed and the dotted curves $\alpha = 0.05$ and $\alpha = 0.1$, respectively. Since planet migration effectively stalls (at least on the time scales of our simulations) when the planet switches to the type II migration regime, the radial location of this switch can be identified in the figure as the point where the planet track turns from being mainly horizontal to being more vertical. For Run 3, the left panel of fig. 4.8 shows that the location at which the migration type switches is approximately consistent with the Crida, Morbidelli, and Masset (2006) prediction for $\alpha = 0.1$, although the actual value of the separation and planet mass at that point are somewhat different for the codes. However, the estimated effective disc viscosity for the codes is $\alpha = 0.03$, and the respective

(solid) curve in fig. 4.8 yields significantly smaller masses. The only exception to that is GIZMO-MFM whose meshless finite mass scheme was shown to provide smaller artificial viscosity (Deng, Mayer, and Meru, 2017).

The results of Run 4 are largely consistent with this picture. We see that the gap opening value of planet mass and separation lie close to the $\alpha = 0.1$ theoretical curve, with GIZMO-MFM transiting into type II migration somewhat earlier once again. One exception to this is PHANTOM, for which the planet seems to cross the migration type dividing line rather uneventfully.

The fact that our simulated gas clumps open gaps at higher masses and later in time than predicted by the Crida, Morbidelli, and Masset (2006) analysis confirms the findings of Malik et al. (2015) who showed that in massive circumstellar discs, gap opening is more difficult than for less massive discs. As shown by Malik et al. (2015), if planets migrates through the horse-shoe region faster than the gap can be excavated by planet toques, the gap remains closed even if C_p falls below unity.

Finally, although our code migration comparison project is not designed to study the longer term planet evolution that occurs in the Type II regime, we can see from fig. 4.8 that there is a significant disagreement in the planet evolution once it crosses over into the Type II regime. While qualitatively we see that planets tend to stall in Type II, as expected, some codes predict that the planets continue to migrate in while others (PHANTOM in the left hand panel) start to migrate outward. This may indicate that the secular evolution of the planets in the Type II migration regime is even more model dependent than the Type II which we mainly aim to study here.

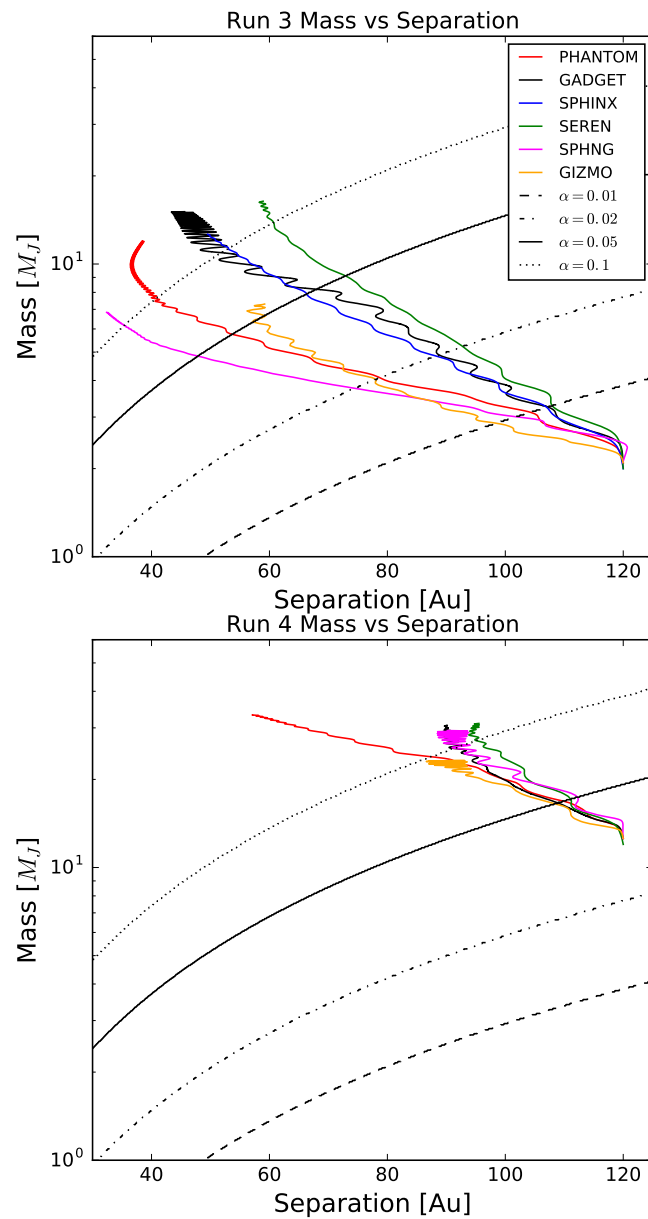


FIGURE 4.8: Planet mass vs separation for Runs 3 and 4 (coloured curves). The black curves running from the bottom left to the top right corners of the panels show the gap opening planet mass (eq. 4.12) for several different values of the viscosity parameter α as specified in the legend. The planet mass-separation tracks turn more vertical when they switch into the Type II regime. As discussed in §4.4.3, the expected gap opening masses are given by the solid curve, but the actual ones are closer to the $\alpha = 0.1$ curve.

Gas accretion time scales

As emphasized by previous authors, there is a competition between the process of gas accretion onto the planet and its inward migration (e.g., Zhu et al., 2012b; Nayakshin, 2017a). This competition plays a significant role in shaping of the outcome of disc fragmentation. It is hence convenient to define, in addition to the migration time scale, an accretion time scale for the planet, t_{acc} ,

$$t_{\text{acc}} = \frac{M_p}{\dot{M}}, \quad (4.14)$$

where \dot{M} is the gas accretion rate onto the planet. The corresponding dimensionless quantity τ_{acc} ,

$$\tau_{\text{acc}} = \frac{t_{\text{acc}}}{T_p}, \quad (4.15)$$

where $T_p = 2\pi/\Omega_p$ is the orbital period at the planet location, will be useful as well.

Bate, Bonnell, and Bromm (2003) studied planet migration and accretion in isothermal discs and found that the following equation describes the gas accretion rate onto the planet well in the Type I migration regime,

$$\dot{M}_{\text{acc}} = b \frac{M_p}{M_*} \Omega_p \rho R^3, \quad (4.16)$$

where $b \approx 2.3$ empirically and ρ is the disc midplane density. By writing $\rho = \Sigma/(2H)$ and expressing

$$\Sigma = \frac{c_s \Omega_p}{\pi G Q}, \quad (4.17)$$

where Q is the Toomre parameter at the planet location, we can re-arrange the Bate, Bonnell, and Bromm (2003) result as

$$\tau_{\text{acc}} = b^{-1}Q. \quad (4.18)$$

Zhu et al. (2012a) used a 2D code to study clump migration and accretion, and provided a 2D estimate for the rate of gas accretion onto the planet,

$$\dot{M} = 4\Sigma\Omega R_H^2 \quad (4.19)$$

Expressing Σ through eq. 4.17 again, we obtain the corresponding gas accretion time scale

$$\tau_{\text{acc}} = \frac{M_p}{\dot{M}T_p} = \frac{3}{8} \frac{R_H}{H} Q. \quad (4.20)$$

Since for our planets $R_H \sim H$ within a factor of two or so, eq. 4.20 is actually not very different from eq. 4.18.

Fig. 4.9 shows dimensionless accretion time scales for Runs 3 and 4. The black curves show the analytic estimates obtained with eqs. 4.18 and 4.20, respectively. For eq. 4.18, we show three curves which use $b = 2.3$ (as in Bate, Bonnell, and Bromm, 2003), and then also $b = 1$, and $1/3$. We can see that both analytic prescriptions predict much faster accretion rates onto the planet than actually measured in the simulations. This is most likely due to the analytic estimates assuming an isothermal equation of state and therefore the maximum efficiency for gas capture onto the planet. In the runs presented here, the gas is not isothermal and heats up due to adiabatic compression in the Hill sphere. The cooling rate β -parameter is $\beta = 10$, which is relatively large. Nayakshin (2017a), see also Humphries and Nayakshin (2018), found that gas accretion onto planets

is significantly suppressed for $\beta \gtrsim$ a few. The isothermal gas accretion rate estimates from Bate, Bonnell, and Bromm (2003) and Zhu et al. (2012b) physically corresponds to the $\beta \ll 1$ regime investigated in Nayakshin (2017a), for which much higher accretion rates were indeed obtained. It appears that $b \approx 1/3$ in eq. 4.18 fits the gas accretion rates in the Type I migration regime best.

Fig. 4.9 also demonstrates that the accretion time increases strongly when the planet switches to the type II migration regime. This has also been seen in previous simulations (e.g., Bate, Bonnell, and Bromm, 2003) and is to be expected as the planet clears its immediate neighbourhood of gas, choking its own growth.

The initial dips in the accretion time for both panels in fig. 4.9 are caused by our artificial initial conditions, in which a massive planet is injected in the disc. The gas within the Hill sphere of the planet then finds itself strongly bound to it and accretes onto the planet on a time scale shorter than the local dynamical time, $1/\Omega$. This initial transient is followed by a more self-consistent evolution in which the gas in the Hill sphere of the planet “knows about its existence”.

4.4.4 Importance of artificial viscosity prescription

Artificial viscosity is used in SPH and grid based codes to treat flow discontinuities such as shocks (Monaghan, 1992; Bodenheimer et al., 2007). The codes we test here differ in their implementation of the artificial viscosity. Some part of the differences in the results of Runs 1-4 (discussed in §4.4) may be due to these numerical technique differences. Varying the viscosity prescriptions for all of the codes would make the presentation of the key results over long and complex. Instead we pick one code, PHANTOM, and investigate how different artificial viscosity choices affect the results for just Run 3.

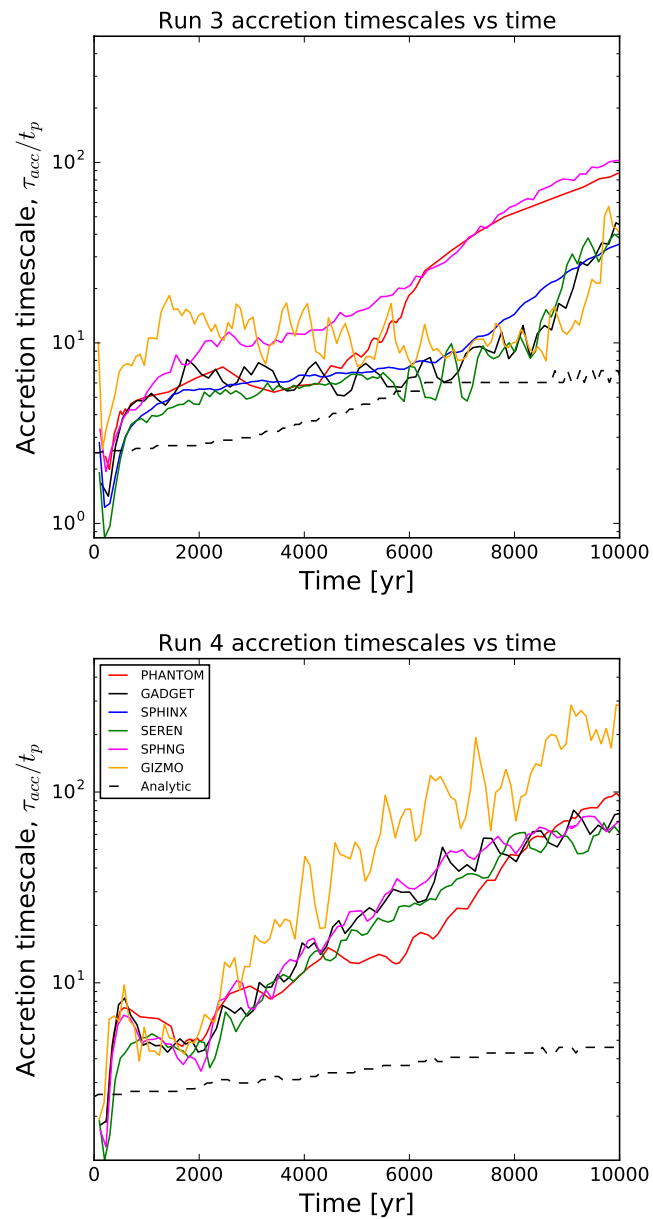


FIGURE 4.9: **Top panel:** Dimensionless accretion time scale against time for Run 3. The black curves are analytical estimates for the accretion time scale given by eqs. 4.18 (for different values of the parameter b) and 4.20, as indicated in the legend. These estimates assume an isothermal equation of state and therefore over-predict the gas accretion rates measured in the simulations. **Bottom panel:** Same but for Run 4. Note that the gas accretion time increases strongly when a gap in the disc is opened.

All modern SPH codes employ artificial viscosity prescriptions that include a term linear in Δv , the velocity difference between two interacting SPH particles, and a term quadratic in Δv (Springel, 2005; Price et al., 2017). That is, the first term enters artificial viscosity with a dimensionless coefficient α_v , and the second with coefficient β_v . In some codes, e.g., GADGET, these coefficients are fixed whereas in others such as PHANTOM they are allowed to vary in time during simulations. Cullen and Dehnen (2010) in particular presented a method in which α_v depends on the time derivative of the particle velocity divergence. The latter is used as a shock indicator and helps to eliminate artificial viscosity away from shocks, reducing unwanted numerical dissipation in dynamically quiet regions. Additionally, there are different suggestions on the appropriate values for the coefficient β_v to use, and in fact this may depend on the problem studied (Price et al., 2017).

Fig. 4.10 shows how the planet separation (top panel) and planet mass (bottom panel) are affected by the changes in the viscosity prescription for Run 3. The solid curves show Run 3 in which the α_v parameter is time-dependent as in the method of Cullen and Dehnen (2010), and is allowed to vary between $0 \leq \alpha_v \leq 1$. The different colours in the solid curves indicate different values of the coefficient β_v , which we varied in a broad range, from $\beta_v = 0.2$ to $\beta_v = 10$. The dashed curves in fig. 4.10 show simulations with the same range in β_v but which now use a fixed value for $\alpha_v = 1$.

First, without reference to the different artificial viscosity values in the figure, we note that the larger the planet mass, the more rapidly the planet migrates, at least until it opens a gap and switches to type II migration. Such a trend simply reflects the fact that more massive planets migrate more rapidly in the Type I regime (eq. 4.7).

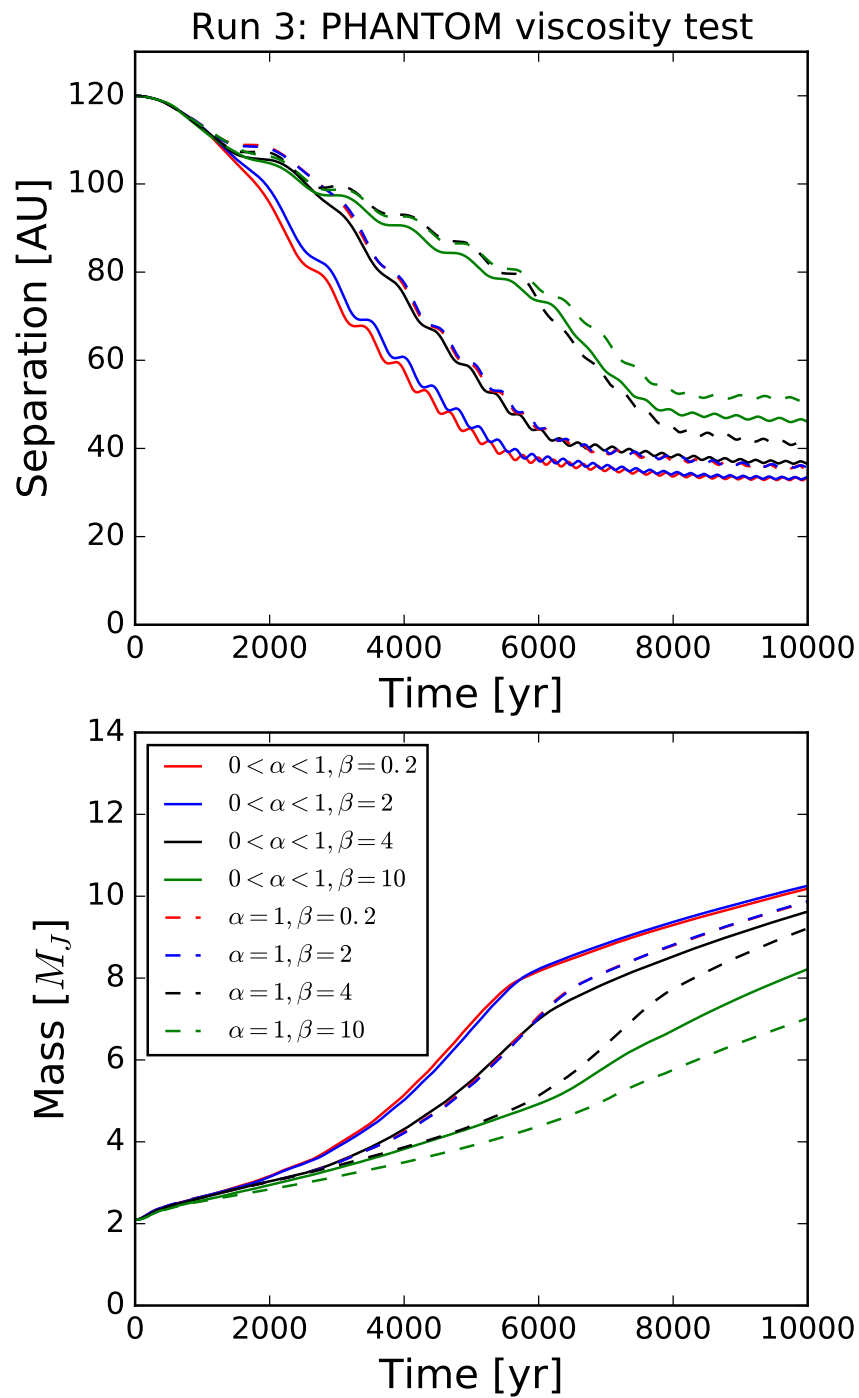


FIGURE 4.10: Differences in the results of Run 3 for PHANTOM when the values of the artificial viscosity parameters α_v and β_v are varied. See §4.4.4 for detail.

Another trend obvious through all of the curves is that the higher artificial viscosity simulations tend to yield smaller gas accretion rates onto the planet. The least viscous run (red solid curve) shows the the largest gas accretion rate onto the sink and the most rapid migration. The most viscous run (green dashed curve) shows the slowest migration and the smallest gas accretion rate. The rest of the runs show a continuous transition between these two extremes.

This gas accretion trend with artificial viscosity is most likely due to the artificial viscosity heating of the gas inside the Hill radius. The larger the gas viscosity, the larger the dissipation rate within the Hill sphere, making the gas hotter. Such sensitivity of gas accretion rate onto the planet to heating within the Hill sphere was seen in the previous literature although for different reasons. Nayakshin and Cha (2013) and Stamatellos (2015) included planet radiative feedback on the surrounding gas, and found that when the feedback is present, it keeps the gas hotter in the planet’s Hill sphere, stifling gas accretion onto it. Nayakshin (2017a) found that slower radiative cooling rates within the Hill sphere, which also makes the gas hotter in that region, likewise leads to a reduction in the gas accretion rate.

In greater detail, we see that the runs with $\beta_v = 0.2$ and $\beta_v = 2$ are virtually indistinguishable, implying that the quadratic term in the artificial viscosity prescription is negligible for these small values of β_v for the given problem. Higher values of β_v however definitely affect the results. We also see that the fixed α_v simulations lead to less massive and less rapidly migrating planets that tend to open a gap sooner.

The range of migration rates and planet masses in fig. 4.10 is large enough to conclude that although the artificial viscosity is not the only reason for differences in the results from the four runs we explored, it is one of the major reasons for these differences. For example, GADGET’s planet separation versus time track

for Run 3 is similar to the green dashed curve in fig. 4.10 for PHANTOM obtained with a fixed $\alpha_v = 1$, as used by GADGET. However, by default GADGET uses $\beta_v = 2\alpha_v$, which is much smaller than $\beta_v = 10$ for the green dashed curve. Clearly, other code differences, both in viscosity implementation (GADGET uses the Balsara, 1995, switch; PHANTOM does not), and in how artificial softening and gas accretion onto the sink is implemented must be at play. A recent study by Stamatellos and Inutsuka (2018) found that the artificial viscosity coefficient α_v can also drive differences in planet accretion/migration.

On the other hand, while PHANTOM simulations suggest a higher artificial viscosity might suppress accretion via spurious heating of the gas surrounding a sink particle, the trend shown by the GIZMO-MFM results suggest the role of numerical viscosity might be more complex. Indeed, as shown in Deng, Mayer, and Meru (2017), the MFM method, which does not employ any artificial viscosity, at variance with all SPH methods, minimizes spurious transport of angular momentum inside self-gravitating disks and results in a lower accretion onto sink particles (see Appendix B in Deng, Mayer, and Meru, 2017). Indeed MFM solves the fluid equations via Riemann solver as in Godunov-type finite volume methods, which removes the need of an artificial viscosity term in the hydro equations (Hopkins, 2015).

Artificial viscosity implementations in SPH can induce enhanced angular momentum transport, and thus accretion, in non-shocking rotating flows inside fluid disks, owing to the contribution of the linear in Δv term (even with correction terms such as the Balsara switch, e.g., Kaufmann et al., 2007). Spurious heating and artificial angular momentum transport are thus two different unwanted effects of artificial viscosity which affect accretion in opposite ways. Quantifying the interplay of these two effects warrants further investigation. Nevertheless, it

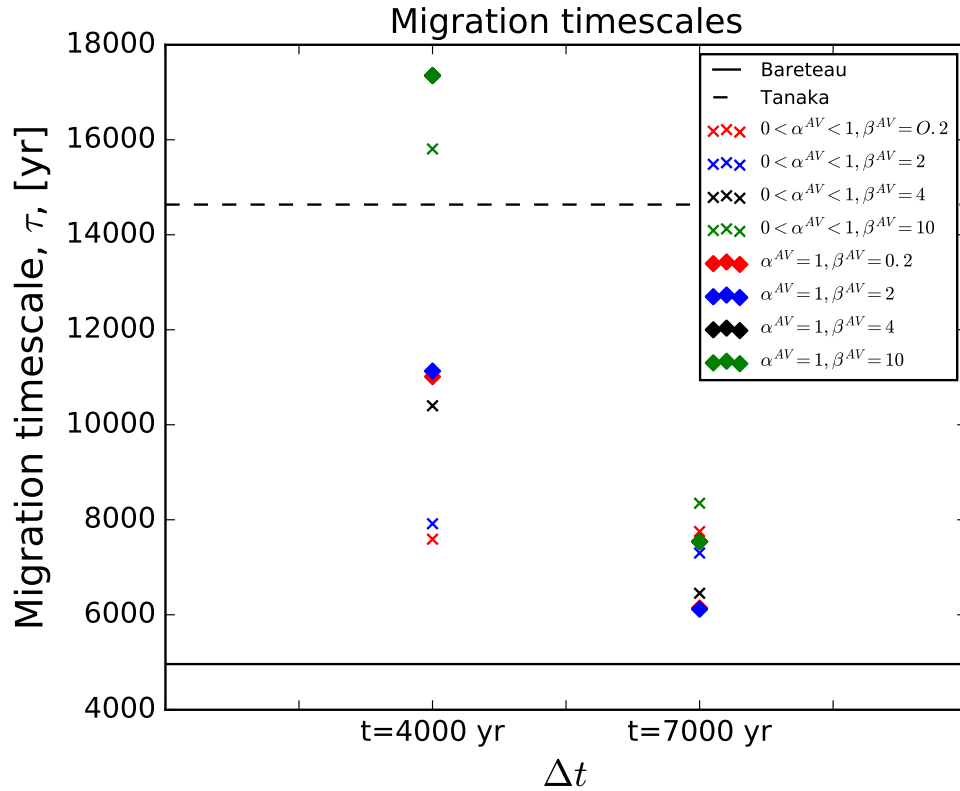


FIGURE 4.11: Migration time scales at 4000 yr and 7000 yr for the viscosity comparison runs. The migration rates are between the Tanaka migration rate (black dashed line) and the Baruteau migration rate (black solid line)

is noteworthy that, in the GIZMO-MFM runs, the reduced accretion limits asymptotically the mass growth of the protoplanet to less than $10M_J$, namely within the gas giant planet regime.

Finally, for completeness Figs. 4.11 shows the time scales τ_4 and τ_7 for the eight PHANTOM runs presented in fig. 4.10, and fig. 4.12 shows the dimensionless accretion time scales.

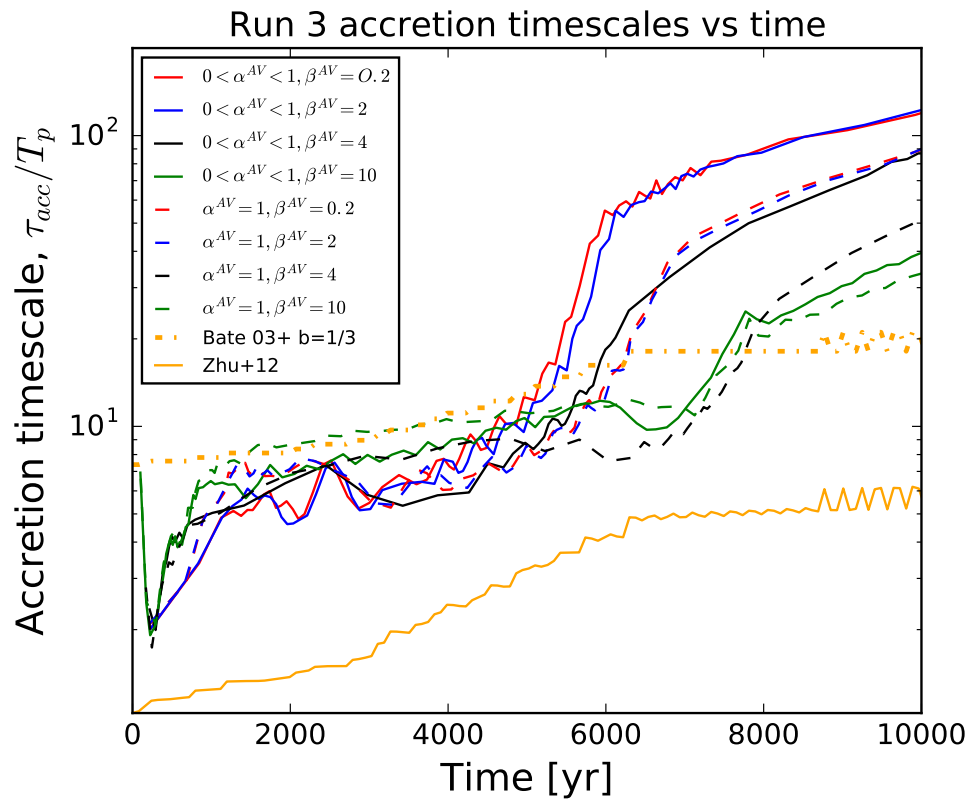


FIGURE 4.12: Accretion timescales vs time for all viscosity comparison runs, with dashed lines representing the suppressed Bate 03 analytic accretion rate.

4.5 Comparison to population synthesis

At the time of writing, there are three detailed population synthesis models that address the evolution of clumps formed by gravitational instability at distances of tens to 100 AU. Such population synthesis is a necessary step to correctly interpret the results of large observational surveys (e.g., Vigan et al., 2017) with respect to how often disc fragmentation might result in the formation of massive planets and/or brown dwarfs.

The population synthesis models differ in assumptions about the initial state of the disc and the clumps, disc dissipation, clump radiative cooling, dust dynamics and core formation, clump migration and accretion. It is of course not possible for us to examine these different approaches here. However, we can investigate a more limited but better defined question: how well would these models reproduce the evolution of the clumps that we see in our numerical models given the same disc and clump properties as our simulations?

To facilitate the population synthesis comparison to the simulations we present, we shall utilize the fact that the disc surface density profiles evolve relatively weakly in Run 3 as the planet remains in the Type I migration regime for most of the codes until it stalls not very far from the disc inner edge. We can therefore use the initial disc surface density profile for this comparison. For Run 4, there is a stronger surface density evolution, but we shall use the same approach (since two of the three population synthesis codes make such an approximation too), hoping that it will capture the essentials of the problem.

We first overview the clump migration approaches. Forgan and Rice (2013b) use the simplified migration scheme from Nayakshin (2010a), in which the Type I migration timescale is

$$t_{\text{I}} = \left(\frac{M_{\text{p}}}{M_{*}} \Omega \right)^{-1} \frac{H}{R}. \quad (4.21)$$

This is derived from the Tanaka, Takeuchi, and Ward (2002) formula (eq. 4.7) by requiring additionally a marginally unstable self-gravitating disc for which the Toomre parameter $Q \approx 1$ everywhere. For type II, the migration time scale is given by the disc viscous time,

$$t_{\text{II}} = t_{\text{visc}} = \frac{1}{\alpha\Omega} \left(\frac{H}{R} \right)^{-2}. \quad (4.22)$$

The switch between Type I and Type II migration occurs when $M_{\text{p}} > M_{\text{t}}$, where M_{t} is the transition mass given by,

$$M_{\text{t}} = 2M_{*} \left(\frac{H}{R} \right)^3 \quad (4.23)$$

as used by Bate, Bonnell, and Bromm (2003). We note that Forgan et al. (2018) have recently presented an updated population synthesis model. We do not include this study in our code comparison here because its migration module is similar to the Müller, Helled, and Mayer (2018) treatment, which is discussed below. Furthermore, Forgan et al. (2018) also consider multiple gas clumps and model their N-body interactions. These effects can be very important in modifying the outcome of disc fragmentation (Hall, Forgan, and Rice, 2017) but is beyond the scope of our one-clump study.

Nayakshin and Fletcher (2015) use the Tanaka, Takeuchi, and Ward (2002) expression for type I migration written as

$$t_{\text{I}} = f_{\text{mig}} \frac{M_{*}^2}{M_{\text{p}} M_{\text{d}}} \frac{H^2}{R^2} \Omega^{-1} \quad (4.24)$$

where $M_d = 2\pi\Sigma(R)R^2$ is a measure of the local disc mass, and f_{mig} is a dimensionless factor, set between 0.5 and 2 for different models. The factor is introduced to mimic the stochastic kicks from spiral density waves or other clumps. The Type II migration time is also set to the viscous time but with a correction multiplicative factor,

$$t_{\text{II}} = t_{\text{visc}} \left(1 + \frac{M_p}{M_d} \right). \quad (4.25)$$

The factor $(1 + M_p/M_d)$ takes into account planet inertia when the disc is less massive than the planet (Syer and Clarke, 1995). The correction is not very important for outer massive discs but may become large in the inner disc ($R \lesssim 10$ AU). The Crida parameter (C_p , eq. 4.12) is used to model the transition between Type I and Type II migration. To prevent a sharp transition when $C_p = 1$, an exponential function of the form, $f = \min(1, \exp[-(C_p - 1)])$ is used to smooth the transition out. Note that C_p is a function of the viscosity parameter α , which is poorly known for protoplanetary discs. Nayakshin and Fletcher (2015) assumed that $\log \alpha$ is a random uniform variable in the limits between $\log(0.005)$ and $\log(0.05)$. We shall evaluate the results for these minimum and maximum values of α . Finally, Nayakshin and Fletcher (2015) use a time-dependent 1D viscous disc model to evolve the disc surface density and other disc properties, and to conserve the angular momentum in the interactions between the disc and the planet, but for comparison below we shall assume the initial disc properties to be consistent with the two other models.

Müller, Helled, and Mayer (2018) use a third set of equations to control planet migration, based on Baruteau, Meru, and Paardekooper (2011), see eq. 4.8. For type II migration, eq. 4.25 is used but without the $(1 + M_p/M_d)$ correction, which however is unimportant for the current aims and scope of the project as it is close

to unity. Müller, Helled, and Mayer (2018) also use the Crida parameter to determine when the planet switches to the type II migration, but consider two additional requirements for gap opening based on the work of Malik et al. (2015). They define three timescales, $\tau_{\text{visc}} = R^2/\nu$, $\tau_{\text{cross}} = 2.5R_{\text{H}}v_r^{-1}$, where v_r is the radial velocity of the planet, and $\tau_{\text{gap}} = q^2(H/R)^5\Omega^{-1}$. The additional requirements demand that $\eta\tau_{\text{gap}} < \tau_{\text{cross}}$ and $\tau_{\text{visc}} < \tau_{\text{cross}}$, where η is a dimensionless factor varied from 10 to 1000, with $\eta = 100$ used as a baseline model. Here we test only the first of these two additional criteria since it was the one used for most of the models in Müller, Helled, and Mayer (2018).

Finally, population synthesis models also differ in how they treat the gas accretion onto clumps. Two of the population synthesis models (Forgan and Rice, 2013b; Nayakshin and Fletcher, 2015) neglected gas accretion onto the clumps, assuming a fixed gas mass unless the clumps are tidally disrupted. Müller, Helled, and Mayer (2018) prescribed a gas accretion rate onto the clumps based on earlier simulations of Galvagni and Mayer (2014). Since our gas clumps accrete a significant amount of gas as they migrate, for a proper comparison with the population synthesis prescriptions we need all of them to take accretion into account. We previously found that the Bate, Bonnell, and Bromm (2003) expressions for gas accretion rates, when reduced down to account for a smaller accretion efficiency of our slowly cooling discs, yields a reasonable match to the accretion time scales of our simulation (fig. 4.9). We therefore use eq. 4.16 with $b = 1/3$ here to let the planets gain mass when investigating Forgan and Rice (2013b) and Nayakshin and Fletcher (2015) models.

We also need to take into account the decrease in the accretion rate when the planet switches from type I to the type II regime, which is clearly seen in fig. 4.9.

To this end we write

$$\dot{M}_p = \dot{M}_{\text{acc}} \left[1 + e^{-(C_p-1)/\Delta C} \right]^{-1}, \quad (4.26)$$

where \dot{M}_{acc} is the accretion rate estimate given by eq. 4.16 where $\Delta C = 0.2$. We shall see below that this yields a decent fit to the planet mass evolution for both Run 3 and Run 4. With this approach, the comparison of population synthesis models to hydrodynamical simulations isolates just the planet migration and gap opening aspects.

Figs. 4.13 and 4.14 show such comparisons for Run 3 and Run 4, respectively. The shaded region represents approximately the range of numerical results obtained for these runs with the different numerical codes. In particular, PHATOM and GIZMO-MFM are selected to show the fastest and the slowest migrating planets for Run 3 in the left panel; the SEREN and GIZMO-MFM curves to show the range of models in the middle and right panels. For Run 4, PHANTOM and SEREN are selected as the extremes for the both planet accretion and migration tracks.

We see that there is a significant difference in how the three population synthesis models compare to the numerical results. The Müller, Helled, and Mayer (2018) study appears to over-estimate somewhat how quickly and how far the planets migrate before they switch into the Type II regime. This seems to be because Müller, Helled, and Mayer (2018) formulae are based on Baruteau, Meru, and Paardekooper (2011) and yield too rapid migration by a factor of a few in the type I regime, as was seen in fig. 4.6. Also, the planet opens a gap a little closer to the star than it does in the simulations. This depends on the parameter η which is set to 100 and 1000 for the solid and the dashed curves, respectively.

The Forgan and Rice (2013b) approach appears to yield too slow a migration

rate. This is because the planet switches into the Type II migration rate immediately, as the transition mass in this approach is set to $2(H/R)^3 M_* \approx 2 M_J$, and the planet is already this massive in the beginning of the Run 3. This under-estimates the planet transition mass, which is found to be in the range of $\sim 7 M_J$ to $\sim 30 M_J$ (cf. fig. 4.8). We found that a much better fit to Run 3 is obtained with the Forgan and Rice (2013b) formulae if the transition mass is increased by a factor of ~ 5 .

The Nayakshin and Fletcher (2015) formulae used Tanaka, Takeuchi, and Ward (2002) expression for the migration rate with a dimensionless factor f_{migr} in front. The factor was a logarithmically uniform random variable in the limits $0.5 < f_{\text{migr}} < 2$ and was meant to mimic possible stochastic kicks that the clumps obtain when interacting with the spiral density waves of the disc (see Baruteau, Meru, and Paardekooper, 2011). In the interest of figure clarity we use $f_{\text{migr}} = 1$ in fig. 4.13 for this model. Further, Nayakshin and Fletcher (2015) use the Crida, Morbidelli, and Masset (2006) switch for gap opening, with the α parameter being a sum of two parts, a constant α and a part driven by self-gravity. We neglect the latter contribution to α here, and show two cases with $\alpha = 0.005$ and 0.05 in fig. 4.13. It is apparent that the smaller α curve (red solid) opens a gap in the disc far more easily than expected. The $\alpha = 0.05$ curve (red dashed) seems more reasonable. However, we must remember that Nayakshin and Fletcher (2015) neglected gas accretion onto the planet. The agreement of their prescriptions with Run 3 would have been worse if we kept the planet mass fixed at $2 M_J$.

Fig. 4.14 shows that for a more massive gas clump none of the population synthesis prescriptions fare particularly well. The Forgan and Rice (2013b) model and the low viscosity model of Nayakshin and Fletcher (2015) open a gap in the disc too early, as for Run 3. The higher viscosity model of Nayakshin and Fletcher (2015) does relatively well in terms of gap opening mass but over-estimates the

speed with which the planet migrates in initially. The Müller, Helled, and Mayer (2018) equations also yield clumps migrating in too rapidly, and the gap is opened too close in compared with numerical simulations.

We therefore conclude that matching numerical results with analytic expressions remain a problem. What is particularly alarming is that seemingly benign changes in the parameters of the population synthesis prescriptions (such as a factor of a few change in the planet transition mass) can yield planet migration rates different by \sim two orders of magnitude as the planet switches into the Type II migration regime prematurely.

4.6 Discussion

4.6.1 Numerics

We set up four different simulations of a gas planet starting at an initial separation of 120 AU in a massive gaseous disc. These 4 Runs differed in treatment of gas accretion onto the planet and the initial planet mass. We then performed these simulations with seven different numerical codes in order to compare their results.

We find differences by a factor of ~ 2 , and sometimes as large as 3, between different codes in the accretion and migration rates. A more detailed analysis using PHANTOM indicates that these differences are to a large degree due to variations in the artificial viscosity prescriptions between the codes, although other factors such as gravitational softening and sink particle treatment probably also contribute.

We also compared our results with the planet migration and accretion prescriptions from three previous population synthesis studies (§4.5 and figs. 4.13 &

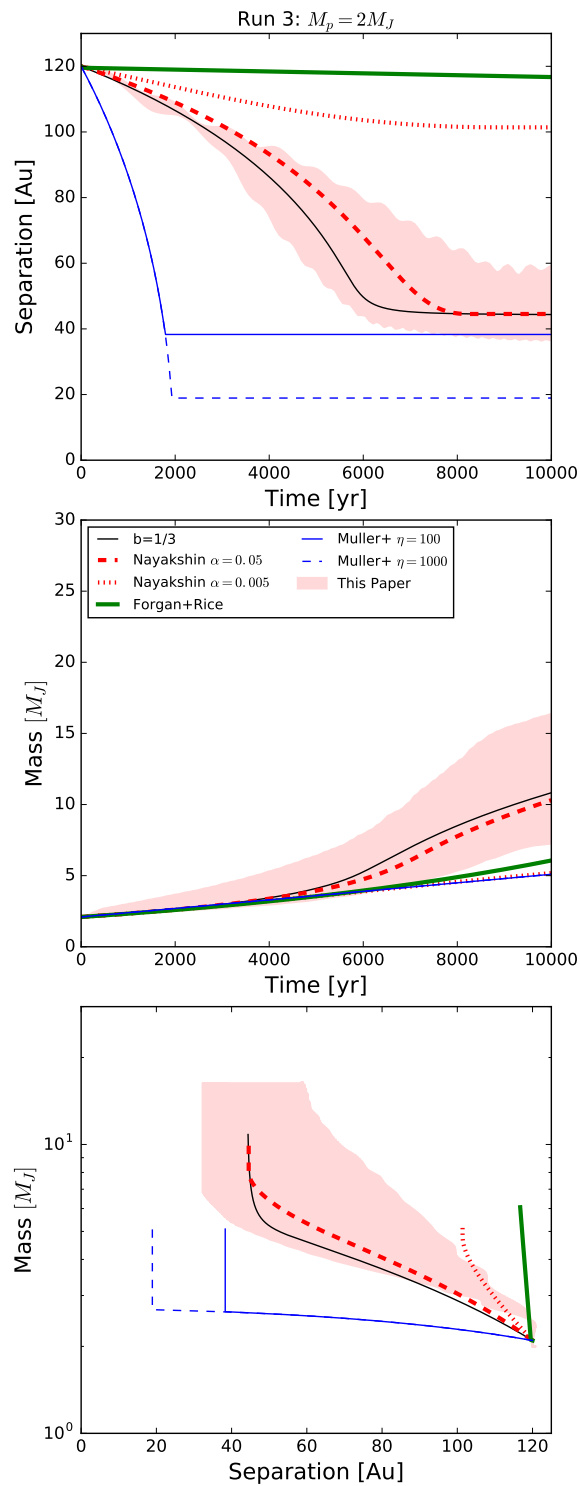


FIGURE 4.13: Comparison of migration and accretion tracks for Run 3, shown as a shaded region, with population synthesis models as shown in the legend. **Top panel:** planet separation vs time; **Middle panel:** planet mass vs time; **Bottom panel:** mass vs separation.

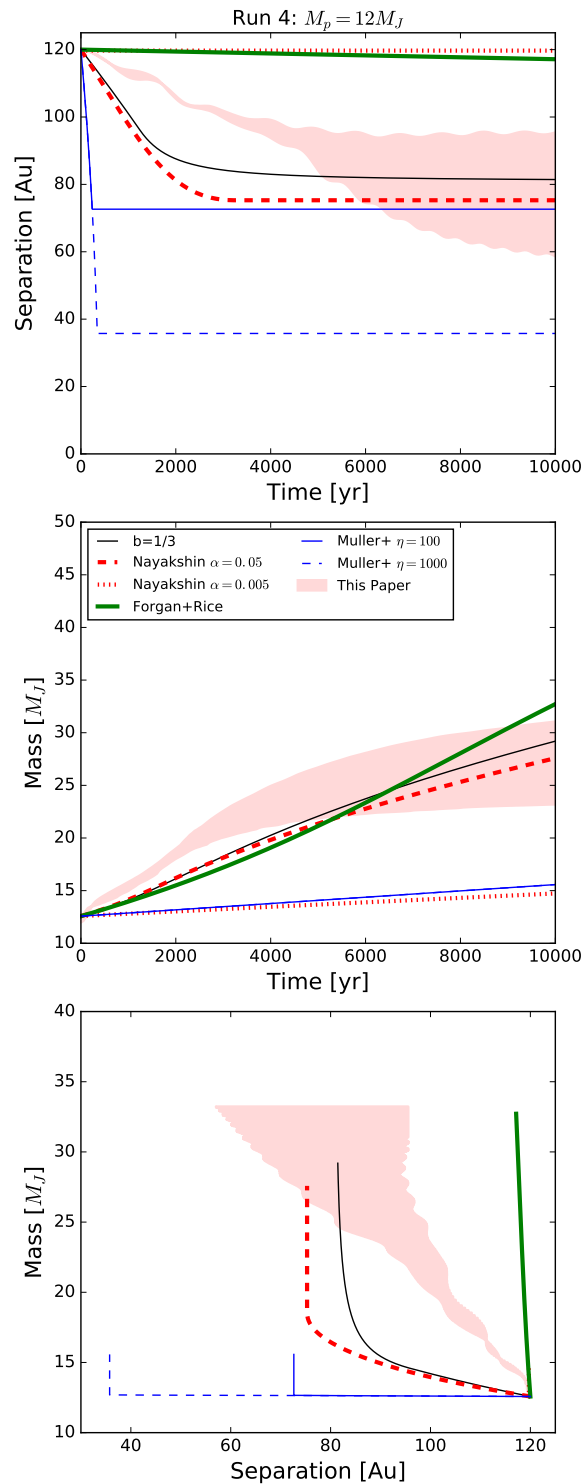


FIGURE 4.14: Same as fig. 4.13 but for Run 4. See §4.5 for more detail.

4.14). The Forgan and Rice (2013b) approach is found to open deep gaps in the disc prematurely. Since planets migrate very slowly in the type II regime, this implies that this study may over-estimate the population of gas giants remaining at wide separation after gas discs are dispersed. The Müller, Helled, and Mayer (2018) study, on the other hand, over-estimates the rate of inward migration of planetary mass clumps. The Nayakshin and Fletcher (2015) study fits the Run 3 results relatively well in the high viscosity case but not for the low viscosity case. In the latter case, clumps open deep gaps in the disc and tend to stall on wide orbits when they should migrate to smaller radii via Type I migration. However, all three population synthesis prescriptions fare poorly for Run 4 in which a more massive planet is considered. Additionally, Forgan and Rice (2013b) and Nayakshin and Fletcher (2015) neglect gas accretion onto clumps.

4.6.2 Observational implications

Recent observational surveys of solar type stars show that only a few % of such stars are orbited by massive planets or brown dwarfs on orbits larger than ~ 10 AU (e.g., Biller et al., 2013; Chauvin et al., 2015; Vigan et al., 2012; Vigan et al., 2017). Let us call this fraction N_{present} . This is a key constraint on the theory of planet and brown dwarf formation via gravitational instabilities of large massive gas discs. However, it is even more important to consider the frequency of such objects in a time-integrated sense, that is, the number of gas clumps formed by disc fragmentation per star. Let this fraction be N_{birth} . The two fractions are clearly connected via

$$N_{\text{present}} = N_{\text{birth}} \times P_{\text{surv}} , \quad (4.27)$$

where $P_{\text{surv}} < 1$ is the probability for a gas clump to survive to the present day at a wide separation.

Detailed calculations and population synthesis approaches are necessary to calculate P_{surv} accurately. Forgan and Rice (2013b) obtained $P_{\text{surv}} \sim 1$, Nayakshin and Fletcher (2015) had $P_{\text{surv}} \lesssim .1$ (Nayakshin, 2016, found a yet smaller value, $P_{\text{surv}} \sim 0.05$, when feedback effects of the luminous core onto the clump are included), and Müller, Helled, and Mayer (2018) found $P_{\text{surv}} \ll 1$ but noted that this depends strongly on model assumptions. Rice et al. (2015) in addition showed that N-body interactions with secondary stars may remove a number of wide separation planets, lowering the fraction of P_{surv} further in the post-disc dispersal phase.

Our simulations and population synthesis comparison (figs. 4.13 and 4.14) demonstrate that just varying the assumptions about the underlying physics of the disc or clumps *by a factor of a few* may influence the results very strongly. One has to also add to this that the exact birth mass of the fragments and the mass of the disc at which it fragments are not known to better than a factor of a few (e.g., Kratter and Lodato, 2016), and the evolution of the clump strongly depends on uncertain disc cooling and dust physics (Nayakshin, 2017a), radiative feedback from the clump (Nayakshin and Cha, 2013; Stamatellos, 2015; Mercer and Stamatellos, 2017), etc. Therefore, the uncertainty in P_{surv} at present is uncomfortably large. At this time we cannot rule out a survival probability that would imply $N_{\text{birth}} > 1$.

What is the best way forward in resolving these uncertainties? Clearly, theoretical and simulation efforts to constrain P_{surv} from first principles should continue. However, other indirect approaches can also help. If the migration processes allow GI planets to populate the whole range of separations between the stellar radius and their birth place, what would be the differences between the objects left behind from this migration and those made by Core Accretion? If

we are able to understand these differences more robustly, then discovering (or not) such unusual objects at separations less than 10 AU may yield independent constraints on P_{surv} and N_{birth} .

4.6.3 Some further exploration of parameter space

Here I present several more runs that I performed with PHANTOM only, to explore how the results change with changes in the initial planet separation and the value for the cooling β_{cool} -parameter.

Fig. 4.15 shows the migration and accretion tracks for planets injected at, R_I , of 180AU, 120AU and 70AU. For each of these initial positions I also run with $\beta_{\text{cool}} = 1, 3, 10$. Firstly it is interesting to note that all the planets apart from the $R_I = 180\text{AU}, \beta_{\text{cool}} = 1$ open a gap, ending migration at approximately the same place in the disc. The lower planet of the figure gives a clue to why this is so. The $R_I = 180\text{AU}, \beta_{\text{cool}} = 1$ case has the most massive planet of all of the runs presented in the figure, which is why a gap is opened in the disc a little further out than for the rest of the runs. The most significant conclusion from these runs is that gap opening at ~ 40 AU in the SPH runs is most certainly due to the inner boundary condition that truncates the disc at ~ 30 AU. Clearly, if the simulations resolved the inner disc further in, by e.g., using a smaller sink radius for the star, then the planet would migrate further inward before opening a gap. This is in fact consistent with results of Nayakshin (2017a) who attempted this numerical experiment and indeed found that planets can then migrate further inward.

Another result consistent with earlier findings of Nayakshin (2017a) and Humphries and Nayakshin (2018), who used GADGET, is that the lower the value of the cooling parameter β_{cool} , the larger is the accreted mass onto the planet.

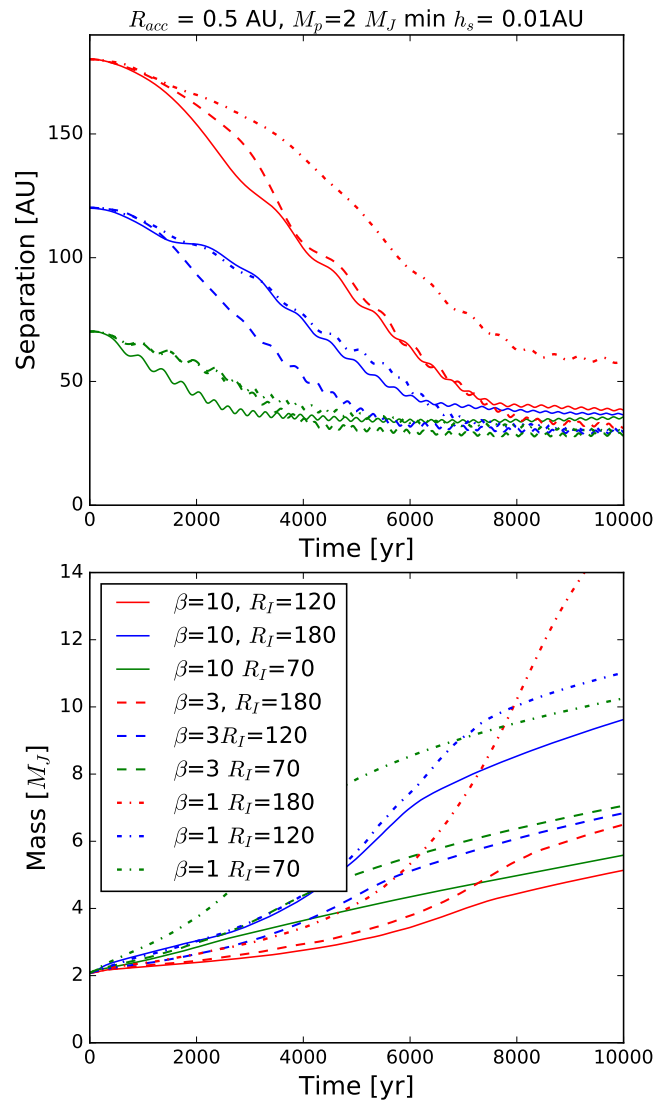


FIGURE 4.15: **Top Panel:** Separation against time, colour representing initial separation and line type grouping same β_{cool} value. **Bottom Panel:** Planet mass, all starting from $2 M_J$ as expected the low β_{cool} runs accrete most mass.

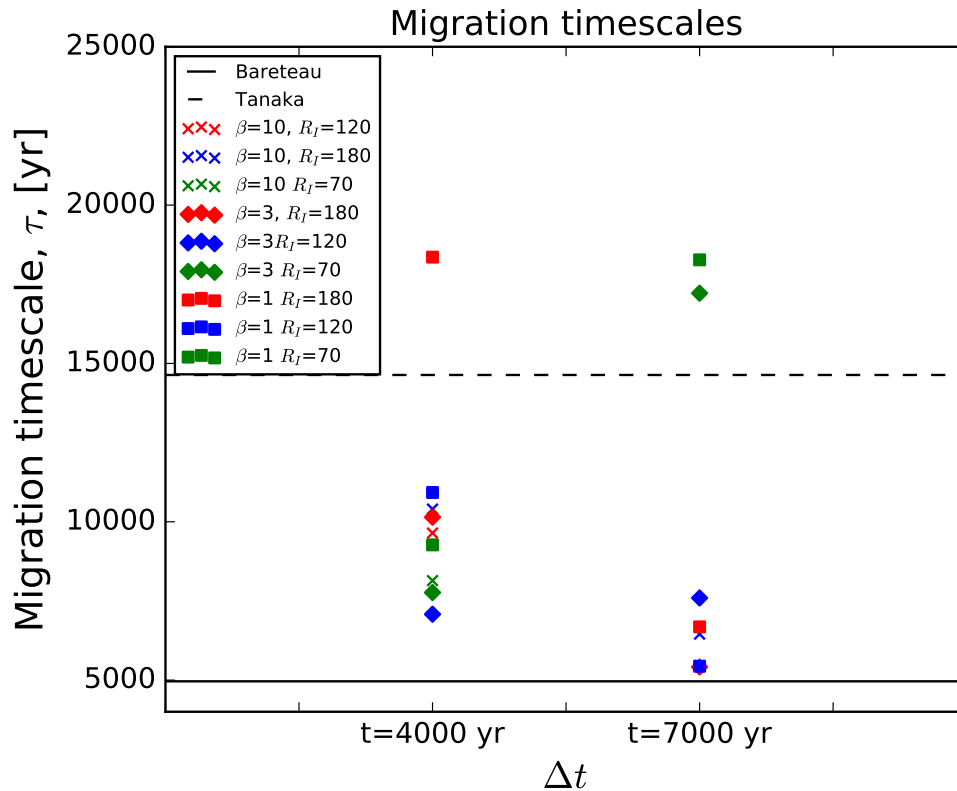


FIGURE 4.16: Migration timescales for PHANTOM runs with different values of β_{cool} and planet starting separation, as shown in the legend.

The migration rates for the test cases all cluster together between the two analytic expectations for migration, fig. 4.16 similar to what is seen in the viscosity test. There are couple of outliers; for example, all three $R_I = 70$ runs have much slower migration timescales at the 7000 year mark, fig. 4.16. This is expected as those runs open a gap much earlier as they reach the 30 – 40 AU region in the disc where we begin to lose resolution. The planet accretion timescales, shown in fig. 4.17 also reflect this behaviour. The closer initial separation runs all have much longer accretion timescales throughout the run and increase rapidly when the planet opens a gap around 4000 years.

Fig. 4.18 shows the shell average SPH smoothing length against radius in the

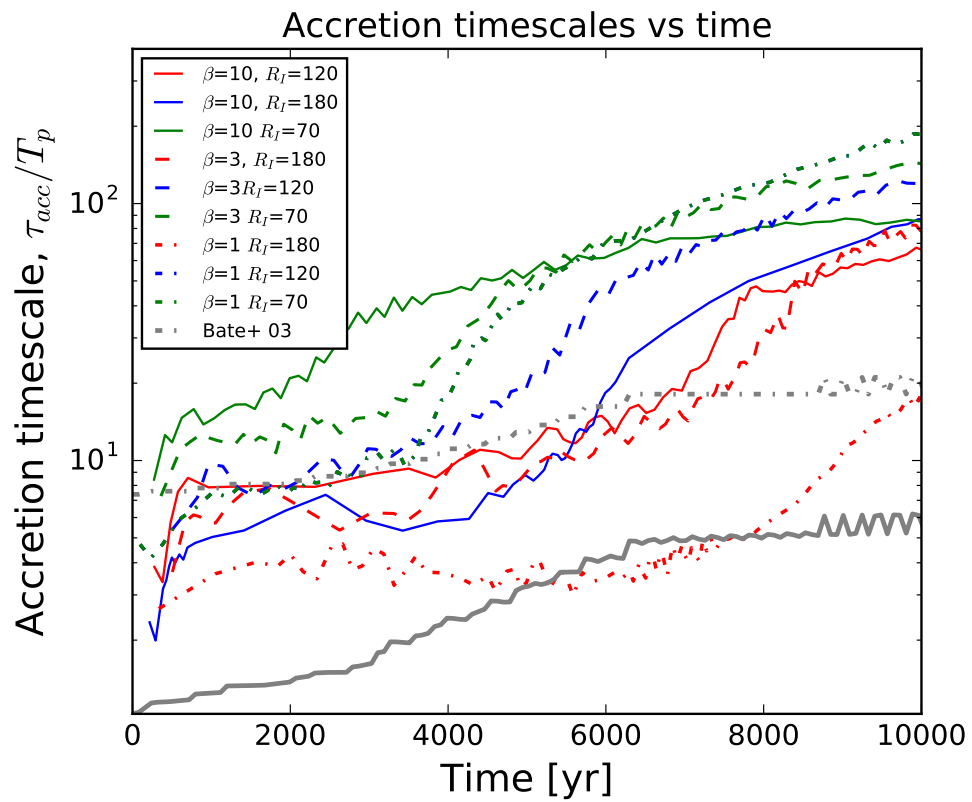


FIGURE 4.17: Same as fig. 4.16 but for the respective accretion timescales.

disc. A lower value of $\langle h \rangle / H$ means better resolution as there are more SPH smoothing lengths per scaleheight. As is expected the effective resolution changes with radius in the disc, with better resolution in the middle 100 Au or so of the disc. Towards the inner edge, inside of ~ 30 Au, $\langle h \rangle / H$ steadily rises, with the value rising more quickly over time. This is due to accretion of particles on to the central sink, thus reducing the number of particles in the inner disc.

4.7 Auxiliary information

Surface density plots (fig. 4.19) show how the planet affects the surface density profile of the disc. We can see the build up of gas around the planet in Run 1 and 2, which we already saw in the plots of the Hill mass for these runs. There is no indication of a deep gap in these cases although a shallow gap starts to develop by the end of the simulations. For Run 3 there is no peak at the planet location which is to be expected as the gas captured by the planet is quickly accreted onto the sink. Finally, a deep gap in the disc can be easily seen for Run 4.

4.7.1 Artificial viscosity implementation in PHANTOM

PHANTOM uses a modified version of the Cullen and Dehnen (2010) α viscosity switch utilizing the derivative of the velocity divergence, as described in Price et al. (2017). This prescription works with the so called signal speed, v_{sig} , defined for an interacting particle pair a and b as

$$v_{\text{sig},a} = \alpha_a^{AV} c_{s,a} + \beta^{AV} | \mathbf{v}_{\mathbf{a},\mathbf{b}} \cdot \hat{\mathbf{r}}_{\mathbf{ab}} | \quad (4.28)$$

where $c_{s,a}$ is the sound speed for particle a and $v_{a,b} \equiv v_a - v_b$ is the velocity difference between particles a and b . Finally, $\hat{\mathbf{r}}_{\mathbf{ab}}$ is the unit vector between a and b . As

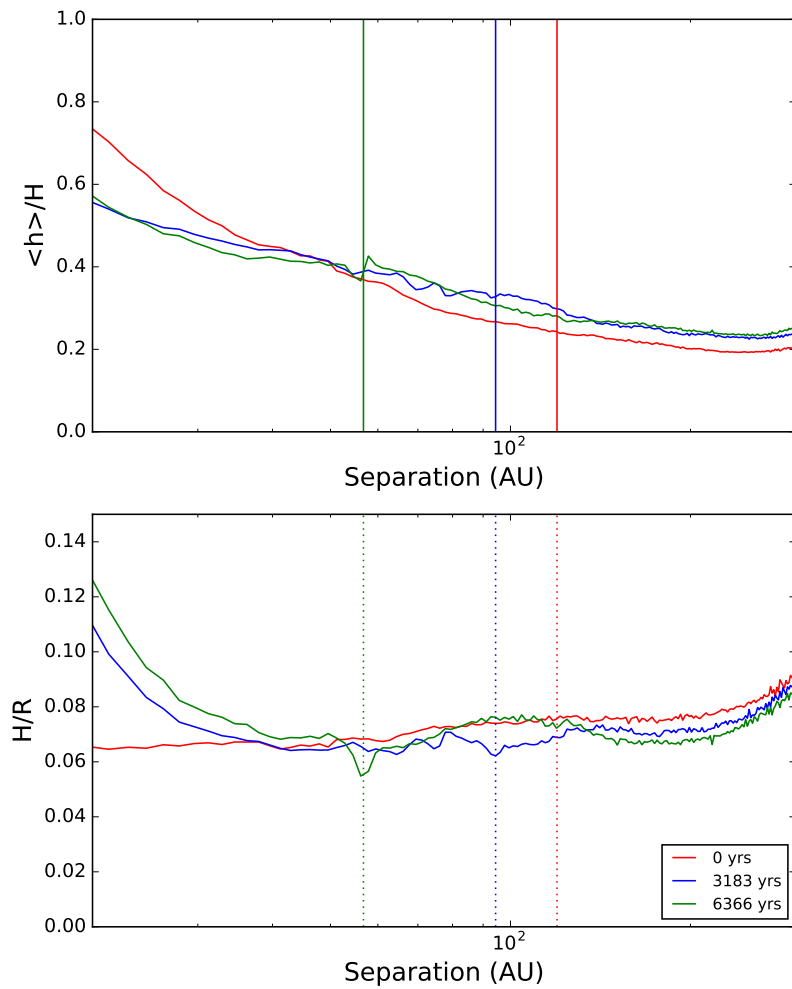


FIGURE 4.18: SPH particle smoothing length ratio to disc scale-height, H , against radius. The red line is the initial condition for the disc, whereas the blue and green lines are at approximately 3000 and 6000 years. The vertical lines of the matching colour correspond to the respective planet locations in the disc.

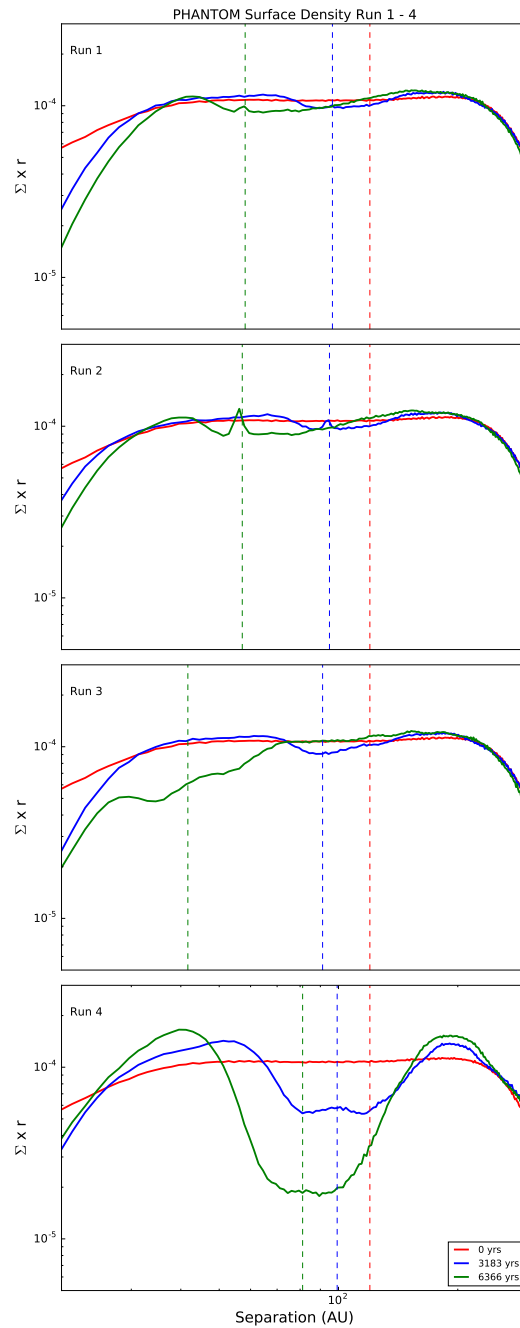


FIGURE 4.19: Surface density plots for the four runs evolved using PHANTOM. Initial profile (red) is the same for all four cases as expected due to the same initial conditions being used. Dashed lines show planet location at matching time as solid curves.

Eq. 4.28 shows α_a^{AV} and β^{AV} are important for controlling the communication between particles; communication becomes most important when trying to detect shocks and to prevent interpenetration between particles. Previous studies, Monaghan (1997) showed a $\beta^{\text{AV}} \geq 2$ is required to prevent particle interpenetration. However, further study (Price and Federrath, 2010) showed $\beta^{\text{AV}} = 4$ was needed for high Mach number, $M > 2$, situations which can be seen in protoplanetary discs.

α_a^{AV} will switch between 0 and 1 depending on conditions that can be set self-consistently in the code by using the gradient of the velocity divergence, (Cullen and Dehnen, 2010). We will now discuss the implementation of this switch in PHANTOM.

While the use of a signal speed is common the implementation of the switch controlling α_a^{AV} can vary greatly between codes. The implementation for artificial viscosity in PHANTOM is as follows, (a more detailed discussion can be found in Price et al. (2017))

$$\alpha_{\text{loc},a} = \min \left(\frac{10h_a^2 A_a}{c_{s,a}^2}, \text{ff}_{\text{max}} \right). \quad (4.29)$$

where $\alpha_{\text{max}} = 1$, and A_a is the shock indicator from Cullen and Dehnen (2010). A_a is briefly the normalised maximum between the negative of the gradient of the velocity divergence of particle a and 0. If $\alpha_{\text{loc},a} > \alpha_a$ then $\alpha_a = \alpha_{\text{loc},a}$, otherwise, α_a is evolved using,

$$\frac{\partial \alpha_a}{\partial t} = - \frac{(\alpha_a - \alpha_{\text{loc},a})}{\tau_a} \quad (4.30)$$

where $\tau_a \equiv h / (\omega_{\text{decay}} v_{\text{sig},a})$ (Morris and Monaghan, 1997) and ω_{decay} is set to 0.1. Eq. 4.30 is then used in the integrator.

$v_{\text{sig},a}$ appears in the equations of motion, momentum and internal energy equations for PHANTOM meaning the setting of α_a^{AV} and β^{AV} crucial for correctly controlling the evolution of a particle.

The selection of α_a^{AV} and β^{AV} is critical for capturing shocks. However, the latter setting and implementation is not universal. For example, α_a^{AV} and β^{AV} can be set separately in PHANTOM, whereas in SPHINX it is the ratio of $\alpha_a^{\text{AV}} / \beta^{\text{AV}}$ which is used for the viscosity switch. In this case β^{AV} is fixed and α_a^{AV} allowed to vary. The effect of this difference in implementation is not fully understood. This simple difference in implementation of the same viscosity switch highlights the problems of comparing results between codes.

4.8 Conclusions

Giant Planets can be born in the outer region of protoplanetary discs through GI, starting life as a self-gravitating gas fragment. Planet migration from the outer regions of protoplanetary discs may explain why observations show few of these planets at wide separations. The migration rates of these gas fragments are crucial in understanding their fate; fast migration could lead to the fragments disruption through tidal stripping or slower migration can allow the fragment to collapse and form a giant planet. We have run a suite of simulations to test the migration of massive protoplanets embedded in a protoplanetary disc with a full 3D treatment. While there is qualitatively good agreement between codes there is some substantial quantitative differences, namely the $\sim 50\%$ difference in migration rate and accretion rate. While significant, this is currently less than the uncertainties in the physics of the thermodynamics and grain physics involved in the problem.

Chapter 5

Conclusion

In this thesis I have considered several physical processes important for the Tidal Downsizing scenario for planet formation. In this scenario self-gravitating protoplanetary discs fragment into gas clump these can be seen as analogous to the first cores in star formation. They are only loosely bound extended objects that are still in the process of collapsing. Once the fragment is formed torques from the disc begin the migration process and the fragment migrates radially in the disc. There follows a competition between contraction and migration to determine the fragments fate. If the fragment can contract rapidly enough it will form a gas giant or brown dwarf. If the fragment is still extended due to slow cooling or heating processes the fragment can be tidally stripped or disrupted. In this case, a solid rocky core is left, the remaining gas and dust is released back into the disc, and larger bodies formed in the fragment can form into a debris disc.

The work reported in this thesis aimed at constraining TD hypothesis through calculations and predictions that could be compared to observations.

In Chapter 2, in particular, I have studied the abundance of different components of planetary systems as a function of system metallicity and contrasted the results with the Core Accretion scenario for planet formation. In CA, planetesimals are the foundations from which all planets grow. The theory predicts

that at high metallicities planetesimal formation is much easier due to the larger reservoir of metals. More planetesimals means the core growth rate is shorter and therefore the formation of gas giants is more likely, as the earlier the core is formed, the longer the planet has to accrete gas. This leads nicely to the observed correlation between gas giants and metallicity (Ida and Lin, 2004b; Mordasini et al., 2009). Planetesimals are also the component parts of a debris disc so DD's should also correlate with metallicity in this picture. However it is seen that DD do not correlate with host metallicity. In contrast, in TD the presence of a gas giant a few AU distance from the star signals that at least this fragment, born at ~ 100 or more AU from the star, was able to migrate inward all this distance without being tidally disrupted. This also means that the fragment did not release any large solids that it could have synthesised inside, thus making the presence of a debris disc less likely. While multi-fragment discs will weaken these strong predictions (see §3.5.3), we still expect some anticorrelation between DDs and gas giants, as observed, whereas sub-giant planets should correlate to some degree with DD presence. Furthermore, as tidal disruptions are less likely at high $[M/H]$, our model naturally explains why DDs do not correlate with host star's metallicity.

Chapter 3, on the other hand, presented results of a code comparison project investigating migration of giant planets in the outer regions of protoplanetary discs. Understanding the migration of these planets is crucial for a better population synthesis modelling reported in Chapter 2. Migration of giant planets is a natural mechanism for explaining the lack of planets seen at wide separations. To test the migration of massive protoplanets embedded in a protoplanetary disc we have run a suite of simulations with a full 3D treatment. While there is qualitatively good agreement between codes there is some substantial quantitative differences. These differences coming from a range of factors including complex

implementations of: artificial viscosity and sink particle accretion.

Finally, in Chapter 4 I presented my work on implementing an implicit timestep for the two-fluid dust scheme into the PHANTOMcode, as well as tests to show the current state of the implementation. Current dust schemes in SPH fall into either the one-fluid model for very small stokes number particles that are well coupled to the gas or the two-fluid model. The two-fluid model treats the dust as a second pressureless fluid that interacts with gas by using a drag term in the evolution equations. This method is best used for dust that has a large stokes number and thus well de-coupled from the gas. However, the integration scheme can become very slow when a dust particles stopping time approaches the timestep. This forces the code to take smaller timesteps to resolve the stopping time. The implicit integration scheme I have been working on would remove the necessity to go to shorter timesteps but estimating the change in dust velocity and not calculating it directly as in the explicit scheme. The implementation is not completely finished, there are still bugs remaining in the implementation. Specifically surrounding the sub-timestepping and super-timestep aspects of the leapfrog algorithm. In simple tests where these more complex timestepping algorithms are not used the implicit dust scheme does work and the expected analytic drag relation is recovered.

5.1 Future Work

Some of the issues I am interested in pursuing later on are: (i) dust and pebble accretion onto self-gravitating clumps in 3D disc simulations; (ii) Grain dynamics once the clump has been disrupted; (iii) Formation of planetesimals inside the gas clumps and how this ties into my work on the formation of debris discs in the TD scenario.

1. HL tau - planets are too young to be formed through core accretion and too low mass to be formed through gravitational instability.
2. rapid migration from wide separations
3. Internals of self-gravitating clump mechanics
4. The inclusion of Dust to 3D models of planet formation through TD.

Bibliography

- Adams, F. C. et al. (2006). “Early Evolution of Stellar Groups and Clusters: Environmental Effects on Forming Planetary Systems”. In: *ApJ* 641, pp. 504–525. DOI: [10.1086/500393](https://doi.org/10.1086/500393). eprint: [astro-ph/0512330](https://arxiv.org/abs/astro-ph/0512330).
- Alexander, R. D. and P. J. Armitage (2007). “Dust dynamics during protoplanetary disc clearing”. In: *MNRAS* 375, pp. 500–512. DOI: [10.1111/j.1365-2966.2006.11341.x](https://doi.org/10.1111/j.1365-2966.2006.11341.x). eprint: [astro-ph/0611821](https://arxiv.org/abs/astro-ph/0611821).
- (2009). “Giant Planet Migration, Disk Evolution, and the Origin of Transitional Disks”. In: *ApJ* 704, pp. 989–1001. DOI: [10.1088/0004-637X/704/2/989](https://doi.org/10.1088/0004-637X/704/2/989). arXiv: [0909.0004](https://arxiv.org/abs/0909.0004) [[astro-ph](https://arxiv.org/abs/astro-ph).EP].
- Alexander, R. D., C. J. Clarke, and J. E. Pringle (2006). “Photoevaporation of protoplanetary discs - II. Evolutionary models and observable properties”. In: *MNRAS* 369, pp. 229–239. DOI: [10.1111/j.1365-2966.2006.10294.x](https://doi.org/10.1111/j.1365-2966.2006.10294.x). eprint: [arXiv:astro-ph/0603254](https://arxiv.org/abs/astro-ph/0603254).
- Alibert, Y. et al. (2005). “Models of giant planet formation with migration and disc evolution”. In: *A&A* 434, pp. 343–353. DOI: [10.1051/0004-6361:20042032](https://doi.org/10.1051/0004-6361:20042032). eprint: [arXiv:astro-ph/0412444](https://arxiv.org/abs/astro-ph/0412444).
- ALMA Partnership et al. (2015). “The 2014 ALMA Long Baseline Campaign: First Results from High Angular Resolution Observations toward the HL Tau Region”. In: *ApJL* 808, L3, p. L3. DOI: [10.1088/2041-8205/808/1/L3](https://doi.org/10.1088/2041-8205/808/1/L3). arXiv: [1503.02649](https://arxiv.org/abs/1503.02649) [[astro-ph](https://arxiv.org/abs/astro-ph).SR].

- Andrews, S. M. and J. P. Williams (2005). "Circumstellar Dust Disks in Taurus-Auriga: The Submillimeter Perspective". In: *ApJ* 631, pp. 1134–1160. DOI: [10.1086/432712](https://doi.org/10.1086/432712). eprint: [arXiv:astro-ph/0506187](https://arxiv.org/abs/astro-ph/0506187).
- Armitage, P. J. (2010). *Astrophysics of Planet Formation*.
- Armitage, P. J. and I. A. Bonnell (2002). "The brown dwarf desert as a consequence of orbital migration". In: *MNRAS* 330, pp. L11–L14. DOI: [10.1046/j.1365-8711.2002.05213.x](https://doi.org/10.1046/j.1365-8711.2002.05213.x). eprint: [arXiv:astro-ph/0112001](https://arxiv.org/abs/astro-ph/0112001).
- Artymowicz, P. (2004). "Dynamics of Gaseous Disks with Planets". In: *Debris Disks and the Formation of Planets*. Ed. by L. Caroff et al. Vol. 324. Astronomical Society of the Pacific Conference Series, p. 39.
- Auvergne, M. et al. (2009). "The CoRoT satellite in flight: description and performance". In: *A&A* 506, pp. 411–424. DOI: [10.1051/0004-6361/200810860](https://doi.org/10.1051/0004-6361/200810860). arXiv: [0901.2206](https://arxiv.org/abs/0901.2206) [[astro-ph](https://arxiv.org/abs/astro-ph).SR].
- Bally, J. and N. Z. Scoville (1982). "Structure and evolution of molecular clouds near H II regions. II - The disk constrained H II region, S106". In: *ApJ* 255, pp. 497–509. DOI: [10.1086/159850](https://doi.org/10.1086/159850).
- Balsara, D. S. (1995). "von Neumann stability analysis of smooth particle hydrodynamics – suggestions for optimal algorithms". In: *Journal of Computational Physics* 121, pp. 357–372. DOI: [10.1016/S0021-9991\(95\)90221-X](https://doi.org/10.1016/S0021-9991(95)90221-X).
- Baruteau, C. and F. Masset (2008). "Type I Planetary Migration in a Self-Gravitating Disk". In: *ApJ* 678, pp. 483–497. DOI: [10.1086/529487](https://doi.org/10.1086/529487). arXiv: [0801.4413](https://arxiv.org/abs/0801.4413).
- Baruteau, C., F. Meru, and S.-J. Paardekooper (2011). "Rapid inward migration of planets formed by gravitational instability". In: *MNRAS* 416, pp. 1971–1982. DOI: [10.1111/j.1365-2966.2011.19172.x](https://doi.org/10.1111/j.1365-2966.2011.19172.x). arXiv: [1106.0487](https://arxiv.org/abs/1106.0487) [[astro-ph](https://arxiv.org/abs/astro-ph).EP].

- Bate, M. R. (2018). “On the diversity and statistical properties of protostellar discs”. In: *MNRAS* 475, pp. 5618–5658. DOI: [10.1093/mnras/sty169](https://doi.org/10.1093/mnras/sty169). arXiv: [1801.07721](https://arxiv.org/abs/1801.07721) [astro-ph.SR].
- Bate, M. R., I. A. Bonnell, and V. Bromm (2003). “The formation of a star cluster: predicting the properties of stars and brown dwarfs”. In: *MNRAS* 339, pp. 577–599. DOI: [10.1046/j.1365-8711.2003.06210.x](https://doi.org/10.1046/j.1365-8711.2003.06210.x). eprint: [arXiv: astro-ph/0212380](https://arxiv.org/abs/astro-ph/0212380).
- Bate, M. R., I. A. Bonnell, and N. M. Price (1995a). “Modelling accretion in protobinary systems”. In: *MNRAS* 277, pp. 362–376. DOI: [10.1093/mnras/277.2.362](https://doi.org/10.1093/mnras/277.2.362). eprint: [astro-ph/9510149](https://arxiv.org/abs/astro-ph/9510149).
- (1995b). “Modelling accretion in protobinary systems”. In: *MNRAS* 277, pp. 362–376.
- Begelman, M. C., C. F. McKee, and G. A. Shields (1983). “Compton heated winds and coronae above accretion disks. I Dynamics”. In: *ApJ* 271, pp. 70–88. DOI: [10.1086/161178](https://doi.org/10.1086/161178).
- Benz, W. (1990). “Smooth Particle Hydrodynamics - a Review”. In: *Numerical Modelling of Nonlinear Stellar Pulsations Problems and Prospects*. Ed. by J. R. Buchler, pp. 269–+.
- Biller, B. A. et al. (2013). “The Gemini/NICI Planet-Finding Campaign: The Frequency of Planets around Young Moving Group Stars”. In: *ApJ* 777, 160, p. 160. DOI: [10.1088/0004-637X/777/2/160](https://doi.org/10.1088/0004-637X/777/2/160). arXiv: [1309.1462](https://arxiv.org/abs/1309.1462) [astro-ph.EP].
- Birkby, J. L. et al. (2017). “Discovery of Water at High Spectral Resolution in the Atmosphere of 51 Peg b”. In: *AJ* 153, 138, p. 138. DOI: [10.3847/1538-3881/aa5c87](https://doi.org/10.3847/1538-3881/aa5c87). arXiv: [1701.07257](https://arxiv.org/abs/1701.07257) [astro-ph.EP].
- Bodenheimer, P. (1974). “Calculations of the early evolution of Jupiter”. In: *Icarus* 23, pp. 319–325. DOI: [10.1016/0019-1035\(74\)90050-5](https://doi.org/10.1016/0019-1035(74)90050-5).

- Bodenheimer, P. et al. (1980). "Calculations of the evolution of the giant planets". In: *Icarus* 41, pp. 293–308. DOI: [10.1016/0019-1035\(80\)90012-3](https://doi.org/10.1016/0019-1035(80)90012-3).
- Bodenheimer, P. et al., eds. (2007). *Numerical Methods in Astrophysics: An Introduction*.
- Boley, A. C. et al. (2010). "Clumps in the outer disk by disk instability: Why they are initially gas giants and the legacy of disruption". In: *Icarus* 207, pp. 509–516. DOI: [10.1016/j.icarus.2010.01.015](https://doi.org/10.1016/j.icarus.2010.01.015). arXiv: [0909.4543](https://arxiv.org/abs/0909.4543).
- Booth, R. A., D. Sijacki, and C. J. Clarke (2015). "Smoothed particle hydrodynamics simulations of gas and dust mixtures". In: *MNRAS* 452, pp. 3932–3947. DOI: [10.1093/mnras/stv1486](https://doi.org/10.1093/mnras/stv1486). arXiv: [1507.01007](https://arxiv.org/abs/1507.01007) [astro-ph.EP].
- Borucki, W. J. et al. (2010). "Kepler Planet-Detection Mission: Introduction and First Results". In: *Science* 327, p. 977. DOI: [10.1126/science.1185402](https://doi.org/10.1126/science.1185402).
- Boss, A. P. (1997). "Giant planet formation by gravitational instability." In: *Science* 276, pp. 1836–1839. DOI: [10.1126/science.276.5320.1836](https://doi.org/10.1126/science.276.5320.1836).
- Bowler, B. P. et al. (2015). "Planets around Low-mass Stars (PALMS). IV. The Outer Architecture of M Dwarf Planetary Systems". In: *ApJS* 216, 7, p. 7. DOI: [10.1088/0067-0049/216/1/7](https://doi.org/10.1088/0067-0049/216/1/7). arXiv: [1411.3722](https://arxiv.org/abs/1411.3722) [astro-ph.EP].
- Bryden, G. et al. (2009). "Planets and Debris Disks: Results from a Spitzer/MIPS Search for Infrared Excess". In: *ApJ* 705, pp. 1226–1236. DOI: [10.1088/0004-637X/705/2/1226](https://doi.org/10.1088/0004-637X/705/2/1226).
- Buchhave, L. A. and D. W. Latham (2015). "The Metallicities of Stars with and without Transiting Planets". In: *ApJ* 808, 187, p. 187. DOI: [10.1088/0004-637X/808/2/187](https://doi.org/10.1088/0004-637X/808/2/187). arXiv: [1507.03557](https://arxiv.org/abs/1507.03557) [astro-ph.EP].
- Buchhave, L. A. et al. (2012). "An abundance of small exoplanets around stars with a wide range of metallicities". In: *NATURE* 486, pp. 375–377. DOI: [10.1038/nature11121](https://doi.org/10.1038/nature11121).

- Buchhave, L. A. et al. (2014). “Three regimes of extrasolar planet radius inferred from host star metallicities”. In: *NATURE* 509, pp. 593–595. DOI: [10.1038/nature13254](https://doi.org/10.1038/nature13254). arXiv: [1405.7695](https://arxiv.org/abs/1405.7695) [astro-ph.EP].
- Burrows, A. et al. (2000). “On the Radii of Close-in Giant Planets”. In: *ApJL* 534, pp. L97–L100. DOI: [10.1086/312638](https://doi.org/10.1086/312638). eprint: [arXiv:astro-ph/0003185](https://arxiv.org/abs/astro-ph/0003185).
- Burrows, A. et al. (2001). “The theory of brown dwarfs and extrasolar giant planets”. In: *Reviews of Modern Physics* 73, pp. 719–765. DOI: [10.1103/RevModPhys.73.719](https://doi.org/10.1103/RevModPhys.73.719). eprint: [arXiv:astro-ph/0103383](https://arxiv.org/abs/astro-ph/0103383).
- Cameron, A. G. W., W. M. Decamp, and P. Bodenheimer (1982). “Evolution of giant gaseous protoplanets embedded in the primitive solar nebula”. In: *Icarus* 49, pp. 298–312. DOI: [10.1016/0019-1035\(82\)90038-0](https://doi.org/10.1016/0019-1035(82)90038-0).
- Cha, S.-H. and S. Nayakshin (2011). “A numerical simulation of a ‘Super-Earth’ core delivery from 100 to 8 au”. In: *MNRAS* 415, pp. 3319–3334. DOI: [10.1111/j.1365-2966.2011.18953.x](https://doi.org/10.1111/j.1365-2966.2011.18953.x). arXiv: [1010.1489](https://arxiv.org/abs/1010.1489) [astro-ph.EP].
- Chauvin, G. et al. (2015). “The VLT/NaCo large program to probe the occurrence of exoplanets and brown dwarfs at wide orbits. II. Survey description, results, and performances”. In: *A&A* 573, A127, A127. DOI: [10.1051/0004-6361/201423564](https://doi.org/10.1051/0004-6361/201423564). arXiv: [1405.1560](https://arxiv.org/abs/1405.1560) [astro-ph.EP].
- Choquet, É. et al. (2015). “First images of debris disks around TWA 7, TWA 25, HD 35650, and HD 377”. In: *ArXiv e-prints*. arXiv: [1512.02220](https://arxiv.org/abs/1512.02220) [astro-ph.SR].
- Clarke, C. J., A. Gendrin, and M. Sotomayor (2001). “The dispersal of circumstellar discs: the role of the ultraviolet switch”. In: *MNRAS* 328, pp. 485–491. DOI: [10.1046/j.1365-8711.2001.04891.x](https://doi.org/10.1046/j.1365-8711.2001.04891.x).
- Crida, A., A. Morbidelli, and F. Masset (2006). “On the width and shape of gaps in protoplanetary disks”. In: *Icarus* 181, pp. 587–604. DOI: [10.1016/j.icarus.2005.10.007](https://doi.org/10.1016/j.icarus.2005.10.007). eprint: [arXiv:astro-ph/0511082](https://arxiv.org/abs/astro-ph/0511082).

- Cuadra, J. et al. (2006). “Galactic Centre stellar winds and Sgr A* accretion”. In: *MNRAS* 366, pp. 358–372. DOI: [10.1111/j.1365-2966.2005.09837.x](https://doi.org/10.1111/j.1365-2966.2005.09837.x).
- Cullen, L. and W. Dehnen (2010). “Inviscid smoothed particle hydrodynamics”. In: *MNRAS* 408, pp. 669–683. DOI: [10.1111/j.1365-2966.2010.17158.x](https://doi.org/10.1111/j.1365-2966.2010.17158.x). arXiv: [1006.1524](https://arxiv.org/abs/1006.1524) [astro-ph.IM].
- Cuzzi, J. N., R. C. Hogan, and K. Shariff (2008). “Toward Planetesimals: Dense Chondrule Clumps in the Protoplanetary Nebula”. In: *ApJ* 687, pp. 1432–1447. DOI: [10.1086/591239](https://doi.org/10.1086/591239). arXiv: [0804.3526](https://arxiv.org/abs/0804.3526).
- Damjanov, I. et al. (2007). “A Comprehensive View of Circumstellar Disks in Chamaeleon I: Infrared Excess, Accretion Signatures, and Binarity”. In: *ApJ* 670, pp. 1337–1346. DOI: [10.1086/522079](https://doi.org/10.1086/522079). arXiv: [0708.0266](https://arxiv.org/abs/0708.0266).
- Dehnen, W. (2000). “A Very Fast and Momentum-conserving Tree Code”. In: *ApJL* 536, pp. L39–L42.
- (2001). “Towards optimal softening in three-dimensional N-body codes - I. Minimizing the force error”. In: *MNRAS* 324, pp. 273–291.
- Dehnen, W. and H. Aly (2012). “Improving convergence in smoothed particle hydrodynamics simulations without pairing instability”. In: *MNRAS* 425, pp. 1068–1082. DOI: [10.1111/j.1365-2966.2012.21439.x](https://doi.org/10.1111/j.1365-2966.2012.21439.x). arXiv: [1204.2471](https://arxiv.org/abs/1204.2471) [astro-ph.IM].
- Deng, H., L. Mayer, and F. Meru (2017). “Convergence of the critical cooling rate for protoplanetary disk fragmentation achieved; the key role of numerical dissipation of angular momentum”. In: *ArXiv e-prints*. arXiv: [1706.00417](https://arxiv.org/abs/1706.00417) [astro-ph.EP].
- Dipierro, G. et al. (2015). “On planet formation in HL Tau”. In: *MNRAS* 453, pp. L73–L77. DOI: [10.1093/mnrasl/slv105](https://doi.org/10.1093/mnrasl/slv105). arXiv: [1507.06719](https://arxiv.org/abs/1507.06719) [astro-ph.EP].

- Dipierro, G. et al. (2016). “Two mechanisms for dust gap opening in protoplanetary discs”. In: *MNRAS*. DOI: [10.1093/mnras1/slw032](https://doi.org/10.1093/mnras1/slw032). arXiv: [1602.07457](https://arxiv.org/abs/1602.07457) [[astro-ph.EP](#)].
- Donnison, J. R. and I. P. Williams (1975). “The effects of tidal forces on the stability and dispersal rates of a protoplanet”. In: *MNRAS* 172, pp. 257–269.
- Dressing, C. D. and D. Charbonneau (2015). “The Occurrence of Potentially Habitable Planets Orbiting M Dwarfs Estimated from the Full Kepler Dataset and an Empirical Measurement of the Detection Sensitivity”. In: *ApJ* 807, 45, p. 45. DOI: [10.1088/0004-637X/807/1/45](https://doi.org/10.1088/0004-637X/807/1/45). arXiv: [1501.01623](https://arxiv.org/abs/1501.01623) [[astro-ph.EP](#)].
- Duffell, P. C. and A. I. MacFadyen (2013). “Gap Opening by Extremely Low-mass Planets in a Viscous Disk”. In: *ApJ* 769, 41, p. 41. DOI: [10.1088/0004-637X/769/1/41](https://doi.org/10.1088/0004-637X/769/1/41). arXiv: [1302.1934](https://arxiv.org/abs/1302.1934) [[astro-ph.EP](#)].
- Durisen, R. H. et al. (2007). “Gravitational Instabilities in Gaseous Protoplanetary Disks and Implications for Giant Planet Formation”. In: *Protostars and Planets V*, pp. 607–622. eprint: [arXiv:astro-ph/0603179](https://arxiv.org/abs/astro-ph/0603179).
- Dürmann, C. and W. Kley (2015). “Migration of massive planets in accreting disks”. In: *A&A* 574, A52, A52. DOI: [10.1051/0004-6361/201424837](https://doi.org/10.1051/0004-6361/201424837). arXiv: [1411.3190](https://arxiv.org/abs/1411.3190) [[astro-ph.EP](#)].
- Ercolano, B., C. J. Clarke, and J. J. Drake (2009). “X-Ray Irradiated Protoplanetary Disk Atmospheres. II. Predictions from Models in Hydrostatic Equilibrium”. In: *ApJ* 699, pp. 1639–1649. DOI: [10.1088/0004-637X/699/2/1639](https://doi.org/10.1088/0004-637X/699/2/1639). arXiv: [0905.1001](https://arxiv.org/abs/0905.1001) [[astro-ph.GA](#)].
- Fabrycky, D. C. et al. (2014). “Architecture of Kepler’s Multi-transiting Systems. II. New Investigations with Twice as Many Candidates”. In: *ApJ* 790, 146, p. 146. DOI: [10.1088/0004-637X/790/2/146](https://doi.org/10.1088/0004-637X/790/2/146). arXiv: [1202.6328](https://arxiv.org/abs/1202.6328) [[astro-ph.EP](#)].

- Fischer, D. A. and J. Valenti (2005). “The Planet-Metallicity Correlation”. In: *ApJ* 622, pp. 1102–1117. DOI: [10.1086/428383](https://doi.org/10.1086/428383).
- Flaherty, K. M. et al. (2015). “Weak Turbulence in the HD 163296 Protoplanetary Disk Revealed by ALMA CO Observations”. In: *ApJ* 813, 99, p. 99. DOI: [10.1088/0004-637X/813/2/99](https://doi.org/10.1088/0004-637X/813/2/99). arXiv: [1510.01375](https://arxiv.org/abs/1510.01375) [[astro-ph.SR](#)].
- Fletcher, M. and S. Nayakshin (2016). “Planets, debris and their host metallicity correlations”. In: *MNRAS* 461, pp. 1850–1861. DOI: [10.1093/mnras/stw1376](https://doi.org/10.1093/mnras/stw1376). arXiv: [1605.08329](https://arxiv.org/abs/1605.08329) [[astro-ph.EP](#)].
- Forgan, D. and K. Rice (2011). “The Jeans mass as a fundamental measure of self-gravitating disc fragmentation and initial fragment mass”. In: *MNRAS* 417, pp. 1928–1937. DOI: [10.1111/j.1365-2966.2011.19380.x](https://doi.org/10.1111/j.1365-2966.2011.19380.x). arXiv: [1107.0831](https://arxiv.org/abs/1107.0831) [[astro-ph.EP](#)].
- (2012). “A lower angular momentum limit for self-gravitating protostellar disc fragmentation”. In: *MNRAS* 420, pp. 299–308. DOI: [10.1111/j.1365-2966.2011.20034.x](https://doi.org/10.1111/j.1365-2966.2011.20034.x). arXiv: [1110.4212](https://arxiv.org/abs/1110.4212) [[astro-ph.SR](#)].
- (2013a). “The effect of irradiation on the Jeans mass in fragmenting self-gravitating protostellar discs”. In: *MNRAS* 430, pp. 2082–2089. DOI: [10.1093/mnras/stt032](https://doi.org/10.1093/mnras/stt032). arXiv: [1301.1151](https://arxiv.org/abs/1301.1151) [[astro-ph.SR](#)].
- (2013b). “Towards a population synthesis model of objects formed by self-gravitating disc fragmentation and tidal downsizing”. In: *MNRAS* 432, pp. 3168–3185. DOI: [10.1093/mnras/stt672](https://doi.org/10.1093/mnras/stt672). arXiv: [1304.4978](https://arxiv.org/abs/1304.4978) [[astro-ph.EP](#)].
- Forgan, D. H. et al. (2018). “Towards a population synthesis model of self-gravitating disc fragmentation and tidal downsizing II: the effect of fragment-fragment interactions”. In: *MNRAS* 474, pp. 5036–5048. DOI: [10.1093/mnras/stx2870](https://doi.org/10.1093/mnras/stx2870). arXiv: [1711.01133](https://arxiv.org/abs/1711.01133) [[astro-ph.EP](#)].

- Galvagni, M. and L. Mayer (2014). “Early evolution of clumps formed via gravitational instability in protoplanetary discs: precursors of Hot Jupiters?” In: *MNRAS* 437, pp. 2909–2921. DOI: [10.1093/mnras/stt2108](https://doi.org/10.1093/mnras/stt2108).
- Galvagni, M. et al. (2012). “The collapse of protoplanetary clumps formed through disc instability: 3D simulations of the pre-dissociation phase”. In: *MNRAS* 427, pp. 1725–1740. DOI: [10.1111/j.1365-2966.2012.22096.x](https://doi.org/10.1111/j.1365-2966.2012.22096.x). arXiv: [1209.2129](https://arxiv.org/abs/1209.2129) [[astro-ph.EP](#)].
- Gammie, C. F. (2001). “Nonlinear Outcome of Gravitational Instability in Cooling, Gaseous Disks”. In: *ApJ* 553, pp. 174–183.
- Gillon, M. et al. (2017). “Seven temperate terrestrial planets around the nearby ultracool dwarf star TRAPPIST-1”. In: *NATURE* 542, pp. 456–460. DOI: [10.1038/nature21360](https://doi.org/10.1038/nature21360). arXiv: [1703.01424](https://arxiv.org/abs/1703.01424) [[astro-ph.EP](#)].
- Gingold, R. A. and J. J. Monaghan (1982). “Kernel estimates as a basis for general particle methods in hydrodynamics”. In: *Journal of Computational Physics* 46, pp. 429–453. DOI: [10.1016/0021-9991\(82\)90025-0](https://doi.org/10.1016/0021-9991(82)90025-0).
- Goldreich, P. and S. Tremaine (1979). “The excitation of density waves at the Lindblad and corotation resonances by an external potential”. In: *ApJ* 233, pp. 857–871. DOI: [10.1086/157448](https://doi.org/10.1086/157448).
- (1980). “Disk-satellite interactions”. In: *ApJ* 241, pp. 425–441. DOI: [10.1086/158356](https://doi.org/10.1086/158356).
- Goldreich, P. and W. R. Ward (1973). “The Formation of Planetesimals”. In: *ApJ* 183, pp. 1051–1062. DOI: [10.1086/152291](https://doi.org/10.1086/152291).
- Gonzalez, G. (1999). “Are stars with planets anomalous?” In: *MNRAS* 308, pp. 447–458. DOI: [10.1046/j.1365-8711.1999.02717.x](https://doi.org/10.1046/j.1365-8711.1999.02717.x).

- Gould, A. et al. (2010). “Frequency of Solar-like Systems and of Ice and Gas Giants Beyond the Snow Line from High-magnification Microlensing Events in 2005–2008”. In: *ApJ* 720, pp. 1073–1089. DOI: [10.1088/0004-637X/720/2/1073](https://doi.org/10.1088/0004-637X/720/2/1073). arXiv: [1001.0572](https://arxiv.org/abs/1001.0572) [astro-ph.EP].
- Greenberg, R. et al. (1978). “Planetesimals to planets - Numerical simulation of collisional evolution”. In: *Icarus* 35, pp. 1–26. DOI: [10.1016/0019-1035\(78\)90057-X](https://doi.org/10.1016/0019-1035(78)90057-X).
- Haisch Jr., K. E., E. A. Lada, and C. J. Lada (2001). “Disk Frequencies and Lifetimes in Young Clusters”. In: *ApJL* 553, pp. L153–L156. DOI: [10.1086/320685](https://doi.org/10.1086/320685). eprint: [astro-ph/0104347](https://arxiv.org/abs/astro-ph/0104347).
- Hall, C., D. Forgan, and K. Rice (2017). “Identifying and analysing protostellar disc fragments in smoothed particle hydrodynamics simulations”. In: *MNRAS* 470, pp. 2517–2538. DOI: [10.1093/mnras/stx1244](https://doi.org/10.1093/mnras/stx1244). arXiv: [1705.06690](https://arxiv.org/abs/1705.06690) [astro-ph.EP].
- Hartmann, L. and S. J. Kenyon (1996). “The FU Orionis Phenomenon”. In: *ARA&A* 34, pp. 207–240. DOI: [10.1146/annurev.astro.34.1.207](https://doi.org/10.1146/annurev.astro.34.1.207).
- Hayashi, C., K. Nakazawa, and Y. Nakagawa (1985). “Formation of the solar system”. In: *Protostars and Planets II*. Ed. by D. C. Black and M. S. Matthews, pp. 1100–1153.
- Helled, R. and P. Bodenheimer (2011). “The effects of metallicity and grain growth and settling on the early evolution of gaseous protoplanets”. In: *Icarus* 211, pp. 939–947. DOI: [10.1016/j.icarus.2010.09.024](https://doi.org/10.1016/j.icarus.2010.09.024). arXiv: [1005.4039](https://arxiv.org/abs/1005.4039) [astro-ph.EP].
- (2014). “The Formation of Uranus and Neptune: Challenges and Implications for Intermediate-mass Exoplanets”. In: *ApJ* 789, 69, p. 69. DOI: [10.1088/0004-637X/789/1/69](https://doi.org/10.1088/0004-637X/789/1/69). arXiv: [1404.5018](https://arxiv.org/abs/1404.5018) [astro-ph.EP].

- Helled, R., M. Podolak, and A. Kovetz (2008). “Grain sedimentation in a giant gaseous protoplanet”. In: *Icarus* 195, pp. 863–870. DOI: [10.1016/j.icarus.2008.01.007](https://doi.org/10.1016/j.icarus.2008.01.007). arXiv: [0801.2435](https://arxiv.org/abs/0801.2435).
- Helled, R. and G. Schubert (2008). “Core formation in giant gaseous protoplanets”. In: *Icarus* 198, pp. 156–162. DOI: [10.1016/j.icarus.2008.08.002](https://doi.org/10.1016/j.icarus.2008.08.002). arXiv: [0808.2787](https://arxiv.org/abs/0808.2787).
- Hellyer, B. (1970). “The fragmentation of the asteroids”. In: *MNRAS* 148, pp. 383–+.
- Hollenbach, D. et al. (1994). “Photoevaporation of disks around massive stars and application to ultracompact H II regions”. In: *ApJ* 428, pp. 654–669. DOI: [10.1086/174276](https://doi.org/10.1086/174276).
- Hopkins, P. F. (2015). “A new class of accurate, mesh-free hydrodynamic simulation methods”. In: *MNRAS* 450, pp. 53–110. DOI: [10.1093/mnras/stv195](https://doi.org/10.1093/mnras/stv195). arXiv: [1409.7395](https://arxiv.org/abs/1409.7395).
- Howard, A. W. et al. (2012). “Planet Occurrence within 0.25 AU of Solar-type Stars from Kepler”. In: *ApJS* 201, 15, p. 15. DOI: [10.1088/0067-0049/201/2/15](https://doi.org/10.1088/0067-0049/201/2/15). arXiv: [1103.2541](https://arxiv.org/abs/1103.2541) [[astro-ph.EP](#)].
- Hubber, D. et al. (2011a). *SEREN: A SPH code for star and planet formation simulations*. Astrophysics Source Code Library. ascl: [1102.010](https://ascl.net/1102.010).
- Hubber, D. A. et al. (2011b). “SEREN - a new SPH code for star and planet formation simulations. Algorithms and tests”. In: *A&A* 529, A27, A27. DOI: [10.1051/0004-6361/201014949](https://doi.org/10.1051/0004-6361/201014949). arXiv: [1102.0721](https://arxiv.org/abs/1102.0721) [[astro-ph.SR](#)].
- Hubickyj, O., P. Bodenheimer, and J. J. Lissauer (2005). “Accretion of the gaseous envelope of Jupiter around a 5–10 Earth-mass core”. In: *Icarus* 179, pp. 415–431. DOI: [10.1016/j.icarus.2005.06.021](https://doi.org/10.1016/j.icarus.2005.06.021).

- Humphries, R. J. and S. Nayakshin (2018). “Changes in the metallicity of gas giant planets due to pebble accretion”. In: *MNRAS*. DOI: [10.1093/mnras/sty569](https://doi.org/10.1093/mnras/sty569).
- Ida, S. and D. N. C. Lin (2004a). “Toward a Deterministic Model of Planetary Formation. I. A Desert in the Mass and Semimajor Axis Distributions of Extrasolar Planets”. In: *ApJ* 604, pp. 388–413. DOI: [10.1086/381724](https://doi.org/10.1086/381724). eprint: [astro-ph/0312144](https://arxiv.org/abs/astro-ph/0312144).
- (2004b). “Toward a Deterministic Model of Planetary Formation. II. The Formation and Retention of Gas Giant Planets around Stars with a Range of Metallicities”. In: *ApJ* 616, pp. 567–572. DOI: [10.1086/424830](https://doi.org/10.1086/424830).
- Johansen, A. et al. (2007). “Rapid planetesimal formation in turbulent circumstellar disks”. In: *NATURE* 448, pp. 1022–1025. DOI: [10.1038/nature06086](https://doi.org/10.1038/nature06086).
- Johansen, A. et al. (2014). “The Multifaceted Planetesimal Formation Process”. In: *Protostars and Planets VI, University of Arizona Press, Tucson*, pp. 547–570. DOI: [10.2458/azu_uapress_9780816531240-ch024](https://doi.org/10.2458/azu_uapress_9780816531240-ch024). arXiv: [1402.1344](https://arxiv.org/abs/1402.1344) [[astro-ph.EP](https://arxiv.org/abs/1402.1344)].
- Johansen, A. et al. (2015). “Growth of asteroids, planetary embryos, and Kuiper belt objects by chondrule accretion”. In: *Science Advances* 1, 1500109, p. 1500109. DOI: [10.1126/sciadv.1500109](https://doi.org/10.1126/sciadv.1500109). arXiv: [1503.07347](https://arxiv.org/abs/1503.07347) [[astro-ph.EP](https://arxiv.org/abs/1503.07347)].
- Johnstone, D., D. Hollenbach, and J. Bally (1998). “Photoevaporation of Disks and Clumps by Nearby Massive Stars: Application to Disk Destruction in the Orion Nebula”. In: *ApJ* 499, pp. 758–+. DOI: [10.1086/305658](https://doi.org/10.1086/305658).
- Kaufmann, T. et al. (2007). “Angular momentum transport and disc morphology in smoothed particle hydrodynamics simulations of galaxy formation”. In: *MNRAS* 375, pp. 53–67. DOI: [10.1111/j.1365-2966.2006.11314.x](https://doi.org/10.1111/j.1365-2966.2006.11314.x). eprint: [astro-ph/0601115](https://arxiv.org/abs/astro-ph/0601115).
- Kawabe, R. et al. (1993). “Discovery of a rotating protoplanetary gas disk around the young star GG Tauri”. In: *ApJL* 404, pp. L63–L66. DOI: [10.1086/186744](https://doi.org/10.1086/186744).

- Kenyon, S. J. and J. X. Luu (1999). “Accretion in the Early Kuiper Belt. II. Fragmentation”. In: *AJ* 118, pp. 1101–1119. DOI: [10.1086/300969](https://doi.org/10.1086/300969). eprint: [arXiv: astro-ph/9904115](https://arxiv.org/abs/astro-ph/9904115).
- Kipping, D. M. and E. Sandford (2016). “Observational biases for transiting planets”. In: *MNRAS* 463, pp. 1323–1331. DOI: [10.1093/mnras/stw1926](https://doi.org/10.1093/mnras/stw1926). arXiv: [1603.05662](https://arxiv.org/abs/1603.05662) [[astro-ph](https://arxiv.org/abs/astro-ph).EP].
- Kóspál, Á. et al. (2009). “On the Relationship Between Debris Disks and Planets”. In: *ApJL* 700, pp. L73–L77. DOI: [10.1088/0004-637X/700/2/L73](https://doi.org/10.1088/0004-637X/700/2/L73). arXiv: [0907.0028](https://arxiv.org/abs/0907.0028) [[astro-ph](https://arxiv.org/abs/astro-ph).SR].
- Kratter, K. M. and G. Lodato (2016). “Gravitational Instabilities in Circumstellar Disks”. In: *ArXiv e-prints*. arXiv: [1603.01280](https://arxiv.org/abs/1603.01280) [[astro-ph](https://arxiv.org/abs/astro-ph).SR].
- Kratter, K. M., R. A. Murray-Clay, and A. N. Youdin (2010). “The Runts of the Litter: Why Planets Formed Through Gravitational Instability Can Only Be Failed Binary Stars”. In: *ApJ* 710, pp. 1375–1386. DOI: [10.1088/0004-637X/710/2/1375](https://doi.org/10.1088/0004-637X/710/2/1375). arXiv: [0909.2644](https://arxiv.org/abs/0909.2644) [[astro-ph](https://arxiv.org/abs/astro-ph).EP].
- Kuiper, G. P. (1951b). “On the Origin of the Solar System”. In: *50th Anniversary of the Yerkes Observatory and Half a Century of Progress in Astrophysics*. Ed. by J. A. Hynek, pp. 357–+.
- (1951a). “On the Origin of the Solar System”. In: *Proceedings of the National Academy of Science* 37, pp. 1–14. DOI: [10.1073/pnas.37.1.1](https://doi.org/10.1073/pnas.37.1.1).
- Laibe, G. and D. J. Price (2011). “DUSTYBOX and DUSTYWAVE: two test problems for numerical simulations of two-fluid astrophysical dust-gas mixtures”. In: *MNRAS* 418, pp. 1491–1497. DOI: [10.1111/j.1365-2966.2011.19291.x](https://doi.org/10.1111/j.1365-2966.2011.19291.x). arXiv: [1106.1736](https://arxiv.org/abs/1106.1736) [[astro-ph](https://arxiv.org/abs/astro-ph).EP].

- Laibe, G. and D. J. Price (2012a). “Dusty gas with smoothed particle hydrodynamics - I. Algorithm and test suite”. In: *MNRAS* 420, pp. 2345–2364. DOI: [10.1111/j.1365-2966.2011.20202.x](https://doi.org/10.1111/j.1365-2966.2011.20202.x). arXiv: [1111.3090](https://arxiv.org/abs/1111.3090) [astro-ph.IM].
- (2012b). “Dusty gas with smoothed particle hydrodynamics - II. Implicit time-stepping and astrophysical drag regimes”. In: *MNRAS* 420, pp. 2365–2376. DOI: [10.1111/j.1365-2966.2011.20201.x](https://doi.org/10.1111/j.1365-2966.2011.20201.x). arXiv: [1111.3089](https://arxiv.org/abs/1111.3089) [astro-ph.IM].
- (2014). “Dusty gas with one fluid”. In: *MNRAS* 440, pp. 2136–2146. DOI: [10.1093/mnras/stu355](https://doi.org/10.1093/mnras/stu355). arXiv: [1402.5248](https://arxiv.org/abs/1402.5248) [astro-ph.EP].
- Lambrechts, M. and A. Johansen (2012). “Rapid growth of gas-giant cores by pebble accretion”. In: *A&A* 544, A32, A32. DOI: [10.1051/0004-6361/201219127](https://doi.org/10.1051/0004-6361/201219127). arXiv: [1205.3030](https://arxiv.org/abs/1205.3030) [astro-ph.EP].
- (2014). “Forming the cores of giant planets from the radial pebble flux in protoplanetary discs”. In: *A&A* 572, A107, A107. DOI: [10.1051/0004-6361/201424343](https://doi.org/10.1051/0004-6361/201424343). arXiv: [1408.6094](https://arxiv.org/abs/1408.6094) [astro-ph.EP].
- Larson, R. B. (1969). “Numerical calculations of the dynamics of collapsing protostar”. In: *MNRAS* 145, pp. 271–+.
- Leinhardt, Z. M. and S. T. Stewart (2009). “Full numerical simulations of catastrophic small body collisions”. In: *Icarus* 199, pp. 542–559. DOI: [10.1016/j.icarus.2008.09.013](https://doi.org/10.1016/j.icarus.2008.09.013). arXiv: [0811.0175](https://arxiv.org/abs/0811.0175).
- Liebes, S. (1964). “Gravitational Lenses”. In: *Physical Review* 133, pp. 835–844. DOI: [10.1103/PhysRev.133.B835](https://doi.org/10.1103/PhysRev.133.B835).
- Lin, D. N. C., P. Bodenheimer, and D. C. Richardson (1996). “Orbital migration of the planetary companion of 51 Pegasi to its present location”. In: *NATURE* 380, pp. 606–607. DOI: [10.1038/380606a0](https://doi.org/10.1038/380606a0).
- Lin, D. N. C. and J. Papaloizou (1979). “Tidal torques on accretion discs in binary systems with extreme mass ratios”. In: *MNRAS* 186, pp. 799–812.

- Lin, D. N. C. and J. Papaloizou (1986). “On the tidal interaction between protoplanets and the protoplanetary disk. III - Orbital migration of protoplanets”. In: *ApJ* 309, pp. 846–857. DOI: [10.1086/164653](https://doi.org/10.1086/164653).
- Lodato, G. and C. J. Clarke (2004). “Massive planets in FU Orionis discs: implications for thermal instability models”. In: *MNRAS* 353, pp. 841–852. DOI: [10.1111/j.1365-2966.2004.08112.x](https://doi.org/10.1111/j.1365-2966.2004.08112.x). eprint: [arXiv:astro-ph/0406264](https://arxiv.org/abs/astro-ph/0406264).
- Lodato, G. and D. J. Price (2010). “On the diffusive propagation of warps in thin accretion discs”. In: *MNRAS* 405, pp. 1212–1226. DOI: [10.1111/j.1365-2966.2010.16526.x](https://doi.org/10.1111/j.1365-2966.2010.16526.x). arXiv: [1002.2973](https://arxiv.org/abs/1002.2973) [[astro-ph](https://arxiv.org/abs/astro-ph).HE].
- Lorén-Aguilar, P. and M. R. Bate (2014). “Two-fluid dust and gas mixtures in smoothed particle hydrodynamics: a semi-implicit approach”. In: *MNRAS* 443, pp. 927–945. DOI: [10.1093/mnras/stu1173](https://doi.org/10.1093/mnras/stu1173). arXiv: [1406.3250](https://arxiv.org/abs/1406.3250) [[astro-ph](https://arxiv.org/abs/astro-ph).EP].
- (2015). “Two-fluid dust and gas mixtures in smoothed particle hydrodynamics II: an improved semi-implicit approach”. In: *MNRAS* 454, pp. 4114–4119. DOI: [10.1093/mnras/stv2262](https://doi.org/10.1093/mnras/stv2262). arXiv: [1509.08374](https://arxiv.org/abs/1509.08374) [[astro-ph](https://arxiv.org/abs/astro-ph).EP].
- (2016). “Toroidal vortices as a solution to the dust migration problem”. In: *MNRAS* 457, pp. L54–L58. DOI: [10.1093/mnras1/slv206](https://doi.org/10.1093/mnras1/slv206). arXiv: [1512.05920](https://arxiv.org/abs/1512.05920) [[astro-ph](https://arxiv.org/abs/astro-ph).EP].
- Low, C. and D. Lynden-Bell (1976). “The minimum Jeans mass or when fragmentation must stop”. In: *MNRAS* 176, pp. 367–390.
- Machida, M. N., S.-i. Inutsuka, and T. Matsumoto (2011). “Recurrent Planet Formation and Intermittent Protostellar Outflows Induced by Episodic Mass Accretion”. In: *ApJ* 729, pp. 42–+. DOI: [10.1088/0004-637X/729/1/42](https://doi.org/10.1088/0004-637X/729/1/42). arXiv: [1101.1997](https://arxiv.org/abs/1101.1997) [[astro-ph](https://arxiv.org/abs/astro-ph).SR].

- Maldonado, J. et al. (2012). “Metallicity of solar-type stars with debris discs and planets”. In: *A&A* 541, A40, A40. DOI: [10.1051/0004-6361/201218800](https://doi.org/10.1051/0004-6361/201218800). arXiv: [1202.5884](https://arxiv.org/abs/1202.5884) [astro-ph.EP].
- Malik, M. et al. (2015). “On the Gap-opening Criterion of Migrating Planets in Protoplanetary Disks”. In: *ApJ* 802, 56, p. 56. DOI: [10.1088/0004-637X/802/1/56](https://doi.org/10.1088/0004-637X/802/1/56). arXiv: [1502.06597](https://arxiv.org/abs/1502.06597) [astro-ph.EP].
- Mannings, V. and M. J. Barlow (1998). “Candidate Main-Sequence Stars with Debris Disks: A New Sample of Vega-like Sources”. In: *ApJ* 497, pp. 330–341. DOI: [10.1086/305432](https://doi.org/10.1086/305432).
- Mao, S. and B. Paczynski (1991). “Gravitational microlensing by double stars and planetary systems”. In: *ApJL* 374, pp. L37–L40. DOI: [10.1086/186066](https://doi.org/10.1086/186066).
- Marley, M. S. et al. (2007). “On the Luminosity of Young Jupiters”. In: *ApJ* 655, pp. 541–549. DOI: [10.1086/509759](https://doi.org/10.1086/509759). eprint: [arXiv:astro-ph/0609739](https://arxiv.org/abs/astro-ph/0609739).
- Marois, C. et al. (2006). “Angular Differential Imaging: A Powerful High-Contrast Imaging Technique”. In: *ApJ* 641, pp. 556–564. DOI: [10.1086/500401](https://doi.org/10.1086/500401). eprint: [astro-ph/0512335](https://arxiv.org/abs/astro-ph/0512335).
- Marois, C. et al. (2008). “Direct Imaging of Multiple Planets Orbiting the Star HR 8799”. In: *Science* 322, pp. 1348–. DOI: [10.1126/science.1166585](https://doi.org/10.1126/science.1166585). arXiv: [0811.2606](https://arxiv.org/abs/0811.2606).
- Marois, C. et al. (2010). “Images of a fourth planet orbiting HR 8799”. In: *NATURE* 468, pp. 1080–1083. DOI: [10.1038/nature09684](https://doi.org/10.1038/nature09684). arXiv: [1011.4918](https://arxiv.org/abs/1011.4918) [astro-ph.EP].
- Marshall, J. P. et al. (2014). “Correlations between the stellar, planetary, and debris components of exoplanet systems observed by Herschel”. In: *A&A* 565, A15, A15. DOI: [10.1051/0004-6361/201323058](https://doi.org/10.1051/0004-6361/201323058). arXiv: [1403.6186](https://arxiv.org/abs/1403.6186) [astro-ph.EP].

- Masset, F. (2000). “FARGO: A fast eulerian transport algorithm for differentially rotating disks”. In: *A&AS* 141, pp. 165–173. DOI: [10.1051/aas:2000116](https://doi.org/10.1051/aas:2000116). eprint: [astro-ph/9910390](https://arxiv.org/abs/astro-ph/9910390).
- Masset, F. S. (2002). “The co-orbital corotation torque in a viscous disk: Numerical simulations”. In: *A&A* 387, pp. 605–623. DOI: [10.1051/0004-6361:20020240](https://doi.org/10.1051/0004-6361:20020240). eprint: [astro-ph/0205211](https://arxiv.org/abs/astro-ph/0205211).
- Masset, F. S. and J. Casoli (2010). “Saturated Torque Formula for Planetary Migration in Viscous Disks with Thermal Diffusion: Recipe for Protoplanet Population Synthesis”. In: *ApJ* 723, pp. 1393–1417. DOI: [10.1088/0004-637X/723/2/1393](https://doi.org/10.1088/0004-637X/723/2/1393). arXiv: [1009.1913](https://arxiv.org/abs/1009.1913) [[astro-ph](https://arxiv.org/abs/astro-ph).EP].
- Masset, F. S. and J. C. B. Papaloizou (2003). “Runaway Migration and the Formation of Hot Jupiters”. In: *ApJ* 588, pp. 494–508. DOI: [10.1086/373892](https://doi.org/10.1086/373892). eprint: [astro-ph/0301171](https://arxiv.org/abs/astro-ph/0301171).
- Masunaga, H., S. M. Miyama, and S.-I. Inutsuka (1998). “A Radiation Hydrodynamic Model for Protostellar Collapse. I. The First Collapse”. In: *ApJ* 495, pp. 346–+. DOI: [10.1086/305281](https://doi.org/10.1086/305281).
- Matteucci, F. (2012). *Chemical Evolution of Galaxies*. DOI: [10.1007/978-3-642-22491-1](https://doi.org/10.1007/978-3-642-22491-1).
- Mayer, L. et al. (2004). “The Evolution of Gravitationally Unstable Protoplanetary Disks: Fragmentation and Possible Giant Planet Formation”. In: *ApJ* 609, pp. 1045–1064. DOI: [10.1086/421288](https://doi.org/10.1086/421288). eprint: [arXiv:astro-ph/0310771](https://arxiv.org/abs/astro-ph/0310771).
- Mayor, M. and D. Queloz (1995). “A Jupiter-mass companion to a solar-type star”. In: *NATURE* 378, pp. 355–359. DOI: [10.1038/378355a0](https://doi.org/10.1038/378355a0).
- Mayor, M. et al. (2011). “The HARPS search for southern extra-solar planets XXXIV. Occurrence, mass distribution and orbital properties of super-Earths and Neptune-mass planets”. In: *ArXiv e-prints (astro-ph 1109.2497)*. arXiv: [1109.2497](https://arxiv.org/abs/1109.2497) [[astro-ph](https://arxiv.org/abs/astro-ph).EP].

- McCrea, W. H. and I. P. Williams (1965). “Segregation of Materials in Cosmogony”. In: *Royal Society of London Proceedings Series A* 287, pp. 143–164.
- Mercer, A. and D. Stamatellos (2017). “The effect of radiative feedback on disc fragmentation”. In: *MNRAS* 465, pp. 2–18. DOI: [10.1093/mnras/stw2714](https://doi.org/10.1093/mnras/stw2714). arXiv: [1610.08248](https://arxiv.org/abs/1610.08248) [astro-ph.EP].
- Meru, F. (2015). “Triggered fragmentation in self-gravitating discs: forming fragments at small radii”. In: *MNRAS* 454, pp. 2529–2538. DOI: [10.1093/mnras/stv2128](https://doi.org/10.1093/mnras/stv2128). arXiv: [1509.03635](https://arxiv.org/abs/1509.03635) [astro-ph.EP].
- Meru, F. and M. R. Bate (2010). “Exploring the conditions required to form giant planets via gravitational instability in massive protoplanetary discs”. In: *MNRAS* 406, pp. 2279–2288. DOI: [10.1111/j.1365-2966.2010.16867.x](https://doi.org/10.1111/j.1365-2966.2010.16867.x). arXiv: [1004.3766](https://arxiv.org/abs/1004.3766) [astro-ph.EP].
- Miller, N. and J. J. Fortney (2011). “The Heavy-element Masses of Extrasolar Giant Planets, Revealed”. In: *ApJL* 736, L29, p. L29. DOI: [10.1088/2041-8205/736/2/L29](https://doi.org/10.1088/2041-8205/736/2/L29). arXiv: [1105.0024](https://arxiv.org/abs/1105.0024) [astro-ph.EP].
- Mizuno, H. (1980). “Formation of the Giant Planets”. In: *Progress of Theoretical Physics* 64, pp. 544–557. DOI: [10.1143/PTP.64.544](https://doi.org/10.1143/PTP.64.544).
- Moe, M., K. M. Kratter, and C. Badenes (2018). “The Close Binary Fraction of Solar-type Stars is Strongly Anti-correlated with Metallicity”. In: *ArXiv e-prints*. arXiv: [1808.02116](https://arxiv.org/abs/1808.02116) [astro-ph.SR].
- Monaghan, J. J. (1992). “Smoothed particle hydrodynamics”. In: *ARA&A* 30, pp. 543–574. DOI: [10.1146/annurev.aa.30.090192.002551](https://doi.org/10.1146/annurev.aa.30.090192.002551).
- (1997). “SPH and Riemann Solvers”. In: *Journal of Computational Physics* 136, pp. 298–307. DOI: [10.1006/jcph.1997.5732](https://doi.org/10.1006/jcph.1997.5732).
- (2002). “SPH compressible turbulence”. In: *MNRAS* 335, pp. 843–852. DOI: [10.1046/j.1365-8711.2002.05678.x](https://doi.org/10.1046/j.1365-8711.2002.05678.x). eprint: [astro-ph/0204118](https://arxiv.org/abs/astro-ph/0204118).

- Monaghan, J. J. and J. C. Lattanzio (1985). “A refined particle method for astrophysical problems”. In: *A&A* 149, pp. 135–143.
- Mordasini, C. et al. (2009). “Extrasolar planet population synthesis. II. Statistical comparison with observations”. In: *A&A* 501, pp. 1161–1184. DOI: [10.1051/0004-6361/200810697](https://doi.org/10.1051/0004-6361/200810697). arXiv: [0904.2542](https://arxiv.org/abs/0904.2542) [[astro-ph.EP](#)].
- Mordasini, C. et al. (2012). “Extrasolar planet population synthesis . IV. Correlations with disk metallicity, mass, and lifetime”. In: *A&A* 541, A97, A97. DOI: [10.1051/0004-6361/201117350](https://doi.org/10.1051/0004-6361/201117350). arXiv: [1201.1036](https://arxiv.org/abs/1201.1036) [[astro-ph.EP](#)].
- Moro-Martín, A. et al. (2007). “Are Debris Disks and Massive Planets Correlated?” In: *ApJ* 658, pp. 1312–1321. DOI: [10.1086/511746](https://doi.org/10.1086/511746). eprint: [astro-ph/0612242](https://arxiv.org/abs/astro-ph/0612242).
- Moro-Martín, A. et al. (2015). “Does the Presence of Planets Affect the Frequency and Properties of Extrasolar Kuiper Belts? Results from the Herschel Debris and Dunes Surveys”. In: *ApJ* 801, 143, p. 143. DOI: [10.1088/0004-637X/801/2/143](https://doi.org/10.1088/0004-637X/801/2/143). arXiv: [1501.03813](https://arxiv.org/abs/1501.03813) [[astro-ph.EP](#)].
- Morris, J.P. and J.J. Monaghan (1997). “A Switch to Reduce SPH Viscosity”. In: *Journal of Computational Physics* 136.1, pp. 41 –50. ISSN: 0021-9991. DOI: <https://doi.org/10.1006/jcph.1997.5690>. URL: <http://www.sciencedirect.com/science/article/pii/S0021999197956904>.
- Müller, S., R. Helled, and L. Mayer (2018). “On the Diversity in Mass and Orbital Radius of Giant Planets Formed via Disk Instability”. In: *ApJ* 854, 112, p. 112. DOI: [10.3847/1538-4357/aaa840](https://doi.org/10.3847/1538-4357/aaa840). arXiv: [1801.03384](https://arxiv.org/abs/1801.03384) [[astro-ph.EP](#)].
- Müller, T. W. A., W. Kley, and F. Meru (2012). “Treating gravity in thin-disk simulations”. In: *A&A* 541, A123, A123. DOI: [10.1051/0004-6361/201118737](https://doi.org/10.1051/0004-6361/201118737). arXiv: [1203.1413](https://arxiv.org/abs/1203.1413) [[astro-ph.EP](#)].
- Murray, J. (1996). “SPH simulations of tidally unstable accretion disks”. In: *IAU Colloq. 158: Cataclysmic Variables and Related Objects*. Ed. by A. Evans and Janet

- H. Wood. Vol. 208. *Astrophysics and Space Science Library*, p. 115. DOI: [10 . 1007/978-94-009-0325-8_34](https://doi.org/10.1007/978-94-009-0325-8_34).
- Nayakshin, S. (2010a). “Formation of planets by tidal downsizing of giant planet embryos”. In: *MNRAS* 408, pp. L36–L40. DOI: [10 . 1111/j . 1745-3933 . 2010 . 00923 . x](https://doi.org/10.1111/j.1745-3933.2010.00923.x). arXiv: [1007.4159](https://arxiv.org/abs/1007.4159) [[astro-ph.EP](#)].
- (2010b). “Grain sedimentation inside giant planet embryos”. In: *MNRAS* 408, pp. 2381–2396. DOI: [10 . 1111/j . 1365-2966 . 2010 . 17289 . x](https://doi.org/10.1111/j.1365-2966.2010.17289.x). arXiv: [1007.4162](https://arxiv.org/abs/1007.4162) [[astro-ph.EP](#)].
- (2011). “Formation of terrestrial planet cores inside giant planet embryos”. In: *MNRAS* 413, pp. 1462–1478. DOI: [10 . 1111 / j . 1365 - 2966 . 2011 . 18230 . x](https://doi.org/10.1111/j.1365-2966.2011.18230.x). arXiv: [1007.4165](https://arxiv.org/abs/1007.4165) [[astro-ph.EP](#)].
- (2015a). “Metal loading of giant gas planets”. In: *MNRAS* 446, pp. 459–469. DOI: [10.1093/mnras/stu2074](https://doi.org/10.1093/mnras/stu2074). arXiv: [1411.5261](https://arxiv.org/abs/1411.5261) [[astro-ph.EP](#)].
- (2015b). “Positive metallicity correlation for coreless giant planets”. In: *MNRAS* 448, pp. L25–L29. DOI: [10 . 1093 / mnras / stl191](https://doi.org/10.1093/mnras/stl191). arXiv: [1411 . 5263](https://arxiv.org/abs/1411.5263) [[astro-ph.EP](#)].
- (2015c). “Tidal downsizing model - I. Numerical methods: saving giant planets from tidal disruptions”. In: *MNRAS* 454, pp. 64–82. DOI: [10 . 1093/mnras / stv1915](https://doi.org/10.1093/mnras/stv1915). arXiv: [1411.5264](https://arxiv.org/abs/1411.5264) [[astro-ph.EP](#)].
- (2015d). “Tidal Downsizing model. II. Planet-metallicity correlations”. In: *ArXiv e-prints* ([arXiv: 1502.07585](https://arxiv.org/abs/1502.07585)).
- (2016). “Tidal Downsizing model - IV. Destructive feedback in planets”. In: *MNRAS* 461, pp. 3194–3211. DOI: [10.1093/mnras/stw1404](https://doi.org/10.1093/mnras/stw1404). arXiv: [1510.01630](https://arxiv.org/abs/1510.01630) [[astro-ph.EP](#)].
- (2017a). “A desert of gas giant planets beyond tens of au: from feast to famine”. In: *MNRAS* 470, pp. 2387–2409. DOI: [10.1093/mnras/stx1351](https://doi.org/10.1093/mnras/stx1351).

- Nayakshin, S. (2017b). “Dawes Review 7: The Tidal Downsizing Hypothesis of Planet Formation”. In: *PASA* 34, e002, e002. DOI: [10.1017/pasa.2016.55](https://doi.org/10.1017/pasa.2016.55). arXiv: [1609.07503](https://arxiv.org/abs/1609.07503) [astro-ph.EP].
- Nayakshin, S. and S.-H. Cha (2012). “An alternative origin for debris rings of planetesimals”. In: *MNRAS* 423, pp. 2104–2119. DOI: [10.1111/j.1365-2966.2012.21003.x](https://doi.org/10.1111/j.1365-2966.2012.21003.x). arXiv: [1203.1182](https://arxiv.org/abs/1203.1182) [astro-ph.EP].
- (2013). “Radiative feedback from protoplanets in self-gravitating protoplanetary discs”. In: *MNRAS* 435, pp. 2099–2108. DOI: [10.1093/mnras/stt1426](https://doi.org/10.1093/mnras/stt1426). arXiv: [1306.4924](https://arxiv.org/abs/1306.4924) [astro-ph.EP].
- Nayakshin, S. and M. Fletcher (2015). “Tidal Downsizing model - III. Planets from sub-Earths to brown dwarfs: structure and metallicity preferences”. In: *MNRAS* 452, pp. 1654–1676. DOI: [10.1093/mnras/stv1354](https://doi.org/10.1093/mnras/stv1354). arXiv: [1504.02365](https://arxiv.org/abs/1504.02365) [astro-ph.EP].
- O’dell, C. R., Z. Wen, and X. Hu (1993). “Discovery of new objects in the Orion nebula on HST images - Shocks, compact sources, and protoplanetary disks”. In: *ApJ* 410, pp. 696–700. DOI: [10.1086/172786](https://doi.org/10.1086/172786).
- Ormel, C. W. and H. H. Klahr (2010). “The effect of gas drag on the growth of protoplanets. Analytical expressions for the accretion of small bodies in laminar disks”. In: *A&A* 520, A43, A43. DOI: [10.1051/0004-6361/201014903](https://doi.org/10.1051/0004-6361/201014903). arXiv: [1007.0916](https://arxiv.org/abs/1007.0916) [astro-ph.EP].
- Oudmaijer, R. D. et al. (1992). “SAO stars with infrared excess in the IRAS Point Source Catalog”. In: *A&AS* 96, pp. 625–643.
- Owen, J. E., C. J. Clarke, and B. Ercolano (2012). “On the theory of disc photoevaporation”. In: *MNRAS* 422, pp. 1880–1901. DOI: [10.1111/j.1365-2966.2011.20337.x](https://doi.org/10.1111/j.1365-2966.2011.20337.x). arXiv: [1112.1087](https://arxiv.org/abs/1112.1087) [astro-ph.SR].

- Owen, J. E., B. Ercolano, and C. J. Clarke (2011). “Protoplanetary disc evolution and dispersal: the implications of X-ray photoevaporation”. In: *MNRAS* 412, pp. 13–25. DOI: [10.1111/j.1365-2966.2010.17818.x](https://doi.org/10.1111/j.1365-2966.2010.17818.x). arXiv: [1010.0826](https://arxiv.org/abs/1010.0826) [astro-ph.SR].
- Owen, J. E. et al. (2010). “Radiation-hydrodynamic models of X-ray and EUV photoevaporating protoplanetary discs”. In: *MNRAS* 401, pp. 1415–1428. DOI: [10.1111/j.1365-2966.2009.15771.x](https://doi.org/10.1111/j.1365-2966.2009.15771.x). arXiv: [0909.4309](https://arxiv.org/abs/0909.4309) [astro-ph.SR].
- Paardekooper, S.-J. and G. Mellema (2006). “Dust flow in gas disks in the presence of embedded planets”. In: *A&A* 453, pp. 1129–1140. DOI: [10.1051/0004-6361:200544449](https://doi.org/10.1051/0004-6361:200544449). eprint: [astro-ph/0603132](https://arxiv.org/abs/astro-ph/0603132).
- Paardekooper, S.-J., H. Rein, and W. Kley (2013). “The formation of systems with closely spaced low-mass planets and the application to Kepler-36”. In: *MNRAS* 434, pp. 3018–3029. DOI: [10.1093/mnras/stt1224](https://doi.org/10.1093/mnras/stt1224). arXiv: [1304.4762](https://arxiv.org/abs/1304.4762) [astro-ph.EP].
- Pascucci, I. et al. (2016). “A Steeper than Linear Disk Mass-Stellar Mass Scaling Relation”. In: *ApJ* 831, 125, p. 125. DOI: [10.3847/0004-637X/831/2/125](https://doi.org/10.3847/0004-637X/831/2/125). arXiv: [1608.03621](https://arxiv.org/abs/1608.03621) [astro-ph.EP].
- Plavchan, P. et al. (2009). “New Debris Disks Around Young, Low-Mass Stars Discovered with the Spitzer Space Telescope”. In: *ApJ* 698, pp. 1068–1094. DOI: [10.1088/0004-637X/698/2/1068](https://doi.org/10.1088/0004-637X/698/2/1068). arXiv: [0904.0819](https://arxiv.org/abs/0904.0819) [astro-ph.SR].
- Pollack, J. B. et al. (1996). “Formation of the Giant Planets by Concurrent Accretion of Solids and Gas”. In: *Icarus* 124, pp. 62–85. DOI: [10.1006/icar.1996.0190](https://doi.org/10.1006/icar.1996.0190).
- Price, D. J. (2012). “Smoothed particle hydrodynamics and magnetohydrodynamics”. In: *Journal of Computational Physics* 231, pp. 759–794. DOI: [10.1016/j.jcp.2010.12.011](https://doi.org/10.1016/j.jcp.2010.12.011). arXiv: [1012.1885](https://arxiv.org/abs/1012.1885) [astro-ph.IM].

- Price, D. J. and C. Federrath (2010). “A comparison between grid and particle methods on the statistics of driven, supersonic, isothermal turbulence”. In: *MNRAS* 406, pp. 1659–1674. DOI: [10.1111/j.1365-2966.2010.16810.x](https://doi.org/10.1111/j.1365-2966.2010.16810.x). arXiv: [1004.1446](https://arxiv.org/abs/1004.1446).
- Price, D. J. and G. Laibe (2015). “A fast and explicit algorithm for simulating the dynamics of small dust grains with smoothed particle hydrodynamics”. In: *MNRAS* 451, pp. 813–826. DOI: [10.1093/mnras/stv996](https://doi.org/10.1093/mnras/stv996). arXiv: [1505.00969](https://arxiv.org/abs/1505.00969) [[astro-ph.IM](https://arxiv.org/abs/1505.00969)].
- Price, D. J. et al. (2017). “Phantom: A smoothed particle hydrodynamics and magnetohydrodynamics code for astrophysics”. In: *ArXiv e-prints*. arXiv: [1702.03930](https://arxiv.org/abs/1702.03930) [[astro-ph.IM](https://arxiv.org/abs/1702.03930)].
- Pringle, J. E. (1981). “Accretion discs in astrophysics”. In: *ARA&A* 19, pp. 137–162. DOI: [10.1146/annurev.aa.19.090181.001033](https://doi.org/10.1146/annurev.aa.19.090181.001033).
- Rafikov, R. R. (2005). “Can Giant Planets Form by Direct Gravitational Instability?” In: *ApJL* 621, pp. L69–L72. DOI: [10.1086/428899](https://doi.org/10.1086/428899).
- Raghavan, D. et al. (2010). “A Survey of Stellar Families: Multiplicity of Solar-type Stars”. In: *ApJS* 190, pp. 1–42. DOI: [10.1088/0067-0049/190/1/1](https://doi.org/10.1088/0067-0049/190/1/1). arXiv: [1007.0414](https://arxiv.org/abs/1007.0414) [[astro-ph.SR](https://arxiv.org/abs/1007.0414)].
- Raymond, S. N. et al. (2011). “Debris disks as signposts of terrestrial planet formation”. In: *A&A* 530, A62, A62. DOI: [10.1051/0004-6361/201116456](https://doi.org/10.1051/0004-6361/201116456). arXiv: [1104.0007](https://arxiv.org/abs/1104.0007) [[astro-ph.EP](https://arxiv.org/abs/1104.0007)].
- Rees, M. J. (1976). “Opacity-limited hierarchical fragmentation and the masses of protostars”. In: *MNRAS* 176, pp. 483–486.
- Reggiani, M. et al. (2016). “The VLT/NaCo large program to probe the occurrence of exoplanets and brown dwarfs at wide orbits . III. The frequency of brown dwarfs and giant planets as companions to solar-type stars”. In: *A&A*

- 586, A147, A147. DOI: [10.1051/0004-6361/201525930](https://doi.org/10.1051/0004-6361/201525930). arXiv: [1510.08453](https://arxiv.org/abs/1510.08453) [astro-ph.EP].
- Ricci, L. et al. (2015). "ALMA Observations of the Debris Disk around the Young Solar Analog HD 107146". In: *ApJ* 798, 124, p. 124. DOI: [10.1088/0004-637X/798/2/124](https://doi.org/10.1088/0004-637X/798/2/124). arXiv: [1410.8265](https://arxiv.org/abs/1410.8265) [astro-ph.EP].
- Rice, K. et al. (2015). "Disc fragmentation rarely forms planetary-mass objects". In: *ArXiv e-prints*. arXiv: [1508.06528](https://arxiv.org/abs/1508.06528) [astro-ph.EP].
- Rice, W. K. M., G. Lodato, and P. J. Armitage (2005). "Investigating fragmentation conditions in self-gravitating accretion discs". In: *MNRAS* 364, pp. L56–L60. DOI: [10.1111/j.1745-3933.2005.00105.x](https://doi.org/10.1111/j.1745-3933.2005.00105.x). eprint: [astro-ph/0509413](https://arxiv.org/abs/astro-ph/0509413).
- Safronov, V. S. (1972). *Evolution of the protoplanetary cloud and formation of the earth and planets*. Jerusalem (Israel): Israel Program for Scientific Translations, Keter Publishing House, 212 p.
- Santerne, A. et al. (2016). "SOPHIE velocimetry of Kepler transit candidates. XVII. The physical properties of giant exoplanets within 400 days of period". In: *A&A* 587, A64, A64. DOI: [10.1051/0004-6361/201527329](https://doi.org/10.1051/0004-6361/201527329). arXiv: [1511.00643](https://arxiv.org/abs/1511.00643) [astro-ph.EP].
- Santos, N. C. et al. (2017). "Observational evidence for two distinct giant planet populations". In: *ArXiv e-prints*. arXiv: [1705.06090](https://arxiv.org/abs/1705.06090) [astro-ph.EP].
- Schneider, J. et al. (2011). "Defining and cataloging exoplanets: the exoplanet.eu database". In: *A&A* 532, A79, A79. DOI: [10.1051/0004-6361/201116713](https://doi.org/10.1051/0004-6361/201116713). arXiv: [1106.0586](https://arxiv.org/abs/1106.0586) [astro-ph.EP].
- Shakura, N. I. and R. A. Sunyaev (1973). "Black holes in binary systems. Observational appearance." In: *A&A* 24, pp. 337–355.

- Shu, F. H., D. Johnstone, and D. Hollenbach (1993). “Photoevaporation of the solar nebula and the formation of the giant planets”. In: *Icarus* 106, p. 92. DOI: [10.1006/icar.1993.1160](https://doi.org/10.1006/icar.1993.1160).
- Shvartzvald, Y. et al. (2016). “The frequency of snowline-region planets from four years of OGLE-MOA-Wise second-generation microlensing”. In: *MNRAS* 457, pp. 4089–4113. DOI: [10.1093/mnras/stw191](https://doi.org/10.1093/mnras/stw191). arXiv: [1510.04297](https://arxiv.org/abs/1510.04297) [astro-ph.EP].
- Sousa, S. G. et al. (2008). “Spectroscopic parameters for 451 stars in the HARPS GTO planet search program. Stellar [Fe/H] and the frequency of exo-Neptunes”. In: *A&A* 487, pp. 373–381. DOI: [10.1051/0004-6361:200809698](https://doi.org/10.1051/0004-6361:200809698). arXiv: [0805.4826](https://arxiv.org/abs/0805.4826).
- Springel, V. (2005). “The cosmological simulation code GADGET-2”. In: *MNRAS* 364, pp. 1105–1134. DOI: [10.1111/j.1365-2966.2005.09655.x](https://doi.org/10.1111/j.1365-2966.2005.09655.x).
- Springel, V. and L. Hernquist (2002). “Cosmological smoothed particle hydrodynamics simulations: the entropy equation”. In: *MNRAS* 333, pp. 649–664.
- Stamatellos, D. (2015). “The Migration of Gas Giant Planets in Gravitationally Unstable Disks”. In: *ApJL* 810, L11, p. L11. DOI: [10.1088/2041-8205/810/1/L11](https://doi.org/10.1088/2041-8205/810/1/L11). arXiv: [1508.01196](https://arxiv.org/abs/1508.01196) [astro-ph.EP].
- Stamatellos, D. and S.-i. Inutsuka (2018). “The diverse lives of massive protoplanets in self-gravitating discs”. In: *MNRAS* 477, pp. 3110–3135. DOI: [10.1093/mnras/sty827](https://doi.org/10.1093/mnras/sty827). arXiv: [1804.00583](https://arxiv.org/abs/1804.00583) [astro-ph.EP].
- Stamatellos, D. and A. P. Whitworth (2008). “Can giant planets form by gravitational fragmentation of discs?”. In: *A&A* 480, pp. 879–887. DOI: [10.1051/0004-6361:20078628](https://doi.org/10.1051/0004-6361:20078628). arXiv: [0709.0966](https://arxiv.org/abs/0709.0966).

- Stamatellos, D. and A. P. Whitworth (2009). “The role of thermodynamics in disc fragmentation”. In: *MNRAS* 400, pp. 1563–1573. DOI: [10.1111/j.1365-2966.2009.15564.x](https://doi.org/10.1111/j.1365-2966.2009.15564.x). arXiv: [0908.2247](https://arxiv.org/abs/0908.2247) [astro-ph.GA].
- Stamatellos, D., A. P. Whitworth, and D. A. Hubber (2011). “The Importance of Episodic Accretion for Low-mass Star Formation”. In: *ApJ* 730, 32, p. 32. DOI: [10.1088/0004-637X/730/1/32](https://doi.org/10.1088/0004-637X/730/1/32). arXiv: [1103.1378](https://arxiv.org/abs/1103.1378).
- Stone, J. M. and M. L. Norman (1992). “ZEUS-2D: A radiation magnetohydrodynamics code for astrophysical flows in two space dimensions. I - The hydrodynamic algorithms and tests.” In: *ApJS* 80, pp. 753–790. DOI: [10.1086/191680](https://doi.org/10.1086/191680).
- Struve, O. (1952). “Proposal for a project of high-precision stellar radial velocity work”. In: *The Observatory* 72, pp. 199–200.
- Svensson, R. and A. A. Zdziarski (1994). “Black hole accretion disks with coroneae”. In: *ApJ* 436, pp. 599–606.
- Syer, D. and C. J. Clarke (1995). “Satellites in discs: regulating the accretion luminosity”. In: *MNRAS* 277, pp. 758–766. eprint: [arXiv:astro-ph/9505021](https://arxiv.org/abs/astro-ph/9505021).
- Takami, M. et al. (2018). “Near-Infrared High-Resolution Imaging Polarimetry of FU Ori-Type Objects: Towards A Unified Scheme for Low-Mass Protostellar Evolution”. In: *ArXiv e-prints*. arXiv: [1807.03499](https://arxiv.org/abs/1807.03499) [astro-ph.SR].
- Takeuchi, T., S. M. Miyama, and D. N. C. Lin (1996). “Gap Formation in Protoplanetary Disks”. In: *ApJ* 460, pp. 832–+. DOI: [10.1086/177013](https://doi.org/10.1086/177013).
- Tanaka, H., T. Takeuchi, and W. R. Ward (2002). “Three-Dimensional Interaction between a Planet and an Isothermal Gaseous Disk. I. Corotation and Lindblad Torques and Planet Migration”. In: *ApJ* 565, pp. 1257–1274.
- Thorngren, D. P. et al. (2016). “The MassMetallicity Relation for Giant Planets”. In: *ApJ* 831, 64, p. 64. DOI: [10.3847/0004-637X/831/1/64](https://doi.org/10.3847/0004-637X/831/1/64). arXiv: [1511.07854](https://arxiv.org/abs/1511.07854) [astro-ph.EP].

- Tobin, J. J. et al. (2016). “A triple protostar system formed via fragmentation of a gravitationally unstable disk”. In: *NATURE* 538, pp. 483–486. DOI: [10.1038/nature20094](https://doi.org/10.1038/nature20094). arXiv: [1610.08524](https://arxiv.org/abs/1610.08524) [[astro-ph.SR](#)].
- Toomre, A. (1964). “On the gravitational stability of a disk of stars”. In: *ApJ* 139, pp. 1217–1238.
- Troup, N. W. et al. (2016). “Companions to APOGEE Stars. I. A Milky Way-spanning Catalog of Stellar and Substellar Companion Candidates and Their Diverse Hosts”. In: *AJ* 151, 85, p. 85. DOI: [10.3847/0004-6256/151/3/85](https://doi.org/10.3847/0004-6256/151/3/85). arXiv: [1601.00688](https://arxiv.org/abs/1601.00688) [[astro-ph.SR](#)].
- Tsukamoto, Y. et al. (2015). “Effects of radiative transfer on the structure of self-gravitating discs, their fragmentation and the evolution of the fragments”. In: *MNRAS* 446, pp. 1175–1190. DOI: [10.1093/mnras/stu2160](https://doi.org/10.1093/mnras/stu2160). arXiv: [1404.7271](https://arxiv.org/abs/1404.7271) [[astro-ph.SR](#)].
- Tychoniec, Ł. et al. (2018). “The VLA Nascent Disk And Multiplicity Survey of Perseus Protostars (VANDAM). IV. Free-Free Emission from Protostars: Links to Infrared Properties, Outflow Tracers, and Protostellar Disk Masses”. In: *ArXiv e-prints*. arXiv: [1806.02434](https://arxiv.org/abs/1806.02434) [[astro-ph.SR](#)].
- Vanderburg, A. et al. (2016). “Radial velocity planet detection biases at the stellar rotational period”. In: *MNRAS* 459, pp. 3565–3573. DOI: [10.1093/mnras/stw863](https://doi.org/10.1093/mnras/stw863). arXiv: [1604.03143](https://arxiv.org/abs/1604.03143) [[astro-ph.EP](#)].
- Vazan, A. and R. Helled (2012). “On the Evolution and Survival of Protoplanets Embedded in a Protoplanetary Disk”. In: *ApJ* 756, 90, p. 90. DOI: [10.1088/0004-637X/756/1/90](https://doi.org/10.1088/0004-637X/756/1/90). arXiv: [1206.5887](https://arxiv.org/abs/1206.5887) [[astro-ph.EP](#)].
- Vigan, A. et al. (2012). “The International Deep Planet Survey. I. The frequency of wide-orbit massive planets around A-stars”. In: *A&A* 544, A9, A9. DOI: [10.1051/0004-6361/201218991](https://doi.org/10.1051/0004-6361/201218991). arXiv: [1206.4048](https://arxiv.org/abs/1206.4048) [[astro-ph.EP](#)].

- Vigan, A. et al. (2017). “The VLT/NaCo large program to probe the occurrence of exoplanets and brown dwarfs at wide orbits. IV. Gravitational instability rarely forms wide, giant planets”. In: *ArXiv e-prints*. arXiv: [1703.05322](https://arxiv.org/abs/1703.05322) [astro-ph.EP].
- Vorobyov, E. I. and S. Basu (2005). “The Origin of Episodic Accretion Bursts in the Early Stages of Star Formation”. In: *ApJL* 633, pp. L137–L140. DOI: [10.1086/498303](https://doi.org/10.1086/498303). eprint: [arXiv:astro-ph/0510014](https://arxiv.org/abs/astro-ph/0510014).
- (2006). “The Burst Mode of Protostellar Accretion”. In: *ApJ* 650, pp. 956–969. DOI: [10.1086/507320](https://doi.org/10.1086/507320). eprint: [arXiv:astro-ph/0607118](https://arxiv.org/abs/astro-ph/0607118).
- (2010). “The Burst Mode of Accretion and Disk Fragmentation in the Early Embedded Stages of Star Formation”. In: *ApJ* 719, pp. 1896–1911. DOI: [10.1088/0004-637X/719/2/1896](https://doi.org/10.1088/0004-637X/719/2/1896). arXiv: [1007.2993](https://arxiv.org/abs/1007.2993) [astro-ph.SR].
- Wadsley, J. W., J. Stadel, and T. Quinn (2004). “Gasoline: a flexible, parallel implementation of TreeSPH”. In: 9, pp. 137–158. DOI: [10.1016/j.newast.2003.08.004](https://doi.org/10.1016/j.newast.2003.08.004). eprint: [astro-ph/0303521](https://arxiv.org/abs/astro-ph/0303521).
- Wadsley, J. W., G. Veeravalli, and H. M. P. Couchman (2008). “On the treatment of entropy mixing in numerical cosmology”. In: *MNRAS* 387, pp. 427–438. DOI: [10.1111/j.1365-2966.2008.13260.x](https://doi.org/10.1111/j.1365-2966.2008.13260.x).
- Wang, J. and D. A. Fischer (2015). “Revealing a Universal Planet-Metallicity Correlation for Planets of Different Solar-Type Stars”. In: *AJ* 149, 14, p. 14. DOI: [10.1088/0004-6256/149/1/14](https://doi.org/10.1088/0004-6256/149/1/14).
- Ward, W. R. (1982). “Tidal Barriers in the Solar Nebula”. In: *Lunar and Planetary Science Conference*. Vol. 13. Lunar and Planetary Science Conference, pp. 831–832.
- (1997). “Protoplanet Migration by Nebula Tides”. In: *Icarus* 126, pp. 261–281. DOI: [10.1006/icar.1996.5647](https://doi.org/10.1006/icar.1996.5647).

- Weidenschilling, S. J. (1977a). “Aerodynamics of solid bodies in the solar nebula”. In: *MNRAS* 180, pp. 57–70.
- (1977b). “The distribution of mass in the planetary system and solar nebula”. In: *Ap&SS* 51, pp. 153–158. DOI: [10.1007/BF00642464](https://doi.org/10.1007/BF00642464).
- (1988). “Formation processes and time scales for meteorite parent bodies”. In: *Meteorites and the Early Solar System*. Ed. by Kerridge, J. F. & Matthews, M. S., pp. 348–371.
- Wendland, H. (1995). “Piecewise polynomial, positive definite and compactly supported radial functions of minimal degree”. In: *Adv. Comp. Math.* 4, pp. 389–396.
- Wetherill, G. W. (1990). “Formation of the earth”. In: *Annual Review of Earth and Planetary Sciences* 18, pp. 205–256. DOI: [10.1146/annurev.ea.18.050190.001225](https://doi.org/10.1146/annurev.ea.18.050190.001225).
- Wheatley, P. J. et al. (2018). “The Next Generation Transit Survey (NGTS)”. In: *MNRAS* 475, pp. 4476–4493. DOI: [10.1093/mnras/stx2836](https://doi.org/10.1093/mnras/stx2836). arXiv: [1710.11100](https://arxiv.org/abs/1710.11100) [[astro-ph.EP](#)].
- Whipple, F. L. (1972). “On certain aerodynamic processes for asteroids and comets”. In: *From Plasma to Planet*. Ed. by A. Elvius, p. 211.
- Williams, J. P. and L. A. Cieza (2011). “Protoplanetary Disks and Their Evolution”. In: *ArXiv e-prints*. arXiv: [1103.0556](https://arxiv.org/abs/1103.0556) [[astro-ph.GA](#)].
- Windmark, F. et al. (2012). “Planetesimal formation by sweep-up: how the bouncing barrier can be beneficial to growth”. In: *A&A* 540, A73, A73. DOI: [10.1051/0004-6361/201118475](https://doi.org/10.1051/0004-6361/201118475). arXiv: [1201.4282](https://arxiv.org/abs/1201.4282) [[astro-ph.EP](#)].
- Winn, J. N. and D. C. Fabrycky (2015). “The Occurrence and Architecture of Exoplanetary Systems”. In: *ARA&A* 53, pp. 409–447. DOI: [10.1146/annurev-astro-082214-122246](https://doi.org/10.1146/annurev-astro-082214-122246). arXiv: [1410.4199](https://arxiv.org/abs/1410.4199) [[astro-ph.EP](#)].

- Wyatt, M. C. (2008). “Evolution of Debris Disks”. In: *ARA&A* 46, pp. 339–383. DOI: [10.1146/annurev.astro.45.051806.110525](https://doi.org/10.1146/annurev.astro.45.051806.110525).
- Wyatt, M. C. et al. (2007). “Transience of Hot Dust around Sun-like Stars”. In: *ApJ* 658, pp. 569–583. DOI: [10.1086/510999](https://doi.org/10.1086/510999). eprint: [arXiv:astro-ph/0610102](https://arxiv.org/abs/astro-ph/0610102).
- Wyatt, M. C. et al. (2012). “Herschel imaging of 61 Vir: implications for the prevalence of debris in low-mass planetary systems”. In: *MNRAS* 424, pp. 1206–1223. DOI: [10.1111/j.1365-2966.2012.21298.x](https://doi.org/10.1111/j.1365-2966.2012.21298.x). arXiv: [1206.2370](https://arxiv.org/abs/1206.2370) [[astro-ph.EP](#)].
- Youdin, A. N. and J. Goodman (2005). “Streaming Instabilities in Protoplanetary Disks”. In: *ApJ* 620, pp. 459–469. DOI: [10.1086/426895](https://doi.org/10.1086/426895). eprint: [arXiv:astro-ph/0409263](https://arxiv.org/abs/astro-ph/0409263).
- Zhu, Z. et al. (2012a). “Challenges in Forming Planets by Gravitational Instability: Disk Irradiation and Clump Migration, Accretion, and Tidal Destruction”. In: *ApJ* 746, 110, p. 110. DOI: [10.1088/0004-637X/746/1/110](https://doi.org/10.1088/0004-637X/746/1/110). arXiv: [1111.6943](https://arxiv.org/abs/1111.6943) [[astro-ph.SR](#)].
- Zhu, Z. et al. (2012b). “Dust Filtration by Planet-induced Gap Edges: Implications for Transitional Disks”. In: *ApJ* 755, 6, p. 6. DOI: [10.1088/0004-637X/755/1/6](https://doi.org/10.1088/0004-637X/755/1/6). arXiv: [1205.5042](https://arxiv.org/abs/1205.5042) [[astro-ph.SR](#)].